


# Tutorial Proposal Form

<b>Name</b>	<b>Yoichi Hori</b>	<b>Country</b>	<b>Japan</b>
<b>Affiliation</b>	<b>University of Tokyo</b>	<b>Position</b>	<b>Professor</b>
<b>Telephone</b>	<b>+81-4-7136-3846</b>	<b>Fax</b>	<b>+81-4-7136-3847</b>
<b>E-mail</b>	<b>hori@k.u-tokyo.ac.jp</b>		
<b>Biography</b>	<p><u>Education Background</u>            1978 B.A. The University of Tokyo, Japan (Electrical Engineering)            1980 M.A. The University of Tokyo, Japan (Electronic Engineering)            1983 Ph.D. The University of Tokyo, Japan (Electronic Engineering)</p> <p><u>Professional Experiences</u>            1983-1984 Research Associate, Dept. of Elec. Eng., Univ. of Tokyo            1984-1988 Assistant Professor, Dept. of Elec. Eng., Univ. of Tokyo            1989-1995 Associate Professor, Dept. of Elec. Eng., Univ. of Tokyo            1995-2000 Associate Professor, Eng. Research Institute, Univ. of Tokyo            2000-2002 Professor, Dept. of Elec. Eng., Univ. of Tokyo            2002-2008 Professor, Institute of Industrial Science, Univ. of Tokyo            2008- present Professor, Dept. of Advanced Energy, Univ. of Tokyo            (1991-1992 Visiting Scientist, University of California, Berkeley, USA)</p> <p><u>Academic Societies</u>            IEEE (Fellow member, IES AdCom member), IEE-Japan (Fellow member, Past President of the Industry Applications Society), The Society of Automotive Engineers of Japan (Director on Technological Developments), The Society of Instrument and Control Engineers, Robotics Society of Japan, Japan Society of Mechanical Engineers, etc. President of Capacitors Forum, Chairman of Motor Technology Symposium of Japan Management Association (JMA), etc.</p>		
<b>Tutorial Topic</b>	Novel EV Society Based on Motor/ Capacitor/ Wireless - Application of Electric Motor, Supercapacitors, and Wireless Power Transfer to Enhance Operation of Future Vehicles –		
<b>Description of the Topic</b>	<p>Future electric vehicles (EVs) will be linked to the electric power system infrastructure; the vehicles will operate through frequent electric charging, as is the case with electric trains.</p> <p>Conventional batteries require a long recharging time; therefore, supercapacitors, rather than batteries, will play an important role in the future for charging of EVs. Supercapacitors have a long operating life, large current density, and environmentally friendly composition. Further, their energy level can be estimated from their terminal voltage. Because our EVs powered by supercapacitors can operate for more than 20 min after being charged for only 30 s, the requirement for constant recharging of EVs is reduced substantially, thereby increasing the efficiency of these EVs.</p> <p>Wireless power transfer based on magnetic resonance is an extremely important technique that needs to be considered for enhancing the efficiency of EVs. In a laboratory experiment, this technique enabled approximately 50 W power transfer with more than 95% efficiency at a distance of more than 50 cm. This distance can be easily extended to several meters by simple repeating antenna.</p> <p>In order to improve energy efficiency and safety of future EVs, the implementation of novel motion control techniques is required. Since EVs are powered by electric motors, they have three major advantages: motor torque generation is quick and accurate, a motor can be attached to each wheel, and motor torque can be estimated precisely. These advantages enable the realization of high performance antilock braking and traction control systems, control of two-dimensional chassis motion, and estimation of road surface condition.</p> <p>In summary, we can achieve a large-scale development of future vehicles that employ three techniques: Electric Motors, Supercapacitors, and Wireless Power Transfer. This eliminates the requirement for engines, high performance Li-ion batteries, and large charging stations.</p>		
<b>Photo</b>			

## Attached papers

- (1) Yoichi Hori, Novel EV Society based on Motor/ Capacitor/ Wireless - Application of Electric Motor, Supercapacitors, and Wireless Power Transfer to Enhance Operation of Future Vehicles -, 2012 IEEE MTTT International Microwave Workshop Series on Innovative Wireless Power Transmission: Technologies, Systems, and Applications (IMWS-IWPT2012) , invited keynote speech, 2012.5.10-11, Kyoto
- (2) Yoichi Hori, Toshiyuki Uchida, Sehoon Oh, Takehiro Imura, Valerio Salvucci, Ryo Minaki, Nam Kanghyun, Wang Yafei and Teck Chuan Beh, Advanced Motion Control and Electric Power Transfer System for Comfortable Secure-Life, GCOE Symposium for Secure Life Electronics, 2010.11.16, Tokyo.
- (3) Yoichi Hori, Yasushi Toyoda and Yoshimasa Tsuruoka, Traction Control of Electric Vehicle based on the Estimation of Road Surface Condition - Basic Experimental Results using the Test EV UOT Electric March -, Proc. PCC Nagaoka '97, Vol. 1, pp. 1-8, 1997, Nagaoka.
- (4) Yoichi Hori, Future Vehicle driven by Electricity and Control -Research on 4 Wheel Motored 'UOT March II'-, IEEE Trans. on Industrial Electronics, Vol. 51, No. 5, pp. 954-962, 2004.
- (5) Cong Geng, Lotfi Mostefai and Yoichi Hori, Direct Yaw Moment Control Evaluation of an In-Wheel-Motored Electric Vehicle Based on Body Slip Angle Fuzzy Observer, IEEE Transactions on Industrial Electronics, Vol. 56, No. 5, pp. 1411-1419, 2009.
- (6) Dejun Yin, Sehoon Oh and Yoichi Hori, A Novel Traction Control for EV Based on Maximum Transmissible Torque Estimation, IEEE Transactions on Industrial Electronics, Vol. 56, No. 6, pp. 2086-2094, 2009.
- (7) Jia-Sheng Hu, Dejun Yin and Yoichi Hori, Fault-tolerant Traction Control of Electric Vehicles, Control Engineering Practice, Vol. 19, pp. 204-213, 2011.
- (8) Jia-Sheng Hu, Dejun Yin, Yoichi Hori and Feng-Rung Hu, A New MTTE Methodology for Electric Vehicle Traction Control, IEEE Industry Applications Magazine, Vol. 18, pp. 23-3, 2012.3-4
- (9) Takahiro Imura, Hiroyuki Okabe and Yoichi Hori, Basic Experimental Study on Helical Antennas of Wireless Power Transfer for Electric Vehicles by using Magnetic Resonant Couplings, VPPC 2009, 2009.9.7-10, Dearborn.
- (10) Takehiro Imura, Hiroyuki Okabe and Yoichi Hori, Study on Open and Short Ended Helical Antennas with Capacitor of Wireless Power Transfer using Magnetic Resonant Couplings, The 10th University of Tokyo - Seoul National University Joint Seminar on Electrical Engineering, 2010.3.12-13, Seoul
- (11) Teck Chuan Beh, Takehiro Imura, Masaki Kato and Yoichi Hori, Basic Study of Improving Efficiency of Wireless Power Transfer via Magnetic Resonance Coupling Based on Impedance Matching, IEEE International Symposium on Industrial Electronics, ISIE 2010, 2010.7.4-7, Bari.
- (12) Koh Kim Ean, Beh Teck Chuan, Takehiro Imura and Yoichi Hori, Multi-receiver and Repeaters Wireless Power Transfer via Magnetic Resonance Coupling – Impedance Matching and Power Division Utilizing Impedance Inverter, The 15th International Conference on Electrical Machines and Systems, ICEMS2012, 2012.10.21-24, Sapporo (to be presented)

# Novel EV Society based on Motor/ Capacitor/ Wireless

– Application of Electric Motor, Supercapacitors, and Wireless Power Transfer to Enhance Operation of Future Vehicles –

Yoichi Hori

University of Tokyo, Department of Advanced Energy,  
5-1-5 Kashiwanoha, Kashiwa, 277-8561, Japan

**Abstract** — Why do we need to supply “big energy” to electric vehicles (EVs) “while stopping” and “for a short time”? The energy form of electricity is absolutely different from gasoline. We may not need to take the same style of gasoline vehicle. Future EVs will be linked to the electric power system infrastructure; the vehicles will operate through frequent electric charging, as is the case with electric trains.

Wireless power transfer based on magnetic resonance will be an extremely important technique to receive energy from the infrastructure. In a laboratory experiment, this technique enabled approximately 1kW power transfer with more than 90% efficiency at a distance of 1 m. It opens a new way to the novel EV world.

Supercapacitors, rather than batteries, will play an important role in the future for charging of EVs. Supercapacitors have a long operating life (a few million times charge/ discharge life), large current density, and environmentally friendly composition. Further, their energy level can be estimated from the terminal voltage. Our EVs powered by supercapacitors can operate for more than 20 min after being charged for only 30 s.

Electric motors have three major advantages: motor torque generation is quick and accurate, a motor can be attached to each wheel, and motor torque can be estimated precisely. These advantages enable the realization of high performance antilock braking and traction control systems, control of two-dimensional chassis motion, and estimation of road surface condition. Such motion control techniques improve energy efficiency and safety of future EVs.

In summary, we can achieve a large-scale development of future vehicles that employ three techniques: Electric Motors, Supercapacitors, and Wireless Power Transfer. This eliminates the requirement for engines, high performance Li-ion batteries, and quick charging stations.

**Index Terms** — Electric vehicle, motor/ motion control, supercapacitors, wireless power transfer.

## I. INTRODUCTION

EVS 22, the international conference on Electric Vehicles, held in Yokohama in October 2006 led to the revival of research related to pure electric vehicles, where I served as the program chairman. Similarly, EVS 23 was held in the US in 2008 as a conference on hybrid electric vehicles (HEVs). EVS 24 and 25 were held in Norway in March 2009 and in China in November 2010, respectively. These conferences clearly indicate a renewed, wide-spread interest in EVs. A variety of people with diverse viewpoints attended these conferences.

Currently, we have arrived at the following general agreement in relation to the fundamental flow of future vehicles: “internal combustion engine vehicles (ICV) → HEV → plug-in hybrid electric vehicles (PHEV) → Pure EV.” This scenario validates my assertion (made more than 10 years ago) pertaining to the requirement of employing the aforementioned flow.

Fig. 1 shows the first PHEV based on Toyota Prius. On a given day, PHEV users can commute from their homes to their offices by utilizing night-time electricity, which was used when the vehicles were charged at the homes of the users; once at their offices, the users can charge the vehicle batteries from the electric consents at their offices. As a result, they can utilize day-time electricity during the reverse commute from their offices to their homes. Consequently, PHEVs following this procedure will perform in a manner similar to pure EVs; this familiarizes users with the pure EV environment. In the scenario of excess daytime electricity, which is a possibility in the near future, the above-mentioned situation will also be beneficial for electric power companies.



Fig. 1. First Plug-in Hybrid Electric Vehicle.

PHEVs will lead to a progressive reduction in daily gasoline usage, consequently eliminating the requirement of gasoline engines and complicated hybrid control systems; this will reduce both the purchase price and the maintenance costs of the vehicle. The huge market established by PHEV will be

changed to pure EVs. In such a scenario, supercapacitors will be used to perform the functions currently performed by high performance batteries.

## II. EVS DRIVEN ONLY BY SUPERCAPACITORS

Supercapacitors (EDLCs: Electric Double Layer Capacitors), occasionally referred to as physical batteries, have the following remarkable advantages as compared to conventional batteries: (1) long operating life (a supercapacitor can be charged and discharged for an average of approximately one million times); (2) extremely high power density; (3) use of environmentally friendly materials; and (4) feature of energy level estimation from terminal voltages.

For their operation, EVs require charging and discharging multiple times a day; this necessitates that their power sources have a long life and low charging time. Therefore, EDLCs are significantly more suitable for applications as power sources in EV in comparison with conventional batteries; this is because the functioning of EDLCs, unlike conventional batteries, is not based on chemical reactions. However, EDLCs have low energy density, although they have high power density. Currently, the EDLC energy density is equivalent to lead-acid batteries, i.e., approximately 1/10 of recent Li-Ion batteries. Improvements for increasing the energy density of EDLCs will require a significant time period; however, the present energy density should probably be sufficient for satisfactory operation of EVs.

implementation considers the fact that large inverters that drive electric trains are designed to operate under as much as 200% voltage variation. When we employ the capacitors between 50 V and 100 V, we can use greater than 75% of the charged energy; this is not possible in the case of conventional batteries. Moreover, the charging time of these capacitors is very short. This enables EDLC-operated EVs of ours to function for greater than 20 min for a 30 s charging.

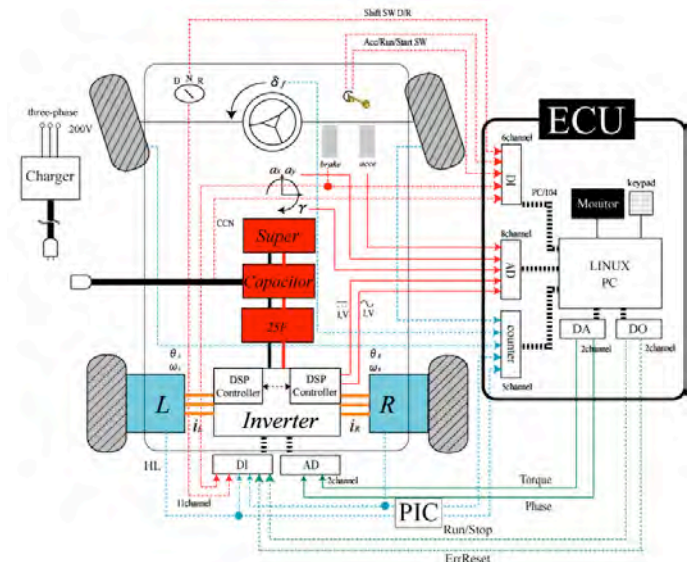


Fig. 3. Control System Configuration of C-COMS 1.



Fig. 2. C-COMS Driven Only by Supercapacitors.

C-COMS 1 shown in Fig. 2 has 21 EDLC modules (approximately 100 V, 100 F in total) connected to the inverters directly, and it operates between 50 V and 100 V. The inverter input voltage needs not be constant. This

The vehicle control system of C-COMS 1 is shown in Fig. 3. A Linux PC is used to compute the reference torque for the inverter on the basis of the velocity of each tire, the steering wheel angle, the acceleration of the vehicle, and the yaw rate. C-COMS 2 shown in Fig. 2 has two direct-driven inwheel motors, and it is used for various motion control experiments; these experiments validate our hypothesis that EVs have remarkable advantages over ICVs.

The concept of these “Capacitor Cars” was actually realized by buses in Shanghai; these buses provide a stable operation, as shown in Figs. 4 and 5. In China, they planned to make 200 buses of this type until the Exposition held in Shanghai in 2010. This system would be extremely suitable for bus transport in most big cities of the world.

Electric transports have become ubiquitous in recent times. Further, there exists an accessible charge infrastructure. Train-like EVs based on frequent recharge can be presently realized; however, their realization is hindered by the large battery requirement. In such a scenario, we can redefine range as the distance from the infrastructure at which we do not feel any significant difference in our comfort level.

In contrast to capacitor buses, battery buses need a huge-scale battery exchange station as is shown in Fig.6, because it takes a long time to recharge battery buses. It is easily known that battery bus is not a realistic solution for metropolitan area.



Fig. 4. Capacitor-operated Bus in Shanghai.



Fig. 5. Illustration of Charging an EV at a Bus-stop.  
(Charging Duration: less than 30 s)



Fig. 6. A Huge-scale Battery Exchange Station.  
(Without this, battery buses cannot be operated.)

### III. MOTION CONTROL OF EVS

The advantages of EVs are similar to those of electric motors. ICVs cannot realize the following three essential aspects:

#### (1) Quick Torque Response of Motors

The torque response of electric motors is 100 times faster than that of engines. Cars do not require energy if they move only in a horizontal direction. Most losses are a result of the friction between the tire and road surface. By applying adhesion control quickly to reduce motor torque against the micro-scale tire slip, the tire would circumvent the problem of friction losses.

UOT March II is shown in Figs. 7 and 8; Figs. 9 and 10 show the results of experiments performed using UOT March II. Please peruse the provided references for a detailed description of the results; these results indicate that the mechanical characteristics can be altered using electrical control.

The reasons for this alteration have not yet been identified. Using UOT March II we can achieve the same performance as current vehicles for half the width of tires and double the fuel efficiency. The most important advantage of these EVs is motion control.

#### (2) Distributed Motor Installation

A single EV motor can be divided into 4 and installed into the wheels of the EV without any significant cost increase, which is not the case with conventional cars. Further, EVs provide a great advantage in high-performance motion control such as Direct Yaw Control (DYC). Motors can easily generate seamless positive and negative torques. It is completely different from conventional 4WD or 4WS, which are based on driving force distribution using differential gear. Recently we have shown that in-wheel motors can generate anti-lift/ dive forces to the road surface, which can be used for active suspension as well as pitch and roll motion controls.

#### (3) Tractable Motor Torque

The motor torque can be easily determined from motor current. In contrast, engines exhibit considerable nonlinearity; as a result, the model description in this case is quite difficult. In case of EVs, we can estimate the force transferred from the tire to the road by using the “driving force observer”. This realizes effective road surface condition estimation. For example, the car can now inform the driver, “We have entered a snowy road.” Consequently, running sensors can be implemented in every car; this will significantly improve driving safety.



Fig. 7. UOT Electric March II.

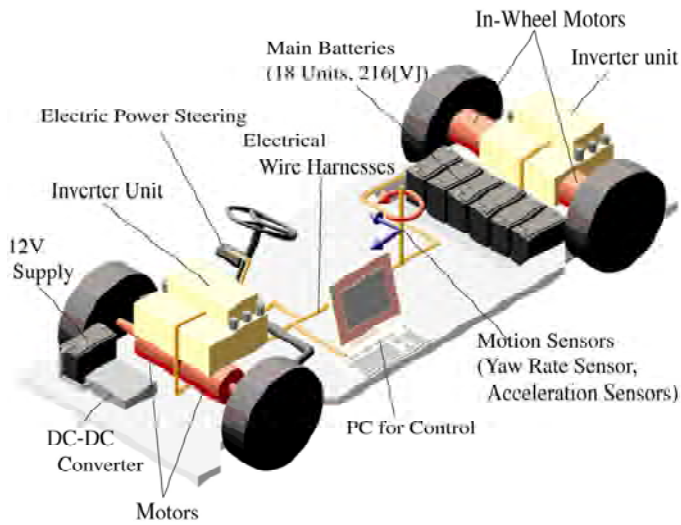


Fig. 8. Configuration of UOT March II.

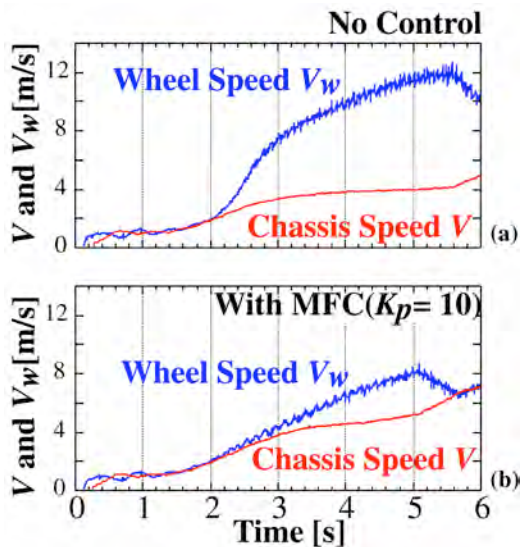


Fig. 9. Adhesion Control.

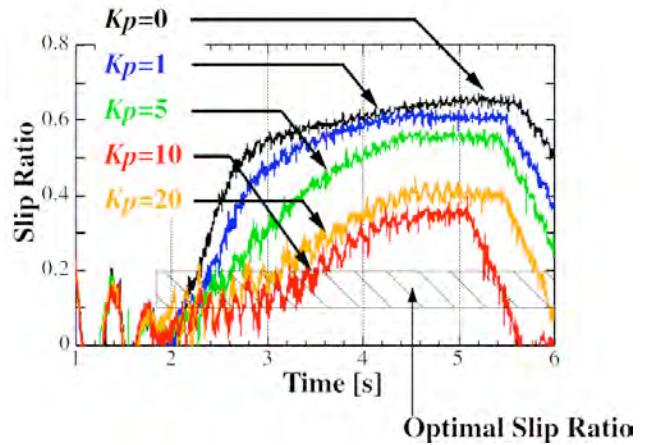


Fig. 10. Variation of Mechanical Characteristics on the basis of Electric Control.

#### IV. WIRELESS POWER TRANSFER SYSTEM

In the near future, energy storage and supply technologies to moving objects will be very important. Wireless power transfer systems capable of operating at 10-500 kHz, 13.56 MHz, and 2.45 GHz are being developed.

Wireless power transfer will be accessible much sooner than we expect; in these power transfer systems, capacitors will play a very important role as the buffer device, instead of batteries. This will reduce the dependency on gasoline stations, thereby reducing the costs involved in the charging of gasoline-operated vehicles in the future, as shown in Fig. 11.

Fig. 12 shows our recent experimental results of wireless power transfer. Here, we use approximately 10 MHz frequency. The energy transfer efficiency between the two antennas is over 90%. Fig. 13 shows good robustness of this system against gap variation and antenna displacement. Fig. 14 shows that by using some repeating antenna the transfer distance can be extended much longer.

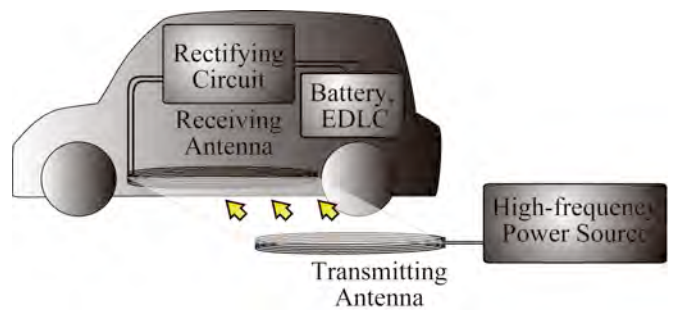


Fig. 11. Wireless Power Transfer System.



Fig. 12. Experiment of Wireless Power Transfer at Hori Lab.

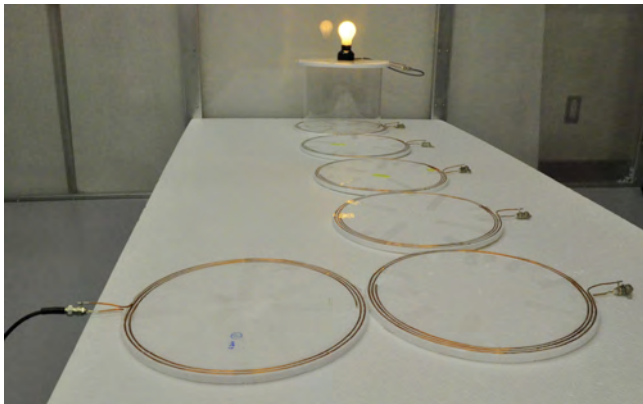


Fig. 14. Transfer Distance Extension using Repeating Antenna.

TABLE I  
RESEACH DIRECTIONS OF WIRELESS POWER TRANSFER

Antenna Design	System Control	Power Electronics
<ul style="list-style-type: none"> <li>• kHz ~ MHz ~ GHz Antennas</li> <li>• Asymmetrical Antennas</li> <li>• Multiple Receiver Analysis</li> <li>• Repeater Antennas</li> </ul>	<ul style="list-style-type: none"> <li>• Impedance Matching System</li> <li>• Frequency Matching System</li> <li>• Battery/Capacitor Charging System</li> </ul>	<ul style="list-style-type: none"> <li>• Efficient Power Source</li> <li>• Analysis with Power Electronics Theories</li> </ul>

## V. CONCLUSION

Capacitors are made of environment friendly materials. This feature will assume increased importance in the future. For example, the use of a permanent magnet for high temperature operation of electric motors is precarious from the viewpoint

of resource availability. Fuel Cell Vehicles (FCVs) are no longer a viable choice as they use 100g Pt per vehicle. FCVs should reset their targets from large and long-range vehicles to small and short-range vehicles.

The realization of future vehicles driven by electricity received from a power network is a strong possibility; motion control will be a very important feature in this realization. Motor/ capacitor/ wireless technology will play an important role in this novel EV society. We are now standing at a very important point in history from the perspective of revolutionizing our daily commutation.

At the end of the paper, three tables are given. I hope they will be of some help for you to understand what I mean in my presentation.

TABLE II  
SUMMARY OF THE PRESENTATION

**Summary**

The biggest problem of EV:  
**Short range of one battery charge**

↓

**What should we do?**

- ① Development of **High Performance Batteries**  
← Most people are absorbed in this.
- ② Development of **Measure to Receive Energy from the Infrastructure**  
← **Wireless power transfer. More budget !**

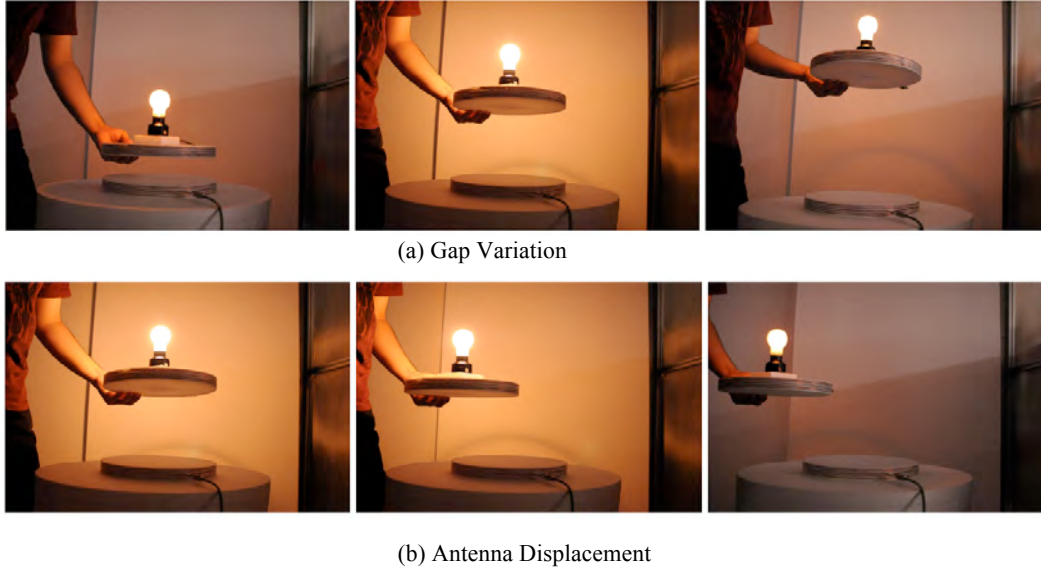
**Let's extend the equivalent range.**  
How long is the range of electric trains?  
..... 0 km or ∞ km

TABLE III  
CONCEPT OF MOTOR/CAPACITOR/WIRELESS

**motor / capacitors / wireless**

**Capacitor Car** = **Suica with auto-charge**

**Wireless P. Transfer** = **Energy version ETC**



(a) Gap Variation

(b) Antenna Displacement

Fig. 13. Robustness of Wireless Power Transfer System against Gap Variation and Antenna Displacement.

#### ACKNOWLEDGEMENT

The authors wish to acknowledge the assistance and support of the IMS Steering Committee.

#### REFERENCES

- [1] Yoichi Hori, Novel EV Society based on Motor/ Capacitor/ Wireless -Application of Electric Motor, Supercapacitors, and Wireless Power Transfer to Enhance Operation of Future Vehicles-, GCOE International Symposium on Secure-Life Electronics, Tokyo, 2012.
- [2] Yoichi Hori, Future Vehicle Society based on Electric Motor, Capacitor and Wireless Power Supply, ECCE-IPEC Sapporo, 2010.
- [3] Yoichi Hori, Application of Electric Motor, Supercapacitor, and Wireless Power Transfer to Enhance Operation of Future Vehicles, IEEE-ISIE 2010, Bari, 2010.
- [4] Yoichi Hori, Motion Control of Electric Vehicle and Prospects of Supercapacitors, IEE Japan Transactions on Electrical and Electronic Engineering, Special issue on Motion Control in Japan, Vol.4, No.2, pp.231-239, 2009.
- [5] Dejun Yin, Sehoon Oh and Yoichi Hori, A Novel Traction Control for EV Based on Maximum Transmissible Torque Estimation, IEEE Transactions on Industrial Electronics, Vol.56, No.6, pp.2086-2094, 2009.
- [6] Cong Geng, Lotfi Mostefai and Yoichi Hori, Direct Yaw Moment Control Evaluation of an In-Wheel-Motored Electric Vehicle Based on Body Slip Angle Fuzzy Observer, IEEE Transactions on Industrial Electronics, Vol.56, No.5, pp.1411-1419, 2009.
- [7] Yoichi Hori: Future Vehicle driven by Electricity and Control - Research on 4 Wheel Motored 'UOT March II' -, IEEE Trans. on Industrial Electronics, Vol.51, No.5, pp.954-962, 2004.
- [8] Shin'ichiro Sakai and Yoichi Hori, Advanced Motion Control of Electric Vehicle with Fast Minor Feedback Loops: Basic Experiments using the 4 Wheel Motored EV "UOT Electric March II", JSAE Review (Elsevier Science), Vol.22, No.4, pp.527-536, 2001.
- [9] Hiroaki Kataoka, Hideo Sado, Shin'ichiro Sakai and Yoichi Hori, Optimal Slip Ratio Estimator for Traction Control System of Electric Vehicle Based on Fuzzy Inference, Electrical Engineering in Japan, Vol.135, No.3, pp.581-586, 2001.
- [10] Shin'ichiro Sakai, Hideo Sado and Yoichi Hori, Novel Skid Detection Method without Vehicle Chassis Speed for Electric Vehicle, JSAE Review (Elsevier Science), Vol.21, No.4, pp.503-510, 2000.
- [11] Yoichi Hori, Shin'ichiro Sakai, Hideo Sado and Toshiyuki Uchida, Motion Control of Electric Vehicle utilizing Fast Torque Response of Electric Motor, 14th IFAC World Congress, 1999.
- [12] Yoichi Hori, Yasushi Toyoda and Yoshimasa Tsuruoka, Traction Control of Electric Vehicle based on the Estimation of Road Surface Condition - Basic Experimental Results using the Test EV UOT Electric March -, Proc. PCC Nagaoka '97, Vol.1, pp.1-8, 1997.

Note: This manuscript is prepared mainly based on the author's papers [1], [2] and [3].



# Advanced Motion Control and Electric Power Transfer System for Comfortable Secure-Life

Yoichi Hori, Toshiyuki Uchida, Sehoon Oh, Takehiro Imura, Valerio Salvucci, Ryo Minaki, Nam Kanghyun, Wang Yafei and Teck Chuan Beh

Department of Advanced Energy, Graduate School of Frontier Sciences, University of Tokyo, 5-1-5 Kashiwanoha, Kashiwa, Chiba, 277-8561, Japan

hori@k.u-tokyo.ac.jp

**Abstract** — We aim to achieve comfortable secure-life with three core techniques. (1). Electric motor, (2). Wireless power transfer (3). Supercapacitor. Electric motor has the following remarkable advantages (1). Quick torque response, (2). Tractable motor torque, (3). Distributed motor installation. These characteristics effectively enable adhesion control of tire and stability control of vehicle motion in Electric vehicles (EVs). In welfare application, we suggested a novel actuator mechanism derived from animal muscles and a safe automatic door without force sensor. We analyzed the effectiveness and safety. Future EVs will be linked to the electric power system infrastructure; the vehicles will operate through frequent electric charging without large energy storage devices. Therefore, it needs energy storage device for quick charge and wireless power transfer technique for easy charge. Supercapacitor has a long life because it has a large current density compared to battery. Our EVs powered by supercapacitor can operate for more than 20 min after being charged for only 30s. Wireless power transfer system in our lab experiment enabled approximately 50 W power transfer with more than 96% efficiency at a distance of more than 20 cm. These techniques provide safe and comfortable human life.

**Keywords** — animal muscle, electric vehicle, motion control, wireless power transfer.

## I. INTRODUCTION

Recently, EVs have been expected to solve the environmental and energy problem. In order to improve the energy efficiency and safety of future EVs, the implementation of novel motion control techniques for EVs is required. Since EVs are powered by electric motors, they have three major advantages: motor torque generation is quick and accurate, a motor can be attached to each wheel, and motor torque can be estimated precisely. [1] In Chapter II, EVs motion control techniques are suggested with these advantages. In addition, we have to figure out how to make the charging process safer and easier for users. When wireless charging can be done to EVs, the viability of supercapacitor (EDLC) as an energy storage medium for EVs can be increased as the EDLC has a longer life span compared to batteries while the problem of having a lower energy density is solved. We propose wireless charging to satisfy these three conditions: high efficiency, large air gaps, and high power in Chapter III. Finally, as society has more elderly people and decreasing birth rate,

we need robots and human interaction to work together with human safety. In Chapter IV, we approach human-friendly robots driven by bi-articular actuators and force sensor less power assist door.

## II. MOTION CONTROL FOR ELECTRIC VEHICLES

Experimental electric vehicles are shown in Fig.1. They consist of In-Wheel Motors, batteries, some controllers and sensors for controlling vehicle dynamics. Right one and center one are equipped with supercapacitors as main power-supply for driving motors.



Fig. 1. Electric vehicle

### A. Roll Stability Control for Electric Vehicles

Along with the increasing demand for Electric vehicle (hereinafter EV), active safety control for EV is gaining more and more concern. Compared with traditional vehicles, EVs generally have narrower tread while height do not change much, this may lead to roll instability in severe driving maneuvers or under outside disturbance such as side wind. Thus, roll stability control is a crucial topic for EV. [3] Vehicle roll motion can be expressed by a 3DOF vehicle model as equation (1) shows,

$$\begin{aligned} MV(\ddot{\beta} + \gamma) &= F_{yfl} + F_{yfr} + F_{yrl} + F_{yrr} \\ I_y \dot{\gamma} &= (F_{yfl} + F_{yrl})l_f - (F_{yfr} + F_{yrr})l_r \\ M_s h_{cr} a_y &= I_r \ddot{\phi} + C_r \dot{\phi} + K_r \phi - M_s g h_{cr} \sin \phi \end{aligned} \quad (1)$$

Since roll angle has a direct relationship with lateral acceleration  $A_y$ , and lateral acceleration sensor is cheap and reliable compared with roll angle sensor,  $A_y$  is used as the control signal for roll motion stabilization. A 2DOF controller with DOB is constructed as shown in Fig. 2.

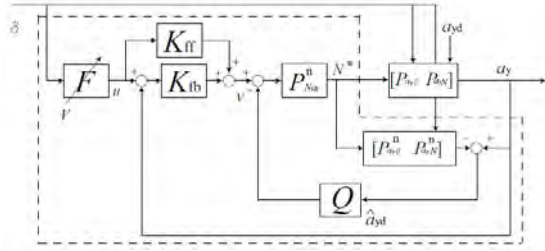


Fig. 2. Block diagram of 2DOF for RSC based on DOB

Experiment is conducted to verify the proposed controller. As Fig. 3 depicts, the lateral acceleration and hence the roll angle can be suppressed compared with the no control case, while the trajectory is almost not affected.

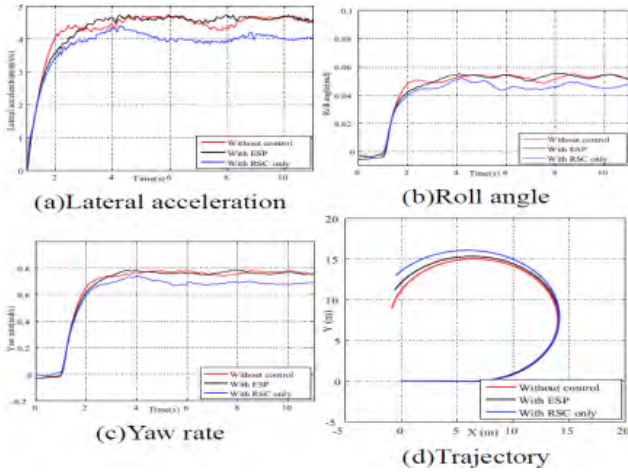


Fig. 3. Experiment results under step steering input

### B. Robust Yaw Stability Control for Electric Vehicles

A robust yaw stability control design based on active steering control is proposed for electric vehicles. [4] The control system consists of an inner-loop controller (i.e., in this paper, called as a Steering Angle-Disturbance Observer(SA-DOB) which rejects an input steering disturbance and an output yaw disturbance simultaneously by feeding a compensation steering angle) and an outer-loop controller (i.e., PI-type Tracking Controller) to achieve the control performances. The controller  $C(s)$  and  $Q$ -filter are designed based on robust control design methods (e.g., mixed sensitivity approach) to account for model variations in nominal vehicle yaw models.

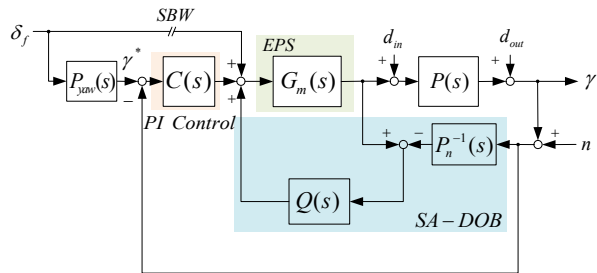
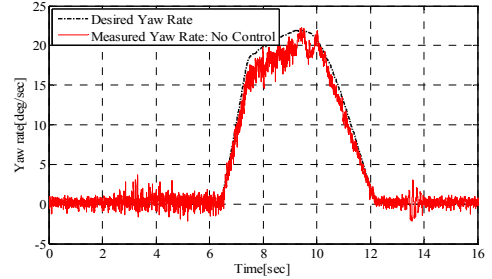
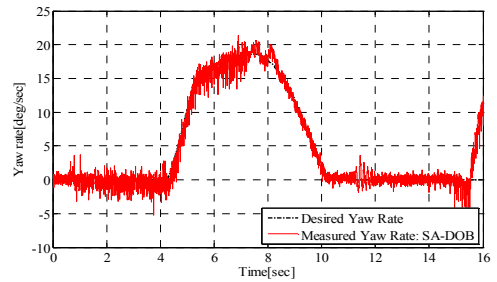


Fig. 4. Control structure of the proposed yaw stability control system

The configuration of a proposed control system is shown in Fig. 4. Experiments with an electric vehicle is carried out to evaluate control performances of the proposed control system. The experimental results are shown in Fig. 5.



(a) Without yaw stability control



(b) With yaw stability control

Fig. 5. Experimental results with electric vehicles

### C. Driver-Friendly Reactive torque control Based on Human Sensitivity to Active Front Steering

Active front steering (AFS) is an effective technique to stabilize the motion control. However, for a vehicle, it is difficult to resolve the problem of interference between driver steering and automatic steering with AFS. When the reaction torque from road surface  $\hat{T}_{RTRS}$  is changed using AFS, it interferes driver steering via the reaction torque. Therefore, we propose the reactive torque control method based on driver sensitivity. [5] The block diagram of the control is shown in Fig. 6.

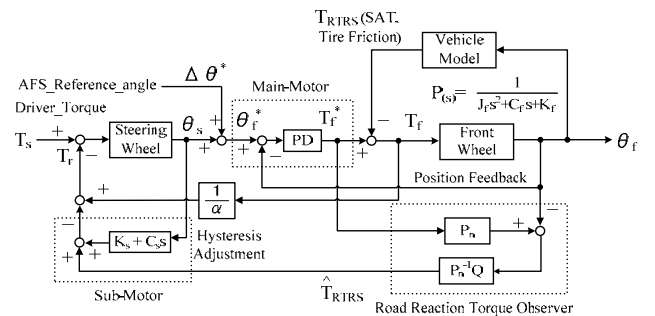


Fig. 6. Reactive torque control based on human sensitivity

It compensates the reaction torque changed by AFS with road reaction torque observer. The experimental result is shown in Fig. 7. The experiment started when the steering wheel was turned to the left by 90°. After a few seconds, as soon as the motion control PC detects a slip in the vehicle. AFS is activated. The front wheel angle is

reduced by 30°. Then, driver maintained steering wheel at 90°. In conventional control, AFS returned the front axle wheel angle and the angle became small. The reaction torque that the driver received from the road surface decreased and the driver perceived that the steering wheel became light. The driver turned the steering wheel increasingly by 100°. If the driver maintained the steering wheel angle of 90°, the front axle wheel angle should have returned to the original 30°. However, in the results, it only returned to 40°. Our proposed technique compensated the reaction torque reduction and exhibited excellent performance in matching the reference angle of the front axle wheel.

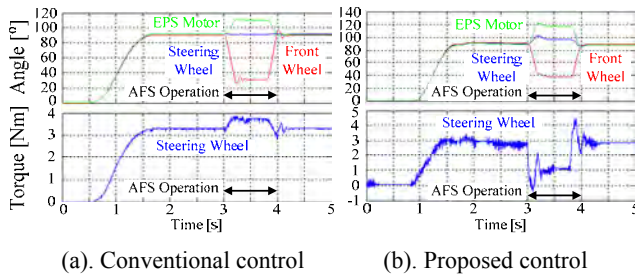


Fig. 7. Experimental results with steering control

### III. WIRELESS POWER TRANSFER SYSTEM VIA MAGNETIC RESONANT COUPLING

Nowadays, with the widespread usage of mobile appliances such as mobile phones and laptops, as well as the recent boom in the environmentally friendly EVs, the need for a technique to wirelessly charge these devices has increased. When wireless power transfer (WPT) is achieved, the process of charging the devices will be made a lot more convenient. Furthermore, as power can be constantly transferred to the devices, the battery size can be reduced. This will reduce the cost and increase the portability of the devices. Also, in the case of EVs, the danger of being electrocuted due to the wear and tear of an old cord, or rain will be avoided, making the charging process safer. When wireless charging can be done to EVs, the viability of supercapacitors (EDLC) as an energy storage medium for EVs can be increased as the EDLC has a longer life span compared to batteries while the problem of having a lower energy density is solved. To achieve wireless charging, the WPT system must satisfy these three conditions: high efficiency, large air gaps, and high power.

Currently, the most common WPT technologies are the electromagnetic induction and the microwave power transfer. However, the electromagnetic induction method has a short range<sup>[6]</sup>, and microwave power transfer has a low efficiency as it involves radiation of electromagnetic waves. Recently, a highly efficient mid-range WPT technology using magnetic resonant coupling, WiTricity, was proposed. It is a system that transfers power in between two resonating antennas through magnetic coupling. It satisfies all three conditions to make wireless

charging possible as it has a high efficiency at mid range. (approximately 90% at 1m and 50% at 2m at 60W)

We studied WPT system at two main frequencies, the 13.56MHz and the ~120kHz band as permitted by the ISM (Industrial Scientific Medical) band. The topics include

- 13.56MHz WPT system : A system based on impedance matching (IM) to increase the efficiency by fixing the resonance frequency at 13.56MHz ( frequency of the power source)
- kHz WPT system : This include the antenna design of a kHz range antenna, and the system to achieve maximum efficiency based on frequency switching of the power source
- Analysis of the WPT system without using S-parameter : An analysis of the WPT system using only voltage and current to study the viability of using only the self resonance frequency of the antennas to transfer power at high efficiency and to prepare for future system designs.

#### A. Theory of Magnetic Resonant Coupling

Until now, this phenomenon was explained using mode coupling theory. However, this theory is often complicated and inconvenient when it comes to designing the circuits around the system. In our previous research, we studied this phenomenon using antenna design theories and circuit design theories. The characteristics of the antennas are explained using equivalent circuits, electromagnetic analysis, and experiments. The frequency characteristic of the antennas and its relation to efficiency is studied.<sup>[6]</sup>

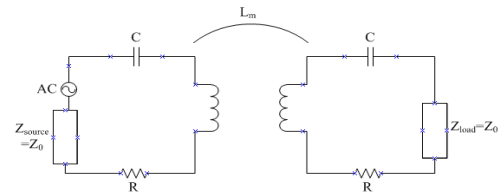


Fig 8. Equivalent circuit of magnetic resonant coupling



Fig 9. The transmitting and receiving antenna used to transmit power to light up a 40W bulb.

Magnetic resonant coupling involves creating an LC resonance, and transferring the power with electromagnetic coupling. Hence, the magnetic coupling can be represented as mutual inductance  $L_m$  as in Fig 8.  $Z_{source}$  represents the characteristic impedance, and  $Z_{load}$  is the impedance of the load. In this paper, they are both considered to be the same at  $Z_0$ , 50 $\Omega$  the default characteristic impedance of most high frequency systems. The ohm loss and the radiation loss of the antennas are

represented by R. Using this equivalent circuit, the resonance frequency, frequency characteristics and efficiency of the antennas can be estimated to an accuracy of up to 5% error. [6]

### B. 13.56MHz WPT System – Impedance Matching

The MHz range has the advantage of smaller sized antennas that contributes to practical design, and also a lower ohmic loss. However, one main problem of a WPT system in this frequency range is the narrow frequency band that can be used due to the ISM band. As the gap between the antennas change, the coupling between the antennas,  $k$ , weaken. Therefore the impedance of the circuit will change, affecting the power transfer efficiency and the resonance frequency. As the maximum power transfer efficiency only occurs in the resonance frequency, a system based on impedance matching (IM) was proposed to fix the resonance frequency of the system to that of the power source (13.56MHz).

Figure 10 shows the diagram of the proposed system. The system involves resonating two antennas with identical self resonance frequency (13.56MHz) using a high frequency power source. Under normal circumstances, the air gap and the load (50Ω in this case) are variable and unknown. In this system, a directional coupler is inserted before the transmitting antenna to measure the reflected power in between the antennas. The IM circuit is made of an LC circuit and it functions as a tuner to change the characteristics of the antennas so that the resonance frequency can be matched to the frequency of the power source. This can be achieved by tuning the parameters so that the reflected power ratio reaches its minimum.

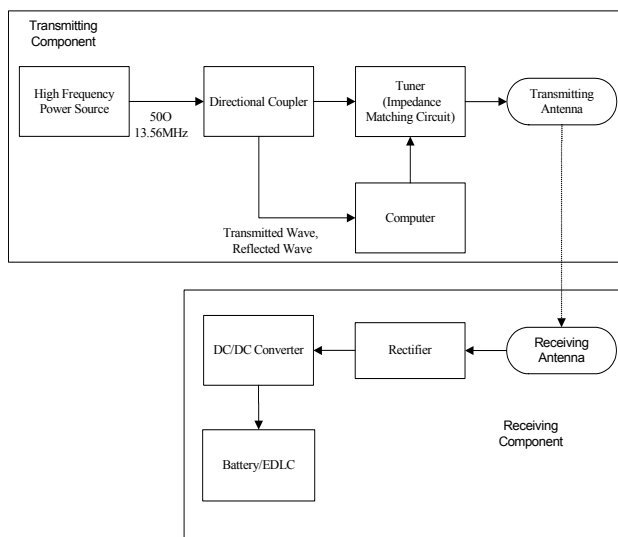
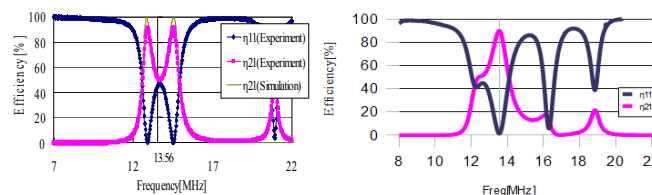


Fig 10. 13.56MHz WPT system with tuning circuits

Using this method, the resonance frequency of the frequency was successfully shifted to 13.56MHz, thus increasing the efficiency as in Figure 11. As a result, the system is more robust to positional shifts of the antennas as in Figure 12. The efficiency of the system after control

is lower than the ideal value due the loss in the components used to match the system. This can be solved by using high Q value components. [7]



(a) Before matching (b) After matching  
Fig 11. Experiment results and comparison with simulations [7]

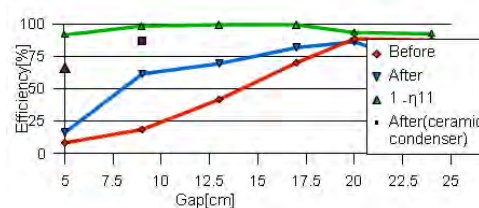


Fig 12. Experiment results. Efficiency (at 13.56MHz) vs Gap Graph [7] ( $1-\eta_{11}$  is shows the ideal efficiency of the system when no ohmic loss occurs)

### C. kHz WPT System – Frequency Control and Antenna Design

Although the antenna size will be larger, there are two important advantages when this system is applied in the kHz system. First, an efficient power source can be easily created for the system using current power electronics technology. Secondly, the usable frequency band (ISM band) is much wider in the kHz range, meaning the maximum efficiency can be achieved by switching the frequency of the power source of the system to the resonance frequency of the antennas.

In this research, we successfully designed an antenna that can operate in the kHz range. It can be done by lowering the self resonance frequency of the antennas by increasing the number of turns. Then a directional coupler was used to measure the reflected power of the system, and a control system is applied on the frequency of the power source. The system is resonated by changing the frequency of the power source so that the reflection ratio of the power reaches its minimum. Using this method, the maximum efficiency was successfully reached even when the gap and resonance frequency of the antennas change (figure 13).

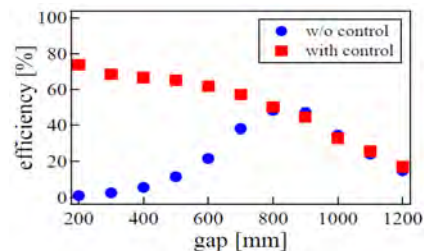


Fig 13. Experiment results. Efficiency of the kHz system before and after frequency control

#### IV. HUMAN FRIENDLY MOTION CONTROL

In recent years robots and human interaction is growing in importance. Differently from industrial robots, for robots that work together with humans safety for the user and environment is a very important factor. A new approach to hardware and control design for such robots is being investigated and can be referred as human-friendly motion control. In our approach human-friendly robots are driven by bi-articular actuators and do not use force sensors.

##### A. Manipulators Equipped with Bi-articular actuators

In conventional manipulators each joint is driven by one actuator. On the contrary, animal limbs present a complex musculoskeletal structure based on mono- and bi-articular muscles. A simplified model of the complex animal musculoskeletal system is shown in Fig. 14. This model is based on 6 contractile actuators - 3 extensors (e1, e2 and e3) and 3 flexors (f1, f2 and f3) coupled in three antagonistic pairs.

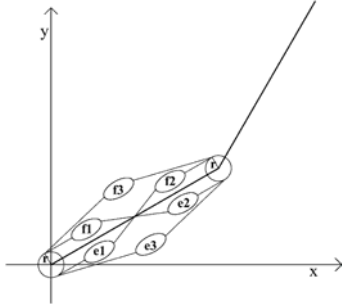


Fig 14. Simplified model of animal musculoskeletal system

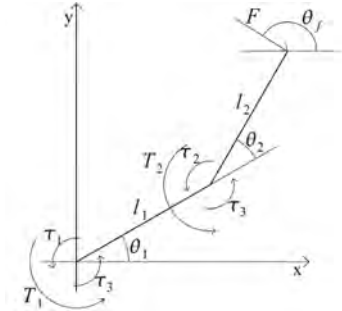


Fig 15. Kinematics of an arm with mono and bi-articular actuators

The kinematics model of the arm driven by bi-articular actuators of Fig. 1 is shown in Fig. 15.  $T_1$  and  $T_2$  are total torques at joint 1 and 2, respectively.  $\tau_1$  and  $\tau_2$  are torques produced by mono- and bi-articular actuators, calculated as:

$$\tau_1 = (f_1 - e_1)r \quad (1)$$

$$\tau_2 = (f_2 - e_2)r \quad (2)$$

$$\tau_3 = (f_3 - e_3)r \quad (3)$$

The kinematics of this system can be expressed by:

$$\begin{cases} T_1 = \tau_1 + \tau_3 \\ T_2 = \tau_2 + \tau_3 \end{cases} \quad (4)$$

Given  $T_1$  and  $T_2$ , it is generally not possible to determine uniquely  $\tau_1$ ,  $\tau_2$  and  $\tau_3$ . This is known as actuator redundancy problem. To resolve actuator redundancy, in

our group we propose a model based on infinity norm. This model has the following advantages:

- 1). Based only on linear function for actuator redundancy resolution,
- 2). Closed form solution,
- 3). Infinity norm method allows a greater output force at the end effector than 2 - norm method (Fig. 16), and
- 4). For  $\infty$  - norm there is no error in output force, which is instead present in Different Phase Control approach (Fig 17) Two manipulator driven by bi-articular actuators shown in Fig.18.

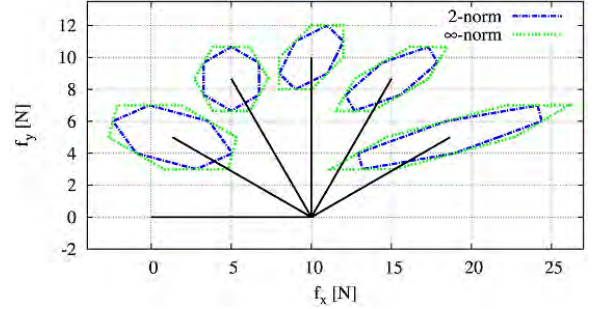


Fig 16. Maximim output force at end effector for 2-norm and infinity norm

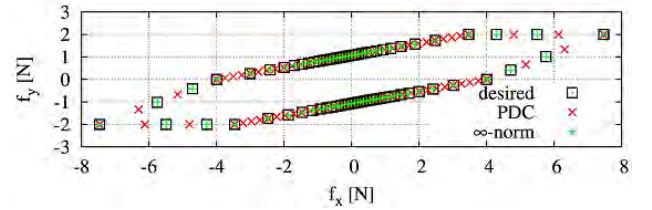


Fig 17. Precision in output force at end effector for DPC and infinity norm ( $\theta_2=30$  deg)

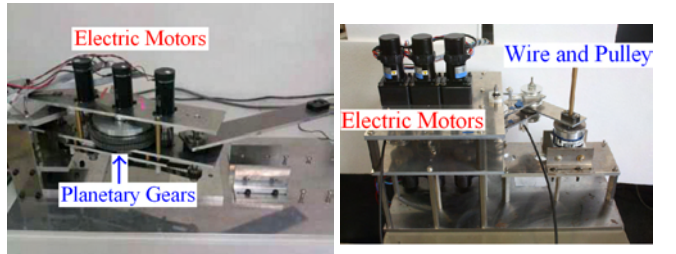


Fig 18. Arm with biarticular actuators based on planetary gear (left) <sup>[10]</sup> and on wire transmission (right).

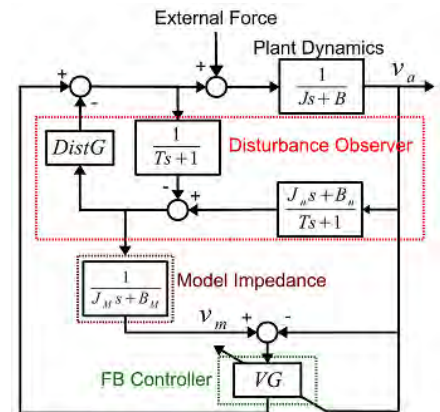


Fig 19. Proposed FSPAC with variable gain

Fig 18 and Fig 19 are being build in order to experimentally validate the infinity norm based redundancy resolution method, as well to implement new controllers based on the concept of viscoelasticity [8] [9].

### B. Force Sensor-less power assist robots

Force Sensor-less Power Assist Control (FSPAC) based on variable gain (VG) to increase robustness and safety of power assist devices have been proposed (Fig. 19). This control design was successfully implemented on a door actuated by a ballscrew system (high friction) or by a linear motor (low friction) (Fig. 20).

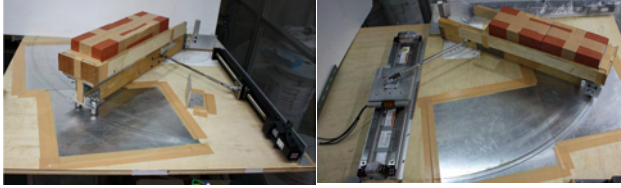


Fig 20. Ball screw type (left) and linear motor (right) system

### C. Train Door Motion Control

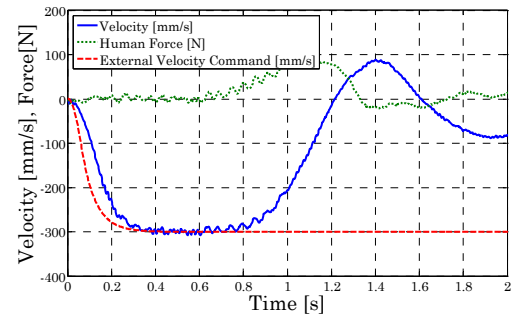
Force sensor-less impedance control [11] with external velocity command to increase safety for the user was implemented on the train door experimental setup shown in Fig 21. The proposed impedance control achieves 2DOF Control between tracking performance for external velocity command and response characteristic for human force (Fig 22).



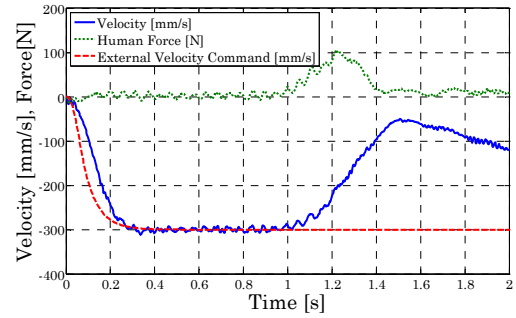
Fig 21. Train door experimental setup

## V. CONCLUSION

We have proposed some advanced motion control techniques to provide comfortable secure-life to human and verified them by experiment at the Hori laboratory. In EVs, we introduced the adhesion control of tire, stability control of vehicle dynamics, and steering assist control for a driver. In the case of human-friendly motion control, we suggested a robot manipulator based on animal musculoskeletal model and force sensor less door with electric motor used as sensor. Finally, we proposed a novel charging system combined with wireless power transfer and supercapacitor for EVs. We believe that these techniques could help human life and create an innovative life style where the infrastructure supports electric vehicles.



(a)  $J_M=J_n, B_M=1/2B_n$



(b)  $J_M=J_n, B_M=B_n$

Fig 22. Experimental result

## REFERENCES

- [1] Y. Hori, S. Sakai, H. Sado and T. Uchida, "Motion Control of Electric Vehicle utilizing Fast Torque Response of Electric Motor", 14th IFAC World Congress, 1999.
- [2] D. Yin, S. Oh and Y Hori, A Novel Traction Control for EV Based on Maximum Transmissible Torque Estimation, IEEE Transactions on Industrial Electronics, Vol.56, No.6, pp.2086-2094, 2009.
- [3] K. Kawashima, T. Uchida, Y. Hori, "Rolling Stability Control of In-wheel Electric Vehicle Based on Two-Degree-of-Freedom Control", The 24th Electric Vehicle Symposium, Session 3E-2, Stavanger, Norway, 2009.05
- [4] K. Nam, S. Oh, and Y.Hori, "Robust Yaw Stability Control for Electric Vehicles Based on Active Steering Control ", The 6<sup>th</sup> IEEE Vehicle Power and Propulsion Conference , 2010.
- [5] R.Minaki, H.Hoshino, Y.Hori, "Experimental Verification of Driver-Friendly Reactive Torque Control Based on Driver Sensitivity to Active Front Steering", The 35th Annual Conference of the IEEE Industrial Electronics Society, 2009.11
- [6] T. Imura, H. Okabe, Y. Hori, "Basic Experimental Study on Helical Antennas of Wireless Power Transfer for Electric Vehicles by using Magnetic Resonant Couplings", IEEE Vehicle Power and Propulsion Conference, pp 936-940, 2009.
- [7] T. Beh, M. Kato, T. Imura, Y. Hori, "Basic Study on Improving Efficiency of Wireless Power Transfer via Magnetic Resonance Coupling Based on Impedance Matching", IEEE International Symposium on Industrial Electronics, pp2011-2016, 2010.
- [8] V. Salvucci, S. Oh, and Y. Hori, "New Approach to Force Sensor-Less Power Assist Control for High Friction and High Inertia Systems," in IEEE ISIE, 2010.
- [9] S. Oh and Y. Hori, "Development of Two-Degree-of-Freedom control for robot manipulator with biarticular muscle torque," ACC, 2009.
- [10] S. Oh, Y. Kimura, and Y. Hori, "Reaction Force Control of Robot Manipulator Based on Biarticular Muscle Viscoelasticity Control," in IEEE International Conference on Advanced Intelligent Mechatronics, 2010.
- [11] T. Koyanagi, S. Inatama, S. Oh, Y. Hori, "Robust and Safe Control Based on Disturbance Observer for Train Doors", ISIE, 2010.

# Traction Control of Electric Vehicle based on the Estimation of Road Surface Condition

## - Basic Experimental Results using the Test EV "UOT Electric March" -

Yoichi Hori, Yasushi Toyoda and Yoshimasa Tsuruoka

Department of Electrical Engineering, University of Tokyo, 7-3-1 Hongo, Bunkyo, Tokyo, 113 Japan

Phone: +81-3-3812-2111 ext 7680, Fax: +81-3-5800-3865

E-mail: hori@kaya.t.u-tokyo.ac.jp, Homepage: <http://www.kaya.t.u-tokyo.ac.jp/>

**Abstract-** The most distinct advantage of electric vehicle is in its quick and precise torque generation. We propose two novel traction control techniques of electric vehicle, i.e., the model following control and the optimal slip ratio control. Their effectiveness is demonstrated by using the test vehicle "UOT Electric March".

### I. INTRODUCTION

Recently a lot of electric vehicles (EV) have been developed to solve environment and energy problems caused by the use of internal combustion engine vehicles (ICV). Some of them already have enough performance in practical use. However, they have not yet utilized the most remarkable advantage of EV. Electric motor torque can be controlled much more quickly and precisely than that of internal combustion engine. Adhesion characteristics between tire and road surface are greatly affected by the control of traction motor. This means that the vehicle stability and safety can be improved by motor torque control. If we can use special low drag tires with smaller energy loss, the range of one battery charge will be drastically expanded.

In this paper, we will propose the novel traction control techniques, which can be firstly realized only by utilizing electric motor's quick torque response. They are the model following control and the optimal slip ratio control. By using a newly developed test vehicle "UOT Electric March", we will show some successful experimental results. In order to achieve the best control performance, the estimation method of road surface condition is proposed and its realizability is shown also by real experiments

### II. STATE-OF-THE-ART OF TRACTION CONTROL

Traction control is the control to suppress tire slip when the vehicle is running, for example, on icy road by controlling the traction force and to improve the driving and cornering performances mainly in acceleration.

We should consider two forces acting on the vehicle body, i.e., the driving (longitudinal) and side (lateral) forces. As depicted in Fig.1, these forces depend on the slip ratio

$\lambda$ .  $\lambda$  is defined by eq.(1), where  $V_w$  and  $V$  are the wheel and vehicle speeds.

$$\lambda = (V_w - V) / V_w \quad (1)$$

The side force takes its maximum value when  $\lambda=0$  and becomes smaller for bigger  $\lambda$ . If  $\lambda$  increases by sudden decrease of road friction, the side force gets smaller drastically. This causes serious problems: drift-out in front wheel driven cars, spin in rear wheel driven cars, and drift-out with rotation in four wheel driven cars. Such a loss of cornering force is extremely dangerous. The average traction force is also decreased.

Traction control can be classified into following two steps:

(1) **longitudinal control**, for example, the adhesion improvement to prevent slip. This is done by controlling the traction force, and

(2) **lateral control**, for example, the yaw control to keep the yaw motion to be zero. This is done mainly by controlling the steering angle.

For the lateral control, the steering angle of the front wheels is the absolutely dominant control input. Such a technique is already well developed for ICV and the results can be applied to EV. For this reason, in this paper, we focus our discussion into (1) **longitudinal control**.

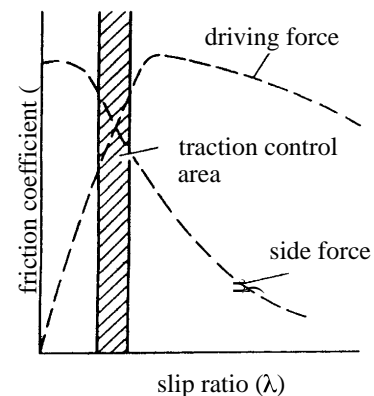


Fig.1. Characteristics of driving and lateral forces

To realize the effective traction control system, we need a sophisticated mechanism quickly to reduce the excessive driving torque. In ICV, this is realized mainly by the following three techniques.

(1) **engine control:** Engine torque itself is suppressed. To reduce air supply is the basic technique, but for quicker response, advanced techniques like fuel-cut and spark timing shift are used together.

(2) **brake control:** Wheel rotation itself can be stopped by braking. This method has quicker response than the engine control. Independent control of left and right tires is effective for  $\mu$ -split braking. Brake control should be used together with the engine control because brake parts often have thermal problem.

(3) **mission control:** Driving torque of the slipping tire is transferred to the non-slipping tire. This technique is effective for  $\mu$ -split road. As the total torque can not be reduced, mission control technique should be applied together with the engine control.

TABLE I summarizes the advantages and disadvantages of these techniques.

TABLE I  
COMPARISON OF TRACTION CONTROLS FOR ICV

	control-lability	response	cost	operation feeling	total
engine control					
brake control				×	
mission control		×			×
engine + mission controls					
engine + brake controls					

### III. ADVANTAGE OF ELECTRIC VEHICLE

Electric Vehicle has great advantages as followings for realization of high performance traction control.

(1) **low cost:** Above mentioned techniques for ICV need additional costly hardware, e.g., throttle and brake actuators. EV does not need anything more. Traction control can be realized only by software. Low cost "basic car" can have high performance traction control.

(2) **quick response:** In ICV, more than 200[ms] are needed to open the throttle actuator. The actual response time is much longer because the mechanical delay is included. In contrast, the response time of electric motor torque is less than 10[ms].

(3) **easy controller design:** In ICV, unknown strong non-linearity lies in the transfer characteristics from the control input (for example, air valve angle to engine, oil pressure of brake system, etc.) to the generated torque. This makes it difficult to construct a mathematical model for controller design. In EV, by applying simple current control, the generated torque is exactly proportional to the torque command.

## IV. MODEL FOLLOWING CONTROL

In this paper, we propose two control strategies: one is the **model following control (MFC)**, and another is the **optimal slip ratio control**. MFC is the starting point of our research project of "Control of Electric Vehicle" and its basic feasibility is demonstrated here by real experiment.

### A. Principle of MFC

Fig.2 shows the block diagram of the model following control.  $I_{com}$  is the current command proportional to the acceleration pedal angle.  $\omega$  is the rotational speed of the driving shaft.  $\omega$  increases drastically when the tire slips. Vehicle dynamics including tire characteristics and road surface friction are very complicated, but if we introduce the slip ratio  $\lambda$ , the vehicle body can be seen as one inertia system having the equivalent inertia moment of

$$J = J_w + Mr^2(1-\lambda) \quad (2)$$

Here,  $J_w$ ,  $M$  and  $r$  are the shaft inertia moment, vehicle weight and tire radius. Eq.(2) means that, when slip occurs, the vehicle seems lighter. Therefore, we use the following inertia moment with  $\lambda=0$  in the reference model.

$$J_{model} = J_w + Mr^2 \quad (3)$$

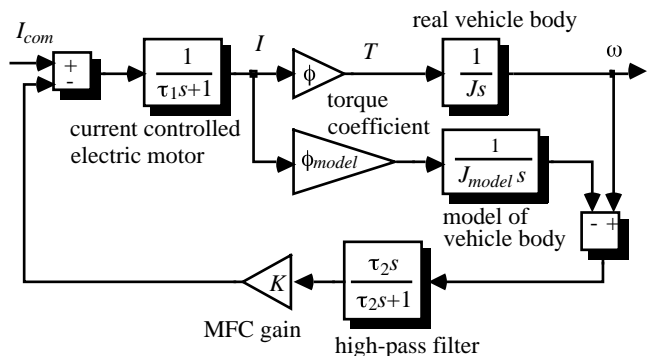


Fig.2. Block diagram of MFC

When there is no slip, actual  $J$  is almost equal to  $J_{model}$ . Any signal is not generated from MFC controller. If the tire slips, the actual wheel speed  $\omega$  increases immediately. The model wheel speed does not increase. By feeding back the speed difference to the motor current command, the



actual motor torque is reduced quickly and it induces re-adhesion.

This control function is needed only in relatively higher frequency region, we used a high pass filter on the feedback pass. In actual implementation, two high pass filters are inserted before taking the difference between actual and model speeds to avoid the offset problem of integrator.

### B. Experimental Result of MFC

Fig.3 shows the slip experiment using UOT Electric March. We used iron plates as slippery road surface. Water is scattered to reduce the friction coefficient. The vehicle is accelerated by the constant current command of 300[A]. The feedback gain  $K$  in Fig.2 is 30. The front wheels are on the slippery area between  $t=1.25[s]$  and  $1.7[s]$ .

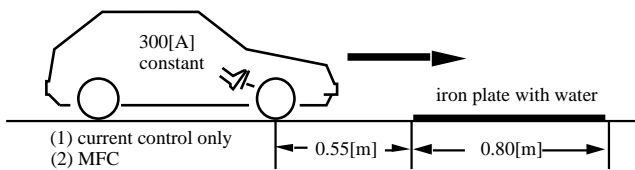


Fig.3. Slip experiment

Experimental results are given in Fig.4. We can see that MFC can reduce the motor current effectively when the vehicle goes onto the slippery area, and then the slip ratio is kept much lower comparing to the current control only. Some vibration seen in the current waveform in Fig.4(a) should be suppressed in the future.

## V. OPTIMAL SLIP RATIO CONTROL

The model following control is a very rough approach although it has been shown that the motor control is really effective for adhesion improvement. If we want more exactly to regulate the slip ratio within the desired range, more precise approach is needed. Fig.5 shows the idea of the optimal slip ratio control developed from this viewpoint. When the optimal slip ratio is decided by the road condition estimator, the slip ratio controller receives the command and realizes it.

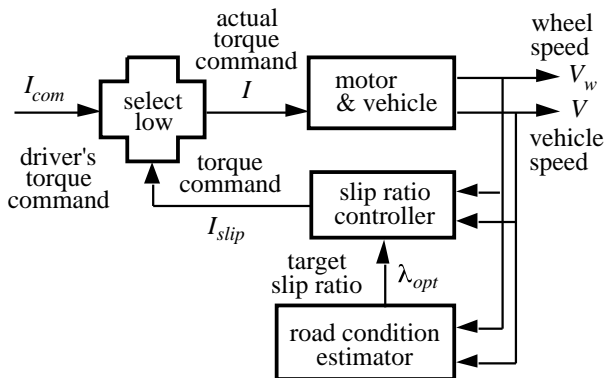
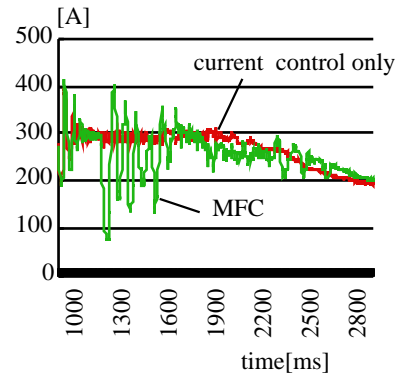
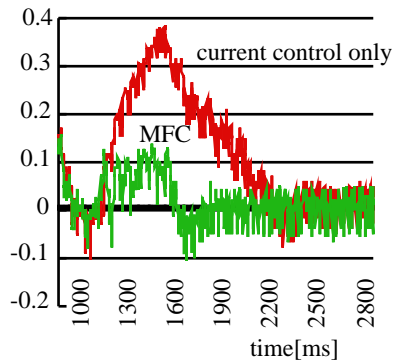


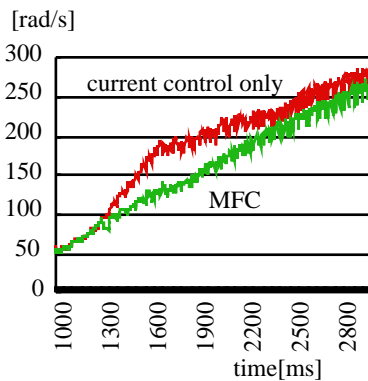
Fig.5. Block diagram of the optimal slip ratio controller



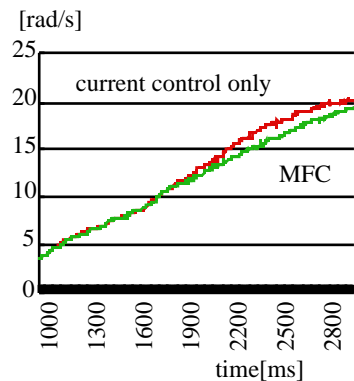
(a) motor current



(b) slip ratio



(c) wheel speed



(d) vehicle speed

Fig.4. Experimental results of MFC

### A. Vehicle Model

We assume that the two motor torques and friction forces are same in left and right, and that the rolling and air frictions are small enough. In Fig.6, the kinematic equations of the wheel and vehicle take the forms of

$$(F_m - F_d) \frac{1}{M_w s} = V_w \quad (4)$$

and

$$F_d \frac{1}{M s} = V \quad (5)$$

where,

- $F_m$  : motor torque (force equivalent)
- $F_d$  : friction force
- $M_w$  : wheel inertia (mass equivalent)
- $M$  : vehicle weight

The friction force between the road and wheel is given by

$$F_d = N \mu(\lambda) \quad (6)$$

where  $N$  is the vertical force given by  $N = Mg$ .

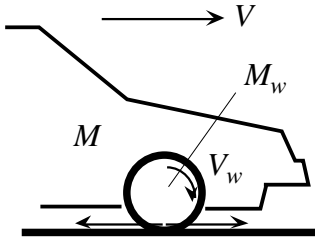


Fig.6. Vehicle model.

From eq.(1), the following perturbation system is derived.

$$\begin{aligned} \Delta \lambda &= \frac{\partial \lambda}{\partial V} \Delta V + \frac{\partial \lambda}{\partial V_w} \Delta V_w \\ &= -\frac{1}{V_{w0}} \Delta V + \frac{V_0}{V_{w0}^2} \Delta V_w \end{aligned} \quad (7)$$

where  $V_{w0}$  and  $V_0$  are the wheel and vehicle speeds at the operational point. The friction force is represented using  $a$ , the gradient of  $\mu-\lambda$  curve, as

$$\Delta \mu = a \Delta \lambda \quad (8)$$

By combining eqs.(7) and (8) with the perturbed forms of eqs. (4) and (5), the transfer function from the motor torque to the slip ratio is finally given by

$$\frac{\Delta \lambda}{\Delta F_m} = \frac{1}{Na} \frac{M(1-\lambda)}{M_w + M(1-\lambda)} \frac{1}{1+\tau s} \quad (9)$$

where the time constant  $\tau$  is given by eq.(10) which is proportional to the wheel speed  $V_{w0}$ .

$$\tau = \frac{1}{Na} \frac{MM_w V_{w0}}{M_w + M(1-\lambda)} \quad (10)$$

The typical value of  $\tau$  in our experimental vehicle is 150 ~ 200[ms] when  $a=1$  and the vehicle speed is around 10[km/h]. Note that  $a$  can be negative in the right-hand side of the peak point of  $\mu-\lambda$  curve.

### B. Design of Slip Ratio Controller

We used a simple P&I controller with a variable gain as the slip ratio controller given by eq.(11). Its nominator compensates for the pole of eq.(9). The integral gain is constant and the proportional gain is proportional to the vehicle speed.

$$K \frac{1+\tau s}{s} \quad (11)$$

Finally, the transfer function from the slip ratio command to the actual slip ratio becomes

$$\frac{\Delta \lambda}{\Delta \lambda^*} = \frac{1}{1 + Na \frac{M_w + M(1-\lambda)}{M(1-\lambda)} \frac{1}{K} s} \quad (12)$$

If  $\lambda \ll 1$ , this is a simple first order delay characteristics with a time constant which can be adjusted by  $K$ . Here, we put this response time 50 ~ 100[ms].

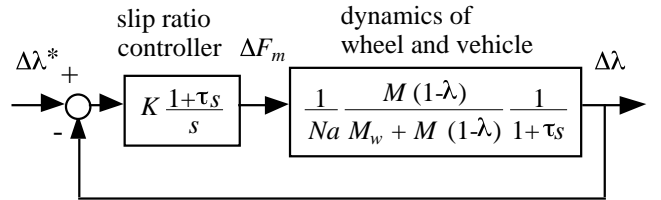


Fig.7. Slip ratio controller

Fig.8 shows the nominal slip ratio used in the slip ratio controller. We defined it by  $a=1$ . The point of  $a=1$  is located just in left side of the peak and is stable. Both of the longitudinal and lateral forces are kept still high.

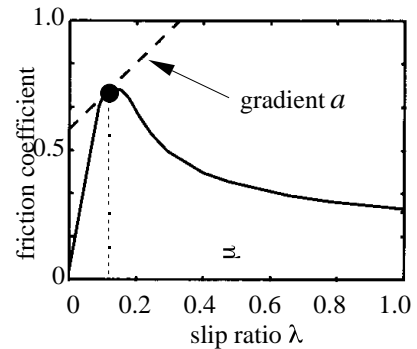


Fig.8. Nominal slip ratio is given by  $a=1$ .

### C. Robustness to Parameter Variation

Because the actual system parameters change widely, we should investigate the robustness of the slip ratio controller. Fig.9 draws the root locus to the continuous change of  $K$  and  $a$ .

From the figure, we can see that the roots move to the left half plane when the controller gain  $K$  increases. It is interesting that this controller stabilizes the system even when actual  $a$  is negative, although the roots move to unstable region.

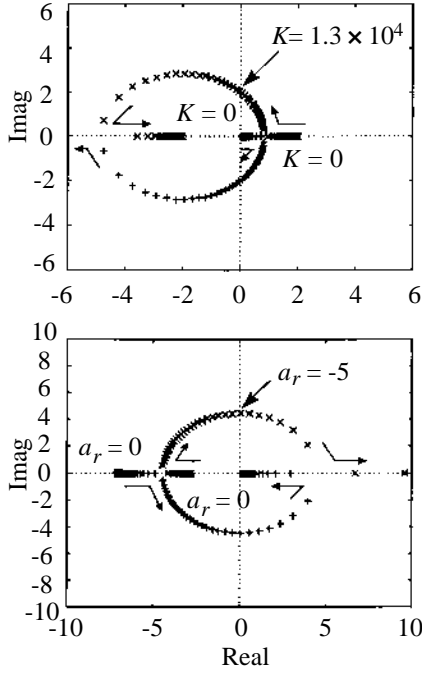


Fig.9. Root locus against parameter variation

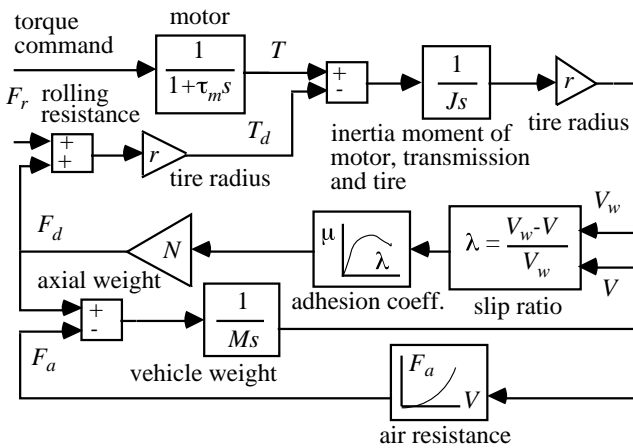


Fig.10 Vehicle model used in the simulation

### D. Simulation of Slip Ratio Control

Fig.10 shows the vehicle model we used in the simulation.  $T$  represents the motor torque and  $r$  the total gear ratio of the drive train.  $F_d$  represents the summation of traction

force transferred to the contact point of tire and road surface. It is the product of traction coefficient  $\mu$  and  $N=Mg$ , the vertical load on the contact point.  $\mu$  is defined as a function of  $\lambda$  (slip), which is given by the measured curve shown in Fig.11.

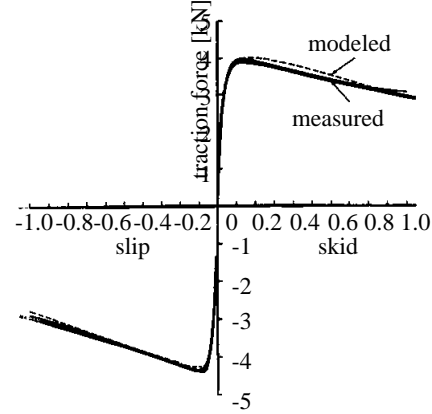


Fig.11.  $\mu$ - $\lambda$  characteristics used in the simulation

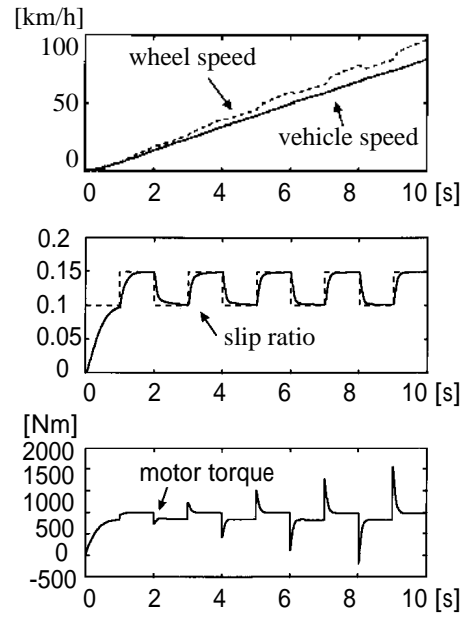


Fig.12 Simulation of the slip ratio control

Fig.12 is the simulation result. The response time of the slip ratio controller is set to be 100[ms]. We can see good response characteristics.

### E. Experimental Results of Slip Ratio Control

Fig.13 shows the experimental results of the slip ratio control using the laboratory-made experimental electric vehicle "UOT Electric March". Here the response time is 50[ms] and the target slip ratio is 0.1 in Fig.13(a) and is changed stepwise from 0.3 to 0.1 in Fig.13(b).

Basically we can see fairly good performances but there are some problems. First, the actual value of  $a$  was much smaller than the nominal value: 1. This made the response

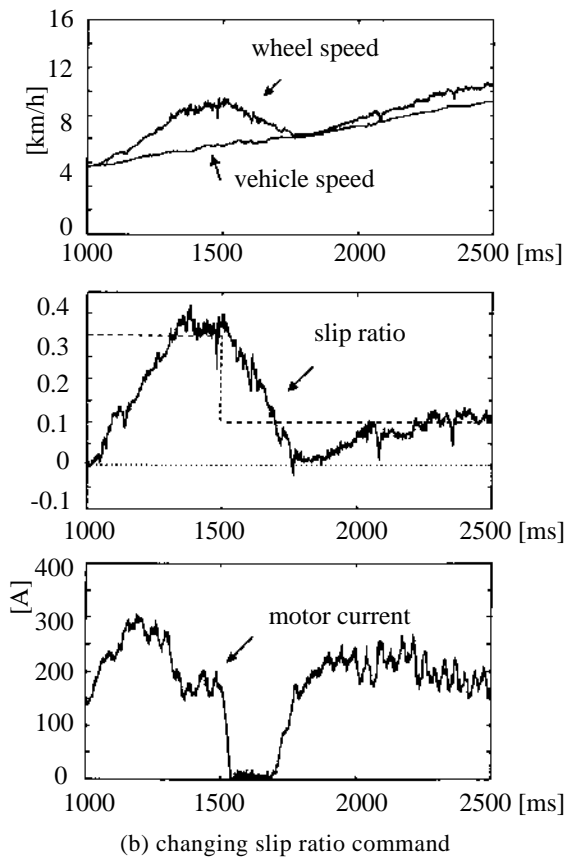
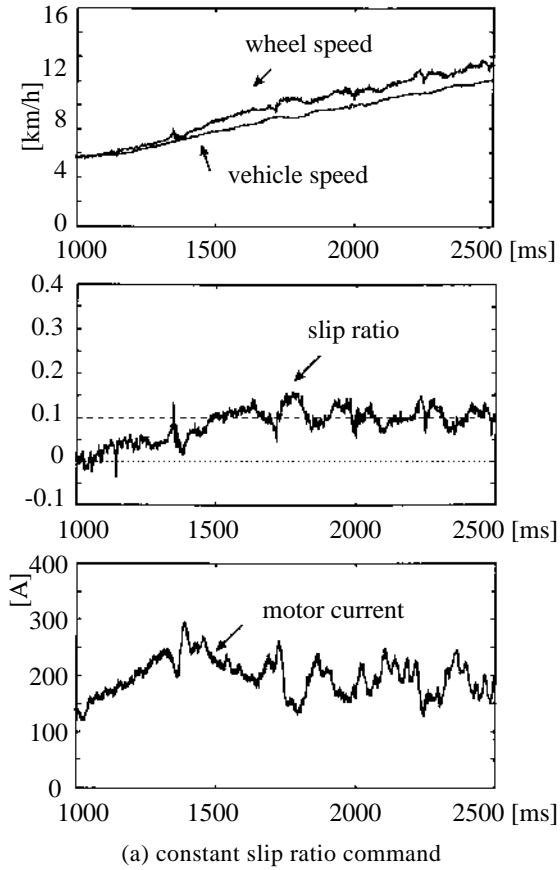


Fig.13. Experimental results of the slip ratio control

time longer than the designed value. Next, in Fig.13(b), we see an undershoot to the slip ratio command of 0.1. This is because the motor controller we used is just an 1-quadrant chopper, who can not absorb the motor current.

## VI. ESTIMATION OF ROAD CONDITION

In the previous chapter, we showed effective slip ratio control. Next problem is how to give the optimal slip ratio to the slip ratio controller.

We showed the relation between the slip ratio  $\lambda$  and the friction coefficient  $\mu$  in Figs.1 and 11, but it varies very widely according to road surface condition as shown in Fig.14. It is clear that the slip ratio where the friction force takes its maximum value vary according to road condition. This means that road condition should be estimated relatively quickly for commanding the optimal slip ratio to the slip ratio control.

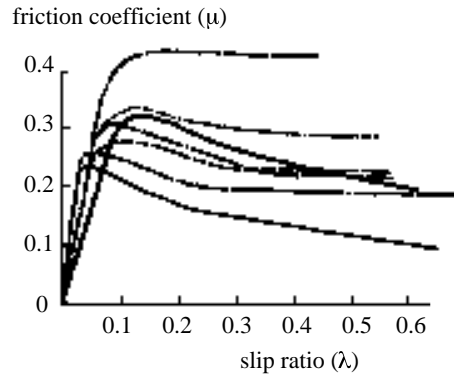


Fig.14. Various Road Condition.  
(Actual explanation of each curves is omitted.)

To know the road surface condition, we should estimate the friction coefficient. If we can measure the vehicle speed directly by using non-driven wheel, the friction coefficient  $\mu$  can be obtained by eq.(13) based on eqs.(3) and (4).

$$\mu = \frac{M}{N} \frac{dV}{dt} \quad (13)$$

When the vehicle speed can not be measured directly, we can estimate  $\mu$  based on eq.(14).

$$\mu = \frac{1}{N} \left( F_m - M_w \frac{dV_w}{dt} \right) \quad (14)$$

In our case, we can use both of these two methods. Fig.15 shows the estimation result of  $\mu$ - $\lambda$  curve of dry asphalt road when no slip control is active. At the point around  $\lambda=0.08$ , the gradient  $a$  of  $\mu$ - $\lambda$  curve is about 1.

Fig.16 shows the estimation results on wet iron surface under the slip ratio control proposed in the previous chapter. Here, the optimal slip ratio is smaller than 0.05.

It is also noticed that, in our experiment shown in Fig.13(a), the actual gradient of  $\mu$ - $\lambda$  curve at  $\lambda=0.1$  was almost -1. We can see that the slip ratio controller is effective even when the operation point is unstable, but, in this case, we should have commanded a lower slip ratio.

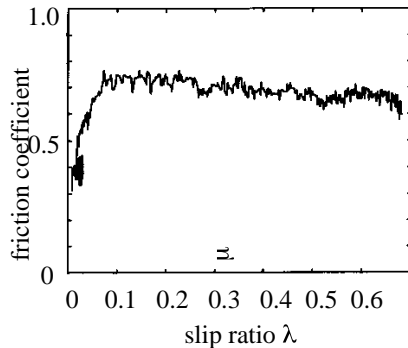


Fig.15. Estimation result of  $\mu$ - $\lambda$  curve of dry asphalt road

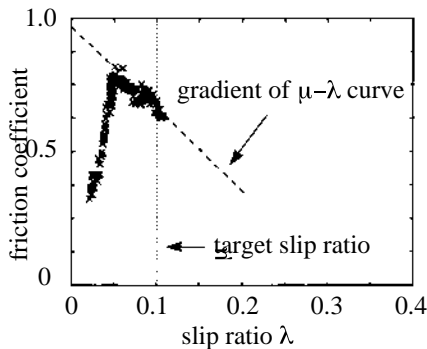


Fig.16. Estimation result of  $\mu$ - $\lambda$  curve of wet iron plate under the slip ratio control

## VII. CONCLUSION

We are proposing a new field of "Motion Control of Electric Vehicle". EV is a very interesting object combining electrical and mechanical engineering fields from the view point of motion control. As an example, we proposed advanced adhesion control utilizing quick and precise torque response of electric motor.

We proposed the Model Following Control and the Optimal Slip Ratio Control. We confirmed that MFC can reduce its torque quickly when the motor speed is suddenly increased by tire slip. Next, we showed that the optimal slip ratio control has more advanced performance. Such kinds of quick controls are firstly realized only in electric vehicles. It is clearly shown that relatively precise control theory can work well in actual experiments.

Advanced adhesion control is helpful for lateral control like yaw disturbance attenuation. This is because the proposed optimal slip ratio control keeps the tire slip within the small region where both of the longitudinal and lateral adhesion coefficients are still high enough.

## ACKNOWLEDGEMENT

The authors would like to express their sincere thanks to Mr. Furuya in Kansai Electric Power Company for his big work on Electric March when he was a graduate student in Hori Laboratory. They also thank Mr. Uchida and Mr. Yamazaki for their help in manufacturing of the vehicle.

## REFERENCES

- [1] M.Ito and K. Isoda, "The Present and Future Trends of Traction Control System", *Jidosha-Gijutsu*, Vol.46, No.2, pp.32-37, 1992. (in Japanese)
- [2] K. Ise, et. al., "The 'Lexus' Traction Control (TRAC) System", SAE Paper 900212, 1990.
- [3] J. Ackermann, "Yaw Disturbance Attenuation by Robust Decoupling of Car Steering", 13th IFAC World Congress, 8b-01-1, pp.1-6, 1996.
- [4] Y. Wang and M. Nagai, "Integrated Control of Four-Wheel-Steer and Yaw Moment to Improve Dynamic Stability Margin", Proc. 35th IEEE-CDC, pp.1783-1784, 1996.
- [5] C. Liu and H. Peng, "Road Friction Coefficient Estimation for Vehicle Path Prediction", *Vehicle System Dynamics Supplement 25*, pp.413-425, Swets & Zeitlinger, 1996.
- [6] A. Daiss and U. Kiencke, "Estimation of Tyre Slip during combined Cornering and Braking Observer Supported Fuzzy Estimation", 13th IFAC World Congress, 8b-02-2, pp.41-46, 1996.
- [7] Hideo Sakai, "Tire Engineering", Grand-Prix Pub. Co., 1987. (in Japanese)
- [8] S. Yamazaki, T. Fujikawa and I. Yamaguchi, "A Study on Braking and Driving Properties of Automotive Tires", *Transactions of the Society of Automotive Engineers of Japan*, Vol.23, No.2, pp.97-102, 1992.
- [9] T.Furuya, Y.Toyoda and Y.Hori, "Implementation of Advanced Adhesion Control for Electric Vehicle", Proc. IEEE Workshop on Advanced Motion Control, AMC-Mie'96, Vol.2, pp.430-435, 1996.

## APPENDIX

### Configuration of UOT Electric March

We developed a real test electric vehicle "UOT Electric March (Todai Sangatsu Go)" seen in Fig.A-1. It is a so-called convert car, whose IC engine is replaced by an electric motor.

The front two wheels are driven by a 19[kW] series-wound DC motor through a 5 speed manual transmission and a differential gear. The 1-quadrant DC chopper supplies power to the motor. Its current limit is 400[A] and can produce maximum torque over 100[Nm], which is enough to perform the slip experiment. Current and speed sensors are also implemented. To detect the vehicle speed, a speed sensor is implemented in the rear wheel.

TABLE A-I  
SPECIFICATION OF UOT ELECTRIC MARCH

<b>Conversion Base</b>	Nissan March (Micra)
size	3785 × 1560 × 1395[mm]
weight	900[kg](batteries included)
<b>Motor</b>	Advanced D.C. Motors, Inc.
type	DC series wound
rated power (@120V)	19[kW](1hr.), 32[kW](5min.)
size/weight	φ 232, length 397[mm], 65[kg]
<b>Controller</b>	Curtis Instruments, Inc.
type	MOSFET PWM Chopper
operating frequency	15[kHz]
rated voltage/current	120[V]/400[A]
<b>Battery</b>	Japan Storage Battery Co.,Ltd. GTX-130E41L
type	lead acid
voltage/capacity	72[V]/92[Ah](5hr)
weight	27.5[kg] × 6
<b>CPU</b>	PC9801NS/T (386SL, 20MHz)
weight	3.2[kg]
A/D and D/A converters	12bit, 8ch / 12bit, 2ch

Fig.A-2 shows the control system of the vehicle and TABLE A-I gives its specification. We use a note-type personal computer to realize the torque control. It not only executes the control algorithm and puts out the voltage command to the chopper, but also reads, shows and records the sensor data. As the control algorithm is written by software (C-language), we can easily investigate various

control strategies.

Fig.A-3 shows the basic experimental results of the current controller.



Fig.A-1 UOT Electric March (Todai Sangatsu Go)

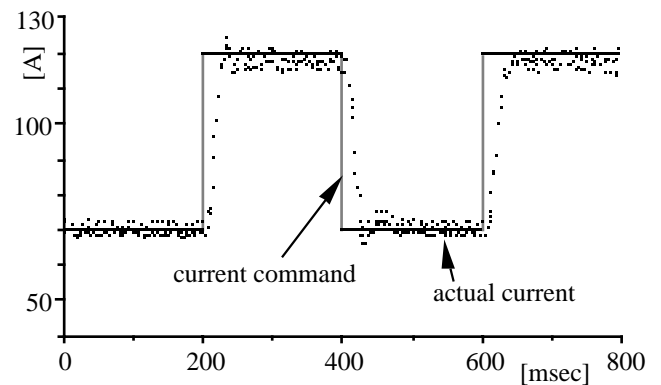


Fig.A-3. Basic experiment on the current response

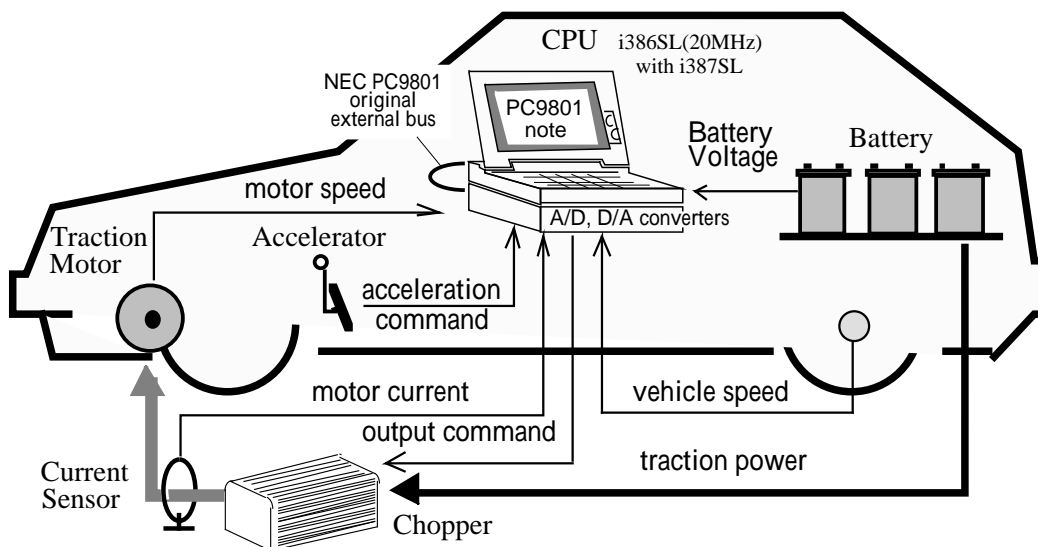


Fig.A-2 Configuration of UOT Electric March

# Future Vehicle Driven by Electricity and Control—Research on Four-Wheel-Motored “UOT Electric March II”

Yoichi Hori, *Senior Member, IEEE*

**Abstract**—The electric vehicle (EV) is the most exciting object to apply “advanced motion control” technique. As an EV is driven by electric motors, it has the following three remarkable advantages: 1) motor torque generation is fast and accurate; 2) motors can be installed in two or four wheels; and 3) motor torque can be known precisely. These advantages enable us to easily realize: 1) high performance antilock braking system and traction control system with minor feedback control at each wheel; 2) chassis motion control like direct yaw control; and 3) estimation of road surface condition. “UOT Electric March II” is our novel experimental EV with four in-wheel motors. This EV is made for intensive study of advanced motion control of an EV.

**Index Terms**—Adhesion control, antilock braking system (ABS), body slip angle estimation, direct yaw control (DYC), electric vehicle (EV), estimation of road surface condition, motion control, slip ratio control (SRC), traction control system (TCS).

## I. THREE ADVANTAGES OF ELECTRIC VEHICLE

RECENTLY, pure electric vehicles (PEVs) have achieved sufficient driving performance thanks to drastic improvements in motors and batteries. On the other hand, hybrid EVs (HEVs), like the Toyota Prius, will be widely used in the next ten years. Fuel-cell vehicles (FCVs) will be the major vehicles in the 21st century. Such development has the strong incentives of energy efficiency and global environmental protection.

However, it is not well recognized that the most distinct advantage of the EV is the quick and precise torque generation of the electric motor. If we do not utilize this merit, the EV will never be used in the future. For example, if a diesel HEV is developed, its energy consumption will be extremely low. The EV cannot compete against such vehicles in terms of energy efficiency or CO<sub>2</sub> emissions. On the contrary, if we recognize the advantage of the EV in control performance and succeed in the development of new concept vehicles, a bright future will be waiting for us.

We can summarize the advantages of the EV into the following three points.

- 1) *Torque generation of an electric motor is very quick and accurate.*

This is the essential advantage. The electric motor’s torque response is several milliseconds, 10–100 times as

fast as that of the internal combustion engine or hydraulic braking system. This enables feedback control and we can change vehicle characteristics without any change in characteristics from the driver. This is exactly based on the concept of a two-degrees-of-freedom (2DOF) control system. A “Super Antilock Brake System (ABS)” will be possible. Moreover, an ABS and traction control system (TCS) can be integrated, because a motor can generate both acceleration or deceleration torques. If we can use low-drag tires, it will greatly contribute to energy saving.

- 2) *A motor can be attached to each wheel.*

Small but powerful electric motors installed into each wheel can generate even the antidiagonal torques on left and right wheels. Distributed motor location can enhance the performance of Vehicle Stability Control (VSC) such as Direct Yaw Control (DYC). It is not permitted for an Internal Combustion engine Vehicle (ICV) to use four engines, but it is all right to use four small motors without a big cost increase.

- 3) *Motor torque can be measured easily.*

There is much smaller uncertainty in driving or braking torque generated by an electrical motor, compared to that of an IC engine or hydraulic brake. It can be known from the motor current. Therefore, a simple “driving force observer” can be designed and we can easily estimate the driving and braking force between tire and road surface in real time. This advantage will contribute greatly to application of new control strategies based on road condition estimation. For example, it will be possible to alert the driver, “We have now entered a snowy road!”

These advantages of the electric motor will open the new possibility of novel vehicle motion control for electric vehicles. Our final target is to realize a novel vehicle control system with four independently controlled in-wheel motors, as depicted in Figs. 1 and 2. It shows the integrated system with “minor feedback control loop at each wheel” and “total chassis controller” as an outer weak feedback loop. Here, Model-Following Control (MFC) is drawn as an example of the minor loop. A very short time delay is required for the actuator to perform such effective feedback controls.

## II. WHAT CAN WE DO WITH AN EV?

As examples of novel control techniques, which can be realized primarily in EVs, we are investigating several techniques.

Manuscript received November 4, 2002; revised April 29, 2004. Abstract published on the Internet July 15, 2004.

The author is with the Institute of Industrial Science, The University of Tokyo, Tokyo 153-8505, Japan (e-mail: hori@iis.u-tokyo.ac.jp).

Digital Object Identifier 10.1109/TIE.2004.834944

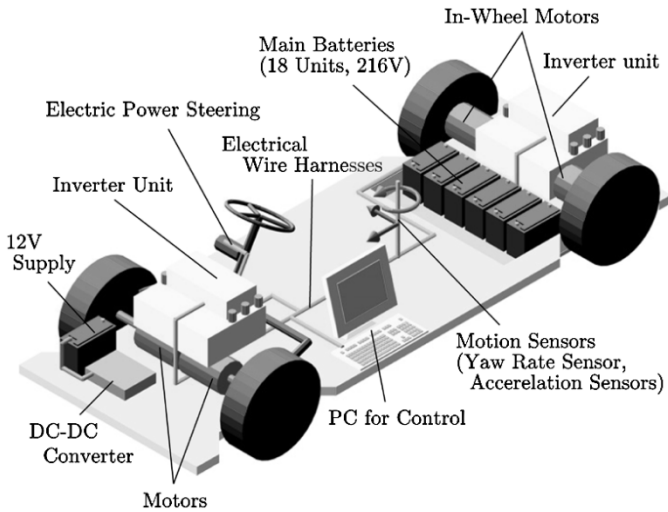


Fig. 1. Sketch of “UOT March II.”

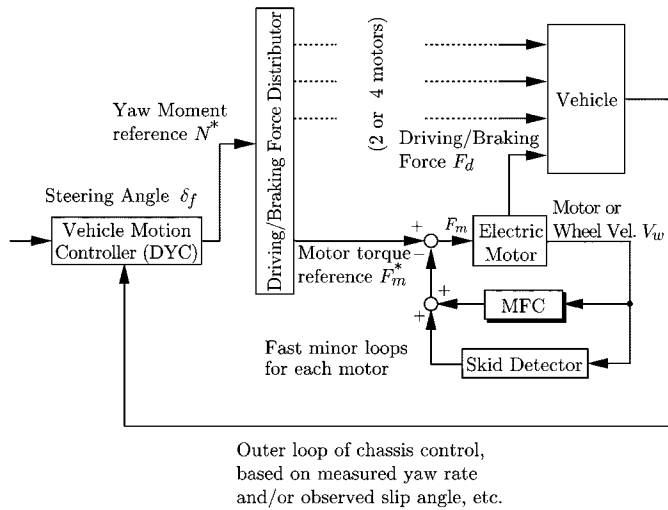


Fig. 2. Control system to be realized in “UOT March II.”

**A. Adhesion Control of Tire and Road Surface**

In this control method, the advantage of an electric motor is most effectively utilized:

- 1) MFC;
- 2) Slip Ratio Control (SRC);
- 3) cooperation with higher level control like DYC;
- 4) wheel skid detection without vehicle speed knowledge.

**B. High-Performance Braking Control**

We can realize a higher performance braking control system like an elevator utilizing an electric motor’s controllability:

- 1) pure electric braking control in a whole speed range;
- 2) hybrid ABS for HEV; fast but small torque electric brake can assist hydraulic brake system, which has big torque but slow response;
- 3) direct control of driving force at each tire.

**C. Two-Dimensional Attitude Control**

The aim of two-dimensional attitude control is basically to find the solution to the problem of how to mix the controls of  $\gamma$

TABLE I  
SPECIFICATIONS OF “UOT ELECTRIC MARCH II”

<b>Drivetrain</b>	<b>4 PM Motors / Meidensya Co.</b>
Max. Power(20 sec.)	36 [kW] (48.3[HP])*
Max. Torque	77* [Nm]
Gear Ratio	5.0
<b>Battery</b>	<b>Lead Acid</b>
Weight	14.0 [kg](for 1 unit)
Total Voltage	228 [V] (with 19 units)
<b>Base Chassis</b>	<b>Nissan March K11</b>
Wheel Base	2360 [m]
Wheel Tread F/R	1365/1325 [m]
Total Weight	1400 [kg]
Wheel Inertia**	8.2 [kg]***
Wheel Radius	0.28 [m]
<b>Controller</b>	
CPU	MMX Pentium 233[MHz]
Rotary Encoder	3600 [ppr]***
Gyro Sensor	Fiber Optical Type

\* ... for only one motor. \*\* ... mass equivalent.  
\*\*\* ... affected by gear ratio.

(yaw rate) and  $\beta$  (body slip angle). It consists of linearization of transfer characteristic from driver’s angle  $\delta_f$  to  $\gamma$  and control  $\beta$  to be zero:

- 1) decoupling control of  $\beta$  and  $\gamma$ ;
- 2) higher performance coordination of Active Front Steering (AFS) and DYC;
- 3) vehicle dynamics control based on  $\beta$  estimation;
- 4) dynamic driving force distribution considering side force and cooperation with suspension system under changing load.

**D. Road Surface Condition Estimation**

As the motor torque can be known easily from the motor current, we can apply various kinds of estimation techniques:

- 1) estimation of gradient of  $\mu-\lambda$  curve;
- 2) estimation of the maximum friction coefficient;
- 3) estimation of the optimal slip ratio to be used for SRC;
- 4) higher performance DYC based on the estimation of road surface condition.

III. NOVEL EXPERIMENTAL ELECTRIC VEHICLE  
“UOT MARCH II”

Our EV “UOT (University of Tokyo) Electric March II” was constructed in 2001. The most remarkable feature of this EV is the in-wheel motor mounted in each wheel. We can control each wheel torque completely and independently. Regenerative braking is, of course, available. We built this EV ourselves by remodeling a Nissan March.

Table I lists the specifications of the “UOT Electric March II.” It uses a permanent-magnet (PM) motor and has a built-in drum brake and reduction gear. The motor unit is as compact as the wheel. Two motors are placed at the ends of each driving shaft, and attached to the base chassis as shown in Fig. 3(a) and (d). The electric motors are controlled by on-board personal computers (PCs).

We use another PC for motion control. They are connected to several sensors, such as, a fiber-optical gyro sensor, three-axis acceleration sensor, and so on. A motion controller is installed



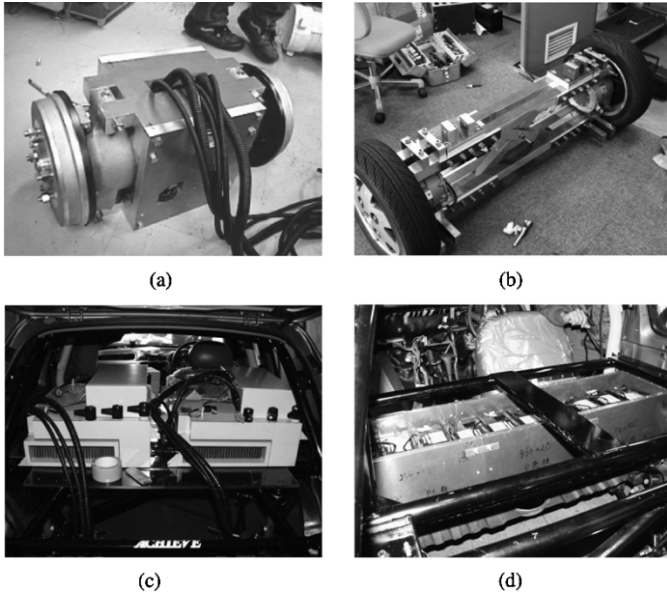


Fig. 3. Main parts of UOT Electric March II. (a) Front motors. (b) Rear motors. (c) Inverters. (d) Batteries.

in the second PC. It outputs the motor torque references, and two inverter units generate the required motor torques. Precise torque generation is achieved by the motor current controller in the inverter units. In order to detect steering angle, the encoder signal for EPS is used.

#### IV. ANTISKID CONTROL IN LONGITUDINAL DIRECTION

In this section, a wheel controller for skid prevention is proposed. The starting point of this idea is to utilize the knowledge obtained in advanced motion control techniques of electric motors. Generally speaking, a feedback controller can change mechanical plant dynamics. For example, the plant can be insensitive to disturbance if an appropriate feedback controller is applied. Fast response of the actuator, which is readily available in an EV, can realize such controls. We propose two anti-slip controllers: MFC and SRC.

##### A. MFC

In the simple model of one wheel shown in Fig. 4, the slip ratio  $\lambda$  is given by

$$\lambda = \frac{V_w - V}{\max(V_w, V)} \quad (1)$$

where  $V$  is the vehicle chassis velocity, and  $V_w$  is the wheel velocity given by  $V_w = r\omega$ .  $r$  and  $\omega$  are the wheel radius and rotational velocity, respectively.

Fig. 5 shows the block diagram of MFC.  $F_m^*$  is the acceleration command roughly proportional to the acceleration pedal angle.  $F_m^* = T^*r$ , where  $T^*$  is the driver's command torque.  $\omega$  increases drastically when the tire slips.

Vehicle dynamics including tire and road surface characteristics are very complicated, but if we use the slip ratio  $\lambda$ , the

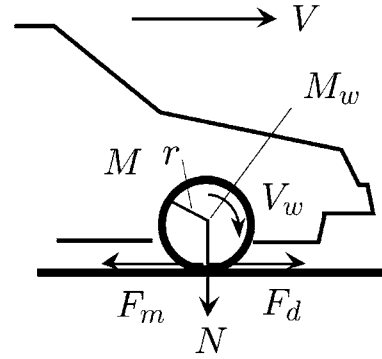


Fig. 4. One wheel model.

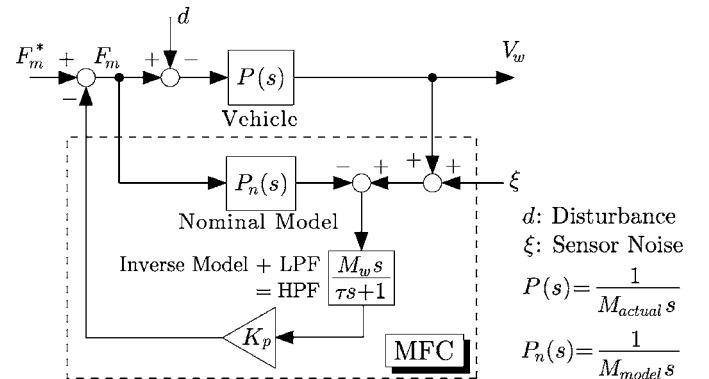


Fig. 5. Block diagram of the proposed feedback controller "MFC."

vehicle body can be seen as one inertia system with the equivalent inertia moment given by

$$M_{\text{actual}} \simeq M_w + M(1 - \lambda). \quad (2)$$

Here,  $M_{\text{actual}}$ ,  $M_w$ , and  $M$  are the total equivalent mass, wheel mass, and equivalent vehicle mass. Equation (2) means that the vehicle seems lighter when the tire slips and  $\lambda$  increases. We used  $M_{\text{model}} = M_w + M$  with  $\lambda = 0$  as the reference model.

When there is no slip,  $M_{\text{actual}}$  is almost equal to  $M_{\text{model}}$ . No control signal is generated from the MFC controller. If the tire slips, actual speed  $\omega$  increases quickly. Model speed does not increase. Hence, by feeding back the speed difference to motor current command, the motor torque is reduced quickly and it induces re-adhesion.

As this control function is needed only in relatively higher frequency region, a high-pass filter with time constant  $\tau$  is used on the feedback path.

When a vehicle starts skidding, the wheel velocity changes rapidly. For example, if a vehicle starts skidding during acceleration, its wheel velocity increases rapidly, and during deceleration, it decreases rapidly due to the wheel lock. Such rapid change of wheel velocity is observed as a sudden drop of wheel inertia moment. Based on this viewpoint, we design the MFC as shown in Fig. 5. Using (3) as the nominal model inertia, this controller can suppress sudden drop of inertia. Applying this controller, the dynamics of the skidding wheel becomes closer to that of the adhesive wheel.

Experiments were carried out with "UOT March-I", which is our first laboratory-made EV constructed in 1997. To simulate

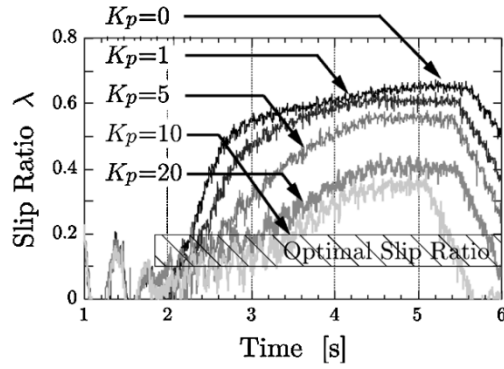
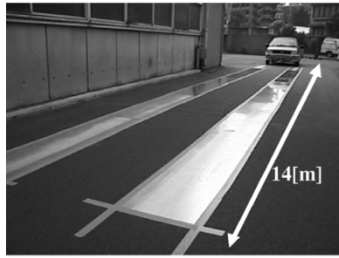


Fig. 6. Experimental results of MFC for skid prevention with  $\tau = 0.1$ .

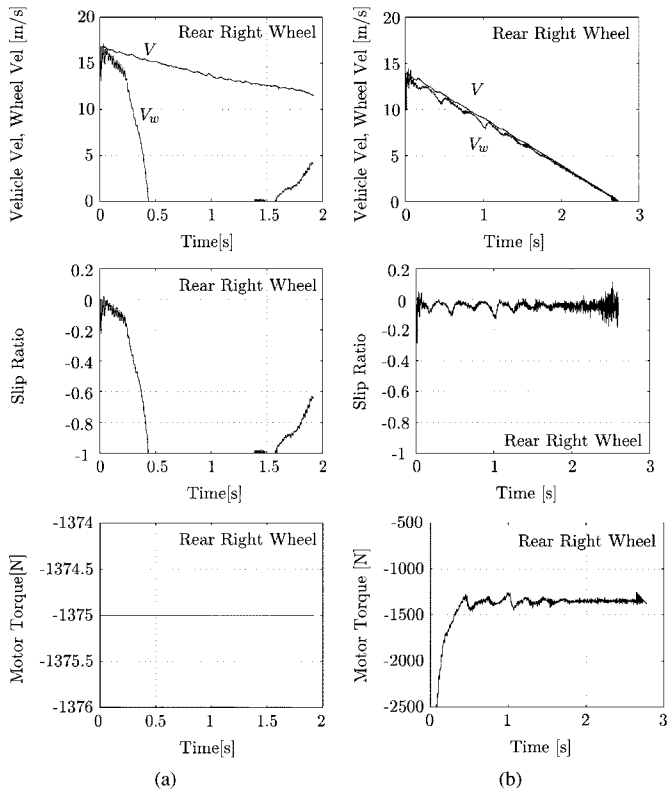


Fig. 7. Results of rapid braking experiment. (a) Without MFC. (b) With MFC.

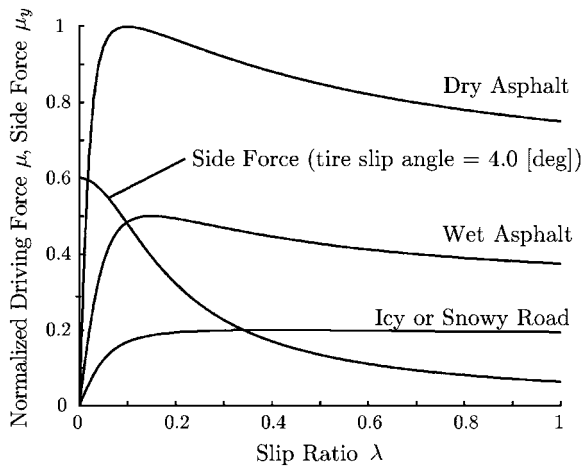


Fig. 8. Typical  $\mu$ - $\lambda$  curve.

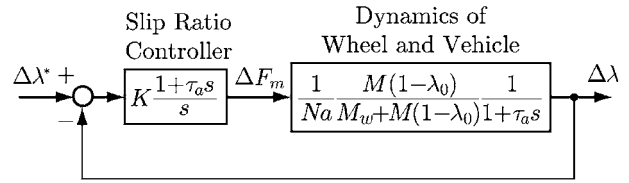


Fig. 9. Slip ratio controller.

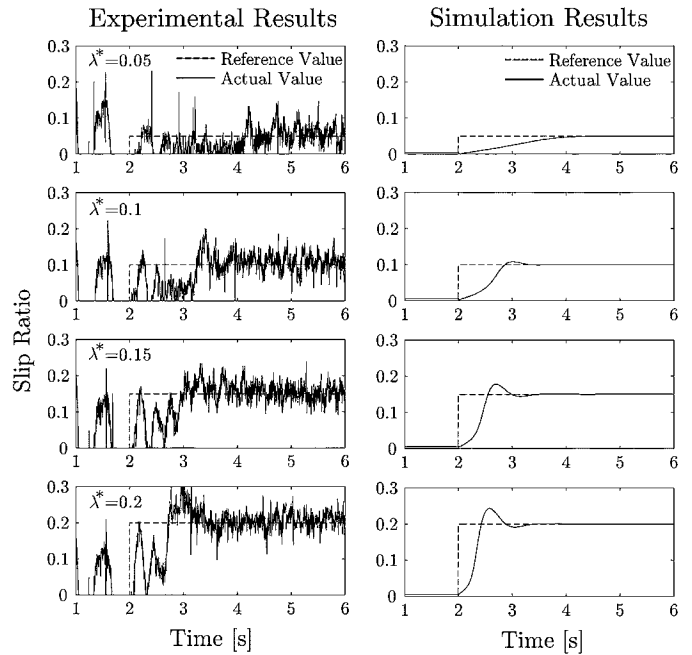


Fig. 10. Experimental results of SRC.

a slippery low- $\mu$  road, we put aluminum plates of 14-m length on the asphalt, and spread water on them. The peak  $\mu$  of this test road was estimated at about 0.5.

Fig. 6 shows the time responses of slip ratio. In these experiments, the vehicle was accelerated on the slippery test road, while the motor torque was increased linearly. Without control, the slip ratio rapidly increases. On the contrary, the increase of slip ratio is suppressed when the proposed controller is applied.

Fig. 7 shows the experimental results using “UOT March II” on a professional test course. The car is decelerated suddenly on the slippery course, where  $\mu_{peak}$  was about 0.5. Without control, the wheel velocity rapidly decreased and the vehicle’s wheels

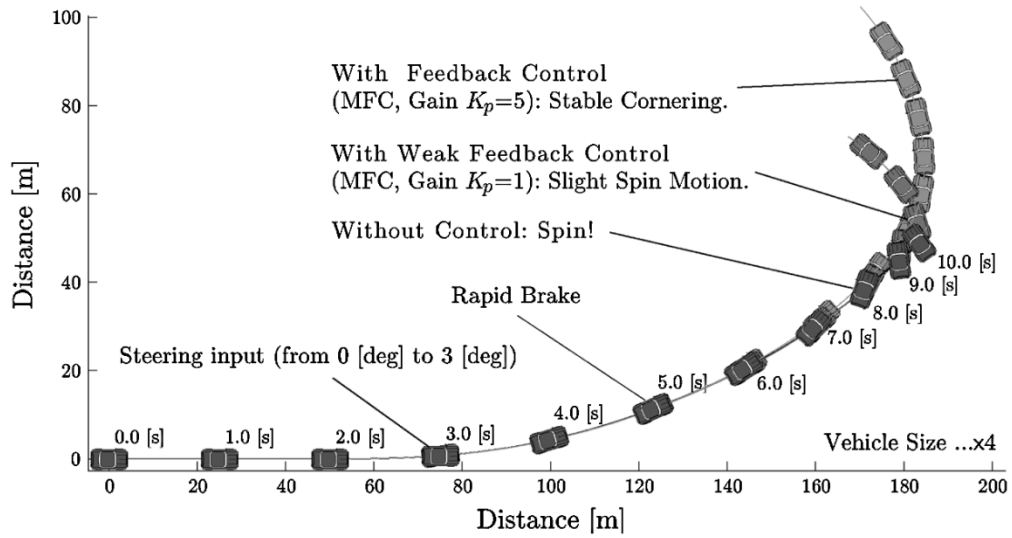


Fig. 11. Stabilizing effect with controlled four wheels is visualized with vehicle trajectory (rapid brake during curve turning, on a slippery road).

were soon locked as seen in Fig. 7(a). In contrast, when MFC is applied, the wheels were not locked, and the vehicle stopped safely [Fig. 7(b)].

### B. SRC

MFC showed that electric motor control can change mechanical characteristics. If we need more exactly to regulate the slip ratio within a specified range, a more precise approach is necessary.

Based on the tire model shown in Fig. 4, under some practical assumptions, the kinetic equations of the wheel and vehicle take the forms of

$$(F_m - F_d) \frac{1}{M_w s} = V_w \quad (3)$$

$$F_d \frac{1}{M s} = V. \quad (4)$$

The friction force between the road and the wheel is given by

$$F_d = N \mu(\lambda) \quad (5)$$

where  $F_m$  is the motor torque (force equivalent),  $F_d$  the friction force,  $M_w$  the wheel inertia (mass equivalent),  $M$  the vehicle weight, and  $N$  the vertical force given by  $N = Mg$ . Fig. 8 gives the typical characteristics of a  $\mu$ - $\lambda$  curve.

From (1), when  $V_w \gg V$ , the perturbation system is given by

$$\begin{aligned} \Delta \lambda &= \frac{\partial \lambda}{\partial V} \Delta V + \frac{\partial \lambda}{\partial V_w} \Delta V_w \\ &= -\frac{1}{V_{w0}} \Delta V + \frac{V_0}{V_{w0}^2} \Delta V_w \end{aligned} \quad (6)$$

where  $V_{w0}$  and  $V_0$  are the wheel and vehicle speeds at a certain operational point. The frictional force is given by  $a$ , the gradient of  $\mu$ - $\lambda$  curve.  $a$  is defined by

$$\Delta \mu = a \Delta \lambda. \quad (7)$$

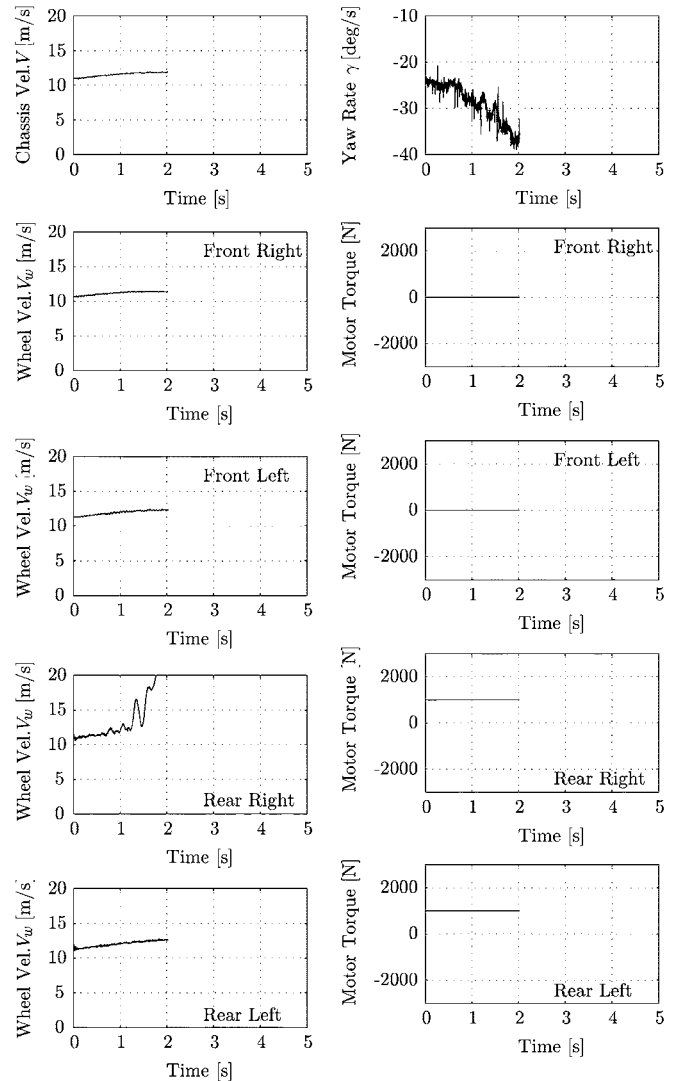


Fig. 12. Unstable cornering with sudden acceleration without MFC.

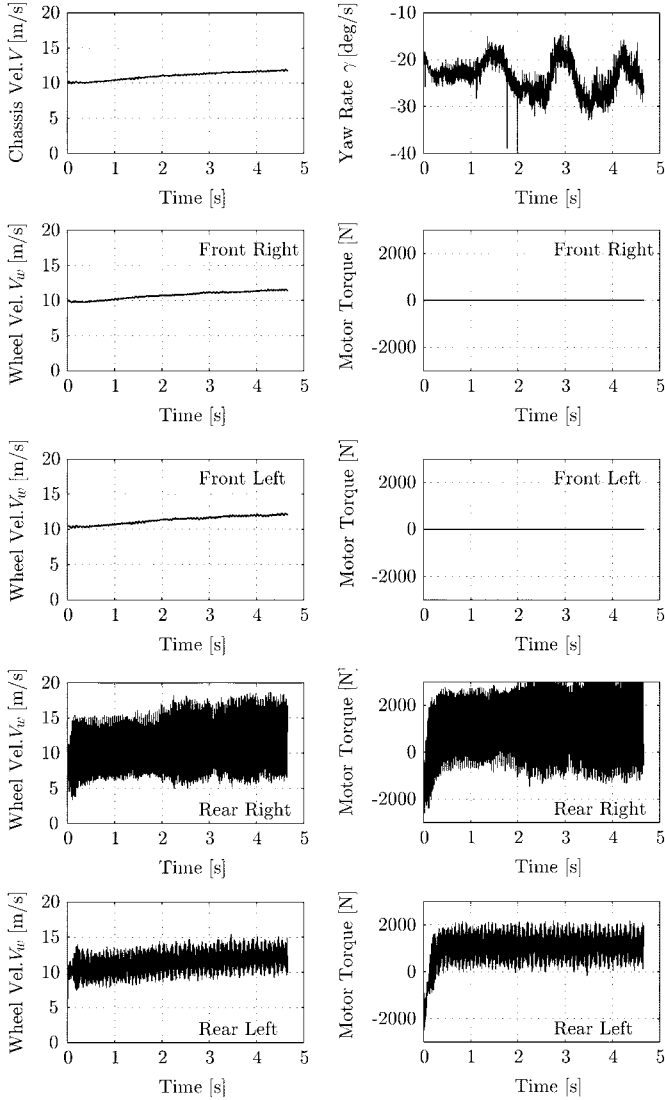


Fig. 13. Vehicle stabilizing effect of our proposed controller MFC.

The transfer function from motor torque to slip ratio is obtained by

$$\frac{\Delta\lambda}{\Delta F_m} = \frac{1}{Na} \frac{M(1-\lambda_0)}{M_w + M(1-\lambda_0)} \frac{1}{1 + \tau_a s}. \quad (8)$$

The time constant  $\tau_a$  is given by (10), which is proportional to the wheel speed  $V_{w0}$

$$\tau_a = \frac{1}{Na} \frac{MM_w V_{w0}}{M_w + M(1-\lambda_0)}. \quad (9)$$

The typical value of  $\tau_a$  is 150–200 ms when  $a = 1$  and the vehicle speed is around 10 km/h.  $a$  can be negative in the right-hand side of the peak of the  $\mu$ - $\lambda$  curve.

A simple proportional–integral (PI) controller with a variable proportional gain is enough as a slip ratio controller. It is given by (11) and drawn in Fig. 9

$$K \frac{1 + \tau_a s}{s}. \quad (10)$$

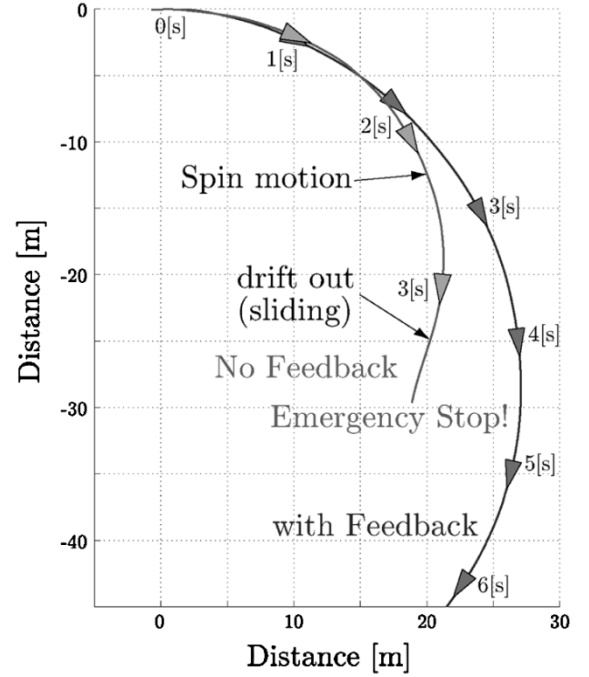


Fig. 14. Stabilizing effect of MFC installed in each wheel.

The transfer function from the slip ratio command to the actual slip ratio becomes

$$\frac{\Delta\lambda}{\Delta\lambda^*} = \frac{1}{1 + Na \frac{M_w + M(1-\lambda_0)}{M(1-\lambda_0)} \frac{1}{K} s}. \quad (11)$$

If  $\lambda_0 \ll 1$ , this is a simple first-order delay system with the time constant adjustable by  $K$ . Here, we put this response time at 50–100 ms.

Fig. 10 shows the experimental results of SRC using ‘‘UOT March I’’ and the corresponding simulations. Here, the target slip ratio is changed stepwise from 0 to various values. We can see good performance in all cases.

## V. LATERAL MOTION STABILIZATION

### A. Vehicle Behavior Simulation With MFC in Each Wheel

In the previous section, the minor feedback control at each wheel was discussed. Next, our interest is in what will happen if we apply such feedback control to every wheel when the vehicle is turning on a slippery road.

Here we assume that an in-wheel motor is independently attached on every wheel, and MFC is applied to each of them. The simulation results (Fig. 11) show that this minor loop can enhance the lateral stability effectively. In simulations, the chassis’s 3DOF nonlinear motion dynamics, four wheels’ rotation, and dynamic load distribution are also carefully considered.

The vehicle starts running on the slippery road where  $\mu_{\text{peak}} = 0.5$ , turning left with steering angle  $\delta_f = 3$  [deg]. Then, at  $t = 5.0$  s, the driver inputs rapid braking torque  $F_m = -1100$  N on each wheel. This torque exceeds the limit of adhesion performance. Therefore, the wheel skid occurs and the chassis starts to spin, although the driver stops braking at  $t = 9.0$  s. This wheel

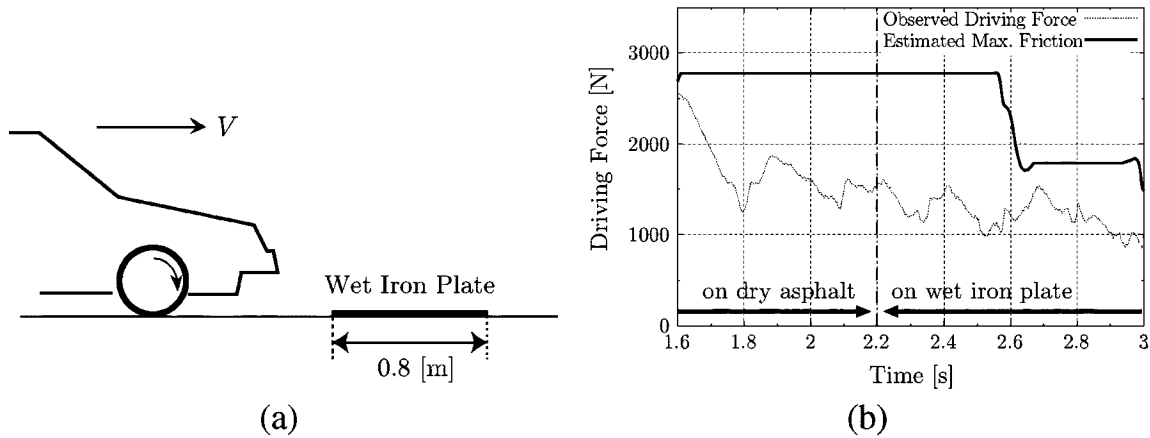


Fig. 15. Experimental results of road condition estimator. The sudden road condition change (a) was sensed with estimated maximum friction force as shown in (b).

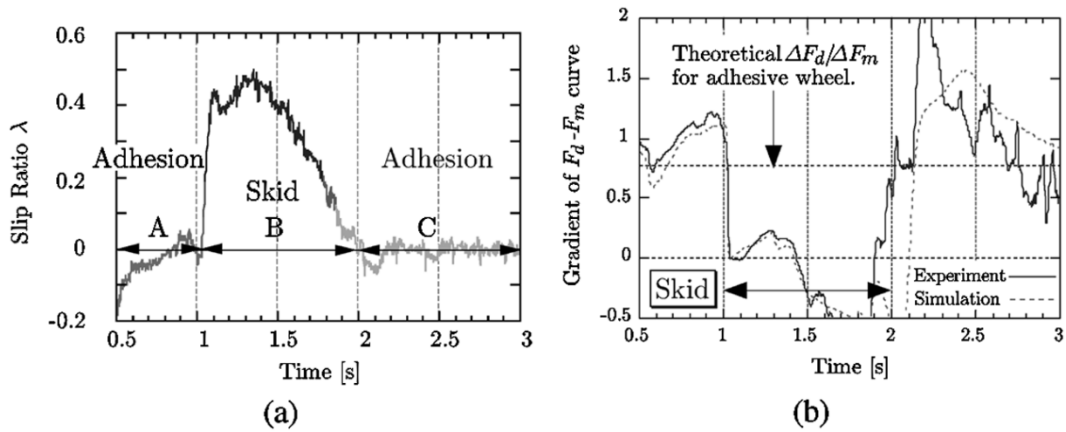


Fig. 16. Experimental results of wheel skid detector. (a) Reference slip ratio indicates that serious skid occurred during 1–2 s, and (b) the proposed method detected it.

skidding is serious, in particular, at the rear-left wheel, since the center of gravity is shifted and the load distribution changed.

On the contrary, if MFC is applied independently for each wheel, such dangerous spin motion is prevented. The rear-left wheel’s torque is reduced automatically. This method MFC uses only the local wheel velocity as the feedback signal in each wheel. Therefore, it differs from conventional attitude control methods like DYC. The autonomous stabilization of lateral motion is achieved only by minor feedback control at each wheel.

**B. Experiments of Stability Improvement by MFC**

Next, we performed actual experiments using “UOT Electric March II” on a slippery road, known as the skid pad. The rear-wheel velocities are controlled independently by the two rear motors, though “UOT March II” has a total of four motors.

At first, “UOT March II” was turning normally in the clockwise direction. The turning radius is about 25–30 m and chassis velocity is about 40 km/h. These values are close to those of the unstable region. In these experiments, acceleration torque of 1000 N was applied to the two rear motors. Without MFC, this rapid acceleration torque causes instability as shown in Fig. 12. The rear right wheel began skidding with much danger. The yaw

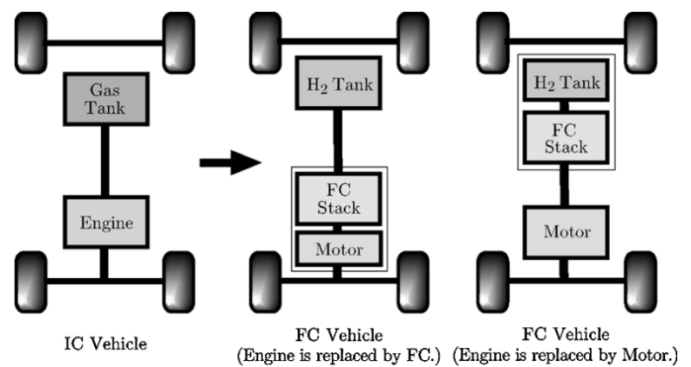


Fig. 17. Two ways to understand FCV.

rate grew into the unstable region. The vehicle was in a spinning motion and completely out of control. On the contrary, as shown in Fig. 13, such dangerous vehicle motion could not be observed.

Fig. 14 shows a comparison of the vehicle’s trajectories. It shows that the MFC controller prevents spinout caused by excessive over steer. One of the remaining problems is the high-frequency oscillation in rear wheel torques. It can be eliminated by appropriate vibration suppression control.

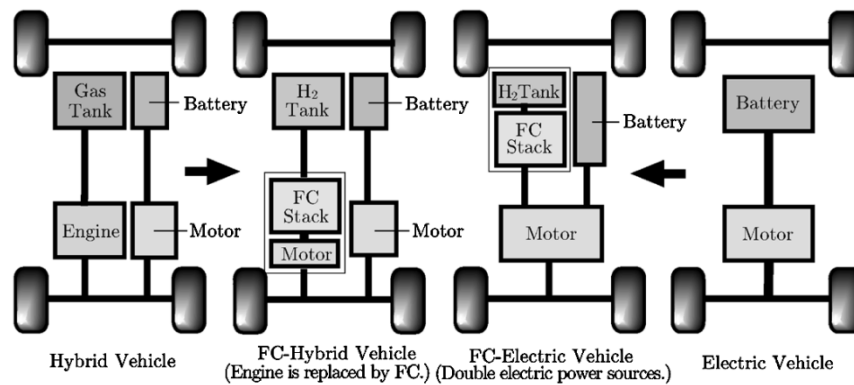


Fig. 18. Two ways to understand FCV with battery, FCHV, or FCEV?

## VI. ESTIMATION OF ROAD SURFACE CONDITION

Some important values like slip ratio  $\lambda$ , body slip angle  $\beta$ , or road peak  $\mu$  cannot be measured with practical sensors. As the motor torque can be generated precisely, its accurate value can be utilized as an information source. Estimation techniques are also important, and estimation of such variables can be easily realized in electric vehicles.

### A. Road Condition Estimation

The accurate value of wheel input torque will contribute greatly to practical and precise estimation. It is available on an EV with an electric motor, but not on vehicles with combustion engines. We have proposed an estimation technique of the peak  $\mu$  or maximum friction force during adhesive driving.

Fig. 15 shows the typical experimental results with UOT March I. This EV runs on the dry asphalt road, then reaches the wet iron plates. The road condition estimator calculates the maximum friction force between tire and road surface. This value indicates the sudden change of road condition, as shown in the figure. Note that even if the actual driving force is always less than the maximum frictional force, this method can still estimate maximum friction force.

This technique can be used as an alarm system to tell the driver “Please be careful. The car has now entered a slippery road!”

### B. Wheel Skid Detection Without Vehicle Speed

Wheel skid detection is another application of accurate torque generation of electric motor. This method can detect the wheel skid without chassis speed measurement. As the motor torque  $F_m$  is known, driving force observer can be designed to estimate the driving force  $F_d$ , which is the friction force between the road and tire. Its principle is identical to the disturbance observer. The skid detection algorithm is very simple. When  $F_m$  increases and  $F_d$  also increases, the tire should be adhesive. When  $F_m$  increases but  $F_d$  does not increase, then it is skidding. Fig. 16 shows the experimental results using UOT March I, where we can see the validity of this method.

## VII. CONCLUSION

In this paper, it has been pointed out that the EV is the most exciting target of advanced motion control techniques. Our

novel experimental EV “UOT March II” completed in 2001 was introduced. This new four-motor EV will play an important role in our novel motion control studies of the EV. As a first attempt, we proved the effectiveness of MFC and SRC. The most remarkable point of our research is in the utilization of the electric motor’s advantages: quick, accurate, and distributed torque generation.

Recent concerns for EVs are mainly focused on energy efficiency and environment, but we believe that future vehicles will be driven by electricity. If so, control is the most exciting and important topic. It is hoped that this paper will open a new field of “motion control” of electric vehicles.

## APPENDIX

### FCV—ENGINE IS REPLACED BY ELECTRIC MOTOR

In this appendix, the configuration of an FCV will be discussed. There are mainly two ways to understand an FCV. In Fig. 17, if we assume that the engine is replaced by an FC-stack and motor, we should compare the engine and FC-stack in various aspects, e.g., energy efficiency or power/weight ratio. On the other hand, if we assume that the gas tank is replaced by an  $H_2$  tank and FC-stack, the engine is replaced by the motor, then we can compare the engine and the motor at various points. We are standing on this viewpoint.

Which do you think is better? We are pursuing the future possibility of the electric motor’s advantage over an IC engine. An FCV uses an electric motor. Our development can be utilized in an FCV as it is. Fig. 18 shows two ways of calling an FCV. If we start from an HEV like the Toyota Prius, an FCHV is the natural name of this vehicle. The reasoning is as follows. As an FC is not enough for power generation and regenerative braking performance, an additional secondary battery and motor should be used together. In this meaning, an FCV is similar to an HEV.

On the contrary, if we understand that an FCV is simply using two types of electric power sources, the electric motor plays an important role as the main actuator. In our development of the March Project, we do not care about the kinds of energy sources. However, the usage of an electric motor is essential and crucial, because we are utilizing the advantages of the electric motor from the viewpoint of control. In this meaning, an FCV should not be called an FCHV but an FCEV.

## ACKNOWLEDGMENT

The author would like to state his great appreciation to many students in the Hori Laboratory and, in particular, to Dr. S. Sakai and colleagues for their hard work and kind help in performing various experiments with the March I and II, and also to T. Okano and K. Furukawa for their help in editing the manuscript.

## REFERENCES

- [1] J. Ackermann, "Yaw disturbance attenuation by robust decoupling of car steering," in *Proc. 13th IFAC World Congr.*, vol. 8b-01-1, 1996, pp. 1–6.
- [2] A. Daiss and U. Kiencke, "Estimation of tire slip during combined cornering and braking observer supported fuzzy estimation," in *Proc. 13th IFAC World Congress*, vol. 8b-02-2, 1996, pp. 41–46.
- [3] Y. Furukawa and M. Abe, "Direct yaw moment control with estimating side-slip angle by using on-board-tire-model," in *Proc. 4th Int. Symp. Advanced Vehicle Control (AVEC)*, Nagoya, Japan, 1998, pp. 431–436.
- [4] T. Furuya, Y. Toyoda, and Y. Hori, "Implementation of advanced adhesion control for electric vehicle," in *Proc. IEEE Workshop Advanced Motion Control (AMC)*, vol. 2, 1996, pp. 430–435.
- [5] F. Gustafsson, "Slip-based tire-road friction estimation," *Automatica*, vol. 33, no. 6, pp. 1087–1099, 1997.
- [6] Y. Hori, Y. Toyoda, and Y. Tsuruoka, "Traction control of electric vehicle based on the estimation of road surface condition, basic experimental results using the test ev "UOT March"," *IEEE Trans. Ind. Applicat.*, vol. 34, pp. 1131–1138, Sept. Oct. 1998.
- [7] N. Iwama *et al.*, "Active control of an automobile—Independent rear wheel torque control—," in *Trans. Soc. Instrum. Contr. Eng.*, vol. 28, 1992, pp. 844–853.
- [8] C. Liu and H. Peng, "Road friction coefficient estimation for vehicle path prediction," *Veh. Syst. Dyn. Suppl.*, vol. 25, pp. 413–425, 1996.
- [9] S. Motoyama *et al.*, "Effect of traction force distribution control on vehicle dynamics," in *Proc. Int. Symp. Advanced Vehicle Control (AVEC)*, 1992.
- [10] T. Okano, C. Tai, T. Inoue, T. Uchida, S. Sakai, and Y. Hori, "Vehicle stability improvement based on MFC independently installed on 4 wheels—Basic experiments using 'UOT Electric March II,'" in *Proc. PCC-Osaka, 2002*, CD-ROM.
- [11] L. R. Ray, "Nonlinear tire force estimation and road friction identification: Simulation and experiments," *Automatica*, vol. 33, no. 10, pp. 1819–1833, 1997.
- [12] H. Sado, S. Sakai, and Y. Hori, "Road condition estimation for traction control in electric vehicle," in *Proc. IEEE Int. Symp. Industrial Electronics*, Slovenia, 1999, pp. 973–978.
- [13] S. Sakai and Y. Hori, "Robustified model matching control for motion control of electric vehicle," in *Proc. IEEE Workshop Advanced Motion Control*, 1998, pp. 574–579.
- [14] S. Sakai, H. Sado, and Y. Hori, "Motion control in an electric vehicle with 4-independently driven in-wheel motors," *IEEE/ASME Trans. Mechatron.*, vol. 4, pp. 9–16, Mar. 1999.
- [15] —, "Novel skid avoidance method without vehicle chassis speed for electric vehicle," in *Proc. Int. Power Electronics Conf. (IPEC-2000)*, vol. 4, 2000, pp. 1979–1984.
- [16] —, "Novel wheel skid detection method for electric vehicles," in *Proc. 16th Electric Vehicle Symp. (EVS16)*, Beijing, China, 1999, p. 75.
- [17] Y. Shibahata *et al.*, "The improvement of vehicle maneuverability by direct yaw moment control," *Proc. 1st Int. Symp. Advanced Vehicle Control (AVEC)*, no. 923081, 1992.
- [18] S. Sakai and Y. Hori, "Advanced vehicle motion control of electric vehicle based on the fast motor torque response," in *Proc. 5th Int. Symp. Advanced Vehicle Control (AVEC)*, 2000, pp. 729–736.
- [19] S. Sakai, H. Sado, and Y. Hori, "Novel skid detection method without vehicle chassis speed for electric vehicle," in *JSAE Rev.*, vol. 21, 2000, pp. 503–510.
- [20] S. Sakai, T. Okano, C. Tai, T. Uchida, and Y. Hori, "4 wheel motored vehicle "The UOT March II"—Experimental EV for novel motion control studies—," in *Proc. First ISA/JEMIMA/SICE Joint Tech. Conf.*, 2001.
- [21] —, "Experimental studies on vehicle motion stabilization with 4 wheel motored EV," in *Proc. EVS-18*, 2001.
- [22] S. K. Sul and S. J. Lee, "An integral battery charger for four-wheel drive electric vehicle," *IEEE Trans. Ind. Applicat.*, vol. 31, Sept./Oct. 1995.
- [23] Y. Wang and M. Nagai, "Integrated control of four-wheel-steer and yaw moment to improve dynamic stability margin," in *Proc. 35th IEEE-CDC*, 1996, pp. 1783–1784.
- [24] S. Yamazaki, T. Fujikawa, and I. Yamaguchi, "A study on braking and driving properties of automotive tires," *Trans. Soc. Automotive Eng. Jpn.*, vol. 23, no. 2, pp. 97–102, 1992.
- [25] S. Yamazaki, T. Suzuki, and I. Yamaguchi, "An estimation method of hydroplaning phenomena of tire during traveling on wet road," in *Proc. JSAE Spring Conf.*, Yokohama, SE, Japan, 1999, pp. 5–8.



**Yoichi Hori** (S'81–M'83–SM'00) received the B.S., M.S., and Ph.D. degrees in electrical engineering from The University of Tokyo, Tokyo, Japan, in 1978, 1980, and 1983, respectively.

In 1983, he joined the Department of Electrical Engineering, The University of Tokyo, as a Research Associate. He later became an Assistant Professor, an Associate Professor, and, in 2000, a Professor. In 2002, he moved to the Institute of Industrial Science at The University of Tokyo, as a Professor in the Information and System Division, Electrical Control System Engineering. During 1991–1992, he was a Visiting Researcher at the University of California, Berkeley. His research fields are control theory and its industrial applications to motion control, mechatronics, robotics, electric vehicles, etc.

Prof. Hori has been the Treasurer of the IEEE Japan Council and Tokyo Section since 2001. He is currently the Vice President of the Industry Applications Society of the Institute of Electrical Engineers of Japan (IEEJ). He was the winner of the 1992 ROBOMECH Award of the Robotics and Mechatronics Society of the Japan Society of Mechanical Engineers (JSME), the 1993 Third Prize in the IEEE-IECON'93 Best Paper Competition, the Best Transactions Paper Award from the IEEE TRANSACTIONS ON INDUSTRIAL ELECTRONICS in 1993, the 2000 Best Transactions Paper Award from the IEEJ. He was one of nine finalists for the Poster Paper Prize at the 1996 IFAC World Congress, and a finalist in the Best Vision Paper Competition at the 2001 IEEE-ICRA. He also received a Technical Committee Prize Award from the Industrial Drives Committee of the IEEE Industry Applications Society in 2001. He is a Member of the IEEJ, Society of Instrument and Control Engineers, Robotics Society of Japan, JSME, and Society of Automotive Engineers of Japan.

# Direct Yaw-Moment Control of an In-Wheel-Motored Electric Vehicle Based on Body Slip Angle Fuzzy Observer

Cong Geng, Lotfi Mostefai, Mouloud Denai, and Yoichi Hori, *Fellow, IEEE*

**Abstract**—A stabilizing observer-based control algorithm for an in-wheel-motored vehicle is proposed, which generates direct yaw moment to compensate for the state deviations. The control scheme is based on a fuzzy rule-based body slip angle ( $\beta$ ) observer. In the design strategy of the fuzzy observer, the vehicle dynamics is represented by Takagi–Sugeno-like fuzzy models. Initially, local equivalent vehicle models are built using the linear approximations of vehicle dynamics for low and high lateral acceleration operating regimes, respectively. The optimal  $\beta$  observer is then designed for each local model using Kalman filter theory. Finally, local observers are combined to form the overall control system by using fuzzy rules. These fuzzy rules represent the qualitative relationships among the variables associated with the nonlinear and uncertain nature of vehicle dynamics, such as tire force saturation and the influence of road adherence. An adaptation mechanism for the fuzzy membership functions has been incorporated to improve the accuracy and performance of the system. The effectiveness of this design approach has been demonstrated in simulations and in a real-time experimental setting.

**Index Terms**—Fuzzy observer, local modeling, state feedback, vehicle lateral dynamics.

## I. INTRODUCTION

**T**HIS PAPER focuses on the design of control strategies to enhance the performance and safety of electric vehicles (EVs) in critical driving situations. It has been commonly recognized that EVs are inherently more suitable to realize active safety stability control over conventional internal combustion engine vehicles. In EVs, the motor torque can be measured and controlled accurately, and in-wheel motors can be installed in each EV's rear and front tires. Based on these structural merits, vehicle motion can be stabilized by additional yaw moment generated as a result of the difference in tire driving or braking forces between the right and left sides of the

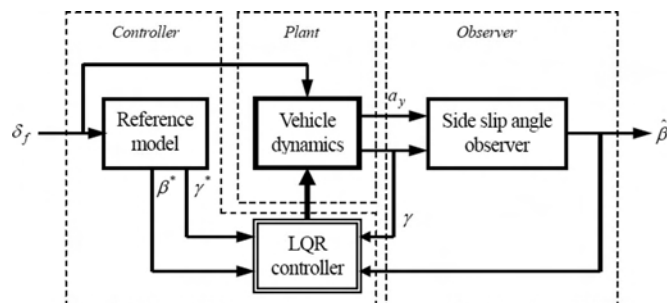


Fig. 1. Vehicle lateral stability control structure.

vehicle, which is the so-called “Direct Yaw-moment Control” (DYC) [1]–[5].

Fig. 1 shows the main concept of the chassis control system utilizing DYC based on the model matching control method and optimal control method [3], [4], [6].

This system is aimed to maintain the driver's handling ability at the physical limit of adhesion between the tires and the road by making the vehicle easily controllable even well below that limit. The dynamics of the 2-DOF vehicle model can describe the driver's familiar characteristics under normal driving conditions. The body slip angle ( $\beta$ ) and yaw rate ( $\gamma$ ) calculated from the model are taken as the desired behavior of the vehicle. By applying the model matching control, the yaw-moment optimal decision can be derived from the deviations of the state feedback compensator of  $\beta$  and  $\gamma$  from their desired values. Since sensors for the direct measurement of  $\beta$  are very expensive, the construction of an observer for its estimation is desirable.

Generally, such state feedback control method is based on the state equations derived from the vehicle dynamics. However, the implementation of these techniques is still difficult since the vehicle dynamics is highly nonlinear, particularly for  $\beta$ . Previous authors' approaches regarding  $\beta$  estimation issue used model-based observers with either linear or nonlinear equivalent vehicle dynamic models [6]–[10]. With regard to linear observer design, the linear 2-DOF vehicle model with fixed parameters is adopted. However, this approach cannot always achieve accurate results in different running situations. In the design of nonlinear observers, tire characteristics are described by nonlinear functions and with more parameters, which can produce relatively more accurate results in different running situations compared with linear observers. However, nonlinear observers have the disadvantages of not having a

Manuscript received June 15, 2008; revised January 6, 2009. First published February 6, 2009; current version published April 29, 2009.

C. Geng is with the University of Tokyo, Tokyo 113-8656, Japan (e-mail: geng@horilab.iis.u-tokyo.ac.jp).

L. Mostefai is with the University Moulay Tahar in Saida, Saida 20000, Algeria.

M. Denai is with Mohamed Boudiaf University of Science and Technology of Oran, Oran 31000, Algeria, and also with the Department of Automatic Control and Systems Engineering, The University of Sheffield, Sheffield, S1 3JD, U.K.

Y. Hori is with the Department of Informatics and Electronics, Institute of Industrial Science, University of Tokyo, Tokyo 153-8505, Japan.

Color versions of one or more of the figures in this paper are available online at <http://ieeexplore.ieee.org>.

Digital Object Identifier 10.1109/TIE.2009.2013737



strong theoretical maturity and still face difficulties regarding their real-time implementation.

The main nonlinearity of vehicle dynamics comes from the tire force saturation imposed by the limits of tire adherence, which makes  $\beta$  response change considerably if the vehicle is cornering much more than usual. In other words, the model structure or parameters should vary according to the different operating regimes for a more practical controller design. In addition, the nonlinear nature of vehicle dynamics is further complicated by the influence of the characteristics of whole chassis elements (tires, suspensions, and steering system). It is hard to determine the physical model parameters theoretically. Therefore, an effective modeling methodology is the key for the system design.

To deal with the difficulties associated with nonlinearity modeling, as well as to make use of the linear observer advantages such as simplicity in the design and implementation, the nonlinear vehicle dynamics is represented by Takagi–Sugeno (T–S) fuzzy models [11], [12]. The local approximation of the nonlinear vehicle model and a dynamical interpolation method are introduced in this paper to construct a fuzzy-model-based control system for  $\beta$  estimation and control. Optimal  $\beta$  observer is designed for each local model using Kalman filter theory. The proposed system is a combination of local linear observers and controllers with varying switching partition.

The first step in the design is concerned with the derivation of the system state equations from the vehicle dynamics and local approximation of nonlinear tire model. These modeling techniques are considered appropriate for online control system design (linear 2-DOF vehicle model as in [13]). In the next step, a fuzzy-based modeling approach is used to get a hybridlike vehicle model, which is calculated as a weighted sum of the outputs of two local linear models. For practical applications, parameter identification is conducted experimentally. An adaptation mechanism of the fuzzy membership functions has been included to make the model fit different running conditions and road friction changes. The membership functions of the weighting factors are chosen to be dependent on lateral acceleration and road friction coefficient. The two local observers are based on local linear tire models, which inherently leads to a relatively simple design, and have been combined into a single overall observer by means of fuzzy rules. Furthermore, the nonlinear global system results show high  $\beta$  estimation capabilities and good adaptation to changing road friction. A series of simulations are performed to evaluate the effectiveness of the proposed  $\beta$  observer when incorporated into a DYC-based control scheme.

## II. VEHICLE DYNAMICS AND FUZZY MODELING

### A. Local Approximation and Linearization of Vehicle Dynamics

The system is based on an in-wheel-motored EV dynamic model (Fig. 2). The main difference with common vehicle dynamics is that the direct yaw moment is an additional input variable, which is caused by individual motor torque between each wheel.

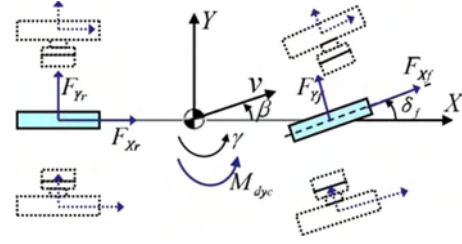


Fig. 2. Two-DOF vehicle model.

The vehicle dynamics is approximately described by the following 2-DOF vehicle model equations:

$$\begin{cases} ma_y = F_{xf} \sin \delta_f + F_{yf} \cos \delta_f + F_{yr} \\ I_z \dot{\gamma} = l_f F_{xf} \sin \delta_f + l_f F_{yf} \cos \delta_f - l_r F_{yr} + N \end{cases} \quad (1)$$

where  $a_y$  denotes the vehicle lateral acceleration,  $\gamma$  is the yaw rate,  $\delta_f$  is the steering angle of the front wheel,  $N$  is the direct yaw moment,  $m$  represents the mass of the vehicle,  $I_z$  is the yaw inertia moment,  $l_f$  denotes the distance between the center of the mass and the front axle,  $l_r$  is the distance between the center of mass and the rear axle,  $F_{xf}$  is the longitudinal force of the front tires, and  $F_{yf}$  and  $F_{yr}$  are the lateral forces of the front and rear tires, respectively.

Let the body slip angle  $\beta$  and yaw rate  $\gamma$  represent the system state variables. By defining the kinematics relationship as  $a_y = v(\dot{\beta} + \gamma)$  and assuming that  $\delta_f$  is relatively small for high speeds, the vehicle's state equations are obtained as follows:

$$\begin{cases} \dot{\beta} = \frac{1}{mv} (F_{yf} + F_{yr}) - \dot{\gamma} \\ \dot{\gamma} = \frac{1}{I_z} (l_f F_{yf} - l_r F_{yr} + N). \end{cases} \quad (2)$$

The model of (2) is nonlinear due to the tire lateral force dynamics. By using local operating regime approximations, the model can be simplified into an equivalent linear 2-DOF model by adopting the equivalent tire cornering stiffness  $C$ , which is defined by

$$C = \frac{F_y}{\alpha} \quad (3)$$

where  $F_y$  is the tire lateral force, and  $\alpha$  is the tire slip angle at its operating point.

By adopting the value of  $C$  given by (3), the nonlinear vehicle dynamic state equation (2) can be transformed into the following equivalent linear state equation at the local operating point:

$$\dot{x} = Ax + Bu \quad (4)$$

in which

$$\mathbf{A} = \begin{bmatrix} a_{11} & a_{12} \\ a_{21} & a_{22} \end{bmatrix} = \begin{bmatrix} \frac{-(2C_f + 2C_r)}{mV} & \frac{-2l_f C_f + 2l_r C_r}{mV^2} - 1 \\ \frac{-2l_f C_f + 2l_r C_r}{I_z} & \frac{-2l_f^2 C_f - 2l_r^2 C_r}{I_z V} \end{bmatrix}$$

$$\mathbf{B} = \begin{bmatrix} b_{11} & b_{12} \\ b_{21} & b_{22} \end{bmatrix} = \begin{bmatrix} \frac{2C_f}{mV} & 0 \\ \frac{2l_f C_f}{I_z} & \frac{1}{I_z} \end{bmatrix}$$

$$\mathbf{x} = \begin{bmatrix} \beta \\ \gamma \end{bmatrix} \quad \mathbf{u} = \begin{bmatrix} \delta_f \\ N \end{bmatrix}$$

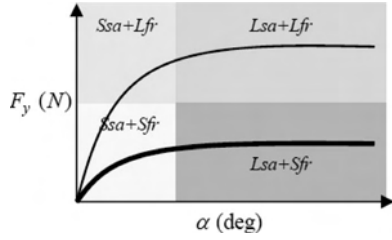


Fig. 3. Tire lateral force characteristics partitioned roughly into four different local dynamics ( $Lsa$  is the large tire slip angle,  $Ssa$  is the small tire slip angle,  $Lfr$  is the large friction, and  $Sfr$  is the small friction).

where  $C_f$  and  $C_r$  are the cornering stiffness values of the front and rear tires, respectively, and  $V$  is the longitudinal velocity.

Since the main nonlinearity in the model comes from the tires, the cornering stiffness of the tires will play an important role in the formulation of the model used in the estimator. According to Fig. 3, these coefficients are large when the tire slip angle assumes small values, which are equivalent to the low lateral acceleration regimes. On the other hand, the stiffness coefficients become small when the tire slip angle increases, which means that the vehicle is running at high lateral accelerations. Hence, to describe the vehicle dynamics by an equivalent linear 2-DOF model, local models with different  $C$  values should be considered, for both low and high lateral accelerations.

### B. Model Parameter Identification

For the local dynamic models, the equivalent tire cornering stiffness values  $C_f$  and  $C_r$  are difficult to determine theoretically because they are influenced by the suspension dynamics, tire characteristics, and steering system. In this paper, an identification method of tire cornering stiffness based on experimental tests performed on the EV is proposed.

According to (2), the steady state cornering relationship with steering angle input can be expressed as follows:

$$\begin{cases} ma_y = F_{yf} + F_{yr} \\ 0 = l_f F_{yf} - l_r F_{yr}. \end{cases} \quad (5)$$

From (5), the expression of the side force applied to the front and rear tires can be deduced as

$$\begin{cases} \hat{F}_{yf} = \frac{l_r}{l} ma_y \\ \hat{F}_{yr} = \frac{l_f}{l} ma_y. \end{cases} \quad (6)$$

Moreover, the body slip angle of front and rear tires can be obtained as

$$\begin{cases} \hat{\alpha}_f = \beta + \frac{\gamma l_f}{V} - \delta_f \\ \hat{\alpha}_r = \beta - \frac{\gamma l_r}{V}. \end{cases} \quad (7)$$

If  $a_y$ ,  $\beta$ , and  $\gamma$  are measured from steady state cornering experiments, it follows from the aforementioned equations that the tire cornering stiffness can be obtained as

$$\begin{cases} \hat{C}_f = \frac{F_{yf}}{-2\alpha_f} \\ \hat{C}_r = \frac{F_{yr}}{-2\alpha_r}. \end{cases} \quad (8)$$

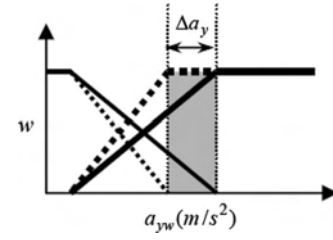


Fig. 4. Membership function adaptation to the lateral acceleration.

For the nonlinearity of vehicle dynamics, cornering experiments with low and high  $a_y$ 's should be conducted, respectively, to identify the different cornering stiffness values in different operating regimes.

### C. Fuzzy Modeling and Local Dynamics

To simplify the fuzzy modeling procedure, the lateral acceleration  $a_y$  will be assigned two fuzzy sets (large and small), as shown in Fig. 4.

Then, using these fuzzy sets, the fuzzy IF-THEN rules for the vehicle dynamic model can be defined as follows.

Rule  $i$ : (local model  $i$ ) IF  $|a_y|$  is  $F_i$ , THEN  $\dot{x} = A_i x + B_i u$ .

The overall vehicle dynamics is described by two models that take the form of (4). The model parameters, namely, the equivalent tire cornering stiffness, are identified according to the steady state regime given by (8).

For the local model 1, the tire works at its small slip region, and  $A_1$  and  $B_1$  are calculated based on the largest value of the cornering stiffness  $C$ . For the local model 2, the tire works at its large slip region, and  $A_2$  and  $B_2$  are calculated for a relatively small value of the cornering stiffness  $C$ .

Finally, the whole nonlinear dynamics of the vehicle are described with the proposed dynamic switching partition by interpolating the two models with fuzzy logic. By a proper choice of the membership function, the vehicle dynamics can be calculated for different operating regimes (from low to high  $a_y$  value).

Therefore, the following is used to represent the fuzzy models covering the vehicle dynamics:

$$\dot{x} = \sum_{i=1}^2 w_i (A_i x + B_i u) \quad (9)$$

where  $w_1$  and  $w_2$  are the membership functions for local models 1 and 2. For design simplicity, trapezoidal membership functions have been used. The formulations of  $w_1(a_y)$  and  $w_2(a_y)$  are as follows:

$$w_1(a_y) = \begin{cases} 1 - \frac{1}{a_{yw}} a_y, & |a_y| \leq a_{yw} \\ 0, & |a_y| > a_{yw} \end{cases} \quad (10)$$

$$w_2(a_y) = \begin{cases} \frac{1}{a_{yw}} a_y, & |a_y| \leq a_{yw} \\ 1, & |a_y| > a_{yw} \end{cases} \quad (11)$$

where the coefficient  $a_{yw}$  describes the value of  $a_y$  at the tire/road adherence limit (road friction coefficient  $\mu$ ) when the tire force is saturated, which is equivalent to severe steering dynamics.

Road condition is one of the most important factors that must be considered in vehicle dynamic stability control, since the road friction coefficient  $\mu$  is uncertain and may change according to the road condition; the fuzzy partition describing the vehicle model must be adaptive to such variations (Fig. 4).

The value of  $\mu$  can be identified with different methods. In EV stability control, one method that the authors adopted previously is to identify the  $\mu$  value by analyzing wheel rotation dynamics, which takes advantage of the accurate knowledge of the EV motor torque values [14], [15]. With the identified  $\mu$  value,  $a_{yw}$  is used as a tuning parameter of the weighting function partition to form an adaptation mechanism to cope with the variation of tire/road adherence conditions. In this paper,  $a_{yw}$  is set to be a linear function of  $\mu$  with the following low-pass filter to remove the noise:

$$a_{yw} = k_{\mu} \frac{1}{1 + T_f s} \mu \quad (12)$$

where  $k_{\mu}$  is the adaptation gain, and  $T_f$  is the constant of first order low-pass filter.

### III. $\beta$ OBSERVER DESIGN BASED ON FUZZY MODELS

#### A. Kalman Filter for Local $\beta$ Observer Design

Based on the local linear models, the  $\beta$  observer is designed with Kalman filter theory [16]–[18]. For the real-time implementation of the design strategy, the continuous-time model of (4) is converted into discrete time model by taking into account process and measurement noises as follows:

$$\begin{aligned} x[n+1] &= G_i x[n] + H_i u[n] + \omega[n] \\ y[n] &= C_i x[n] + D_i u[n] + v[n] \end{aligned} \quad (13)$$

where the covariance vectors of process and measurement noises are assumed to be the same for all dynamics

$$E(\omega[n]\omega[n]^T) = Q \quad E(v[n]v[n]^T) = R. \quad (14)$$

The sampled equations with a zeroth-order hold are obtained as

$$\begin{aligned} G_i &= \begin{bmatrix} 1 + T_s a_{11} & T_s a_{12} \\ T_s a_{21} & 1 + T_s a_{21} \end{bmatrix} \\ H_i &= \begin{bmatrix} T_s b_{11} & T_s b_{12} \\ T_s b_{21} & T_s b_{21} \end{bmatrix} \end{aligned} \quad (15)$$

where  $T_s$  is the sampling time.

Using the discrete state space equation (13), a discrete form of Kalman estimator can be applied for each linear observer. The vehicle lateral acceleration  $a_y$  and yaw rate  $\gamma$  are two measurable variables and are chosen as output variables of the observer

$$\begin{aligned} y &= \begin{bmatrix} \gamma \\ a_y \end{bmatrix} \\ C &= \begin{bmatrix} 0 & 1 \\ \nu a_{11} & \nu(a_{12} + 1) \end{bmatrix} \\ D &= \begin{bmatrix} 0 & 0 \\ \nu b_{11} & 0 \end{bmatrix}. \end{aligned} \quad (16)$$

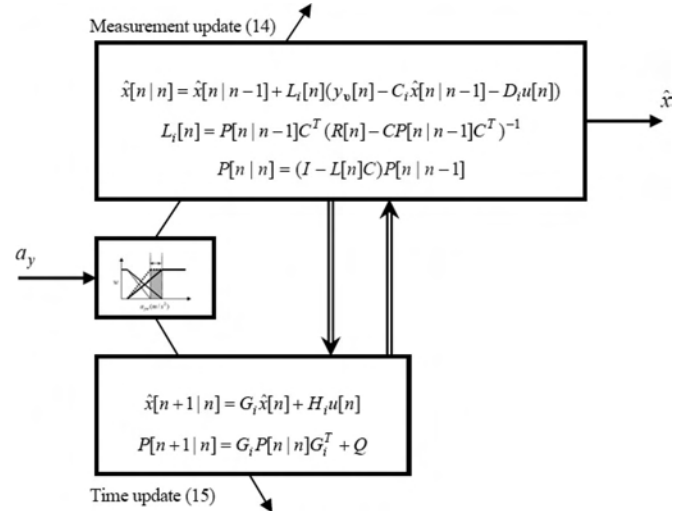


Fig. 5. Implementation of the estimation algorithm based on Kalman filter theory.

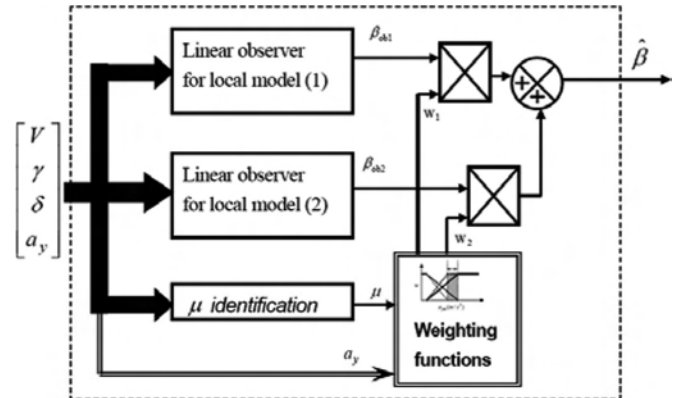


Fig. 6. Structure of hybrid adaptive observer.

The recursive discrete Kalman filter algorithm is then applied separately to estimate local dynamics, as shown in Fig. 5. Where  $\hat{x}$  and  $\hat{y}$  are the estimates of  $x$  and  $y$ , respectively,  $L_i$  is the feedback gain of local observer, which is derived using the Kalman filter theory.

#### B. Hybridlike Observer Design Based on Fuzzy Models

A hybridlike observer is designed based on the fuzzy discrete time vehicle models by applying the Kalman filter theory [9]. The proposed observer structure is as shown in Fig. 6.

The observer consists of two Kalman-filter-based local observers related to the aforementioned local models 1 and 2, respectively. The observer outputs are the estimates of  $\beta_{ob1}$  and  $\beta_{ob2}$ , respectively.

The fuzzy rules for  $\beta$  observer are defined by the following IF–THEN rule structure.

Rule  $i$ : (local observer  $i$ ) IF  $|a_y|$  is  $F_i$ , THEN  $\hat{\beta}_{ob} = \hat{\beta}_{obi}$ .

By introducing this fuzzy logic concept, two local linear models were sufficient to cover the main nonlinear features of the dynamics and give the proposed observer the ability to overcome the limitations associated with the linear observer

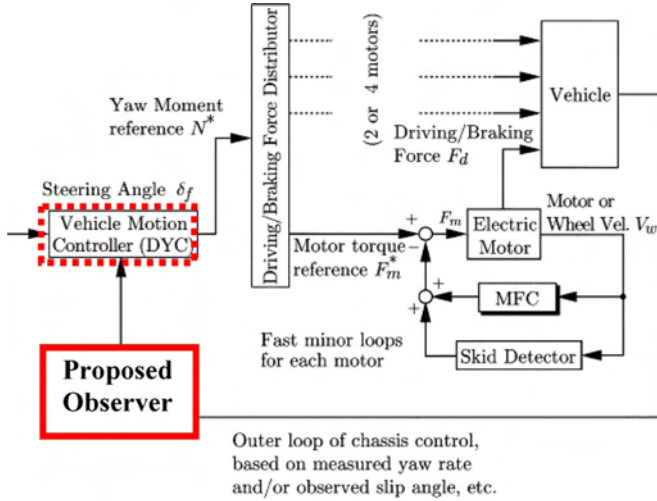


Fig. 7. Vehicle stability control applied to UOT MARCH II.

in terms of performances. The overall fuzzy observer is given by

$$\hat{\beta}_{ob} = \sum_{i=1}^2 w_i \hat{\beta}_{obi}. \quad (17)$$

The advantages of a linear observer such as simple design and noncomputationally intensive are conserved while addressing the nonlinear problem at the same time.

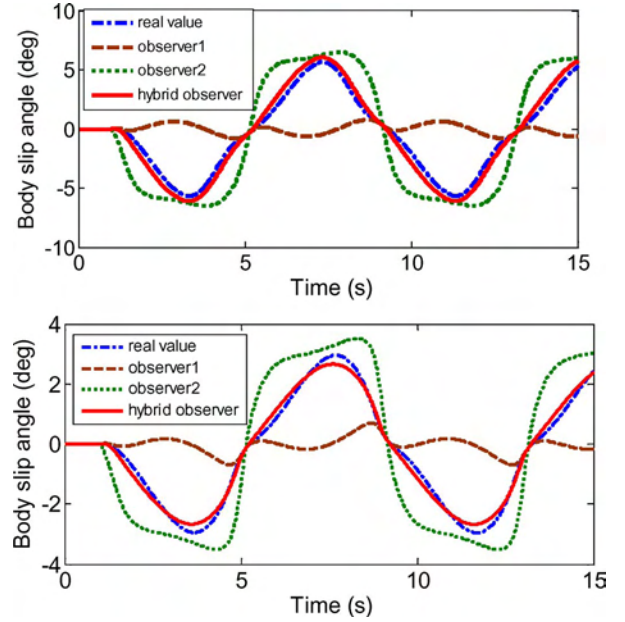
#### IV. SIMULATION AND EXPERIMENTAL RESULT ANALYSIS

##### A. Description of the Experimental Vehicle and Control Architecture

A full description of the EV University of Tokyo (UOT) MARCH II is presented in the Appendix. The parameters used in the following simulations and observer/controller design have been obtained in a previous study [19]. Fig. 7 shows the overall dynamical control scheme applied to UOT MARCH II. With reference to Fig. 1, we can clearly distinguish the parts which we have developed in this paper, namely, 1) the (red thick line)  $\beta$  observer already implemented and tested and 2) the (red dotted line) control to be tested in the near future for safety reasons. According to the configuration of the vehicle using four in-wheel motors, an optimal driving/braking force distribution system has been developed in former research to be applied with the DYC control unit [20].

##### B. Simulation and Experimental Studies of the Observer

The effectiveness of the proposed observer structure is tested via simulations. A sinusoidal steering angle input is chosen to simulate consecutive lane change maneuvers of the vehicle body. The amplitude of input steering angle is large enough to make the tire span both the linear and nonlinear working regions. Simulation results related to different road friction conditions are shown in Fig. 8. It is clear that both of the subobservers used to generate the proposed structure cannot fit well the real value for the whole operating conditions. This can


 Fig. 8. Simulation results of the hybrid observer under (top panel) large road friction situation ( $\mu = 0.85$ ) and (bottom panel) small road friction situation ( $\mu = 0.4$ ).

be explained by the fact that they are based on a local model with fixed parameters describing a limited segment of vehicle operating regime. Comparatively, the hybrid observer gives a better estimation, follows closely the real values, and has even the ability to adapt to different road friction conditions.

To evaluate the proposed control scheme under more realistic conditions, field tests are conducted on our experimental EV ‘‘UOT March II.’’ UOT March II is equipped with an acceleration sensor, a gyro sensor, and a noncontact speed meter, which provide measurements of the vehicle state variables.

Figs. 9 and 10 show the results of field tests of the observer in moderate and severe cornering situations. The experiments demonstrate that the observer is very effective and suitable for real-time applications due to its high onboard computational speed.

#### V. SIMULATION OF OPTIMAL YAW-MOMENT CONTROL BASED ON THE PROPOSED $\beta$ OBSERVER

##### A. Desired Model and State Deviation Equation

As shown in Fig. 1, the control scheme is applied for DYC system design by using the model matching control method.

The desired state variables of  $\beta$  and  $\gamma$  are determined by a 2-DOF linear model with front wheel steering angle as input according to (4) and are expressed as follows:

$$\begin{bmatrix} \dot{\beta}_d \\ \dot{\gamma}_d \end{bmatrix} = A \begin{bmatrix} \beta_d \\ \gamma_d \end{bmatrix} + \begin{bmatrix} b_{11} \\ b_{21} \end{bmatrix} \delta_f. \quad (18)$$

In addition,  $\gamma$  should be constrained by its adhesion saturation value as follows:

$$\gamma_d \leq \frac{\mu g}{V}. \quad (19)$$

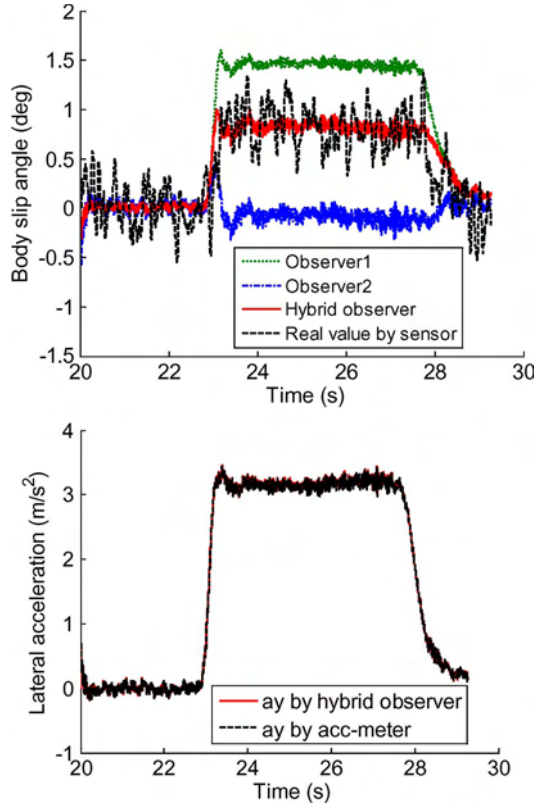


Fig. 9. Experimental field test results of  $\beta$  observer (steering angle =  $90^\circ$ ;  $v = 40$  km/h).

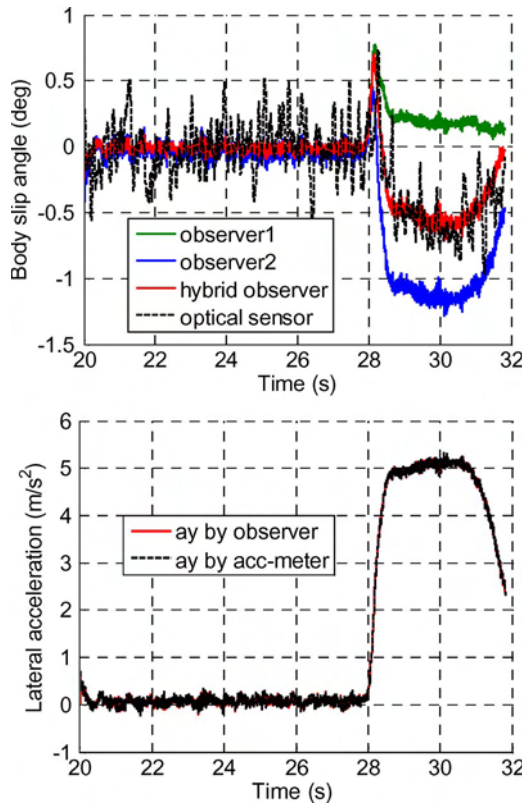


Fig. 10. Experimental field test results of  $\beta$  observer (steering angle =  $90^\circ$ ;  $v = 60$  km/h).

The state deviation variable between the desired value  $X_d$  and actual value  $X$  is assumed to be as follows:

$$E = X - X_d = \begin{bmatrix} \Delta\beta \\ \Delta\gamma \end{bmatrix} = \begin{bmatrix} \beta - \beta_d \\ \gamma - \gamma_d \end{bmatrix}. \quad (20)$$

According to (4) and (18), the differentiation of (20) leads to the error dynamics

$$\dot{E} = \dot{X} - \dot{X}_d = A.E + \begin{bmatrix} b_{12} \\ b_{22} \end{bmatrix} N. \quad (21)$$

Equation (21) describes the dynamic relationship between the direct yaw moment and vehicle motion state deviations. It shows that, when a vehicle motion deviation appears, exerting a direct yaw moment can reduce them to make the vehicle regain stability.

### B. Optimal Yaw-Moment Decision Algorithm

Based on the linear quadratic regulator method, the optimal control input can be calculated by state feedback deviations as follows:

$$N^* = -k_1(\beta - \beta_d) - k_2(\gamma - \gamma_d) \quad (22)$$

where the feedback gains  $k_1$  and  $k_2$  related to the local model are determined so that the following performance index is minimized:

$$J = \frac{1}{2} \int_0^\infty [q_1 \Delta\beta^2(t) + q_2 \Delta\gamma^2(t) + N^2(t)] dt \quad (23)$$

where  $q_1$  and  $q_2$  are the weighting coefficients of the state deviations, which can be chosen to modulate the controller sensitivity with respect to  $\beta$  and  $\gamma$  deviations. For this purpose, the coefficient  $\omega_\beta$  ( $0 \leq \omega_\beta \leq 1$ ) is introduced in the performance index as a weighting factor on  $\beta$  deviation. We define  $q_1 = q^2 \omega_\beta$  and  $q_2 = q^2 (1 - \omega_\beta)$ , and (23) can be rewritten as

$$J = \frac{q}{2} \int_0^\infty [\omega_\beta \Delta\beta^2(t) + (1 - \omega_\beta) \Delta\gamma^2(t) + N^2(t)] dt. \quad (24)$$

Small values of  $\beta$  produce a more important  $\gamma$  matching control, whereas larger values lead to a more important  $\beta$  control. In addition, the vehicle stability is more sensitive to  $\beta$  deviation under low adhesion road conditions than it is under high adhesion road conditions. Therefore,  $\omega_\beta$  is dependent on  $\beta$  and the road friction coefficient  $\mu$  and is chosen as follows:

$$\omega_\beta = \begin{cases} \frac{|\beta|}{\mu \cdot \beta_0}, & \text{if } |\beta| < \mu \cdot \beta_0 \\ 1, & \text{else} \end{cases} \quad (25)$$

where  $\beta_0$  is a threshold value which has been set to  $10^\circ$  based on the authors' experience.

The graph of  $\omega_\beta$  as a function of  $\beta$  is shown in Fig. 11.

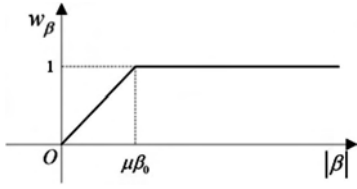


Fig. 11. Weight of body slip angle deviation for optimal yaw-moment decision.

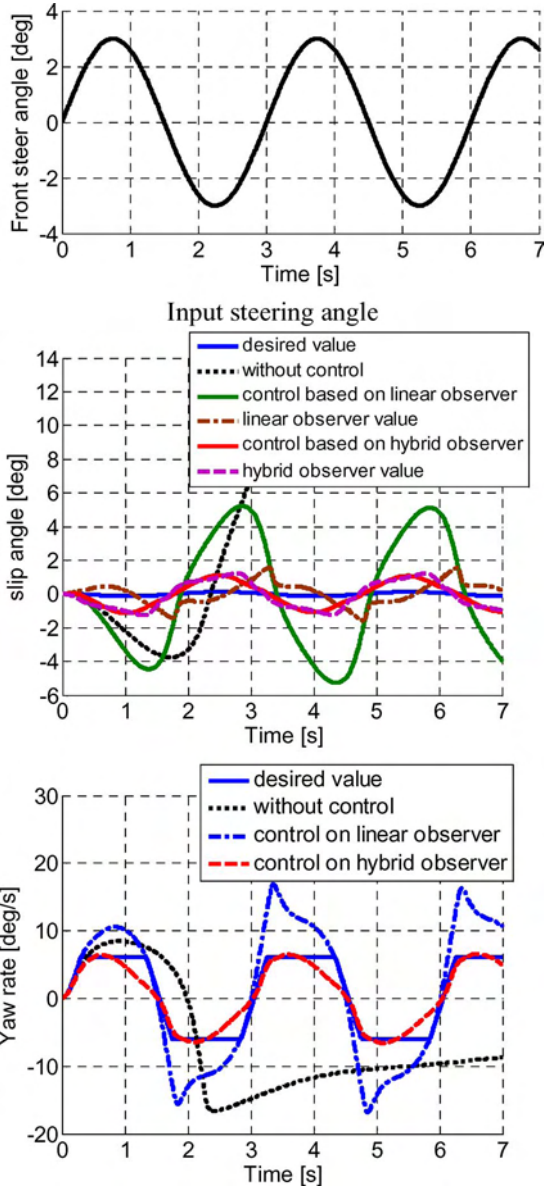


Fig. 12. (Top panel) Slip angle and (bottom panel) yaw rate under  $\beta$  control.

C. Simulation Results of Body Slip Angle Control

In the following simulations, full four-wheel vehicle dynamics with nonlinear tire model is used as a mathematical model.

In the simulation study and experimental validation, the actuation dynamics will not be considered. They rely essentially on the current control of electric motors. So far, it is well known that the use of electric motors as actuators is one of the advantages of EVs and, at the same time, presents a negligible

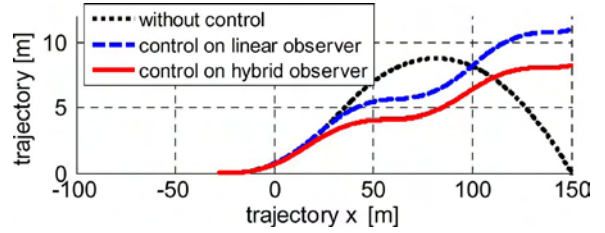


Fig. 13. Vehicle trajectory with and without  $\beta$  control.

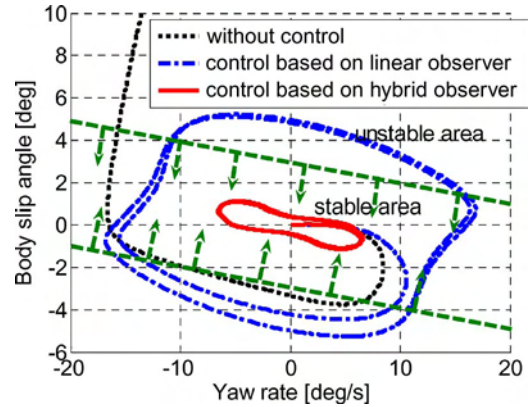


Fig. 14. Control trajectories in  $\beta$ - $\gamma$  phase plane.

short delay (i.e., a few milliseconds) in the overall controlled system compared to the vehicle dynamics.

Fig. 12 shows the simulation results with sinusoidal front steering angle input when the road friction coefficient is 0.3 and the vehicle is running at a speed of 100 km/h. This can represent a critical driving situation of continuous lane change maneuver on slippery road. If the control is set off,  $\beta$  can assume larger values, causing the vehicle to lose its stability and unable to accomplish the lane change as in normal situations (Fig. 13). With the proposed hybrid observer, an accurate estimation of body slip angle is obtained. By applying DYC based on the hybrid observer, the yaw rate  $\gamma$  is successfully controlled to the desired value, and the body slip angle  $\beta$  is guaranteed to be limited. However, if DYC was based on the linear observer, the incorrect estimation of body slip angle will lead to control deterioration.

Fig. 14 shows the  $\beta$ - $\gamma$  phase plane trajectory related to the simulation results. Under DYC control, a limited trajectory loop is drawn by the vehicle within the stable area defined for our vehicle. Without  $\beta$  control, this trajectory of  $\beta$ - $\gamma$  phase plane cannot be satisfied and becomes much larger until the vehicle leaves the stable area, putting the passengers in danger.

VI. CONCLUSION

This paper has presented an algorithmic solution of the nonlinear vehicle dynamic control problem, which has been validated both in a simulation environment and in real time. A state observer has been designed for an in-wheel-motored EV with DYC using fuzzy modeling techniques. T-S fuzzy models were employed for approximating the nonlinear vehicle dynamics with linear local models. An adaptation mechanism was introduced to adjust the fuzzy membership functions in

TABLE I  
SPECIFICATIONS OF UOT ELECTRIC MARCH II

<b>Drivetrain</b>	<b>4 PM Motors / Meidensya Co.</b>
Max. Power (20 sec.)	36 [kW] (48.3 [HP])*
Max. Torque	77* [Nm]
Gear Ratio	5.0
<b>Battery</b>	<b>Lead Acid</b>
Weight	14.0 [kg](for 1 unit)
Total Voltage	228 [V] (with 19 units)
<b>Base Chassis</b>	<b>Nissan March K11</b>
Wheel Base	2360 [m]
Wheel Tread F/R	1365/1325 [m]
Total Weight	1400 [kg]
Wheel Inertia**	8.2 [kg]***
Wheel Radius	0.28 [m]
<b>Controller</b>	
CPU	MMX Pentium 233 [MHz]
Rotary Encoder	3600 [ppr]***
Gyro Sensor	Fiber Optical Type

\* ... for only one motor. \*\* ... mass equivalent.  
\*\*\* ... affected by gear ratio.

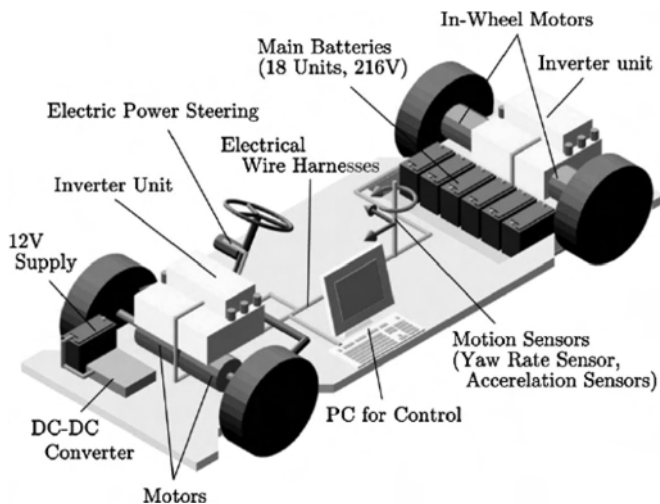


Fig. 15. Sketch of the "UOT MARCH II."

response to changes in road friction conditions. The local observer design was based on the Kalman filter theory and was combined with an interpolating mechanism which provided the link between the underlying local dynamics. The quantitative accuracy and the adaptation performance of the proposed observer have been verified in simulations and experimentally. We have shown that the designed controller relies critically on the estimated value of  $\beta$ , and further research and effort will be devoted into the implementation of a full dynamic stability control of the UOT MARCH II.

#### APPENDIX DESCRIPTION OF "UOT MARCH II"

The EV named "UOT Electric March II" was constructed in 2001 (Table I). The most special feature of this EV is the in-wheel motor mounted in each wheel. We can control each wheel torque completely and independently. Regenerative braking is also available. Former researchers from Hori Laboratory at the UOT contributed to build this EV by remodeling a Nissan March. Fig. 15 shows a sketch of the "UOT MARCH II."

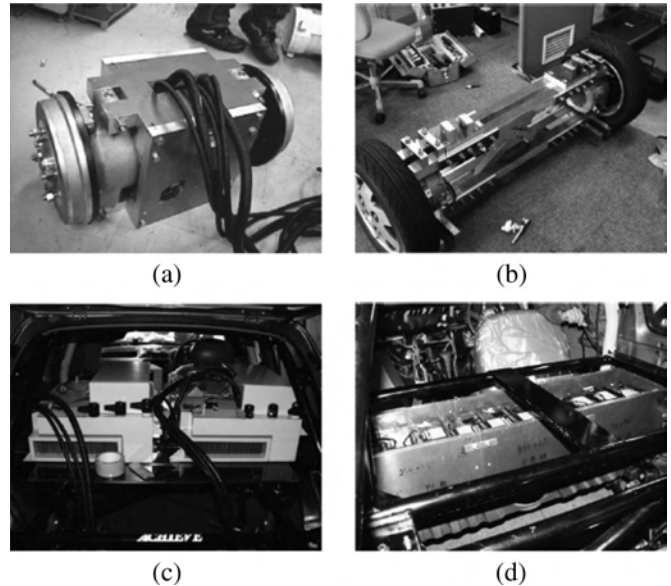


Fig. 16. Photographs of the vehicle. (a) Front motors. (b) Rear motors. (c) Inverters. (d) Batteries.

Fig. 16 shows the photographs of the main parts of the vehicle developed in our laboratory.

#### REFERENCES

- [1] Y. Hori, "Future vehicle driven by electricity and control research on 4 wheel motored 'UOT March II,'" in *Proc. 7th AMC*, 2002, pp. 1–14.
- [2] D. Kim, S. Hwang, and H. Kim, "Vehicle stability enhancement of four-wheel-drive hybrid electric vehicle using rear motor control," *IEEE Trans. Veh. Technol.*, vol. 57, no. 2, pp. 727–735, Mar. 2008.
- [3] K. Kin, O. Yano, and H. Urabe, "Enhancements in vehicle stability and steerability with slip control," *JSAE Rev.*, vol. 24, no. 1, pp. 71–79, Jan. 2003.
- [4] M. Canale, L. Fagiano, A. Ferrara, and C. Vecchio, "Vehicle yaw control via second-order sliding-mode technique," *IEEE Trans. Ind. Electron.*, vol. 55, no. 11, pp. 3908–3916, Nov. 2008.
- [5] N. Mutoh, Y. Hayano, H. Yahagi, and K. Takita, "Electric braking control methods for electric vehicles with independently driven front and rear wheels," *IEEE Trans. Ind. Electron.*, vol. 54, no. 2, pp. 1168–1176, Apr. 2007.
- [6] C. Arndt, J. Karidas, and R. Busch, "Design and validation of a vehicle state estimator," in *Proc. 7th AVEC*, 2004, pp. 41–45.
- [7] L. Imsland, T. A. Johansen, T. I. Fossen, H. F. Grip, J. C. Kalkkuhl, and A. Suissa, "Vehicle velocity estimation using nonlinear observers," *Automatica*, vol. 42, no. 12, pp. 2091–2103, Dec. 2006.
- [8] F. Cheli, E. Sabbion, M. Pesce, and S. Melzi, "A methodology for vehicle sideslip angle identification: Comparison with experimental data," *Vehicle Syst. Dyn.*, vol. 45, no. 6, pp. 549–563, Jun. 2007.
- [9] T. A. Wenzel, K. J. Burnham, M. Blundell, and R. Williams, "Motion dual extended Kalman filter for vehicle state and parameter estimation," *Vehicle Syst. Dyn.*, vol. 44, no. 2, pp. 153–171, Feb. 2006.
- [10] A. Haddoun, M. El Hachemi Benbouzid, D. Diallo, R. Abdessemed, J. Ghouili, and K. Srairi, "Modeling, analysis, and neural network control of an EV electrical differential," *IEEE Trans. Ind. Electron.*, vol. 55, no. 6, pp. 2286–2294, Jun. 2008.
- [11] R. Babuska and H. Verbruggen, "An overview of fuzzy modeling for control," *Control Eng. Pract.*, vol. 4, no. 11, pp. 1593–1606, Nov. 1996.
- [12] D. Simon, "Kalman filtering for fuzzy discrete time dynamic systems," *Appl. Soft Comput.*, vol. 3, no. 3, pp. 191–207, Nov. 2003.
- [13] Y. Aoki, T. Uchida, and Y. Hori, "Experimental demonstration of body slip angle control based on a novel linear observer for electric vehicle," in *Proc. 31st IEEE IECON*, 2005, pp. 2620–2625.
- [14] C. S. Liu and H. Peng, "Road friction coefficient estimation for vehicle path prediction," *Vehicle Syst. Dyn.*, vol. 25, pp. 413–425, 1996. Suppl.
- [15] Y. Hori, "Future vehicle driven by electricity and control-research on four wheel motored 'UOT MARCH II,'" *IEEE Trans. Ind. Electron.*, vol. 51, no. 5, pp. 954–962, Oct. 2004.

- [16] P. J. T. Venhovens and K. Naab, "Vehicle dynamics estimation using Kalman filters," *Vehicle Syst. Dyn.*, vol. 32, no. 2/3, pp. 171–184, Aug. 1999.
- [17] M. C. Best, T. J. Gordon, and P. J. Dixon, "An extended adaptive Kalman filter for real-time state estimation of vehicle handling dynamics," *Vehicle Syst. Dyn.*, vol. 34, no. 1, pp. 57–75, Jul. 2000.
- [18] R. E. Kalman, "New result in linear filtering and prediction theory," *Trans. ASME, J. Basic Eng., Ser. D*, vol. 83, pp. 95–108, 1961.
- [19] C. Geng and Y. Hori, "Nonlinear body slip angle observer for electric vehicle stability control," in *Proc. 23rd EVS*, 2007, CD-ROM.
- [20] C. Geng, T. Uchida, and Y. Hori, "Body slip angle estimation and control for electric vehicle with in-wheel motors," in *Proc. 33rd IEEE IECON*, 2007, pp. 351–355.



**Moulood Denai** received the B.S. degree in electrical engineering from the University of Algiers, Algiers, Algeria, in 1982, and the Ph.D. degree in control engineering from The University of Sheffield, Sheffield, U.K., in 1988.

He is a Professor at Mohamed Boudiaf University of Science and Technology of Oran, Oran, Algeria. Currently, he is on research leave in the Department of Automatic Control and Systems Engineering, The University of Sheffield. His main fields of interest are intelligent control design; intelligent fault detection

in power systems; advanced control of power devices; modeling and control of electric power systems; modeling, simulation, and control design for efficiency optimization in the field of renewable energies such as solar and wind; investigation of power electronics interface for renewable energy systems; modeling and control of life science systems; data mining; and knowledge discovery for system modeling.



**Cong Geng** received the M.S. degree in vehicle engineering from Jilin University of Technology, Changchun, China, in 1996. She is currently working toward the Ph.D. degree at the University of Tokyo, Tokyo, Japan.

She joined the Department of Transportation and Traffic, Jilin University of Technology, as an Assistant Professor and became a Lecturer in 1999. She became a Lecturer at Beijing Jiaotong University, Beijing, China, in 2000. She is interested in vehicle dynamics analysis and control technology. Her studies

currently focus on advanced motion control of electric vehicles.



**Yoichi Hori** (S'81–M'83–SM'00–F'05) was born on July 14, 1955. He received the B.S., M.S., and Ph.D. degrees in electrical engineering from the University of Tokyo, Tokyo, Japan, in 1978, 1980, and 1983, respectively.

In 1983, he joined the Department of Electrical Engineering, University of Tokyo, as a Research Associate. He later became an Assistant Professor, an Associate Professor, and, in 2000, a Professor. During 1991–1992, he was a Visiting Researcher at the University of California, Berkeley. Since 2002,

he has been with the Institute of Industrial Science, University of Tokyo, as a Professor of electrical control system engineering in the Department of Informatics and Electronics. His research fields are control theory and its industrial applications to motion control, mechatronics, robotics, electric vehicles, etc.

Dr. Hori is a member of the Institute of Electrical Engineers of Japan (IEE-Japan), Japan Society of Mechanical Engineering, Society of Instrument and Control Engineers, Robotics Society of Japan, Society of Automobile Engineers of Japan, and Japan Society for Simulation Technology, among others. He was the Treasurer of IEEE Japan Council and Tokyo Section during 2001–2002. He is currently an AdCom member of the IEEE Industrial Electronics Society. He was the Vice President of the IEE-Japan Industry Applications Society during 2004–2005. He is the Chairman of the Energy Capacitor Storage System Forum and the Motor Technology Symposium of the Japan Management Association. He was the winner of the Best Paper Awards from the IEEE TRANSACTIONS ON INDUSTRIAL ELECTRONICS in 1993 and 2001.



**Lotfi Mostefai** received the M.S. degree in electrical control engineering from Mohamed Boudiaf University of Science and Technology of Oran, Oran, Algeria, in 2002. He is currently working toward the Ph.D. degree at Mohamed Boudiaf University of Science and Technology of Oran.

He lectured on "control engineering" and "microprocessors and microcontrollers in industrial applications" at the University Moulay Tahar, Saida, Algeria. He was with the Hori Laboratory, Institute of Industrial Science, University of Tokyo, Tokyo,

Japan, as a Research Student in 2006. His research interests are optimal and robust control, motion control systems, smart materials and their applications, automotive engineering, and renewable energies.



# A Novel Traction Control for EV Based on Maximum Transmissible Torque Estimation

Dejun Yin, *Student Member, IEEE*, Sehoon Oh, *Member, IEEE*, and Yoichi Hori, *Fellow, IEEE*

**Abstract**—Controlling an immeasurable state with an indirect control input is a difficult problem faced in traction control of vehicles. Research on motion control of electric vehicles (EVs) has progressed considerably, but traction control has not been so sophisticated and practical because of this difficulty. Therefore, this paper takes advantage of the features of driving motors to estimate the maximum transmissible torque output in real time based on a purely kinematic relationship. An innovative controller that follows the estimated value directly and constrains the torque reference for slip prevention is then proposed. By analysis and comparison with prior control methods, the resulting control design approach is shown to be more effective and more practical, both in simulation and on an experimental EV.

**Index Terms**—Antislip, electric vehicle (EV), maximum transmissible torque estimation (MTTE), traction control.

## I. INTRODUCTION

**D**UE TO THE drastically increasing price of oil and the growing concern about global environmental problems, research on electric vehicles (EVs) is drawing more and more attention, and significant improvements in power electronics, energy storage, and control technology have been achieved [1]–[3].

From the viewpoint of motion control, compared with internal combustion engine vehicles, the advantages of EVs can be summarized as follows [4]:

- 1) quick torque generation;
- 2) easy torque measurement;
- 3) independently equipped motors for each wheel.

The torque output of the motor can be easily calculated from the motor current. This merit makes it easy to estimate the driving or braking forces between tire and road surface in real time, which contributes a great deal to application of new control strategies based on road condition estimation. The independently equipped motors provide higher power/weight density, higher redundancy for safety, and better dynamic performance [5], [6].

Manuscript received August 24, 2008; revised February 10, 2009. First published March 16, 2009; current version published June 3, 2009. This work was supported by the Global COE Program under “Secure-Life Electronics,” The University of Tokyo, Tokyo, Japan.

D. Yin is with the Department of Electrical Engineering, Graduate School of Engineering, The University of Tokyo, Tokyo 113-8656, Japan (e-mail: yin@horilab.iis.u-tokyo.ac.jp).

S. Oh is with the Institute of Industrial Science, The University of Tokyo, Tokyo 153-8505, Japan (e-mail: sehoon@horilab.iis.u-tokyo.ac.jp).

Y. Hori is with the Department of Advanced Energy, Graduate School of Frontier Sciences, The University of Tokyo, Tokyo 153-8505, Japan.

Color versions of one or more of the figures in this paper are available online at <http://ieeexplore.ieee.org>.

Digital Object Identifier 10.1109/TIE.2009.2016507

By introducing computer control technology, vehicle chassis control systems have made significant technological progress over the last decade to enhance vehicle stability and handling performance in critical dynamic situations. Among these controllers are systems such as the antilock braking system (ABS) [7], [8], the direct yaw control system [9], [11], the integrated vehicle dynamic control system, etc. However, the effective operation of each of these control systems is based on some basic assumptions, for example, the output torque being able to accurately work on the vehicle.

For this purpose, traction control, as a primary control for vehicles, is developed to ensure the effectiveness of the torque output. The key to traction control is antislip control, when the vehicle is driven or brakes on a slippery road, particularly for light vehicles because they are more inclined to skid on slippery roads. Traction control must not only guarantee the effectiveness of the torque output to maintain vehicle stability but also provide some information about tire–road conditions to other vehicle control systems. Moreover, a well-managed traction control system can cover the functions of ABS, because motors can generate deceleration torque as easily as acceleration torque [12]. Based on the core traction control, more complicated 2-DOF motion control for vehicles can be synthesized by introduction of some information on steering angle, yaw rate, etc. [13], [14]. From the viewpoint of the relation between safety and cost, a more advanced traction control synthesis also means lower energy consumption.

However, actual vehicles present challenges to research on traction control. For example, the real chassis velocity is not available, and the friction force that drives the vehicle is immeasurable. Depending on whether chassis velocity is calculated, the control implementations for antislip control fall into two classes. In general traction control systems that need the chassis velocity, due to physical and economic reasons, the nondriven wheels are utilized to provide an approximate vehicle velocity. However, this method is not applicable when the vehicle is accelerated by 4WD systems or decelerated by brakes equipped in these wheels. For this reason, the accelerometer measurement is also used to calculate the velocity value, but it cannot avoid offset and error problems. Other sensors, e.g., optical sensors [15], sensors of magnetic markers [16], [17], etc., can also obtain the chassis velocity. However, they are too sensitive and reliant on the driving environment or too expensive to be applied in actual vehicles. Some antislip control systems [7], [8], [18] try to realize optimal slip ratio controls according to the Magic Formula [19]. However, these systems not only need extra sensors for the acquisition of chassis velocity or acceleration but are also more difficult to realize

than expected, because the tuned algorithms and parameters for specific tire–road conditions cannot adapt quickly to the significant variation in the instantaneous immeasurable relationship between slip ratio and friction coefficient in different driving conditions.

On the other hand, some controllers, for example, model following control (MFC), do not need information on chassis velocity or even acceleration sensors. In these systems, the controllers only make use of torque and wheel rotation as input variables for calculation. Fewer sensors contribute not only to lower cost but also higher reliability and greater independence from driving conditions, which are the most outstanding merits of this class of control systems. Accordingly, research on more practical and more sophisticated antislip control based on MFC continues until now. Sakai and Hori [20] proposed a primary MFC system for antislip control. Saito *et al.* [13], [14] modified it and proposed a novel stability analysis to decide on the maximum feedback gain, and furthermore, they took the antislip control as a core subsystem and extended it to 2-DOF motion control. Akiba *et al.* improved the control performance by introduction of back electromotive force, and added a conditional limiter to avoid some of its inherent drawbacks [21]. Nevertheless, these control designs based on compensation have to consider the worst stability case to decide on the compensation gain, which impairs the performance of antislip control. Furthermore, gain tuning for some specific tire–road conditions also limits the practicability of this method.

Therefore, this paper, making use of the advantages of EVs, focuses on the development of a core traction control system based on the maximum transmissible torque estimation (MTTE) that requires neither chassis velocity nor information about tire–road conditions. In this system, use is made of only the torque reference and the wheel rotation to estimate the maximum transmissible torque to the road surface, and then, the estimated torque is applied for antislip control implementation.

The rest of this paper is structured as follows. Section II describes an EV modified for experiments. Section III presents a longitudinal model of vehicles and analyzes the features of antislip control. MTTE and a control algorithm based on it are then proposed. Comparing with MFC for antislip control, Section IV demonstrates simulations and experiments. A detailed discussion follows in Section V, analyzing the features of the proposed control method.

## II. EXPERIMENTAL EV

In order to implement and verify the proposed control system, a commercial EV, i.e., COMS, which is made by Toyota Auto Body Company, Ltd., as shown in Fig. 1, was modified to fulfill the experiments' requirements. Each rear wheel is equipped with an interior permanent-magnet synchronous motor and can be controlled independently.

As shown in Fig. 2, a control computer is added to take the place of the previous ECU to operate the motion control. The computer receives the acceleration reference signal from the acceleration pedal sensor, the forward/backward signal from the shift switch, and the wheel rotation from the inverter. Then, the calculated torque reference of the left and the right rear wheel



Fig. 1. COMS3—A new experimental electric vehicle.

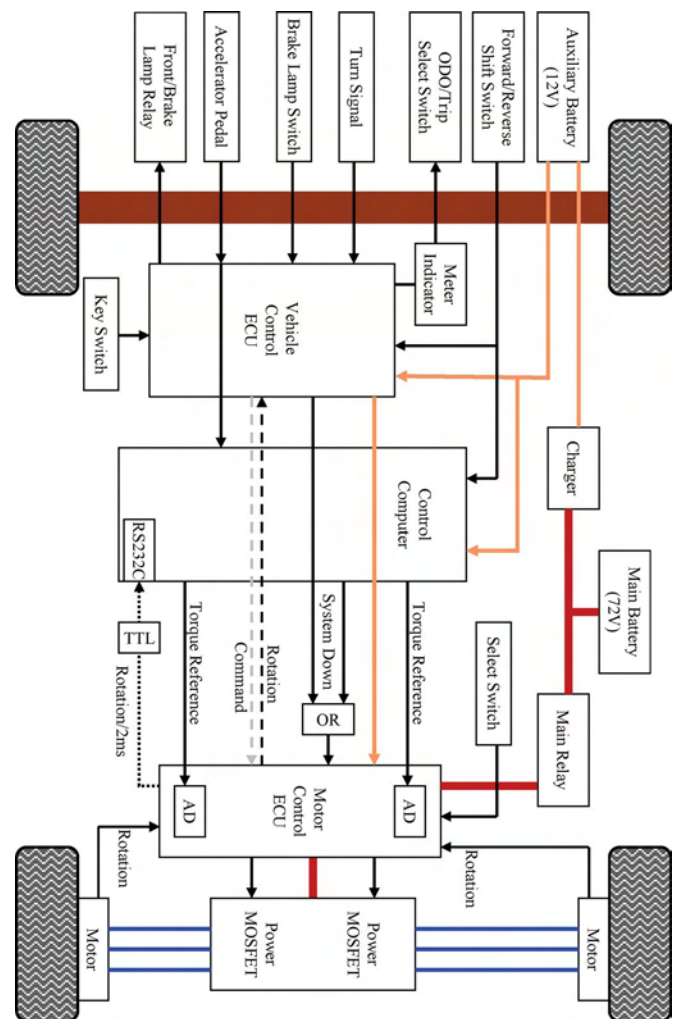


Fig. 2. Schematic of the electrical system of COMS3.

are independently sent to the inverter by two analog signal lines. Table I lists the main specifications.

The most outstanding feature of the modified inverter is that the minimum refresh time of the torque reference is decreased from 10 to 2 ms, which makes it possible to actualize the torque reference more quickly and accurately. The increased maximum rate of change of the torque reference permits faster torque variation for high-performance motion control.

TABLE I  
SPECIFICATION OF COMS3

Total Weight	360kg
Max. Power	2000W × 2
Max. Torque	100Nm × 2
Wheel Inertia	0.5kgm <sup>2</sup> × 2
Wheel Radius	0.22m
Sampling Time	0.01s
Controller	PentiumM1.8G, 1GB RAM
A/D and D/A	12 bit
Shaft Encoder	36 pulse/round

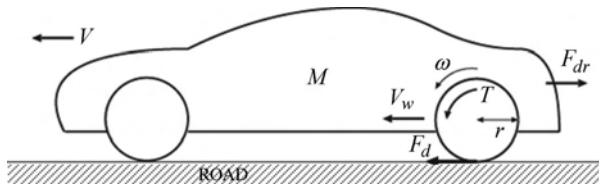


Fig. 3. Dynamic longitudinal model of the vehicle.

TABLE II  
PARAMETER LIST

Symbol	Definition
$J_w$	Wheel Inertia
$V_w$	Wheel Velocity (Circumferential Velocity)
$\omega$	Wheel Rotation
$T$	Driving Torque
$r$	Wheel Radius
$F_d$	Friction Force (Driving Force)
$M$	Vehicle Mass
$N$	Vehicle Weight
$V$	Chassis Velocity (Vehicle Velocity)
$F_{dr}$	Driving Resistance
$\lambda$	Slip Ratio
$\mu$	Friction Coefficient

III. MTTE FOR ANTISLIP CONTROL

A. Longitudinal Model and Dynamic Analysis

Because only longitudinal motion is discussed in this paper, the dynamic longitudinal model of the vehicle can be described as in Fig. 3, and the parameter definition is listed in Table II.

Generally, the dynamic differential equations for the calculation of longitudinal motion of the vehicle are described as follows:

$$J_w \dot{\omega} = T - rF_d \tag{1}$$

$$M \dot{V} = F_d - F_{dr} \tag{2}$$

$$V_w = r\omega \tag{3}$$

$$F_d(\lambda) = \mu N. \tag{4}$$

The interrelationships between slip ratio and friction coefficient can be described by various formulas. Here, as shown in

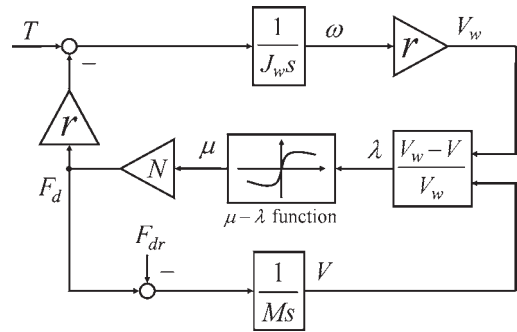


Fig. 4. One-wheel vehicle model with Magic Formula.

Fig. 4, the widely adopted Magic Formula is applied to build a vehicle model for the following simulations.

B. MTTE

In this paper, in order to avoid the complicated  $\mu-\lambda$  relation, only the dynamic relation between tire and chassis is considered based on the following considerations, which transform the antislip control into a maximum transmissible torque control.

- 1) Whatever kind of tire–road condition the vehicle is driven in, the kinematic relationship between wheel and chassis is always fixed and known.
- 2) During the acceleration phase, considering stability and tire abrasion, a well-managed control of the velocity difference between wheel and chassis is more important than the mere pursuit of absolute maximum acceleration.
- 3) If wheel and chassis accelerations are well controlled, then the difference between wheel and chassis velocities, i.e., the slip, is also well controlled.

According to (1) and (3), the driving force, i.e., the friction force between the tire and the road surface, can be calculated as (5). Assuming that  $T$  is constant, it can be found that the higher the  $V_w$ , the lower the  $F_d$ . In normal road conditions,  $F_d$  is less than the maximum friction force from the road and increases as  $T$  goes up. However, when slip occurs,  $F_d$  equals the maximum friction force that the tire–road relation can provide and cannot increase with  $T$ . Here, there are only two parameters, namely,  $r$  and  $J_w$ , so  $F_d$  is easily calculated in most tire–road conditions

$$F_d = \frac{T}{r} - \frac{J_w \dot{V}_w}{r^2}. \tag{5}$$

When slip starts to occur, the difference between the velocities of the wheel and the chassis becomes larger and larger, i.e., the acceleration of the wheel is larger than that of the chassis. Furthermore, according to the Magic Formula, the difference between the accelerations will increase with the slip.

Therefore, the condition that the slip does not start or become more severe is that the acceleration of the wheel is close to that of the chassis. Moreover, considering the  $\mu-\lambda$  relation described in the Magic Formula, an appropriate difference between chassis velocity and wheel velocity is necessary to provide the friction force. Accordingly, the approximation

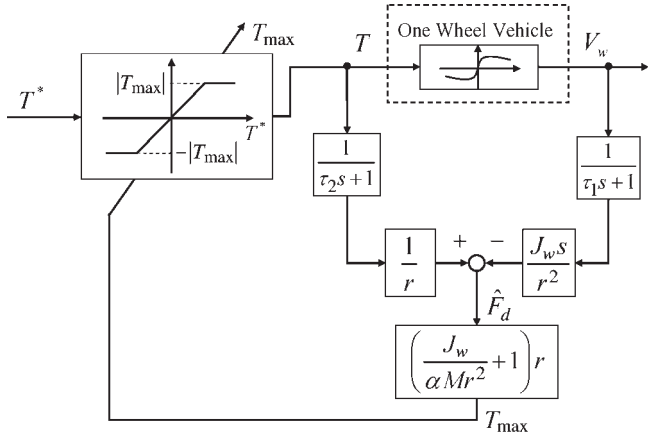


Fig. 5. Control system based on MTTE.

between the accelerations of the chassis and the wheel can be described by a relaxation factor, i.e.,  $\alpha$

$$\alpha = \frac{\dot{V}^*}{\dot{V}_w}, \quad \text{i.e.,} \quad \alpha = \frac{(F_d - F_{dr})/M}{(T_{\max} - rF_d)r/J_w}. \quad (6)$$

In order to satisfy the condition that slip does not occur or become larger,  $\alpha$  should be close to one. With a designed  $\alpha$ , when the vehicle enters a slippery road,  $T_{\max}$  must be reduced adaptively following the decrease of  $F_d$  to satisfy (6), the no-slip condition.

Since the friction force from the road is available from (5), the maximum transmissible torque  $T_{\max}$  can be calculated as

$$T_{\max} = \left( \frac{J_w}{\alpha M r^2} + 1 \right) r F_d. \quad (7)$$

This formula indicates that a given  $F_d$  allows a certain maximum torque output from the wheel so as not to increase the slip. Here, it must be pointed out that the driving resistance  $F_{dr}$  is assumed to be zero, which will result in an overevaluation of  $T_{\max}$  and consequently impair the antislip performance. However,  $F_{dr}$  is a variable that is related with chassis velocity and vehicle shape and can be calculated or estimated in real time if higher antislip performance is required or if the vehicle runs at high speed [22]–[24]. Although the vehicle mass  $M$  can also be estimated online [25]–[28], in this paper, it is assumed to be constant.

Finally, the proposed controller can use  $T_{\max}$  to constrain the torque reference if necessary.

### C. Controller Design

The torque controller is designed as in Fig. 5, in which the limiter with a variable saturation value is expected to realize the control of torque output according to the dynamic situation. Under normal conditions, the torque reference is expected to pass through the controller without any effect. On the other hand, when on a slippery road, the controller can constrain the torque output to be close to  $T_{\max}$ .

First, the estimator uses the commanded torque into the inverter and the rotation speed of the wheel to calculate the friction force, and it then estimates the maximum transmissible torque according to (7). Finally, the controller utilizes

the estimated torque value as a saturation value to limit the torque output. In essence, the estimation shown in Fig. 5 is a disturbance observer.

Here, although it will cause some phase shift, duo to the low resolution of the shaft encoder installed in the wheel, a low-pass filter (LPF) with a time constant of  $\tau_1$  is introduced to smooth the digital signal  $V_w$  for the differentiator that follows. In order to keep the filtered signals in phase, another LPF with a time constant of  $\tau_2$  is added for  $T$ .

### D. Stability Analysis

Considering that the Magic Formula included in the vehicle model shown in Fig. 4 is nonlinear, this paper makes use of an equivalent model [13], [14] for stability analysis to decide on parameters.

Slip occurs when part of the outputted torque cannot be transmitted to the chassis by the tire–road interaction, resulting in lower chassis acceleration than that of the wheel. Here, (8) uses  $\Delta$  to describe the ratio of the undertransmitted torque. In addition, taking into account the ideal state and the worst slip case in which the wheel spins completely idly, i.e., the inertia of the whole system equals the inertia of the wheel,  $J_w$ , the variation range of  $\Delta$  is also available

$$\dot{V} - \dot{V}_w = -\frac{\Delta T}{Mr}, \quad \Delta \in [0, Mr^2/J_w]. \quad (8)$$

According to (1), (2), and (8), the dynamic longitudinal model of the vehicle can be simplified as

$$J\dot{\omega} = T \quad (9)$$

where a single-input–single-output system masks the complicated interaction among tire, chassis, and road, which contributes to stability analysis. That is, the unwanted wheel acceleration that causes slip can be regarded as the result of a decrease in system inertia. Furthermore,  $\Delta$  can also be treated as a description of variation in system inertia. Here, as shown in (10),  $J$  is the equivalent inertia of the whole vehicle system from the viewpoint of the driving wheel, and  $J_n$  is the nominal inertia where no slip occurs

$$J = \frac{J_n}{1 + \Delta}, \quad J_n = J_w + Mr^2. \quad (10)$$

Consequently, use is made of (9) to take place of the vehicle model shown in Fig. 5 for stability analysis. When the vehicle rapidly accelerates on a slippery road, the estimated  $T_{\max}$  will constrain  $T^*$  and take its place to be treated as the input value to the motor. In this case, the whole system will automatically transform into a closed-loop feedback system, as shown in Fig. 6. Here, in order to analyze the stability easily, the delay of the electromechanical system is simplified as a LPF with a time constant of  $\tau$ .

Fig. 7, as the equivalent block diagram of Fig. 6, is used for the analysis of the closed-loop stability against  $\Delta$ , the model variation. The  $T_{zw}$  in Fig. 7 is described in

$$T_{zw} = \frac{-J_w K}{J_n r \tau \tau_1 s^2 + J_n ((r - K)\tau + r\tau_1) s + J_n r - Mr^2 K}. \quad (11)$$

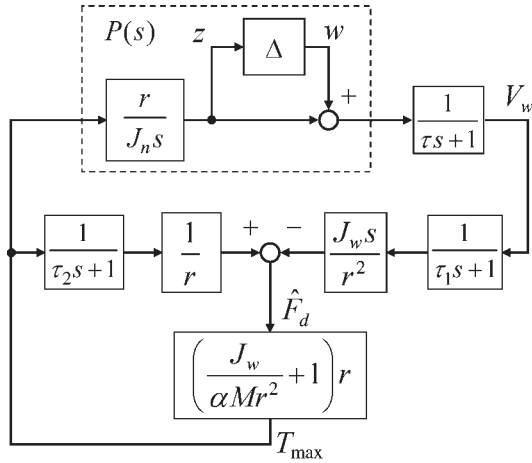


Fig. 6. Equivalent closed-loop control system.

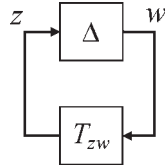


Fig. 7. Equivalent block diagram. Here,  $T_{zw}$  is the transfer function from  $w$  to  $z$  in Fig. 6.

Here,

$$K = \left( \frac{J_w}{\alpha M r^2} + 1 \right) r. \quad (12)$$

As a result, the following conditions in (14) must be satisfied to ensure the closed-loop stability, i.e., ensure the real part of the roots of the characteristic equation (13) to be negative [29]. Here,  $\tau_2$  is assumed to be equal to  $\tau_1$  to simplify the solution

$$1 - T_{zw} \Delta = 0 \quad (13)$$

$$\left\{ \begin{array}{l} K < \frac{M r^2 + J_w}{M r^2 - \Delta J_w} r, \\ \tau_1 > \frac{K - r}{r} \tau, \end{array} \right. \quad \text{i.e.,} \quad \left\{ \begin{array}{l} \alpha > \frac{1 - J_w \Delta / M r^2}{1 + \Delta} \\ \tau_1 > \frac{J_w \tau}{\alpha M r^2}. \end{array} \right. \quad (14)$$

It can be found in (14) that if there is no limiter, when the vehicle runs in a normal state,  $\alpha$  must be larger than one to fulfill the requirement for stability. However, considering (7), when  $\alpha$  is larger than one,  $T_{\max}$  will always be restrained to be smaller than the torque that the tire–road interface can provide, which will impair the acceleration performance.

Therefore, in this paper,  $\alpha$  is designed to be slightly smaller than one to ensure acceleration performance while improving the antislip performance.

### E. Compensation for Acceleration Performance

In real experiments, even in normal road conditions,  $T_{\max}$  may be smaller than  $T^*$  due to system delay at the acceleration start, which will cause a suddenly commanded acceleration to be temporarily constrained by  $T_{\max}$  during the acceleration phase.

In order to avoid this problem, the increasing rate of  $T^*$  is amplified as a stimulation to make the undervalued  $T_{\max}$  to

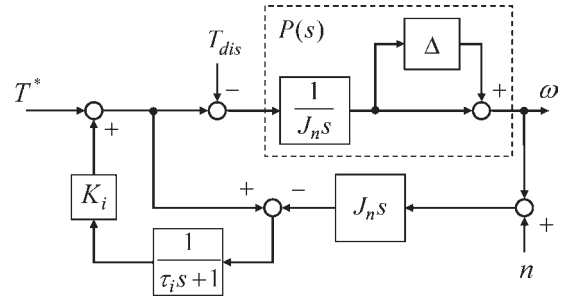


Fig. 8. Block diagram of MFC for slip prevention.

meet the acceleration reference. Here,  $T'_{\max}$  is used instead of  $T_{\max}$  as the input to the controller, whose relation is described by (15). Here,  $G$  is a compensation gain. Additionally, the over expanded  $T'_{\max}$  can be automatically constrained by the following controller:

$$T'_{\max} = T_{\max} + \dot{T}^* G, \quad \dot{T}^* > 0. \quad (15)$$

## IV. SIMULATION AND EXPERIMENTAL RESULTS

### A. MFC for Antislip Control

This paper uses the antislip control system based on the MFC presented in [13] and [14], shown in Fig. 8, for the following comparison.

$K_i$ , shown in (16), must fulfill the condition for robust stability. Considering the worst slip case,  $K_{im}$  is used to represent the maximum feedback gain that ensures robust stability

$$K_i < \frac{1}{\Delta}, \quad \Delta \in [0, M r^2 / J_w] \quad (16)$$

$$K_{im} = \frac{J_w}{M r^2}. \quad (17)$$

In the following simulations and experiments, the same parameters of the vehicle are adopted for comparison, and  $\tau_i$  is equal to  $\tau_1$ .

### B. Simulation Results

Simulation systems were synthesized based on the models of Figs. 5 and 8, respectively.

Fig. 9 shows the stability of the control system in which  $\alpha$  is designed to be smaller than one for two different slip states. In this simulation, the system delay is shortened to make the primary tendency clear.

Figs. 10 and 11 show the simulation results with variations in  $\alpha$  and  $\tau_1$ . Additionally, Fig. 12 shows the simulation results of MFC for comparison. The maximum friction coefficient of the slippery road is 0.3. Here,  $\tau_1$ ,  $\tau_2$ , and  $\tau_i$  are set to 50 ms, and  $\tau = 40$  ms.

### C. Experimental Results

Controllers designed based on the simulated algorithm were applied to COMS3 for the experiments. In these experiments, the slippery road was simulated by an acrylic sheet with a length

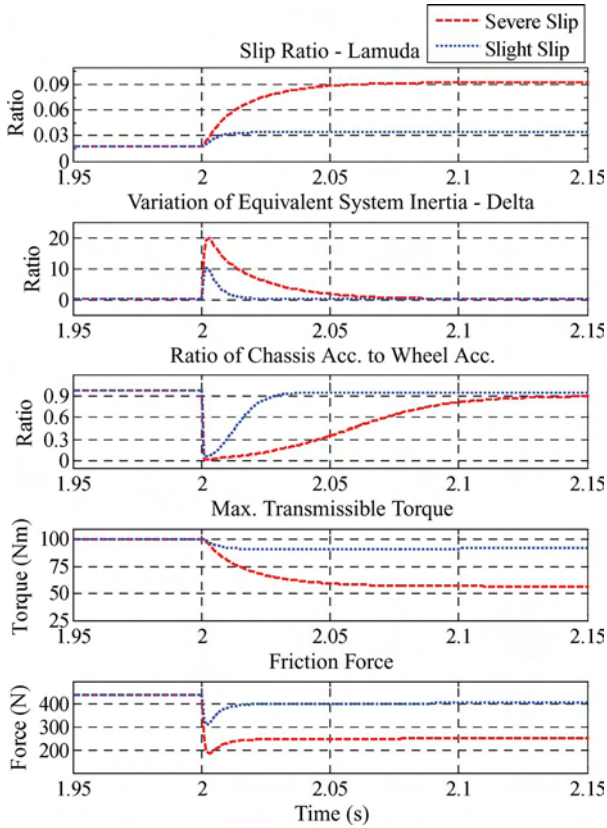


Fig. 9. Antislip performance and system stability when  $\alpha = 0.9$ . In the simulation of severe slip, the maximum friction coefficient is set to 0.3, and the slight slip is set to 0.6. Here, the commonly used  $\lambda$  and  $\Delta$  are utilized to describe the extent of the slip.

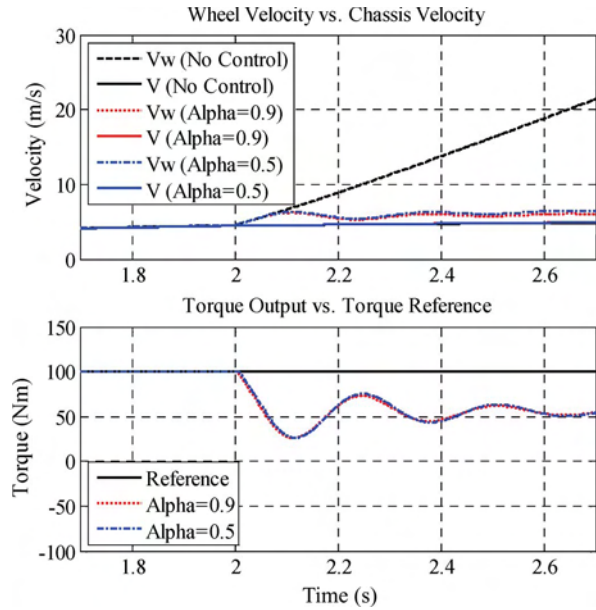


Fig. 10. Comparison of simulation results with variation in  $\alpha$ .

of 1.2 m and lubricated with water. The initial velocity of the vehicle was set higher than 1 m/s to avoid the immeasurable zone of the shaft sensors installed in the wheels.

Here, it must be pointed out that, in order to detect the chassis velocity, only the left rear wheel is driven by the motor, while

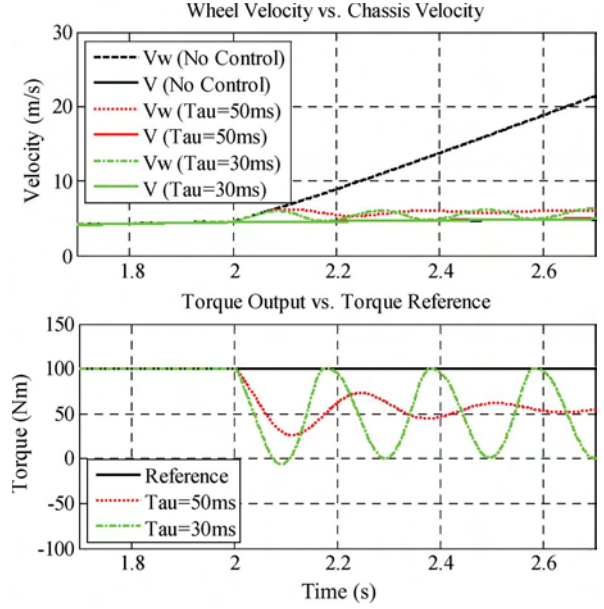


Fig. 11. Comparison of simulation results with variation in  $\tau_1$ .

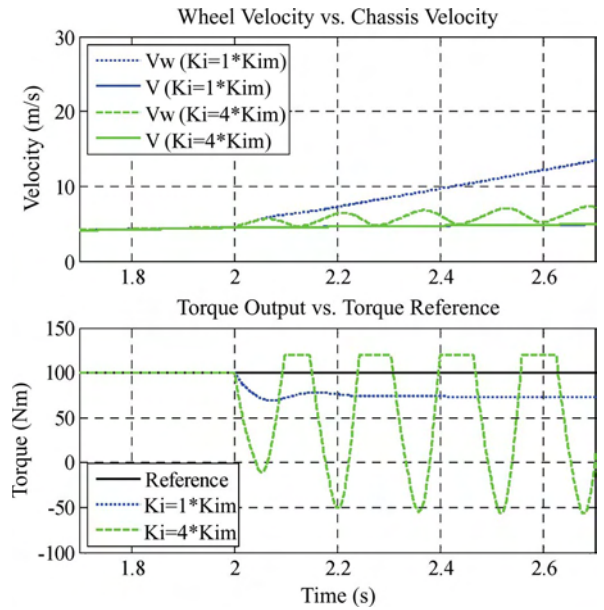


Fig. 12. Comparison of simulation results of MFC with variation in  $K_i$ . Although the largest  $K_i$  for stability is  $K_{im}$ , the simulation result of  $K_i = 4 * K_{im}$  is shown for comparison.

the right rear wheel rolls freely to provide a reference value of the chassis velocity for comparison.

Figs. 13 and 14 show the experimental results with variations in  $\alpha$  and  $\tau_1$ , and Fig. 15 shows the results using MFC for comparison. Fig. 16 shows the performance of acceleration compensation with  $G = 0.1$ .

## V. DISCUSSION

### A. Relaxation Factor and Stability

According to (1) and (7),  $T_{max}$  can be rewritten as

$$T_{max} = T + \frac{J_w}{r} \left( \frac{1}{\alpha} \dot{V} - \dot{V}_w \right) \quad (18)$$

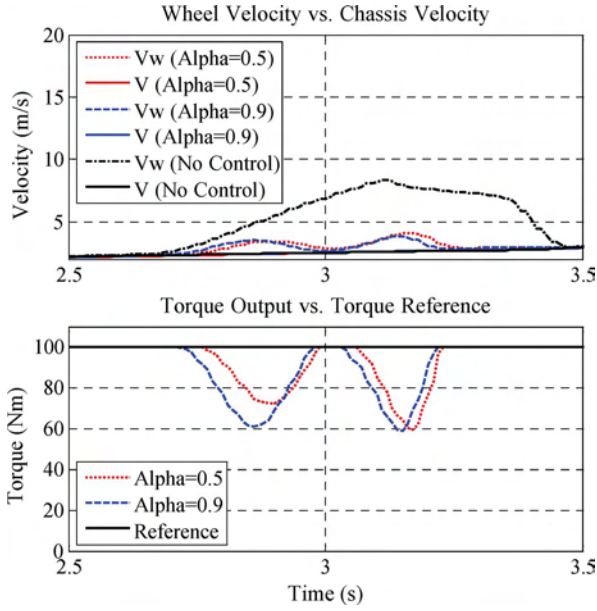


Fig. 13. Comparison of experimental results with variation in  $\alpha$ . In this experiment,  $\tau_1$  and  $\tau_2$  are fixed at 50 ms.

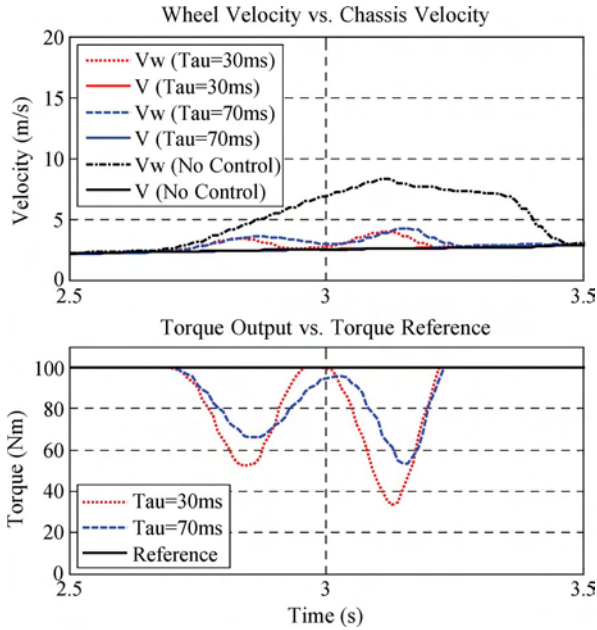


Fig. 14. Comparison of experimental results with variation in  $\tau_1$ . In this experiment,  $\alpha$  is fixed at 0.9.

where it can be found that when  $\alpha$  is smaller than 1 and the vehicle runs in no-slip conditions,  $T_{max}$  will be larger than  $T^*$ , and the unwanted torque will be eliminated by the limiter, which keeps the system stable and responsive to the driver's torque reference.

On the other hand, when the vehicle enters a slippery road, as shown in Fig. 9, due to the system delay, a sudden slip will occur at first, and then, the whole system will work in the following two different states.

- 1) Slight slip that makes (14) valid, i.e., the system is theoretically unstable. However, a well-designed  $\alpha$  will allow  $T_{max}$  to rise to increase the slip properly, according to

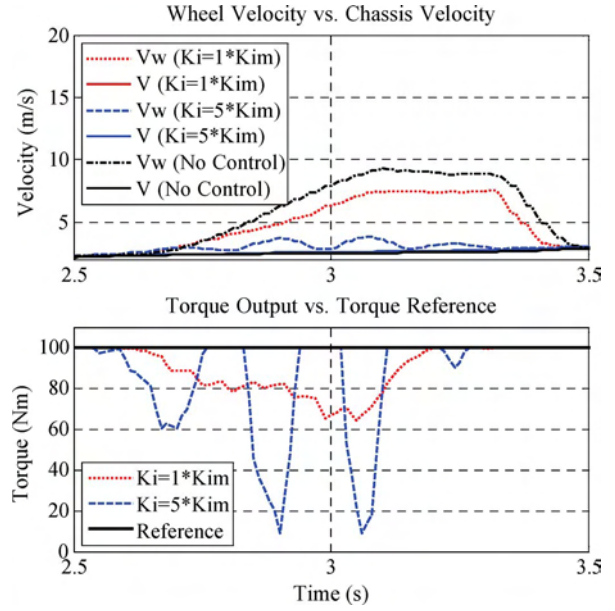


Fig. 15. Comparison of simulation results of MFC with variation in  $K_i$ .

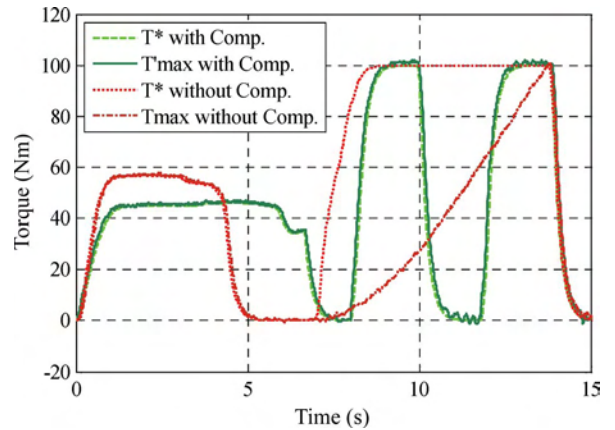


Fig. 16.  $T^*$  versus  $T_{max}$  in experiments with/without compensation.

the Magic Formula, so as to provide an increased friction force, as expected.

- 2) A severe slip that satisfies (14) occurs. The system is stable, i.e.,  $T_{max}$  will become smaller and smaller to restrain the slip. The ratio of the acceleration of the chassis to that of the wheel will become larger and larger to meet the designed  $\alpha$ .

In conclusion, the simulations and experiments indicate that a relaxation factor  $\alpha$  that is smaller than one makes the system work at a critical state, which results in the best antislip performance while keeping the system stable.

### B. Performance of the Proposed Antislip Control

Figs. 10 and 13 show that, compared to the no-control case, the difference between the wheel velocity and the chassis velocity caused mainly by the delay in the control system does not increase. The estimated maximum transmissible torque is close to the input reference torque in the normal road and corresponds

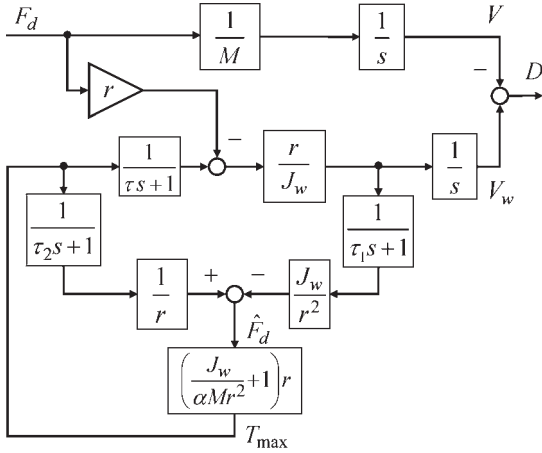


Fig. 17. Equivalent closed-loop control system without consideration of the  $\mu$ - $\lambda$  relation.

to the maximum friction force allowed by the slippery tire-road surface.

The results also indicate that the larger the  $\alpha$ , the better the antislip performance. A larger relaxation factor further limits the difference between the accelerations of the chassis and the wheel. In fact, when the control system falls into an antislip state, it also transforms into a closed-loop feedback system shown as Fig. 17. Here,  $D$  represents the extent of the slip, and the relation between  $D$  and  $F_d$  is not considered. The transfer function from  $F_d$  to  $D$  indicates the effect of  $\alpha$  in

$$\frac{D}{F_d} = \frac{-\alpha(J_w + Mr^2) [\tau\tau_1 s^2 + (\tau + \tau_1)s] + J_w(1 - \alpha)}{\alpha J_w M [\tau\tau_1 s^2 + (\tau + \tau_1)s + 1] s}. \quad (19)$$

Figs. 11 and 14 show that an insufficiently large value of  $\tau_1$ , particularly when it is smaller than the delay time of the electromechanical system, can cause the control system to become unstable and result in more severe torque oscillation, which makes driving operation feel rough. However, a larger time constant in the LPF means a larger phase shift that results in a more severe slip at the start of the slip.

### C. Comparison With MFC

Figs. 12 and 15 show that, compared with the control based on MTTE, MFC cannot provide a good tradeoff between antislip performance and control stability. With  $K_{im}$ , which is the largest feedback gain that ensures system stability for any slip state, the control synthesis cannot constrain the slip, as expected. With a much larger  $K_i$ , the control synthesis succeeded in constraining the slip, but the torque output was too oscillatory. The experiments also showed that, even in normal conditions, MFC with a large feedback gain can cause system instability.

Additionally, although a well-tuned  $K_i$  can make a good tradeoff for a specific tire-road condition, such a system will become unstable in more slippery conditions, which limits the practicality of this method.

On the other hand, with a different control philosophy, the proposed control based on MTTE does not depend on the error

between the expected output and the real output to decide on the control output, but it follows the estimated load directly to calculate the control input, i.e., according to its needs, which contributes to higher control performance and higher applicability in any tire-road condition. From this viewpoint, the proposed control topology can be called load following control.

Compared with other control systems, the proposed control has some other merits. The driver can directly control the acceleration at any time, because the driver will be given the priority to take back the control of the motor from the controller immediately only if  $T^*$  becomes smaller than  $T_{max}$ . In addition, MTTE cannot only provide  $T_{max}$  for antislip control in critical situations but also inform other vehicle control systems of the tire-road situation.

### D. Compensation

Fig. 16 shows that the deterioration of pedal response caused by large system delay may occur in the control system without compensation. In this case, the control system must take a long time to restore the direct control of acceleration to the driver. The experiments also indicate that, without this compensation, for higher  $\alpha$ , loss of control occurs more frequently.

However, the additional increasing rate of  $T^*$  provides compensation to follow the acceleration reference, avoiding this problem. In fact, if  $T^*$  remains constant, the compensation will not affect the antislip control performance.

## VI. CONCLUSION

This paper has proposed an estimator of maximum transmissible torque and applied it to the control of the driving motors in EVs for slip prevention.

This estimator, which does not calculate chassis velocity, instead using only the input torque and output rotation of the wheel, provides a good foundation for antislip control. The effectiveness of the estimation showed that motors can act not only as actuators but also as a good platform for state estimation because of their inherently fast and accurate torque response. The experiments and simulations verified the effectiveness of the estimation in antislip control. Additionally, this estimator is also expected to provide the maximum transmissible torque for other vehicle control systems to enhance their control performance when the vehicle runs in slippery conditions.

The controller that was designed to cooperate with the estimator can provide higher antislip performance while maintaining control stability. When excessive torque is commanded, this controller constrains the control output to follow the actual maximum driving force between the tire and the road surface, which provides high adaptability to the control system in different tire-road conditions. In addition, the acceleration compensation resolved the problem of deterioration of pedal response due to system delay.

Comparative experiments and simulations with variations of control variables proved the effectiveness and practicality of the proposed control design.

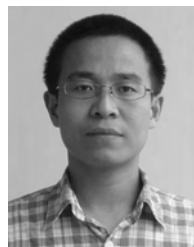


## ACKNOWLEDGMENT

The authors would like to thank the engineers at Aisin AW Company, Ltd., for their cooperation on the inverter modification, and Eric Wu of Keio University, Minato, Japan, for the advice and for improving the readability of this paper.

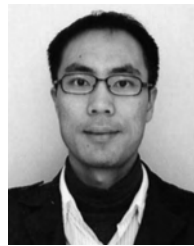
## REFERENCES

- [1] K. T. Chau, C. C. Chan, and C. Liu, "Overview of permanent-magnet brushless drives for electric and hybrid electric vehicles," *IEEE Trans. Ind. Electron.*, vol. 55, no. 6, pp. 2246–2257, Jun. 2008.
- [2] A. Affanni, A. Bellini, G. Franceschini, P. Guglielmi, and C. Tassoni, "Battery choice and management for new-generation electric vehicles," *IEEE Trans. Ind. Electron.*, vol. 52, no. 5, pp. 1343–1349, Oct. 2005.
- [3] M. Nagai, "The perspectives of research for enhancing active safety based on advanced control technology," *Veh. Syst. Dyn.*, vol. 45, no. 5, pp. 413–431, May 2007.
- [4] Y. Hori, "Future vehicle driven by electricity and control—Research on four-wheel-motored 'UOT electric march II'," *IEEE Trans. Ind. Electron.*, vol. 51, no. 5, pp. 954–962, Oct. 2004.
- [5] P. He and Y. Hori, "Optimum traction force distribution for stability improvement of 4WD EV in critical driving condition," in *IEEE Int. Workshop Adv. Motion Control*, 2006, pp. 596–601.
- [6] N. Mutoh, Y. Takahashi, and Y. Tomita, "Failsafe drive performance of FRID electric vehicles with the structure driven by the front and rear wheels independently," *IEEE Trans. Ind. Electron.*, vol. 55, no. 6, pp. 2306–2315, Jun. 2008.
- [7] M. Schinkel and K. Hunt, "Anti-lock braking control using a sliding mode like approach," in *Proc. Amer. Control Conf.*, 2002, vol. 3, pp. 2386–2391.
- [8] C. B. Patil, R. G. Longoria, and J. Limroth, "Control prototyping for an anti-lock braking control system on a scaled vehicle," in *Proc. IEEE Conf. Decision Control*, 2003, vol. 5, pp. 4962–4967.
- [9] F. Tahami, S. Farhangi, and R. Kazemi, "A fuzzy logic direct yaw-moment control system for all-wheel-drive electric vehicles," *Veh. Syst. Dyn.*, vol. 41, no. 3, pp. 203–221, 2004.
- [10] T. Mizushima, P. Raksincharoensak, and M. Nagai, "Direct yaw-moment control adapted to driver behavior recognition," in *Proc. SICE-ICASE Int. Joint Conf.*, 2006, pp. 534–539.
- [11] M. Canale, L. Fagiano, A. Ferrara, and C. Vecchio, "Vehicle yaw control via second-order sliding-mode technique," *IEEE Trans. Ind. Electron.*, vol. 55, no. 11, pp. 3908–3916, Nov. 2008.
- [12] N. Mutoh, Y. Hayano, H. Yahagi, and K. Takita, "Electric braking control methods for electric vehicles with independently driven front and rear wheels," *IEEE Trans. Ind. Electron.*, vol. 54, no. 2, pp. 1168–1176, Apr. 2007.
- [13] T. Saito, H. Fujimoto, and T. Noguchi, "Yaw-moment stabilization control of small electric vehicle," *Trans. IEE Jpn. Ind. Instrum. Control*, vol. IIC-02, no. 15–44, pp. 83–88, 2002.
- [14] H. Fujimoto, T. Saito, and T. Noguchi, "Motion stabilization control of electric vehicle under snowy conditions based on yaw-moment observer," in *Proc. IEEE Int. Workshop Adv. Motion Control*, 2004, pp. 35–40.
- [15] J. D. Turner and L. Austin, "Sensors for automotive telematics," *Meas. Sci. Technol.*, vol. 11, no. 2, pp. R58–R79, Feb. 2000.
- [16] H. Lee and M. Tomizuka, "Adaptive vehicle traction force control for intelligent vehicle highway systems (IVHSs)," *IEEE Trans. Ind. Electron.*, vol. 50, no. 1, pp. 37–47, Feb. 2003.
- [17] S. Suryanarayanan and M. Tomizuka, "Appropriate sensor placement for fault-tolerant lane-keeping control of automated vehicles," *IEEE/ASME Trans. Mechatronics*, vol. 12, no. 4, pp. 465–471, Aug. 2007.
- [18] K. Fujii and H. Fujimoto, "Traction control based on slip ratio estimation without detecting vehicle speed for electric vehicle," in *Proc. 4th Power Convers. Conf.—Nagoya*, 2007, pp. 688–693.
- [19] H. B. Pacejka and E. Bakker, "The Magic Formula tyre model," *Veh. Syst. Dyn.*, vol. 21, no. 1, pp. 1–18, 1992.
- [20] S.-I. Sakai and Y. Hori, "Advantage of electric motor for anti skid control of electric vehicle," *Eur. Power Electron. J.*, vol. 11, no. 4, pp. 26–32, 2001.
- [21] T. Akiba, R. Shirato, T. Fujita, and J. Tamura, "A study of novel traction control model for electric motor driven vehicle," in *Proc. 4th Power Convers. Conf.—Nagoya*, 2007, pp. 699–704.
- [22] S.-I. Sakai, H. Sado, and Y. Hori, "Motion control in an electric vehicle with 4 independently driven in-wheel motors," *IEEE/ASME Trans. Mechatronics*, vol. 4, no. 1, pp. 9–16, Mar. 1999.
- [23] J.-Y. Cao, B.-G. Cao, and Z. Liu, "Driving resistance estimation based on unknown input observer," *J. Appl. Sci.*, vol. 6, no. 4, pp. 888–891, 2006.
- [24] K. Fujii and H. Fujimoto, "Slip ratio estimation and control based on driving resistance estimation without vehicle speed detection for electric vehicle," in *Proc. Soc. Instrum. Control Eng.*, no. 084-1-3, pp. 1–6, 2007.
- [25] M. Ikeda, T. Ono, and N. Aoki, "Dynamic mass measurement of moving vehicles," *Trans. Soc. Instrum. Control Eng.*, vol. 28, no. 1, pp. 50–58, 1992.
- [26] A. Vahidi, A. Stefanopoulou, and H. Peng, "Recursive least squares with forgetting for online estimation of vehicle mass and road grade: Theory and experiments," *Veh. Syst. Dyn.*, vol. 43, no. 1, pp. 31–55, Jan. 2005.
- [27] V. Winstead and I. V. Kolmanovsky, "Estimation of road grade and vehicle mass via model predictive control," in *Proc. IEEE Conf. Control Appl.*, 2005, pp. 1588–1593.
- [28] R.-A. Phornsuk, H. Hiroshi, A. Masatoshi, and O. Shigeto, "Adaptive controller design for anti-slip system of EV," in *Proc. IEEE Conf. Robot., Autom. Mechatronics*, 2006, pp. 1–6, 4018749.
- [29] P. A. Ioannou and J. Sun, *Robust Adaptive Control*. Englewood Cliffs, NJ: Prentice-Hall, 1995, pp. 79–104.



**Dejun Yin** (S'08) received the B.S. and M.S. degrees in electrical engineering from Harbin Institute of Technology, Harbin, China, in 1999 and 2001, respectively, and the M.S. degree in electronics engineering from Chiba Institute of Technology, Chiba, Japan, in 2002, where he worked on embedded control system design in mechanical-electronics engineering for nearly five years. He is currently working toward the Ph.D. degree in electrical engineering in the Department of Electrical Engineering, The University of Tokyo, Tokyo, Japan, performing research on the development of motion control for electric vehicles.

Mr. Yin is a member of the Institute of Electrical Engineers of Japan and the Society of Automotive Engineers of Japan.



**Sehoon Oh** (S'05–M'06) received the B.S., M.S., and Ph.D. degrees in electrical engineering from The University of Tokyo, Tokyo, Japan, in 1998, 2000, and 2005, respectively.

He is currently a Designated Research Associate with the Institute of Industrial Science, The University of Tokyo. His research fields include the development of human-friendly motion control algorithms and assistive devices for people.

Dr. Oh is a member of the Institute of Electrical Engineers of Japan, the Society of Instrument and Control Engineers, and the Robotic Society of Japan.



**Yoichi Hori** (S'81–M'83–SM'00–F'05) received the B.S., M.S., and Ph.D. degrees in electrical engineering from The University of Tokyo, Tokyo, Japan, in 1978, 1980, and 1983, respectively.

In 1983, he joined the Department of Electrical Engineering, The University of Tokyo, as a Research Associate, where he later became an Assistant Professor, an Associate Professor, and, in 2000, a Professor. In 2002, he moved to the Institute of Industrial Science as a Professor in the Information and System Division and, in 2008, to the Department of Advanced Energy, Graduate School of Frontier Sciences, The University of Tokyo. During 1991–1992, he was a Visiting Researcher with the University of California, Berkeley. His research fields include control theory and its industrial applications to motion control, mechatronics, robotics, electric vehicles, etc.

Prof. Hori has been the Treasurer of the IEEE Japan Council and Tokyo Section since 2001. He was the recipient of the Best Paper Award from the IEEE TRANSACTIONS ON INDUSTRIAL ELECTRONICS in 1993 and 2001 and of the 2000 Best Paper Award from the Institute of Electrical Engineers of Japan (IEEJ). He is a member of the Society of Instrument and Control Engineers, the Robotics Society of Japan, the Japan Society of Mechanical Engineers, the Society of Automotive Engineers of Japan, etc. He is currently the President of the Industry Applications Society of the IEEJ, the President of the Capacitors Forum, and the Chairman of the Motor Technology Symposium of the Japan Management Association.



## Fault-tolerant traction control of electric vehicles

Jia-Sheng Hu<sup>a,\*</sup>, Dejun Yin<sup>b</sup>, Yoichi Hori<sup>c</sup>

<sup>a</sup> Department of Greenery, National University of Tainan, Tainan 700, Taiwan

<sup>b</sup> Electric Vehicle Laboratory, Keio University, Kanagawa 212-0054, Japan

<sup>c</sup> Department of Advanced Energy, University of Tokyo, Tokyo 153-8505, Japan

### ARTICLE INFO

#### Article history:

Received 18 January 2010

Accepted 19 November 2010

Available online 24 December 2010

#### Keywords:

Fault tolerance

Traction control

Electric vehicles

Anti-slip control

Disturbance estimation

### ABSTRACT

This paper investigates a new traction control approach that requires neither chassis velocity nor information about tire–road conditions. Plant fault subject to the uncertainties of the mathematical model and slightly sensor fault are concerned. For general traction control of vehicles, the variation of model behavior may break down the steering stability if the chassis velocity is not monitored. This paper presents a fault-tolerant approach based on the maximum transmissible torque estimation (MTTE) scheme which has the ability to prevent electric vehicles from skidding. A PI-type disturbance observer is employed to enhance the steering stability of the MTTE approach. This proposed approach does not require both the differentiator and the inversion of the controlled plant. Finally, illustrated examples are given for evaluating the fault-tolerant performance and feasibility of the presented anti-slip strategy.

© 2010 Elsevier Ltd. All rights reserved.

### 1. Introduction

As the development of technology continues to rapidly grow, control technology and daily life are becoming increasingly inter-related. However, unanticipated breakdowns can happen in any control system due to internal malfunctions or external distractions. Since the prices of most home electronic appliances are quite affordable, malfunctions can simply be solved by purchasing new ones; however, for complex control systems with greater consumer costs, the consequences of these passive solutions result in paying higher prices. For example, systems such as aircrafts, ships, satellites, nuclear power plants, space shuttles, and high-speed rails are all extremely high in manufacturing costs, and if malfunction happens and is not able to be eliminated or repaired, the resulting cost is tremendous. Traction control is an example. For passenger involved in electric automobile systems, traction control is a core for stabilizing the movements of automobiles. In addition to guaranteeing the safety of automobile systems in any driving conditions, one must also have adequate driving abilities. Under slippery, muddy, and flat tire conditions, wheel inertia changes and results in deteriorating controllability in traction control. Hence, research has been focusing on adopting robust control theory, which can endow electric vehicles with fault-tolerant performance. Fully electric vehicles powered by batteries can achieve quieter and pollution-free operation, which has offered a solution to next generation vehicles. Unlike internal combustion engine vehicles, electric vehicles use independently equipped motors to drive each

wheel. The independently equipped motors provide higher power/weight density, higher reliability for safety, and better dynamic performance. These aspects make it easy to estimate the driving or braking forces between tires and road surfaces in real time, which contributes a great deal to the application of new traction control strategies based on road condition estimation (Hori, 2004; He & Hori, 2006; Yang & Lo, 2008).

For advanced vehicles today, many technologies embedded in the micro-controller unit (MCU) enhance the vehicle stability and handling performance in critically dynamic situations. For example, the antilock braking system (ABS) (Patil, Longoria, & Limroth, 2003; Schinkel & Hunt, 2002), electronic differential (ED) (Tsai & Hu, 2007; Urakubo, Tsuchiya, & Tsujita, 2001), direct yaw-posture control (DYC) (Mizushima, Raksincharoensak, & Nagai, 2006; Tahami, Farhangi, & Kazemi, 2004), traction control (Bennett, Patton, & Daley, 1999; Poursamad & Montazeri, 2008), and so on, are all solutions implemented to improve both vehicle stability and handling. Traction control is often interested in the performance of anti-slip mechanisms. When a vehicle is driven or brakes on a slippery road, traction control must not only guarantee the effectiveness of the torque output to maintain vehicle stability, but also provide some information about tire–road conditions to other vehicle control systems. Moreover, a well-managed traction control system can cover the functions of ABS, because motors can generate deceleration and acceleration torque with equal ease (Mutoh, Hayano, Yahagi, & Takita, 2007). However, in practice, vehicle systems actually face challenges on restricting the development of traction control. For example, the real chassis velocity is not available, and the friction force which drives the vehicle is immeasurable (Baffet, Charara, & Lechner, 2009). In general, traction control systems that need chassis velocity, their non-driven wheels are utilized to provide an approximate vehicle velocity due to physical

\* Corresponding author. Tel.: +886 6 2605051; fax: +886 6 2602205.  
E-mail address: [jogson@ieee.org](mailto:jogson@ieee.org) (J.-S. Hu).

and economic reasons. However, this method is not applicable when the vehicle is accelerated by 4WD systems or decelerated by brakes equipped in these wheels. Other sensors, e.g., optical sensors (Saito, Fujimoto, & Noguchi, 2002), magnetic markers (Fujimoto, Saito, & Noguchi, 2004), etc., can also obtain chassis velocity. However, they are too sensitive and reliant on the driving environment or too expensive to be applied in actual vehicles. Some anti-slip control systems (Fujii & Fujimoto, 2007; Patil et al., 2003; Schinkel & Hunt, 2002) try to realize optimal slip-ratio controls according to the Magic Formula (Pacejka & Bakker, 1992). These systems not only need extra sensors for the acquisition of chassis velocity and/or acceleration, but are also more difficult to realize than expected. This is because the tuned algorithms and parameters for specific tire–road conditions cannot be adapted quickly enough to compensate the significant variation found in the instantaneous, immeasurable relationship between the slip ratio and the friction coefficient. In order to overcome these problems, the Model Following Control (MFC) approaches (Fujimoto et al., 2004; Sakai & Hori, 2001; Saito et al., 2002), which do not need information on chassis velocity or even acceleration sensors are proposed. In these systems, the controllers only make use of torque and wheel rotation as input variables for calculation. Fewer sensors contribute not only to lower costs, but also to increase reliability and independence from driving conditions, which are the most outstanding features of this class of control systems. Nevertheless, these control designs based on compensation have to consider the worst stability case to decide the compensation gain, which impairs the performance of anti-slip control. Furthermore, gain tuning for some specific tire–road conditions also limits the practicability of this method. Recently, the Maximum Transmissible Torque Estimation (MTTE) approach (Yin & Hori, 2008) that requires neither chassis velocity nor information about tire–road conditions, and therefore further upgrades the anti-slip performance of electric vehicles. In this system, use is only made of the torque reference and the wheel rotation speed to estimate the maximum transmissible torque to the road surface, then the estimated torque is applied for anti-slip control implementation. This approach also shows its benefits for vehicle mass-perturbed operation. Since a human being is involved in the operation of a vehicle, the total mass potentially varies with different drivers and passengers. Nevertheless, the MTTE approach is sensitive to the varying of wheel inertia. If the tires get flat, the anti-slip performance of MTTE will deteriorate gradually.

Model uncertainties are considered as systematic faults (Campos-Delgado, Martinez-Martinez, & Zhou, 2005; Patton, Frank, & Clark, 2000), and these faults are unpreventable and non-measurable in automobile control systems. Normally, due to the existence of different levels of faults in a general automobile control system, the anti-slip function of traction control will deteriorate and even cause malfunctions (Bennet et al., 1999). Additionally, feedback control is established upon the output measurement. Sensor faults deteriorating the measurement signals and increasing the instability. Therefore, a fine traction control of electric vehicles should equip those vehicles with fault-tolerant abilities. For example, different passengers have different

weights, and this causes the vehicle mass to be unpredictable. In addition, the wheel inertia changes because of abrasion, repairs, tire-flattening, and practical adhesion of mud and stones. For traction control, these two factors have significant impacts on anti-slip function in traction control. Therefore, to develop traction control with fault-tolerant techniques is practically competitive. This paper aims to make use of the advantages of electric vehicles to develop a new traction control approach with fault-tolerant performance and is structured as follows. Section 2 describes the MTTE approach for anti-slip control. Section 3 discusses the PI-type disturbance estimation in general state-space cases. Details of the proposed approach are presented in Section 4. The specification of the experimental vehicle is introduced in Section 5. Section 6 gives practical examples for evaluating the presented anti-slip strategy. Finally, Section 7 offers some concluding remarks.

## 2. MTTE-based anti-slip control

Consider a longitudinal motion of a four-wheeled vehicle, as depicted in Fig. 1; the dynamic differential equations for the longitudinal motion of the vehicle can be described as

$$J_w \dot{\omega} = T - rF_d \tag{1}$$

$$M \dot{V} = F_d - F_{dr} \tag{2}$$

$$V_w = r\omega \tag{3}$$

$$F_d(\lambda) = \mu N \tag{4}$$

where the definition of all parameters are listed in Table 1. Generally, the nonlinear interrelationships between the slip ratio  $\lambda$  and friction coefficient  $\mu$  formed by tire dynamics can be modeled by the widely adopted Magic Formula (Pacejka & Bakker, 1992) as shown in Fig. 2.

The concept of MTTE approach for vehicle anti-slip control is first proposed in the study of Yin and Hori (2008). As mentioned in

**Table 1**  
Parameter list.

Symbol	Definition
$J_w$	Wheel inertia
$V_w$	Wheel velocity (circumferential velocity)
$\omega$	Wheel rotation
$T$	Driving torque
$r$	Wheel radius
$F_d$	Friction force (driving force)
$M$	Vehicle MASS
$N$	Vehicle weight
$V$	Chassis velocity (vehicle velocity)
$F_{dr}$	Driving resistance
$\lambda$	Slip ratio
$\mu$	Friction coefficient

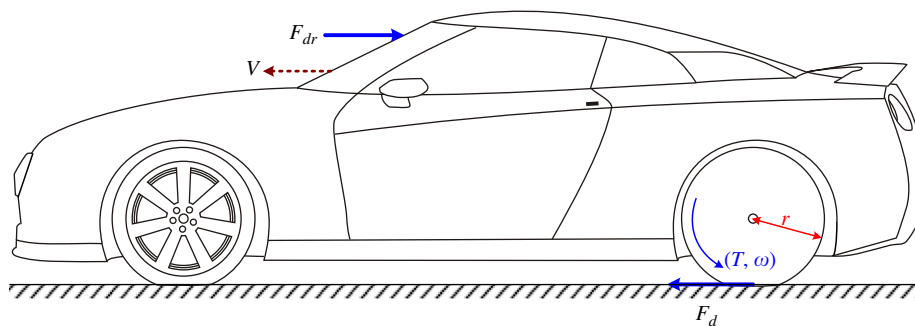


**Fig. 1.** Dynamic longitudinal model of vehicle.

Section 1, this approach shows its benefits for vehicle mass-perturbed operation. The MTTE approach can achieve an acceptable anti-slip control performance under common operation requirements. However, the MTTE approach is sensitive to varying wheel inertia. If the wheel inertia varies, the anti-slip performance of the MTTE will deteriorate gradually. This paper is devoted to improve the anti-slip performance of the MTTE approach under such concerned abnormal operations. A new MTTE control approach with fault-tolerant performance will be proposed in Section 4. Based on study of Yin and Hori (2008), the following considerations are concerned.

- (1) Whatever kind of tire–road condition the vehicle is driven on, the kinematic relationship between the wheel and the chassis is always fixed and known.
- (2) During the acceleration phase, considering stability and tire abrasion, well-managed control of the velocity difference between wheel and chassis is more important than the mere pursuit of absolute maximum acceleration.
- (3) If the wheel and the chassis accelerations are well-controlled, the difference between the wheel and the chassis velocities, i.e. the slip is also well-controlled.

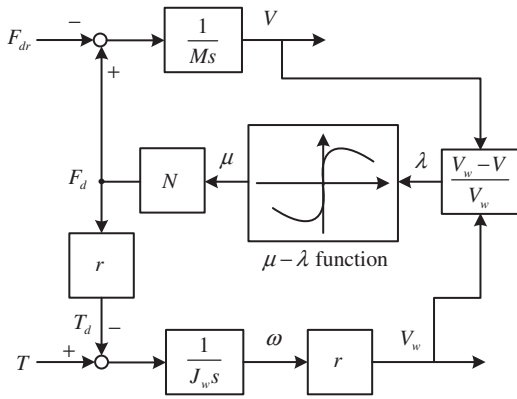


Fig. 2. One wheel of vehicle model with magic formula.

Here from (1) and (3), the driving force, i.e. the friction force between the tire and the road surface, can be calculated as

$$F_d = \frac{T}{r} - \frac{J_w \dot{V}_w}{r^2} \quad (5)$$

In normal road conditions,  $F_d$  is less than the maximum friction force from the road and increases as  $T$  goes up. However, when slip occurs,  $F_d$  cannot increase by  $T$ . Thus, when slip is occurring, the difference between the velocities of the wheel and the chassis become larger and larger, i.e. the acceleration of the wheel is larger than that of the chassis. Moreover, considering the  $\mu-\lambda$  relation described in the Magic Formula, an appropriate difference between chassis velocity and wheel velocity is necessary to support the desired friction force. From (2) and (5),  $\alpha$  is defined as

$$\alpha = \frac{\dot{V}}{\dot{V}_w}, \quad \text{i.e. } \alpha = \frac{(F_d - F_{dr})/M}{(T_{max} - rF_d)r/J_w} \quad (6)$$

where  $T_{max}$  is regarded as the maximum transmissible torque. It serves as a relaxation factor for smoothing the control system. In order to satisfy the condition that slip does not occur or become larger,  $\alpha$  should be close to 1. With a designated  $\alpha$ , when the vehicle encounters a slippery road,  $T_{max}$  must be reduced adaptively according to the decrease of  $F_d$ . Hence, if the friction force  $F_d$  is estimable, the maximum transmissible torque,  $T_{max}$  can be formulated as

$$T_{max} = \left( \frac{J_w}{\alpha M r^2} + 1 \right) r \hat{F}_d \quad (7)$$

This formula indicates that a given estimated friction force  $\hat{F}_d$  allows a certain maximum torque output from the wheel so as not to increase the slip. Hence, the proposed control scheme utilizes  $T_{max}$  to construct and constrain the driving torque  $T$  as

$$\begin{aligned} -|T_{max}| < T^* < |T_{max}|, \quad T &= T^* \\ T^* \geq |T_{max}|, \quad T &= |T_{max}| \\ T^* \leq -|T_{max}|, \quad T &= -|T_{max}| \end{aligned} \quad (8)$$

Note that from (2), it is clear that the driving resistance  $F_{dr}$  can be regarded as one of the perturbation sources of the dynamic vehicle mass  $M$ . Although the vehicle mass  $M$  can also be estimated online (Ikeda, Ono, & Aoki 1992; Vahidi, Stefanopoulou, & Peng, 2005;

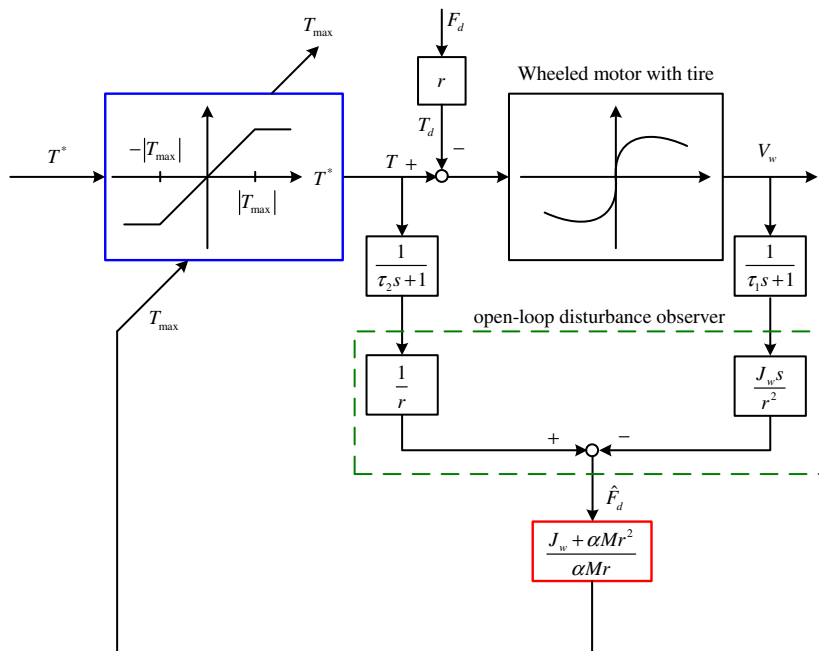


Fig. 3. Control system based on MTTE.

Winstead & Kolmanovsky, 2005), in this paper, it is assumed to be a nominal value.

Fig. 3 shows the main control scheme of the MTTE. As shown in Fig. 3, a limiter with a variable saturation value is expected to realize the control of driving torque according to the dynamic situation. The estimated disturbance force  $\hat{F}_d$  is driven from the model inversion of the controlled plant and driving torque  $T$ . Consequently, a differentiator is needed. Under normal conditions, the torque reference is expected to pass through the controller without any effect. Conversely, when on a slippery road, the controller can constrain the torque output to be close to  $T_{max}$ . Based on (7), an open-loop friction force estimator is employed based on the linear nominal model of the wheeled motor to produce the maximum transmissible torque. For practical convenience, two low-pass filters with the time constants  $\tau_1$  and  $\tau_2$ , respectively, are employed to smoothen the noises of digital signals and the differentiator which follows.

### 3. PI-type disturbance estimation in state-space form

As illustrated in Fig. 3, the MTTE approach uses an open-loop disturbance observer to estimate the friction force between the tire and road. In order to improve the anti-slip performance of the MTTE, a closed-loop disturbance observer is of interest. Conventional PI control approaches have been adopted in many industrial applications, in which the proportional (P) part provides a constant gain control and the integral (I) gain provides the stiffness to eliminate the DC drop. The PI-type compensator is utilized in the observer structure since it provides better robustness against model inaccuracies and step disturbances than the conventional Luenberger observer. It can estimate both the system states and external disturbances. In this paper, a PI-type disturbance observer (Tsai, Tseng, & Cheng, 2000) will be utilized in the MTTE scheme to enhance the anti-slip performance. In order to analyze the performance of the PI observer into general form, the PI-type disturbance estimator is formulated in state-space form in the following.

Consider the state-space realization of a linear system given by

$$\dot{x} = Ax + Bu + BT_d \quad y = Cx \quad (9)$$

where the internal state  $x \in \mathbb{R}^n$ , input  $u \in \mathbb{R}^r$  and output  $y \in \mathbb{R}^m$ , respectively, as well as  $T_d \in \mathbb{R}^p$  denote the external disturbance. Herein, one assumes that all of the initial state conditions are zero and  $B_d \in \mathbb{R}^{n \times p}$  is of full-column rank so that

$$p \leq m \quad (10)$$

For the nominal case, a full-order PI observer shown in Fig. 4, is given by

$$\begin{aligned} \dot{\hat{x}} &= (A-HC)\hat{x} + B_d\hat{x}_i + Bu + Hy \\ \dot{\hat{x}}_i &= -K\hat{x} + Ky \quad \hat{T}_d = \hat{x}_i \end{aligned} \quad (11)$$

where  $H \in \mathbb{R}^{n \times m}$  and  $K \in \mathbb{R}^{p \times m}$  are observer gains. It yields

$$\begin{aligned} \begin{bmatrix} \dot{\hat{x}} \\ \dot{\hat{x}}_i \end{bmatrix} &= \begin{bmatrix} A & 0 & 0 \\ HC & A-HC & B_d \\ KC & -KC & 0 \end{bmatrix} \begin{bmatrix} \hat{x} \\ \hat{x}_i \end{bmatrix} + \begin{bmatrix} B & B_d \\ B & 0 \\ 0 & 0 \end{bmatrix} \begin{bmatrix} u \\ T_d \end{bmatrix} \\ \hat{T}_d &= \begin{bmatrix} 0 & 0 & I_p \end{bmatrix} \begin{bmatrix} \hat{x} \\ \hat{x}_i \end{bmatrix} \end{aligned} \quad (12)$$

Define  $x_e = \hat{x} - x$  and  $\hat{x}_i = \hat{T}_d$ . First, consider the disturbance-free case, i.e.,  $T_d = 0$ . It can be found from (9) and (11) that

$$\dot{x}_e = \hat{\dot{x}} - \dot{x} = (A-HC)x_e + B_d\hat{T}_d \quad (13)$$

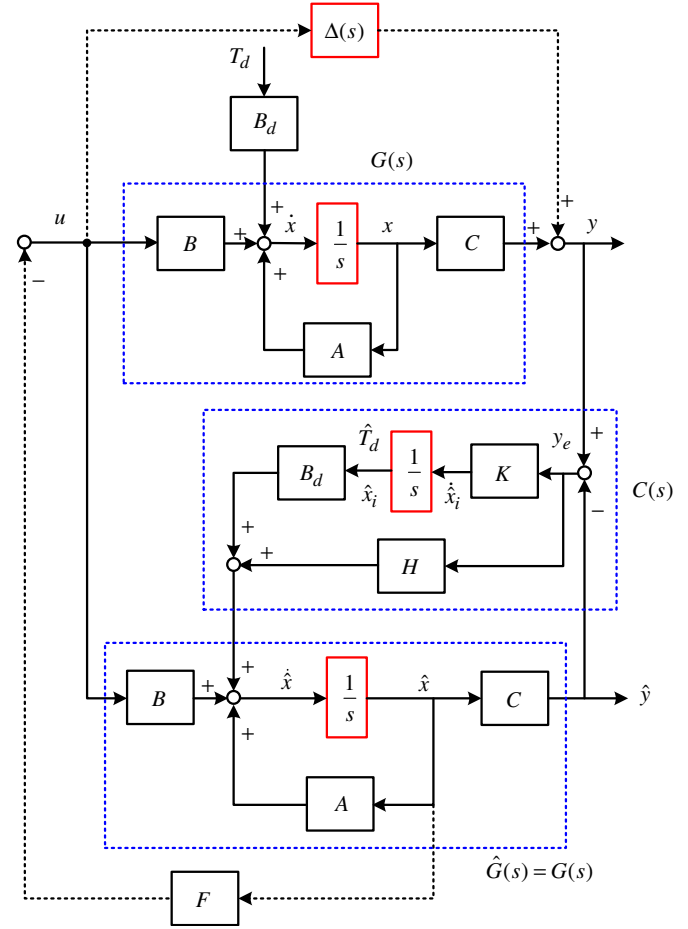


Fig. 4. PI observer.

and

$$\dot{\hat{x}}_i = \dot{\hat{T}}_d = -KCx_e \quad (14)$$

Taking the Laplace transformation from (13) and (14) gives

$$\hat{x}_e - x = [sI_n - (A-HC)]^{-1} B_d \hat{T}_d \quad (15)$$

$$\hat{T}_d = -(sI_p)^{-1} KC(\hat{x} - x) \quad (16)$$

Assume that P-gain  $H$ , of the observer is chosen such that  $A-HC$  is a Hurwitz matrix and I-gain  $K$  is chosen such that  $KC$  is of full-row rank. Substituting (16) into (15) will yield

$$\begin{aligned} \{I_n + [sI_n - (A-HC)]^{-1} B_d (sI_p)^{-1} KC\} \hat{x} \\ = \{I_n + [sI_n - (A-HC)]^{-1} B_d (sI_p)^{-1} KC\} x \end{aligned} \quad (17)$$

i.e.,  $x = \hat{x}$ . Consider the PI observer with disturbance  $T_d \neq 0$ . From (9) and (11) one obtains

$$\dot{x}_e = \hat{\dot{x}} - \dot{x} = (A-HC)x_e + B_d(\hat{T}_d - T_d) \quad (18)$$

Rearranging (18) yields

$$\hat{\dot{x}} = x + [sI_n - (A-HC)]^{-1} B_d(\hat{T}_d - T_d) \quad (19)$$

Substituting (16) into (19) yields

$$\hat{T}_d = \{sI_p + KC[sI_n - (A-HC)]^{-1} B_d\}^{-1} KC[sI_n - (A-HC)]^{-1} B_d T_d \quad (20)$$

Then one has  $\hat{T}_d = T_d$  in the steady state (i.e.  $s=0$ ). Moreover, for the case of  $\hat{T}_d = T_d$ , it also implies  $\hat{x} = x$  from (19). Hence, the PI observer can be used to estimate both the system states and

disturbances. Let

$$A_x = \begin{bmatrix} A & B_d \\ 0 & 0 \end{bmatrix}, \quad B_x = \begin{bmatrix} B \\ 0 \end{bmatrix}, \quad H_x = \begin{bmatrix} H \\ K \end{bmatrix}, \quad C_x = [C \quad 0], \quad F_x = [F \quad 0] \quad (21)$$

Then the control system can be represented by

$$\begin{bmatrix} \dot{\hat{x}} \\ \dot{\hat{x}}_i \end{bmatrix} = A_x \begin{bmatrix} \hat{x} \\ \hat{x}_i \end{bmatrix} + B_x u + H_x \left( y - C_x \begin{bmatrix} \hat{x} \\ \hat{x}_i \end{bmatrix} \right)$$

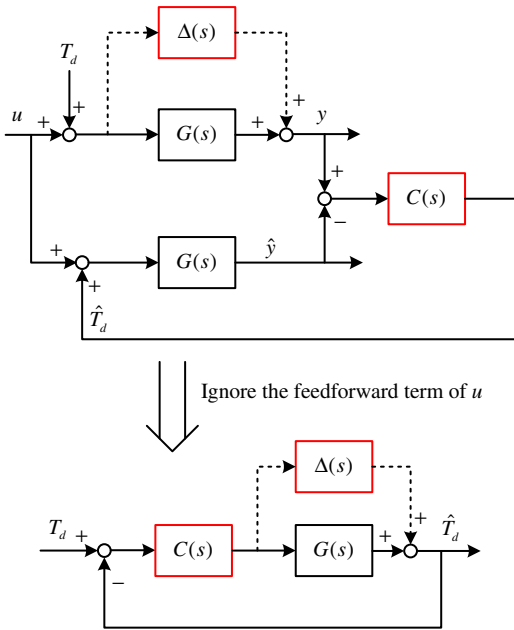


Fig. 5. Disturbance estimation with model uncertainty.

$$u = -F_x \begin{bmatrix} \hat{x} \\ \hat{x}_i \end{bmatrix} \quad (22)$$

As  $(C, A)$  is observable and

$$\text{rank} \left( \begin{bmatrix} A & B_d \\ C & 0 \end{bmatrix} \right) = n + p \quad (23)$$

then one knows from Duan, Liu, and Thompson (2001) that  $(C_x, A_x)$  is observable. This implies that the observer gains  $(H, K)$  can be determined. Readers can refer to Hu, Hu, and Cheng (2009) for the PI observer design of merely detectable systems. Note that the observer poles are often chosen faster than the state feedback controller by a factor of 2–6.

Considering to the affection of model uncertainty of  $\Delta(s)$ , Fig. 4 can be simplified into the upper part of Fig. 5. Additionally, without considering the feedforward term of  $u$ , the upper part of Fig. 5 can be equivalent to its lower part. It is obvious that, the PI compensator  $C(s)$  in the closed-loop structure offers a mechanism to minimize the modeling error caused by  $\Delta(s)$  in a short time. Consequently, the PI compensator enhances the robust estimation performance against modeling error.

#### 4. Proposed fault-tolerant anti-slip control strategy

Model uncertainty and sensor fault are the main faults concerned in this study. The MTTE scheme has proved its robustness to the varying of vehicle mass  $M$  in study of Hu, Yin, Hori, and Hu (2009). Readers can refer to the discussion for further comprehension. Fig. 6 illustrates the proposed fault-tolerant MTTE control system which incorporates the PI observer into Fig. 6 with a friction detection unit. The disturbance torque  $T_d$  comes from the operation friction. When the vehicle is operated on a slippery road, it causes  $T_d$  to become very small, and due to that, the tires cannot provide sufficient friction.

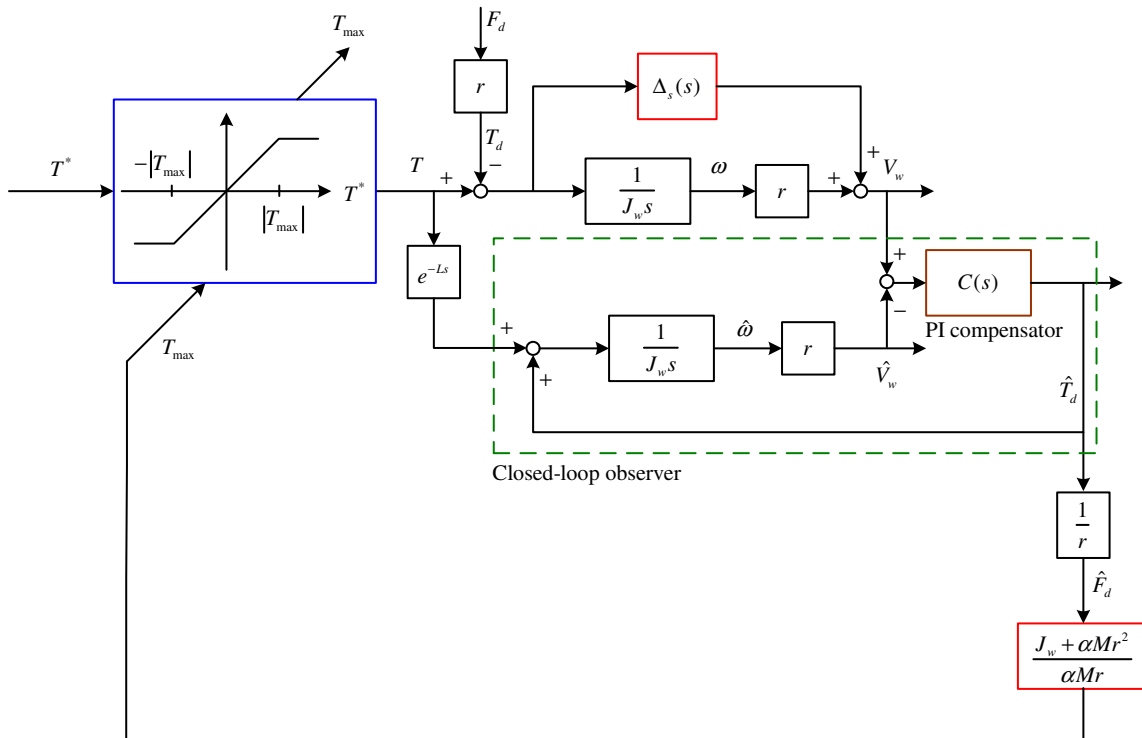


Fig. 6. Proposed robust MTTE control system.

Skidding often happens in braking and racing of an operated vehicle when tire adhesion cannot firmly grip the surface of the road. This phenomenon is often referred to as the magic formula (i.e., the  $\mu-\lambda$  relation). However, the  $\mu-\lambda$  relation is immeasurable in real time. Therefore, in the proposed approach, the nonlinear behavior between the tire and road (i.e., the magic formula) is regarded as an uncertain source which deteriorates the steering stability and causes some abnormal malfunction when derived. In Fig. 6, this deterioration is regarded as one source of wheel inertia perturbations.

Faults such as noise will always exist in a regular process; however, not all faults will cause the system to fail. To design a robust strategy against different faults, the model uncertainties and system faults have to be integrated (Campos-Delgado et al., 2005). According to the investigation of Hu and Tsai (2008), the sensor fault in a wheel motor can be considered as an additive disturbance (noise) of the actual output measurement. Hence in this study, the model uncertainty and sensor fault are integrated as  $\Delta_s(s)$  in the proposed system, which has significant effects to the vehicle skidding. Here, let  $\Delta_s(s)$  denote the integrated faults caused by model uncertainty and sensor fault (Campos-Delgado et al., 2005). The uncertain dynamics of  $\Delta_s(s)$  can also represent different slippery driving situations. When  $\Delta_s(s) \approx 0$ , it means the driving condition is normal. For a slippery road surface,  $\Delta_s(s) \neq 0$ . It is commonly known that an open-loop disturbance observer has the following drawbacks:

- (1) An open-loop disturbance observer does not have a feedback mechanism to compensate for the modeling errors. Therefore, its robustness is often not sufficient.
- (2) An open-loop disturbance observer utilizes the inversion of a controlled plant to acquire the disturbance estimation information. However, sometimes the inversion is not easy to carry out.

The PI observer as presented in Section 3 is employed for estimating the disturbance torque, especially when skidding occurs. As discussed in Section 3, the closed-loop dynamics of the PI observer can guarantee certain robustness for disturbance torque estimation. Due to the closed-loop dynamics of the PI observer, the estimated disturbance torque  $\hat{T}_d$  in the proposed system can enhance the performance of MTTE against skidding. It also offers better robustness for parameter variation. Unlike the conventional MTTE approach, the proposed approach does not need to utilize the differentiator.

The proposed system is fault-tolerant against model uncertainty and slightly sensor fault. Its verification is discussed in the following. Fig. 7 shows a simplified linear model of the proposed scheme where  $J_{wn}$  denotes the nominal value of wheel inertia  $J_w$  and  $\Delta_s(s)$  stands for the slippery perturbation caused by model uncertainty and sensor fault. Formulate the proposed system into the standard control configuration as Fig. 8, system robustness is revealed by determining  $\|T_{zw}(s)\|_\infty \leq \gamma$  such that  $\|\Delta_s(s)\|_\infty < (1/\gamma)$ . As mentioned in Sections 2 and 3, a PI compensator is employed in the closed-loop observer stage as

$$C(s) = K_p + K_i \frac{1}{s} \tag{24}$$

Note that the dynamics of the delay element can be approximated as

$$e^{-Ls} \approx \frac{1}{1+Ls} \tag{25}$$

The delay time in a practical system is less than 30 ms. Hence it has higher bandwidth of dynamics than the vehicle system. Consequently, it can be omitted in the formulation. Then from

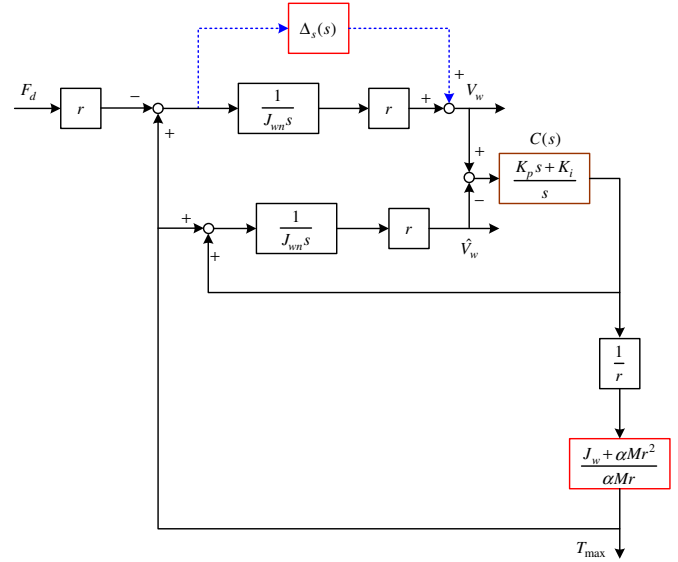


Fig. 7. A simplified scheme of proposed control.

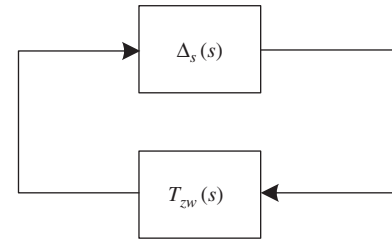


Fig. 8. Standard control configuration.

Fig. 7, one has

$$T_{zw}(s) = \frac{T_{max}}{F_d} = -\frac{K_p(J_{wn} + \alpha Mr^2)s + K_i(J_{wn} + \alpha Mr^2)}{J_{wn}\alpha Ms^2 + K_p\alpha Mr s + K_i\alpha Mr} \tag{26}$$

As mentioned in Section 2,  $\alpha$  should be close to 1. Therefore, if  $\alpha Mr^2 \gg J_{wn}$

$$\tag{27}$$

then (26) can be simplified as

$$\frac{T_{max}}{F_d} = -\frac{K_p r^2 s + K_i r^2}{J_{wn} s^2 + K_p r s + K_i r}. \tag{28}$$

Convincingly, the condition of (27) is satisfied in most commercial vehicles. Accordingly, when the anti-slip system confronts the Type I (Step-type) or Type II (Ramp-type) disturbances (Franklin, Powell, & Emami-Naeini, 1995), Eq. (28) can be further simplified as

$$\frac{T_{max}}{F_d} \approx -r \tag{29}$$

This means the system of  $\|T_{zw}\|_\infty \approx r$  is stable if and only if  $\|\Delta_s(s)\|_\infty < (1/r)$ .

Based on the investigation of Hu and Tsai (2008), sensor fault of wheel motor can be regarded as perturbations of wheel inertia. Hence the perturbation caused by  $\Delta J_w$  to the proposed system can be considered as the combination of sensor fault and modeling inaccuracy of actual wheel inertia. Now consider the effect of inertia uncertainty  $\Delta J_w$  to real driving. It yields  $J_w = \Delta J_w + J_{wn}$ . Since the vehicle mass is larger than the wheels, in most commercial vehicles,  $\alpha Mr^2 \gg \Delta J_w + J_{wn}$  is always upheld. Moreover, the mass of passengers can also increase  $M$  to satisfy the condition of (27). From (28), it is obvious that the PI observer dominates the performance

of the proposed system. Under proper designed PI gains and the condition of (27), the varying of  $J_w$  caused by  $\Delta J_w$  cannot affect the anti-slip control system so much. Hence the proposed control approach for vehicle traction control can achieve insensitive performance to the varying of  $J_w$ .

**5. Experimental electric vehicle**

In order to evaluate the proposed traction control strategy, a commercial electric vehicle, COMS3, which is assembled by TOYOTA Auto Body Co. Ltd. shown in Fig. 9, was modified to carry out the experiments. In the modified car, each rear wheel is equipped with an Interior Permanent Magnet Synchronous Motor (IPMSM) and can be controlled independently. As illustrated in

**Table 2**  
Specification of COMS3.

Total weight	360 kg
Maximum power/per wheel	2000 W
Maximum torque/per wheel	100 Nm
Wheel inertia/per wheel	0.5 kg m <sup>2</sup>
Wheel radius	0.22 m
Sampling time	0.01 s
Controller	Pentium M 1.8G with 1 GB RAM using Linux
A/D and D/A	12 bits
Shaft encoder	36 pulses/round



Fig. 9. Experimental electric vehicle: COMS3.



Fig. 11. Setting of slippery road experiment.

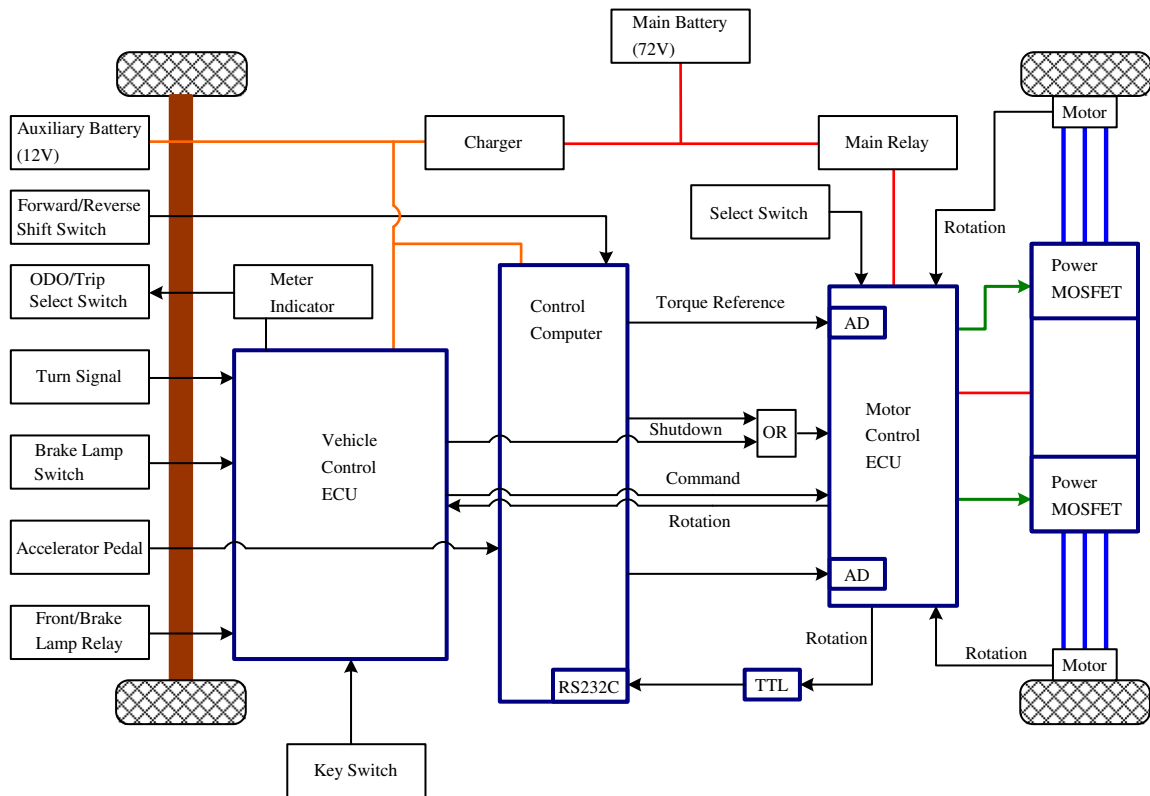


Fig. 10. Schematics of COMS3 electrical system.



Fig. 10, a control computer is equipped to take the place of the previous Electronic Control Unit (ECU) to operate the motion control. The computer receives the acceleration reference signal from the acceleration pedal sensor, the forward/backward signal from the shift switch and the wheel rotation from the inverter. Then, the corresponding calculated torque references of the left and the right rear wheels are independently sent to the inverter by two analog transmission lines. Table 2 lists the main specifications.

The most outstanding feature of the modified inverter is that the minimum refresh time of the torque reference decreased from 10 to 2 ms, outperforming its commercial counterpart, which makes it possible to actualize the torque reference more quickly and accurately. The increased maximum rate of change of the torque

reference permits faster torque variation for high performance motion control.

### 6. Examples and discussions

In this section, the proposed traction control strategy is evaluated practically on COMS3. In the experiments, the relaxation factor of MTTE scheme is set as  $\alpha = 0.9$ . The time constants of LPFs in the comparison experiment are set as  $\tau_1 = \tau_2 = 0.05$ . It is known that the passenger's weight varies; hence, this paper adopts the PI compensator as the kernel of disturbance estimation. The PI gains of the PI compensator (24) are set as  $K_p = 70$  and  $K_i = 60$ . As shown in

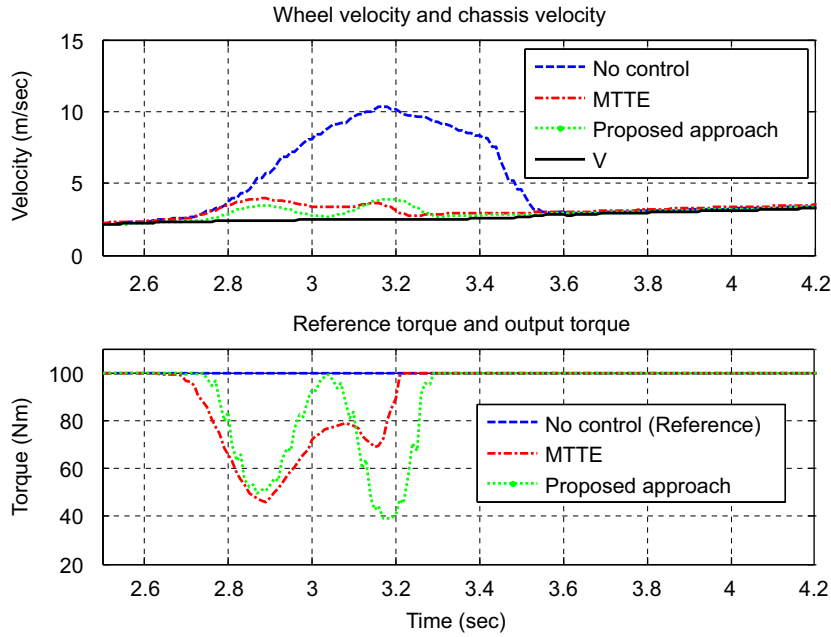


Fig. 12. Practical comparisons between MTTE and proposed approach to nominal  $J_w$ .

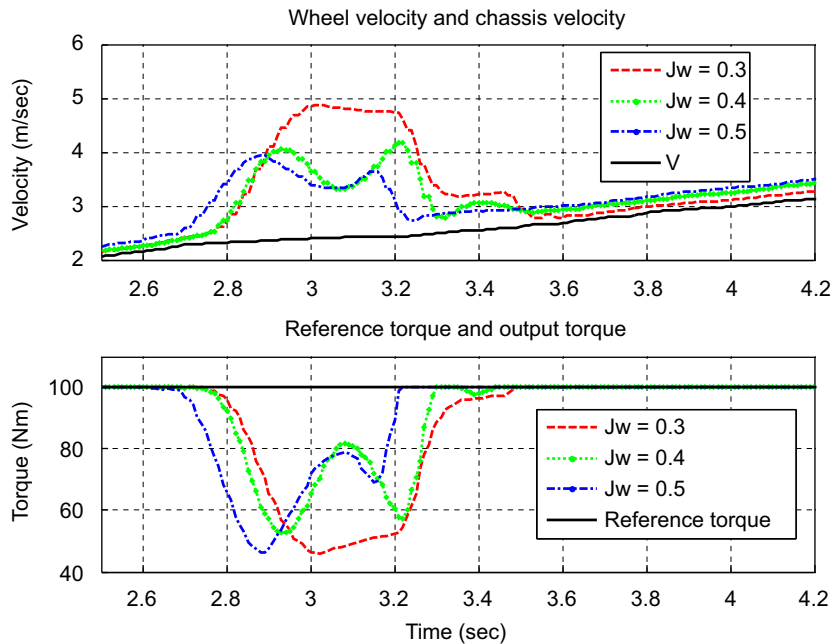


Fig. 13. Experimental results of MTTE approach to different  $J_w$ .

Fig. 11, the slippery road was constructed by an acrylic sheet with a length of 1.2 m and lubricated with water. The initial velocity of the vehicle was set higher than 1 m/s to avoid the immeasurable zone of the shaft sensors installed in the wheels. As mentioned in Section 4, the driving torque delay in the proposed approach is exploited to adjust the phase of the estimated disturbance. The anti-slip performance of MTTE deteriorates if the phase of estimated disturbance shifts so much. Additionally, the digital delay of the motor driver has significant effects on the closed-loop observers and the proposed scheme. According to the practical tests of study of Hu, Yin et al. (2009), with proper driving torque delay of  $L$  as 20 ms, the proposed approach can achieve a feasible performance. Hence, in the following, all experiments of the proposed approach utilize this delay parameter.

The MTTE-based schemes can prevent vehicle skid. These approaches compensate the reference torque into a limited value when encountering a slippery road. Based on the experimental result of Fig. 12, the reference torque of MTTE-based approaches is constrained without divergence. Fig. 12 is evaluated under the nominal wheel inertia. As can be seen in this figure, both the MTTE and proposed approaches yield marked anti-slip performances. Nevertheless, as indicated in the practical results in Fig. 13, the anti-slip performance of MTTE impairs with the variance of wheel inertia. In addition, Fig. 14 shows the same test using the proposed approach. Apparently, the proposed approach overcomes this problem. The proposed approach has better fault-tolerant anti-slip performance against varying wheel inertia in real time.

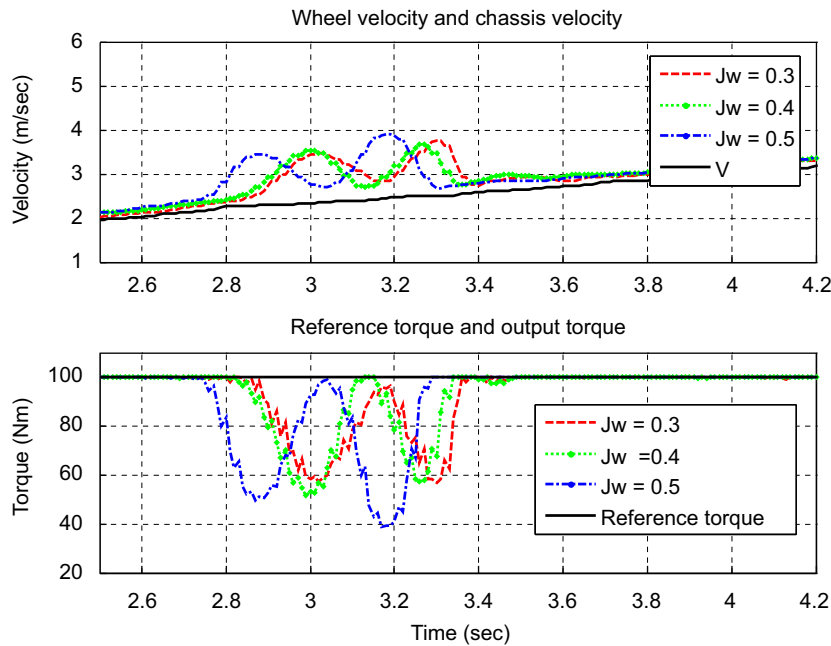


Fig. 14. Experimental results of proposed approach to different  $J_w$ .

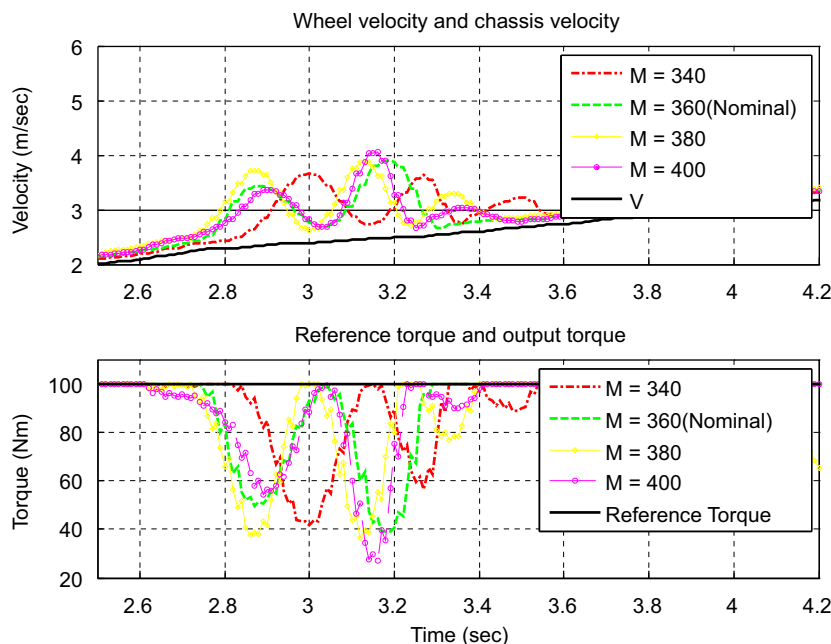


Fig. 15. Experimental results of proposed approach to different  $M$ .

Fig. 15 shows the performance testing of the proposed approach against different vehicle mass. It is unpredictable that different passengers will change the mass of the whole vehicle. Fig. 15 shows its practical performance. It is no doubt that the proposed approach is robust in spite of different passengers sitting in the vehicle. As illustrated in Fig. 15, the proposed traction control validates anti-slip in different vehicle masses. From Figs. 14 and 15, it is evident that the proposed traction control approach has consistent performance to the variation of wheel inertia  $J_w$  and vehicle mass  $M$ . As shown in these figures, the proposed anti-slip system offers an effective performance in maintaining the driving stability under more probable, real-life situations, and therefore the steering safety of the electric vehicles can be further enhanced.

## 7. Conclusions

This paper has presented a fault-tolerant traction control with robust performance in electric vehicles. This approach endowed the conventional MTTE approach with a fault-tolerant ability for preventing skidding of electric vehicles in many common steering situations. It provided a good basis for anti-slip control as well as other more advanced motion control systems in vehicles. A PI-type disturbance observer which enhances the friction torque estimation has been employed in the proposed scheme. The phase lag problem of disturbance estimation to closed-loop observer and digital implementation has been overcome by the driving torque delay. It has been verified that the proposed traction control has benefits such as preventing possible failures in a slippery driving situation. The experimental results have substantiated that the proposed approach has the ability to improve the safety of electric vehicles in practice.

## Acknowledgments

This work was supported by National Science Council (NSC) of Taiwan, under projects NSC 99-2218-E-024-001 and NSC 98-2914-I-006-018. The authors would like to thank Ms. Chia-Chen Lai for her assistance during this work.

## References

- Baffet, G., Charara, A., & Lechner, D. (2009). Estimation of vehicle sideslip, tire force and wheel cornering stiffness. *Control Engineering Practice*, 17, 1255–1264.
- Bennett, S. M., Patton, R. J., & Daley, S. (1999). Sensor fault-tolerant control of a rail traction drive. *Control Engineering Practice*, 7, 217–225.
- Campos-Delgado, D. U., Martinez-Martinez, S., & Zhou, K. (2005). Integrated fault-tolerant scheme for a dc speed drive. *IEEE Transaction on Mechatronics*, 10, 419–427.
- Duan, G.-R., Liu, G.-P., & Thompson, S. (2001). Eigenstructure assignment design for proportional-integral observers: Continuous-time case. *IEE Proceedings of the Control Theory Application*, 148, 263–267.
- Franklin, G. F., Powell, J. D., & Emami-Naeini, A. (1995). *Feedback control of dynamic systems*. New York: Addison Wesley.
- Fujii, K., & Fujimoto, H. (2007). Traction control based on slip ratio estimation without detecting vehicle speed for electric vehicle. In *Proceedings of fourth power conversion conference*, Nagoya, Japan.
- Fujimoto, H., Saito, T., & Noguchi, T. (2004). Motion stabilization control of electric vehicle under snowy conditions based on yaw-moment observer. In *Proceedings of IEEE international workshop on advanced motion control*, Kawasaki, Japan.
- He, P., & Hori, Y. (2006). Optimum traction force distribution for stability improvement of 4WD EV in critical driving condition. In *Proceedings of IEEE international workshop on advanced motion control*, Istanbul, Turkey.
- Hori, Y. (2004). Future vehicle driven by electricity and Control-research on four-wheel-motored "UOT electric march II". *IEEE Transaction on Industrial Electronics*, 51, 954–962.
- Hu, J.-S., Hu, F.-R., & Cheng, M.-Y. (2009). A partial pole placement approach to proportional-integral observer design. *Proceedings of the Institution of Mechanical Engineers, Part I, Journal of Systems and Control Engineering*, 23, 253–262.
- Hu, J.-S., & Tsai, M.-C. (2008). Design of robust stabilization and fault diagnosis for an auto-balancing two-wheeled cart. *Advanced Robotics*, 22, 319–338.
- Hu, J.-S., Yin, D., Hori, Y., & Hu, F.-R. (2009). A new MTTE methodology for electric vehicle traction control. In *Proceedings of the 12th international conference on electrical machines and systems*, Tokyo, Japan.
- Ikeda, M., Ono, T., & Aoki, N. (1992). Dynamic mass measurement of moving vehicles. *Transactions of the Society of Instrument and Control Engineers*, 28, 50–58.
- Mizushima, T., Raksincharoensak, P., & Nagai, M. (2006). Direct yaw-moment control adapted to driver behavior recognition. In *Proceedings of SICE-ICASE international joint conference*, Busan, Korea.
- Mutoh, N., Hayano, Y., Yahagi, H., & Takita, K. (2007). Electric braking control methods for electric vehicles with independently driven front and rear wheels. *IEEE Transaction on Industrial Electronics*, 54, 1168–1176.
- Pacejka, H. B., & Bakker, E. (1992). The magic formula tyre model. *Vehicle System Dynamics*, 21, 1–18.
- Patil, C.B., Longoria, R.G., & Limroth, J. (2003). Control prototyping for an anti-lock braking control system on a scaled vehicle. In *Proceedings of the IEEE conference on decision and control*, Hawaii, USA.
- Patton, R. J., Frank, P. M., & Clark, R. N. (2000). *Issues of fault diagnosis for dynamic systems*. New York: Springer.
- Poursamad, A., & Montazeri, M. (2008). Design of genetic-fuzzy control strategy for parallel hybrid electric vehicles. *Control Engineering Practice*, 16, 861–873.
- Saito, T., Fujimoto, H., & Noguchi, T. (2002). Yaw-moment stabilization control of small electric vehicle. In *Proceedings of the IEEJ technical meeting on industrial instrumentation and control*, Tokyo, Japan.
- Sakai, S., & Hori, Y. (2001). Advantage of electric motor for anti skid control of electric vehicle. *European Power Electronics Journal*, 11, 26–32.
- Schinkel, M., & Hunt, K. (2002). Anti-lock braking control using a sliding mode like approach. In *Proceedings of the American control conference*, Anchorage, USA.
- Tahami, F., Farhangi, S., & Kazemi, R. (2004). A fuzzy logic direct yaw-moment control system for all-wheel-drive electric vehicles. *Vehicle System Dynamics*, 41, 203–221.
- Tsai, M.-C., & Hu, J.-S. (2007). Pilot control of an auto-balancing two-wheeled cart. *Advanced Robotics*, 21, 817–827.
- Tsai, M.-C., Tseng, E.-C., & Cheng, M.-Y. (2000). Design of a torque observer for detecting abnormal load. *Control Engineering Practice*, 8, 259–269.
- Urakubo, T., Tsuchiya, K., & Tsujita, K. (2001T). Motion control of a two-wheeled mobile robot. *Advanced Robotics*, 15, 711–728.
- Vahidi, A., Stefanopoulou, A., & Peng, H. (2005). Recursive least squares with forgetting for online estimation of vehicle mass and road grade: theory and experiments. *Vehicle System Dynamics*, 43, 31–55.
- Winstead, V., & Kolmanovsky, I.V. (2005). Estimation of road grade and vehicle mass via model predictive control. In *Proceedings of IEEE conference on control applications*, Toronto, Canada.
- Yang, Y.-P., & Lo, C.-P. (2008). Current distribution control of dual directly driven wheel motors for electric vehicles. *Control Engineering Practice*, 16, 1285–1292.
- Yin, D., & Hori, Y. (2008). A new approach to traction control of EV based on maximum effective torque estimation. In *Proceedings of the 34th annual conference of the IEEE industrial electronics society*, Florida, USA.

BY JIA-SHENG HU, DEJUN YIN,  
YOICHI HORI, & FENG-RUNG HU

**I**N MOTION CONTROL OF electric vehicles (EVs), the undetectable road conditions and varying vehicle parameters challenge the steering ability and validity. This article investigates a new traction control (TC) approach that uses the maximum transmissible torque estimation (MTTE) scheme to carry out the antislip control of EVs. A closed-loop disturbance observer is employed to enhance the steering stability and to improve the robustness on perturbation in wheel inertia of the MTTE approach. This proposed scheme, which contains the closed-loop friction torque estimator, does not require the use of any differentiator. Additionally, the inversion of the controlled plant is unnecessary. The real experiment demonstrated the effectiveness and feasibility of the presented antislip strategy.

### Overuse of Petrochemical Energy

From the beginning of the 21st century, industrial engineering has entered into a period of rapid expansion and development. The Earth's



© COMSTOCK, PHOTODISC

# ELECTRIC VEHICLE TRACTION CONTROL

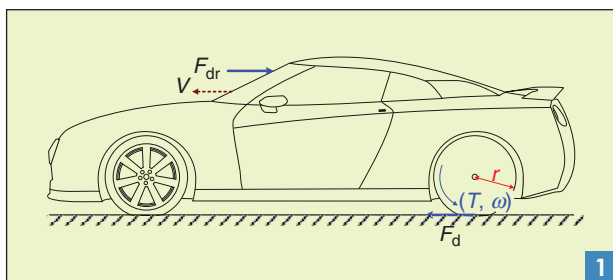
A new MTTE methodology

Digital Object Identifier 10.1109/MIAS.2011.2175519  
Date of publication: 23 December 2011

limited petrochemical resources have been overused, and, consequently, the price of oil has risen in recent years. Apparently, the worst consequences of overusing petrochemical energy are air pollution problems and the greenhouse effect, where both are increasingly causing serious consequences. To reduce our dependence on petrochemical resources and decrease the deterioration of the Earth's environment, the United Nations (UN) passed the Kyoto Protocol [1] in 1997. Basically, the Kyoto Protocol progressively restricts the emissions of carbon dioxide (CO<sub>2</sub>) in every industrialized country. Consequently, this protocol has resulted in a massive impact on vehicle engineering. EVs that are completely powered by batteries can achieve quieter and pollution-free operation and have offered a solution for pollution. Unlike internal combustion engine vehicles, EVs use independently equipped motors to drive each wheel. The individual output torque of the motor can be obtained from the motor current. This aspect makes it easy to estimate the driving or braking forces between tires and road surfaces in real time, which contributes a great deal to the application of new control strategies based on road condition estimation. The independently equipped motors provide higher power/weight density, higher reliability for safety, and better dynamic performance [2]–[4].

For advanced vehicles today, many technologies embedded in the microcontroller unit enhance vehicle stability and handling performance in critically dynamic situations. For example, the antilock braking system (ABS) [5], [6], electronic differential [5], [7], [8], direct yaw-posture control [9], [10], and TC [2] are the measures implemented to improve both vehicle stability and handling. TC maintains the performance of antislip mechanisms. When a vehicle is driven or brakes on a slippery road, TC must not only guarantee the effectiveness of the torque output to maintain vehicle stability but also provide some information about tire-road conditions to other vehicle control systems. Moreover, a well-managed TC system can cover the functions of ABSs because motors can generate deceleration torque as easily as acceleration torque [11].

However, in practice, vehicle systems face the challenge of restricting the development of TC. For example, the real chassis velocity is not available, and the friction force that drives the vehicle is immeasurable. In general, TC systems that need chassis velocity, the nondriven wheels, are used to provide an approximate vehicle velocity due to physical and economic reasons. However, this method is not applicable when the vehicle is accelerated by four-wheel drive systems or decelerated by brakes equipped in these wheels. For this reason, the accelerometer measurement is also used to calculate the velocity value, but it cannot avoid offset and error



**A dynamic longitudinal model of a vehicle.**

problems. Other sensors, e.g., optical sensors [12] and sensors of magnetic markers [13], can also obtain chassis velocity. However, they are too sensitive and reliant on the driving environment or too expensive to be applied in actual vehicles.

Some antislip control systems [5], [6], [14] try to realize optimal slip-ratio controls according to the magic formula [15]. These systems not only need extra sensors for the acquisition of chassis velocity or acceleration but also are more difficult to realize than expected. This is because the tuned algorithms and parameters for the specific tire-road conditions cannot be adapted quickly enough to compensate for the significant variation found in the instantaneous, immeasurable relationship between the slip ratio and the friction coefficient. To overcome these problems, the model-following control approaches [12], [13], [16] do not need information on chassis velocity, or even, acceleration sensors are proposed. In these systems, the controllers only make use of torque and wheel rotation as input variables for calculation. Fewer sensors contribute not only to lowering costs but also to increasing reliability and independence from driving conditions, which are the most outstanding features of this class of control systems. Nevertheless, these control designs based on compensation have to consider the worst stability case to decide the compensation gain, which impairs the performance of antislip control. Furthermore, gain tuning for some specific tire-road conditions also limits the practicability of this method. Recently, the MTTE approach [17] that requires neither chassis velocity nor information about tire-road conditions further upgrades the antislip performance of EVs. In this system, the usage is only made for the torque reference and the wheel rotation to estimate the maximum transmissible torque to the road surface, and then, the estimated torque is applied for antislip control implementation. This approach also shows its benefits for vehicle mass-perturbed operation. Since a human being is involved in the operation of a vehicle, the total mass potentially varies with different drivers and passengers. However, the MTTE approach is sensitive when the wheel inertia varies. In this case, such as getting flat tires or adhering to foreign masters, the antislip performance of the MTTE approach will deteriorate gradually.

### MTTE Approach for Antislip Control

Considering a longitudinal motion of a four-wheeled vehicle, as depicted in Figure 1, the dynamic differential equations for the longitudinal motion of the vehicle can be described as

$$J_w \dot{\omega} = T - rF_d, \quad (1)$$

$$M\dot{V} = F_d - F_{dr}, \quad (2)$$

$$V_w = r\omega, \quad (3)$$

$$F_d(\lambda) = \mu N, \quad (4)$$

where the definitions of the parameters are listed in Table 1. Generally, the nonlinear interrelationships between the slip ratio  $\lambda$  and friction coefficient  $\mu$  formed by the tire's dynamics can be modeled by the widely adopted magic formula [15] shown in Figure 2.

The concept of MTTE approach for vehicle antislip control is first introduced in [17]. Readers can refer to [17] for

the stability analysis and performance test of the MTTE. As mentioned earlier, this approach shows its benefits for vehicle mass-perturbed operation. The MTTE approach can achieve an acceptable antislip control performance under common operation requirements. However, the MTTE approach is sensitive when the wheel inertia varies. It is difficult to detect the wheel inertia  $J_w$  in real time in actual vehicles [18], [19]. This article is devoted to improve the antislip performance of the MTTE approach under such concerned and abnormal operations. A new MTTE control scheme with robust performance is proposed in the “Examples and Discussions” section. Based on our previous MTTE approach [17], the following parameters are taken into account.

- 1) Whatever kind of tire-road condition the vehicle is driven on, the kinematic relationship between the wheel and the chassis is always fixed and known.
- 2) During the acceleration phase, considering stability and tire abrasion, well-managed control of the velocity difference between wheel and chassis is more important than the pursuit of absolute maximum acceleration.
- 3) If the wheel and chassis accelerations are well controlled, the difference between the wheel and chassis velocities, i.e., the slip, is also well controlled.

Here, from (1) and (3), the driving force, i.e., the friction force between the tire and the road surface, can be calculated as

$$F_d = \frac{T}{r} - \frac{J_w \dot{V}_w}{r^2}. \quad (5)$$

Under normal road conditions,  $F_d$  is less than the maximum friction force from the road and increases as  $T$  increases. However, when slip occurs,  $F_d$  cannot increase by  $T$ . Hence, when slip occurs, the difference between the velocities of the wheel and the chassis become larger and larger, i.e., the acceleration of the wheel is larger than that of the chassis. Additionally, considering the  $\mu - \lambda$  relation described in the magic formula, an appropriate difference between chassis velocity and wheel velocity is necessary to support the desired friction force. In this article,  $\alpha$  is defined as

$$\alpha = \frac{\dot{V}}{\dot{V}_w}, \quad \text{i.e.,} \quad \alpha = \frac{(F_d - F_{dr})/M}{(T_{\max} - rF_d)r/J_w}. \quad (6)$$

It serves as a relaxation factor for smoothing the control system. To satisfy the condition that slip does not occur or becomes larger,  $\alpha$  should be close to one. Assume that  $F_{dr} = 0$ , with a designed  $\alpha$ , when the vehicle encounters a slippery road,  $T_{\max}$  must be reduced adaptively according to the decrease of  $F_d$ . If the friction force  $F_d$  is estimable, the maximum transmissible torque,  $T_{\max}$ , can be formulated as

$$T_{\max} = \left( \frac{J_w}{\alpha M r^2} + 1 \right) r \hat{F}_d. \quad (7)$$

This formula indicates that a given estimated friction force  $\hat{F}_d$  allows a certain maximum torque output from the wheel so as not to increase the slip. Hence, the proposed

TABLE 1. PARAMETER LIST.

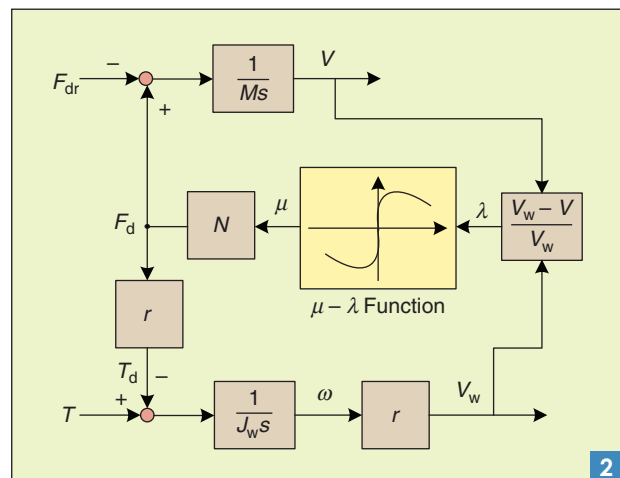
Symbol	Definition
$J_w$	Wheel inertia
$V_w$	Wheel velocity (circumferential velocity)
$\omega$	Wheel rotation
$T$	Driving torque
$r$	Wheel radius
$F_d$	Friction force (driving force)
$M$	Vehicle mass
$N$	Vehicle weight
$V$	Chassis velocity (vehicle velocity)
$F_{dr}$	Driving resistance
$\lambda$	Slip ratio
$\mu$	Friction coefficient

control scheme uses  $T_{\max}$  to construct and constrain the driving torque  $T$  according to the logic as

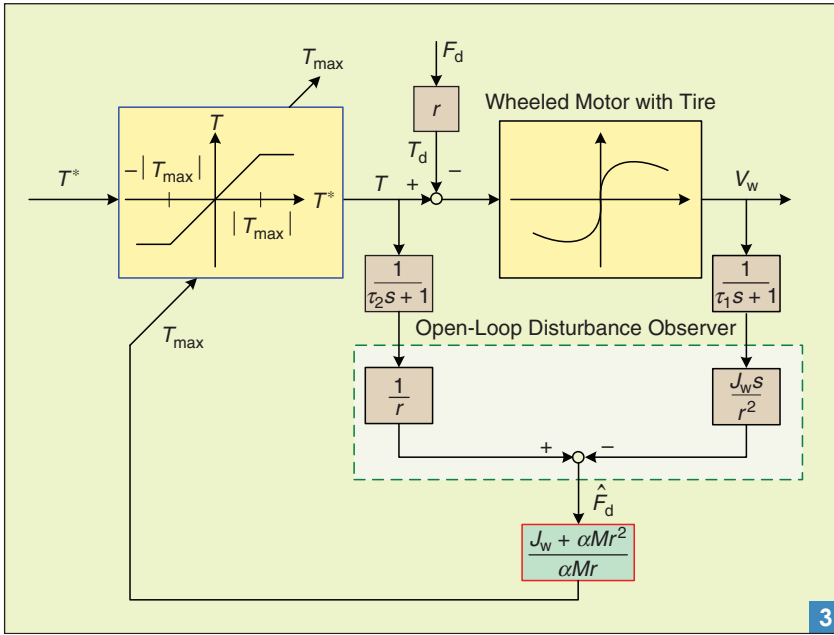
$$\begin{aligned} -|T_{\max}| < T^* < |T_{\max}|, T &= T^*; \\ T^* &\geq |T_{\max}|, T = |T_{\max}|; \\ T^* &\leq -|T_{\max}|, T = -|T_{\max}|. \end{aligned} \quad (8)$$

From (2), it is clear that the driving resistance  $F_{dr}$  can be regarded as one of the perturbation sources of the vehicle mass  $M$ . Although the vehicle mass  $M$  can be estimated online [20]–[23], in this article, it is assumed to be a constant.

Figure 3 shows the main control scheme of the MTTE. As shown in the figure, a limiter with a variable saturation value is expected to realize the control of torque output according to the dynamic situation. The estimated disturbance force  $\hat{F}_d$  is driven from the model inversion of the controlled plant and command torque  $T$ . Consequently, a differentiator is needed. Under normal conditions, the torque reference is expected to pass through the controller without any effect. Conversely, when on a slippery



One wheel of a vehicle model with the magic formula.



A control system based on the MTTE. 3

road, the controller can constrain the torque output to be close to  $T_{max}$ . Based on (7), an open-loop friction force estimator is employed using the linear nominal model of the wheeled motor to produce the maximum transmissible torque. For practical convenience, two low-pass filters (LPFs) with the time constants of  $\tau_1$  and  $\tau_2$ , respectively, are introduced to smoothen the noises of digital signals and the differentiator that follows. Note that the bandwidths of the LPFs are often designed to be double or higher than the system's bandwidth. Hence, in motion control analysis, the LPFs can be ignored.

Here, one can examine that the MTTE approach is effective when the vehicle mass  $M$  varies. Figure 4 shows a simplified linear model of the MTTE scheme, where  $M_n$  denotes the nominal value of vehicle mass  $M$ , and  $\Delta_d(s)$  stands for the perturbation caused by the passenger and driving resistance  $F_{dr}$ . Hence, from Figure 4, one has

$$\frac{T_{max}}{F_d} = \frac{J_w}{\alpha M_n r} + r. \quad (9)$$

Note that, if

$$\alpha M_n r \gg J_w, \quad (10)$$

one can be convinced that the condition of (10) is satisfied in most commercial vehicles. Then

$$\frac{T_{max}}{F_d} \approx r. \quad (11)$$

Now consider the mass perturbation of  $\Delta M$ . From (8), it yields

$$\frac{T_{max}}{F_d} = \frac{J_w}{\alpha(M_n + \Delta M)r} + r. \quad (12)$$

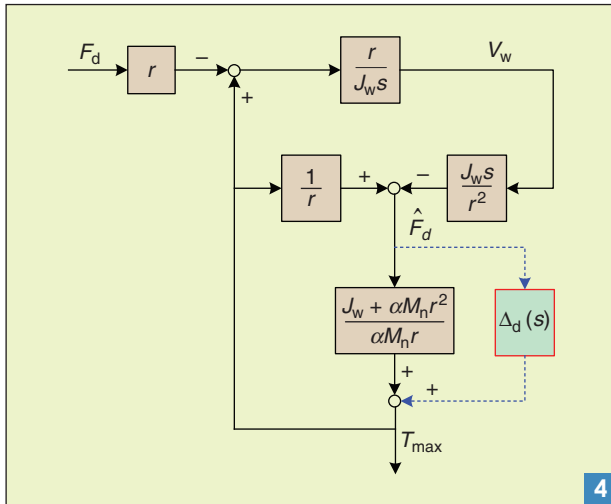
Obviously, from (12), the antislip performance of the MTTE will be enhanced when  $\Delta M$  is a positive value (i.e., the mass is gaining) and reduced when  $\Delta M$  is a negative value. Additionally, in common vehicles, the MTTE approach is insensitive when the vehicle mass varies. Since passenger and driving resistance are the primary perturbations of  $M_n$ , the MTTE approach reveals its merits for general driving environments.

### Disturbance Estimation

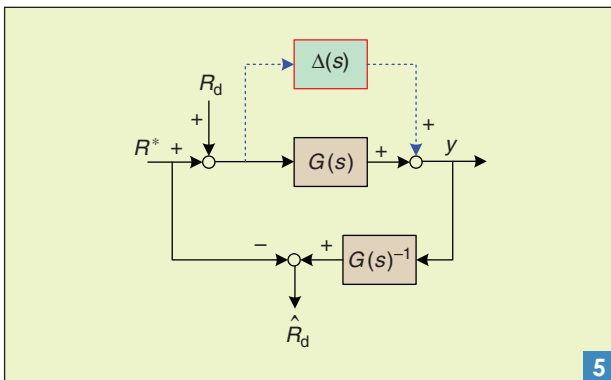
The disturbance estimation is often employed in motion control to improve the disturbance rejection ability. Figure 5 shows the general structure of open-loop disturbance estimation. As can be seen in this figure, one can obtain

$$\hat{R}_d = [(R^* + R_d)(G(s) + \Delta(s))]G(s)^{-1} - R^*. \quad (13)$$

If  $\Delta(s) \neq 0$ , then  $\hat{R}_d \neq R_d$ . Without the adjustment mechanism, the estimation accuracy decreases based on the



A simplified MTTE control scheme. 4



Disturbance estimation based on an open-loop observer. 5

deterioration of modeling error. As shown in Figure 3, the MTTE approach uses an open-loop disturbance observer to estimate the friction force between the tire and road. To improve the antislip performance of MTTE, a closed-loop disturbance observer is of interest.

Figure 6 shows the general structure of closed-loop disturbance estimation. As can be seen in this figure, one can obtain

$$\hat{R}_d = C(s)[(R^* + R_d)(G(s) + \Delta(s)) - (R^* + \hat{R}_d)G(s)]. \quad (14)$$

If  $\Delta(s) = 0$ , (14) becomes a low-pass dynamics as  $\hat{T}_d = (C(s)G(s))/(1 + C(s)G(s)R_d)$ . Moreover, from (14), without considering the feed-forward term of  $R^*$ , the closed-loop observer system of (14) can be reconstructed into a compensation problem, as illustrated in Figure 7. It is obvious that the compensator  $C(s)$  in the closed-loop structure offers a mechanism to minimize the modeling error caused by  $\Delta(s)$  in a short time. Consequently, the compensator enhances the robust estimation performance against modeling error. Since the modeling error is unpredictable, the disturbance estimation based on a closed-loop observer is preferred.

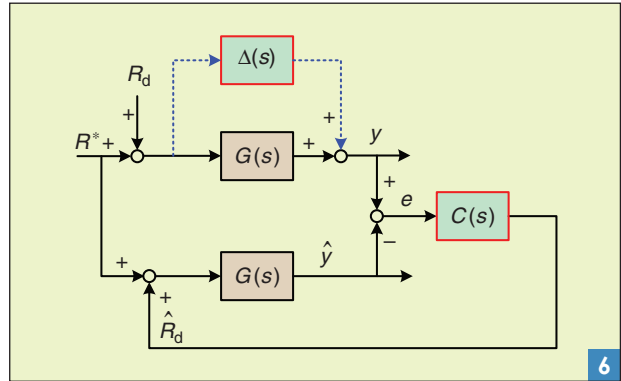
In this article, a proportional-integral (PI)-type disturbance observer is used in the MTTE scheme to improve antislip performance. Conventional PI control approaches have been adopted in many industrial applications, in which the proportional (P) part provides a constant gain control and the integral (I) gain provides the stiffness to eliminate the dc drop. The PI-type compensator is used in the observer structure since it provides better robustness against model inaccuracies and step disturbances than the conventional Luenberger observer [24], and it can estimate both the system states and external disturbances. The PI-type disturbance estimator has a more complex structure than the classical Luenberger observer. Hence, its design of observer gains also requires some techniques. For a general case, the PI-type disturbance estimator is often formulated in a state-space form. To avoid missing the focus of this article, the readers can refer to [25] for the general PI-type disturbance estimator designs.

### Proposed Antislip Control Strategy

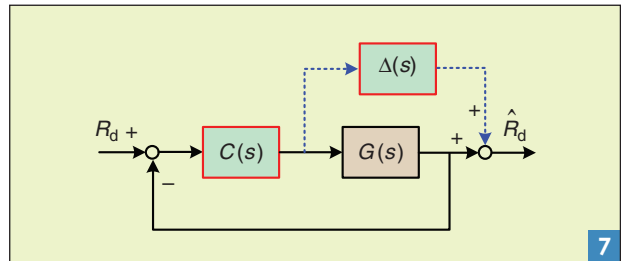
Figure 8 shows the proposed MTTE control system that embedded a closed-loop compensator into Figure 8 with a friction detection unit. The disturbance torque  $T_d$  comes from the operation friction. When the vehicle is operated on a slippery road, it will cause the  $T_d$  to become very small because of the insufficient friction of the tires. Skid often happens during braking and racing of an operated vehicle when the tire's adhesion cannot firmly grip the surface of the road. This phenomenon is often referred as the magic formula. However, the  $\mu - \lambda$  relation is immeasurable in real time. Therefore, in the proposed approach, the nonlinear behavior between the tire and road is

regarded as an uncertainty source that deteriorates the steering stability and causes some abnormal faults in driving. Here, let  $\Delta_s(s)$  denote the slip perturbation on the wheeled motor. The uncertain dynamics of  $\Delta_s(s)$  represents the role of different slippery driving situations. When  $\Delta_s(s) \approx 0$ , it means the driving condition is fine. In contrast, for a slippery surface of road,  $\Delta_s(s) \neq 0$ . As discussed in the "Disturbance Estimation" section, the open-loop disturbance observer has the following drawbacks.

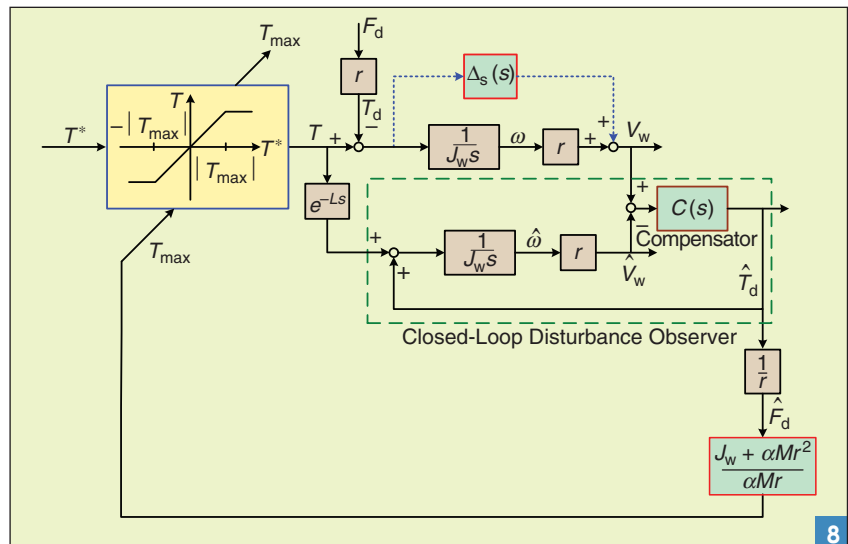
- 1) The open-loop disturbance observer does not have a feedback mechanism to compensate the modeling errors. Therefore, its robustness is often not good.



Disturbance estimation based on a closed-loop observer.



The equivalent control block diagram of disturbance estimation.



The proposed robust MTTE control system.



2) The open-loop disturbance observer uses the inversion of controlled plant to acquire the estimation information of disturbance. However, sometimes the inversion is not easy to take.

Because of the closed-loop dynamics of the compensator, the estimated disturbance torque  $\hat{T}_d$  in a proposed system can enhance the performance of the MTTE against the skid. It also offers better robustness to the varying parameter. Unlike the conventional MTTE approach, the proposed approach does not need to use the differentiator. Note that the proposed MTTE approach employs a closed-

loop observer to counteract the effects of disturbance. Hence, it is sensitive to the phase of the estimated disturbance. Consequently, the delay element  $e^{-Ls}$ , for preview purpose, is set up for compensating the digital delay of the fully digital power electronics driver. This preview strategy coordinates the phase of the estimated disturbance torque.

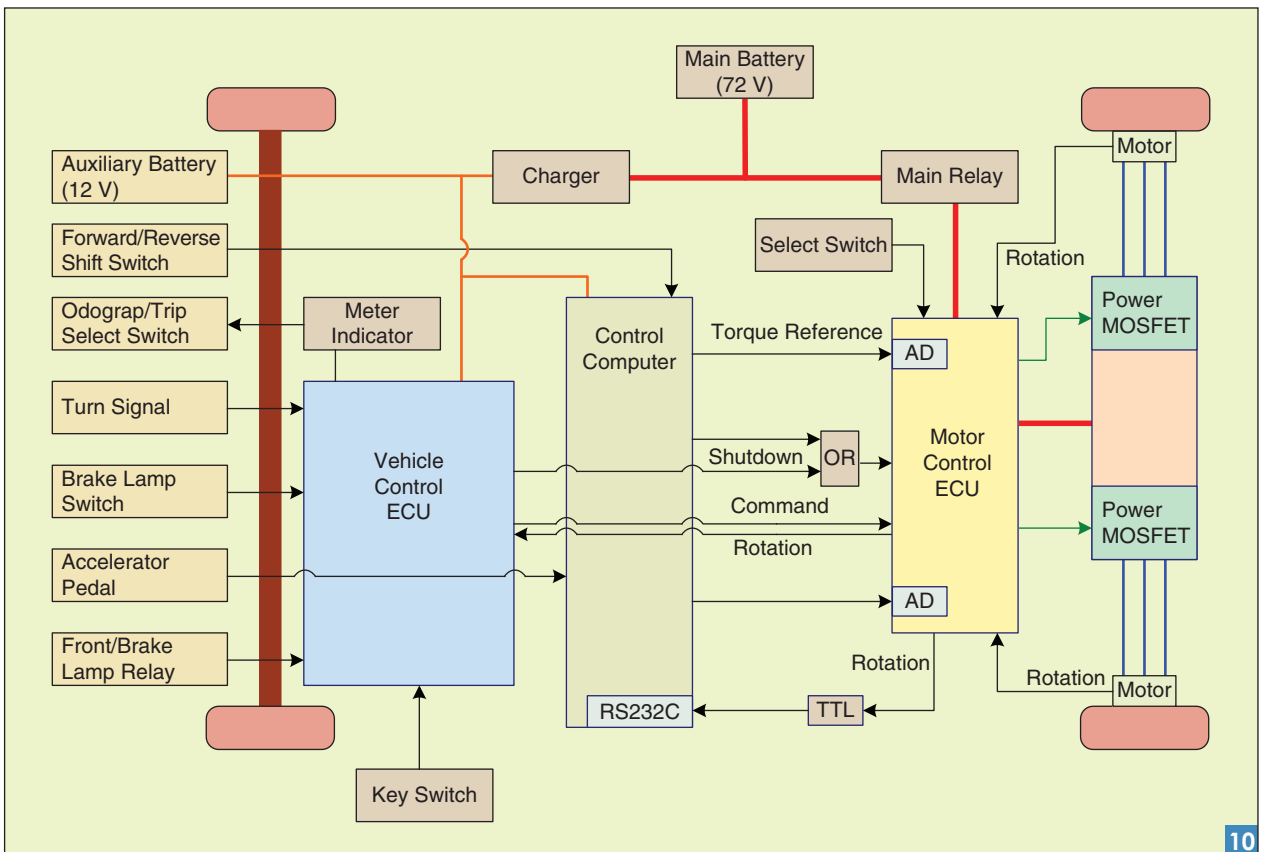
### Experimental EV

For the sake of implementing and evaluating the proposed control system, a commercial EV, COMS3, which is assembled by Toyota Auto Body Co. Ltd., shown in Figure 9, was modified to carry out the requirements of the experiments. In the testing car, each rear wheel is equipped with an interior permanent magnet synchronous motor and can be independently controlled. As illustrated in Figure 10, a control computer is embedded to take the place of the previous electronic control unit (ECU) to operate the motion control. The computer receives the acceleration reference signal from the acceleration pedal sensor, the forward/backward signal from the shift switch, and the wheel rotation from the inverter. Then, the corresponding calculated torque reference of the left and the right rear wheel is independently sent to the inverter by two analog signal lines. Table 2 lists the main specifications.

The most outstanding feature of the modified inverter is that the minimum refresh time of the torque reference is decreased from 10 to 2 ms, which makes it possible to actualize the torque reference more quickly and accurately. The increased maximum rate of change of the torque reference permits faster torque variation for high-performance motion control.



An experimental EV: COMS3.



The schematics of a COMS3 electrical system.

**TABLE 2. SPECIFICATION OF COMS3.**

Total weight	360 kg
Maximum power per wheel	2,000 W
Maximum torque per wheel	100 N . m
Wheel inertia per wheel	0.5 kg . m <sup>2</sup>
Wheel radius	0.22 m
Sampling time	0.01 s
Controller	Pentium M1.8G, 1-GB RAM using Linux
A/D and D/A	12 b
Shaft encoder	36 pulses/round

**Examples and Discussions**

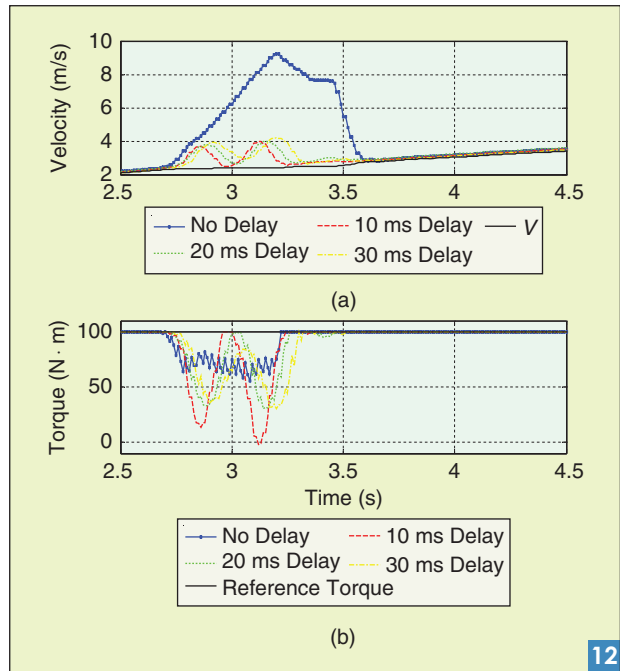
In this section, the proposed TC strategy is evaluated experimentally on COMS3. In the experiments, the relaxation factor of the MTTE scheme is set as  $\alpha = 0.9$ . The time constants of LPFs in the comparison MTTE experiment are set as  $\tau_1 = \tau_2 = 0.05$ . As mentioned in the “MTTE Approach for Antislip Control” section, the passenger’s weight variable is regarded as the model uncertainty in the problem formulation. Hence, this article adopts the PI compensator

$$C(s) = K \left( K_p + K_i \frac{1}{s} \right) \tag{15}$$

as the kernel of disturbance estimation. Set the PI gains of the PI compensator as  $K = 1, K_p = 70$ , and  $K_i = 60$ , where  $K$  is a factor for adjusting the bandwidth. As shown in Figure 11, the slippery road was set by an acrylic sheet with a length of 1.2 m and lubricated with water. As mentioned in the “Examples and Discussions” section, the reference command delay (preview) in the proposed approach is exploited to adjust the phase of the estimated disturbance. The antislip performance of the MTTE deteriorates if the phase of estimated disturbance shifts so much. Under a proper antislip control, the wheel velocity should be as close to the chassis velocity as possible. As can be seen in Figure 12, the proposed approach cannot achieve any antislip performance (i.e., the vehicle is skidded) if the reference signal is not delayed. Figure 12 also shows the measured results, and the digital delay of motor driver has significant affections to the closed-loop observers and the proposed scheme. According to the



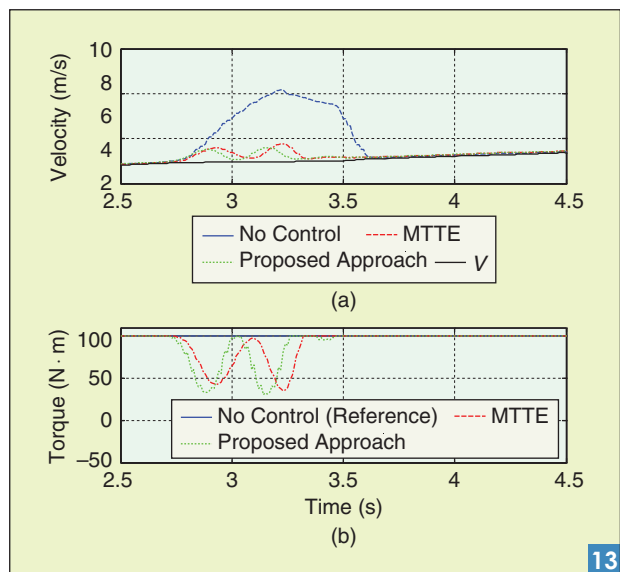
**11** The setting of a slippery road for the experiment.



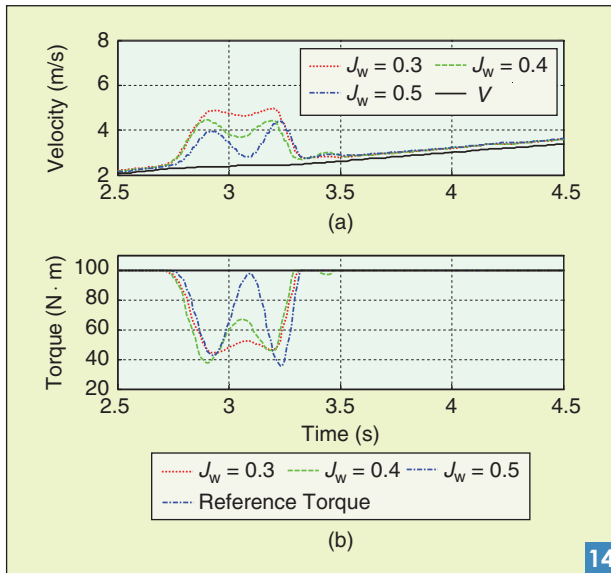
**12** Experimental results for different delay time  $L$ . (a) Wheel and chassis velocities. (b) Reference and output torques.

practical tests of Figure 12, with a proper command delay of 20 ms, the proposed approach can achieve a feasible performance. Hence, in the following, all experiments following the proposed approach use this delay parameter.

As mentioned in the “MTTE Approach for Antislip Control” section, the MTTE scheme can be employed to prevent vehicle skid. These approaches can compensate the reference torque into a limited value when encountering a slippery road. Based on the experimental result of Figure 13, the reference torque of MTTE-based approaches is constrained without divergence. Figure 13 is evaluated when the nominal wheel inertia of  $J_w = 0.5 \text{ kg} \cdot \text{m}^2$ . As shown in this figure,



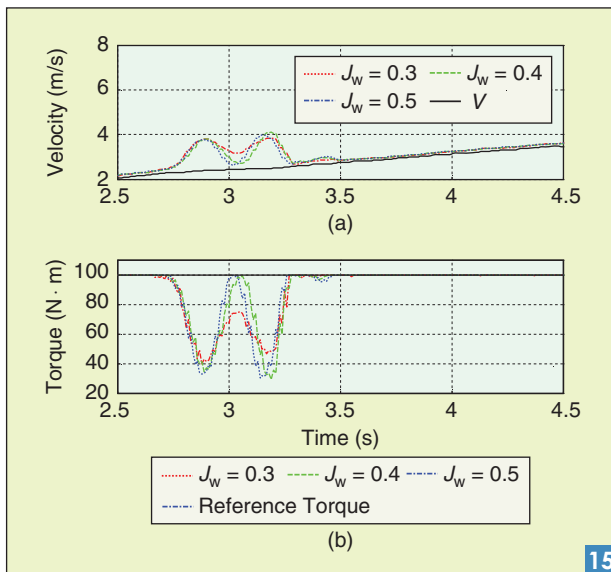
**13** Practical comparisons between MTTE and the proposed approach to a nominal wheel inertia of  $J_w = 0.5 \text{ kg} \cdot \text{m}^2$ . (a) Wheel and chassis velocities. (b) Reference and output torques.



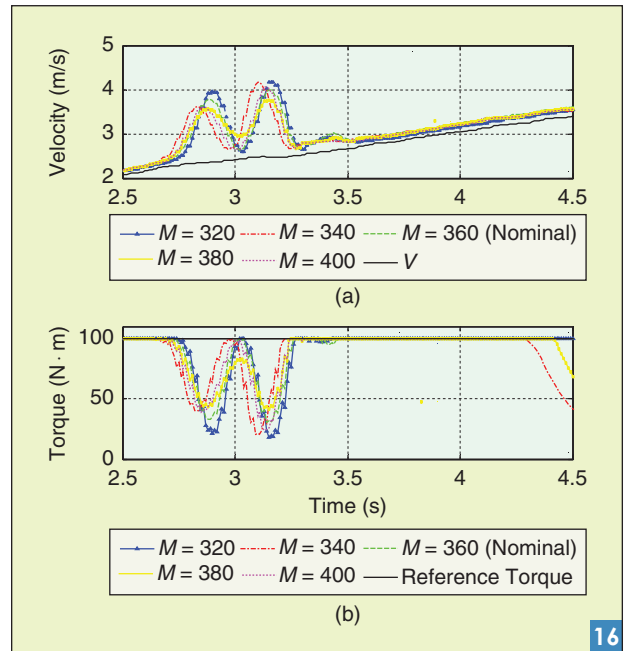
The experimental results of MTTE to different  $J_w$ . (a) Wheel and chassis velocities. (b) Reference and output torques.

both the MTTE and the proposed approach have good antislip performance. However, as indicated in the practical results in Figure 14, the performance of MTTE deteriorates when the wheel inertia varies. In addition, Figure 15 shows the same testing using the proposed approach and, hence, overcomes this problem. The proposed approach has robust antislip performance when the wheel inertia varies in real time.

The conventional MTTE is robust to the variations in vehicle mass  $M$ . The discussion and practical verification of this variation can be found in [17]. To avoid duplication, this experiment has been omitted. Figure 16 shows the performance evaluation of the proposed approach against different vehicle mass. It is unpredictable that different passengers will change the mass of the whole vehicle. As discussed in the “MTTE Approach for Antislip Control” section, Figure 16



The experimental results of the proposed approach to different  $J_w$ . (a) Wheel and chassis velocities. (b) Reference and output torques.

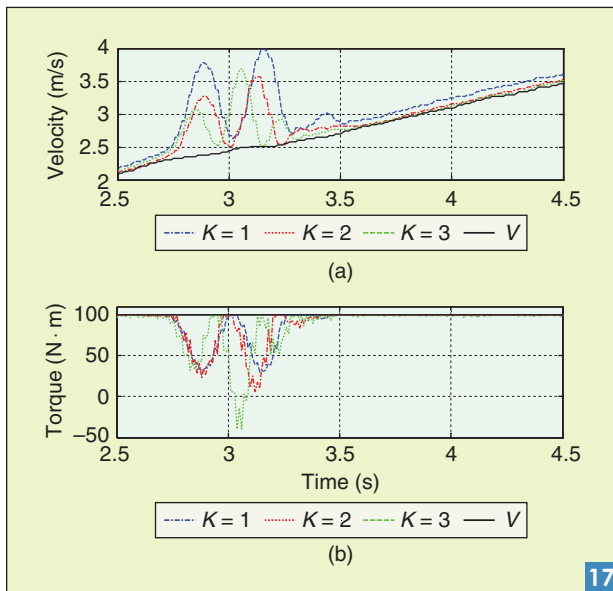


The experimental results of the proposed approach to different  $M$ . (a) Wheel and chassis velocities. (b) Reference and output torques.

shows its practical verification. There is no doubt that the proposed approach is robust despite different passengers sitting in the vehicle. As presented in Figure 16, the antislip control validates different vehicle mass. From Figures 15 and 16, it is evident that the proposed TC approach has consistent performance when the wheel inertia  $J_w$  and vehicle mass  $M$  vary. As shown in these figures, the proposed antislip system offers an effective performance to maintain the driving stability under common situations, and, therefore, the steering safety of the EVs can be further enhanced. Note that the closed-loop observer poles are often chosen faster than the controlled system by a factor of two to six. When this occurs, the controller poles dominate the overall system. Consequently, the observer has a higher bandwidth, i.e., placing all the observer poles further away than the feedback controller. Nevertheless, because of the inherent actuator saturation problem, the observer poles cannot be arbitrarily placed. Thus, the selection of suitable observer gains should be delicately designed according to practical conditions. Practical tests are given in Figure 17. If one sets the bandwidth parameter  $K$  higher (e.g., two or three), then the output torque may begin to oscillate and cause the vehicle to run unstably. This tradeoff should be noted in designing an effective antislip control based on the proposed approach.

## Conclusions

In this study, the concept of maximum transmissible torque has been proven to be valid on EV TC. Unlike the previous approaches on gasoline engine cars, this approach is cost-effective. Therefore, these methodologies facilitate the development and popularity of EVs. Furthermore, based on this core TC, more complicated two degrees of freedom motion control for vehicles can be synthesized by introducing information such as steering angle and yaw rate. The stability of vehicle steering can be further enhanced. Control issues such as full-car side-slip prevention and sensor fusion could be



**17**  
The experimental results of the proposed approach to different  $K$ . (a) Wheel and chassis velocities. (b) Reference and output torques.

considered for advanced investigation. This article has presented a new TC approach that embedded the strategies of MTTE with robust performance in EVs. This approach has indicated that the motor can not only act as a general actuator but also as a measurement device because of its inherent features, which provides a good basis for antislip control as well as other more advanced motion control systems in vehicles. A closed-loop disturbance observer that enhances the friction torque estimation has been employed in the proposed scheme. Within the proposed scheme, the differentiator and inversion of the controlled plant are unnecessary. It has been verified that the proposed control system has benefits such as preventing possible failures in a slippery driving situation. The experimental results have substantiated that the proposed MTTE strategy has the ability, in practice, to improve the safety of EV.

## Acknowledgments

The authors thank Chia-Chen Lai for her assistance during this work and also express their thanks to the anonymous referees for their valuable comments. This work was partially supported by Yen Tjing Ling Industrial Research Institute of Taiwan under grant project 97PD03 and from the National Science Council (NSC) of Taiwan under contract NSC 98-2115-M-142-001.

## References

- [1] United Nations. (2011). Kyoto Protocol [Online]. Available: [http://unfccc.int/kyoto\\_protocol/items/2830.php](http://unfccc.int/kyoto_protocol/items/2830.php)
- [2] Y. Hori, Y. Toyoda, and Y. Tsuruoka, "Traction control of electric vehicle: Basic experimental results using the test EV 'UOT electric March'," *IEEE Trans. Ind. Applicat.*, vol. 34, no. 5, pp. 1131–1138, 1998.
- [3] P. He and Y. Hori, "Optimum traction force distribution for stability improvement of 4WD EV in critical driving condition," in *Proc. IEEE Int. Workshop Advanced Motion Control*, Istanbul, Turkey, 2006, pp. 596–601.
- [4] K. M. Rahman, N. R. Patel, T. G. Ward, J. M. Nagashima, F. Caricchi, and F. Crescimbeni, "Application of direct-drive wheel motor for fuel cell electric and hybrid electric vehicle propulsion

- system," *IEEE Trans. Ind. Applicat.*, vol. 42, no. 5, pp. 1185–1192, 2006.
- [5] M. Schinkel and K. Hunt, "Anti-lock braking control using a sliding mode like approach," in *Proc. American Control Conf.*, Anchorage, AL, 2002, pp. 2386–2391.
- [6] C. B. Patil, R. G. Longoria, and J. Limroth, "Control prototyping for an anti-lock braking control system on a scaled vehicle," in *Proc. IEEE Conf. Decision and Control*, Hawaii, 2003, pp. 4962–4967.
- [7] M.-C. Tsai and J.-S. Hu, "Pilot control of an auto-balancing two-wheeled cart," *Adv. Robot.*, vol. 21, no. 7, pp. 817–827, 2007.
- [8] Y.-S. Ha and S. Yuta, "Trajectory tracking control for navigation of the inverse pendulum type self-contained mobile robot," *Robot. Auton. Syst.*, vol. 17, no. 1–2, pp. 65–80, 1996.
- [9] F. Tahami, S. Farhangi, and R. Kazemi, "A fuzzy logic direct yaw-moment control system for all-wheel-drive electric vehicles," *Vehicle Syst. Dyn.*, vol. 41, no. 3, pp. 203–221, 2004.
- [10] T. Mizushima, P. Raksincharoensak, and M. Nagai, "Direct yaw-moment control adapted to driver behavior recognition," in *Proc. SICE-JCISE Int. Joint Conf.*, Busan, Korea, 2006, pp. 534–539.
- [11] N. Mutoh, Y. Hayano, H. Yahagi, and K. Takita, "Electric braking control methods for electric vehicles with independently driven front and rear wheels," *IEEE Trans. Ind. Electron.*, vol. 54, no. 2, pp. 1168–1176, 2007.
- [12] T. Saito, H. Fujimoto, and T. Noguchi, "Yaw-moment stabilization control of small electric vehicle," in *Proc. IEE Japan Tech. Meeting Industrial Instrumentation and Control*, Tokyo, Japan, 2002, pp. 83–88.
- [13] H. Fujimoto, T. Saito, and T. Noguchi, "Motion stabilization control of electric vehicle under snowy conditions based on yaw-moment observer," in *Proc. IEEE Int. Workshop Advanced Motion Control*, Kawasaki, Japan, 2004, pp. 35–40.
- [14] K. Fujii and H. Fujimoto, "Traction control based on slip ratio estimation without detecting vehicle speed for electric vehicle," in *Proc. 4th Power Conversion Conf.*, Nagoya, Japan, 2007, pp. 688–693.
- [15] H. B. Pacejka and E. Bakker, "The magic formula tire model," *Vehicle Syst. Dyn.*, vol. 21, suppl. 1, pp. 1–18, 1992.
- [16] S. Sakai and Y. Hori, "Advantage of electric motor for anti skid control of electric vehicle," *Eur. Power Electron. J.*, vol. 11, no. 4, pp. 26–32, 2001.
- [17] D. Yin and Y. Hori, "A new approach to traction control of EV based on maximum effective torque estimation," in *Proc. 34th Annu. Conf. IEEE Industrial Electronics Society*, Florida, FL, 2008, pp. 2764–2769.
- [18] K.-B. Lee and F. Blaabjerg, "Robust and stable disturbance observer of servo system for low-speed operation," *IEEE Trans. Ind. Applicat.*, vol. 43, no. 3, pp. 627–635, 2007.
- [19] S. Sakai, H. Sado, and Y. Hori, "Motion control in an electric vehicle with four independently driven in-wheel motors," *IEEE/ASME Trans. Mechatron.*, vol. 4, no. 1, pp. 9–16, 1999.
- [20] M. Ikeda, T. Ono, and N. Aoki, "Dynamic mass measurement of moving vehicles," *Trans. Soc. Instrum. Contr. Eng.*, vol. 28, no. 1, pp. 50–58, 1992.
- [21] A. Vahidi, A. Stefanopoulou, and H. Peng, "Recursive least squares with forgetting for online estimation of vehicle mass and road grade: Theory and experiments," *Vehicle Syst. Dyn.*, vol. 43, no. 1, pp. 31–55, 2005.
- [22] V. Winstead and I. V. Kolmanovskiy, "Estimation of road grade and vehicle mass via model predictive control," in *Proc. IEEE Conf. Control Applications*, Toronto, Canada, 2005, pp. 1588–1593.
- [23] P. Ratiroch-Anant, H. Hiroshi, A. Masatoshi, and O. Shigeto, "Adaptive controller design for anti-slip system of EV," in *Proc. IEEE Conf. Robotics, Automation and Mechatronics*, Bangkok, Thailand, 2006, pp. 1–6.
- [24] G. Ellis, *Control System Design Guide*. San Diego, CA: Academic, 2000.
- [25] J.-S. Hu, F.-R. Hu, and M.-Y. Cheng, "A partial pole placement approach to proportional-integral observer design," *Proc. Inst. Mech. Eng., Part I, J. Syst. Contr. Eng.*, vol. 223, no. 2, pp. 253–262, 2009.

*Jia-Sheng Hu (jogson@ieee.org) is with the National University of Tainan in Tainan, Taiwan. Dejun Yin is with Keio University in Kanagawa, Japan. Yoichi Hori is with the University of Tokyo in Tokyo, Japan. Feng-Rung Hu is with the National Taichung University in Taichung, Taiwan. Hu and Yin are Members of the IEEE. Hori is a Fellow of the IEEE. This article first appeared as "A New MTTE Methodology for Electric Vehicle Traction Control" at the 12th International Conference on Electrical Machines and Systems.*

# Study on Open and Short Ended Helical Antennas with Capacitor of Wireless Power Transfer using Magnetic Resonant Couplings

Takehiro Imura, *Student Member, IEEE*, Hiroyuki Okabe, and Yoichi Hori, *Fellow, IEEE*

**Abstract**—In the technology of wireless power transfer, electromagnetic coupling using resonance can transfer across a large air gap without losing its high efficiency and power. In this technology, the role of antennas is very important. In this paper, magnetic resonant coupling using helical antennas is proposed. The helical antennas are two types- one is open ended and the other is short ended helical antennas and specifications of these antennas were studied which is related to the efficiency of power transfer wirelessly. The capacitor is installed to antennas in series and parallel is studied. High efficiency power transfer is possible when resonance is in series. The short ended helical antennas with an in series capacitor makes series resonance which makes resonance frequencies lower than open ended helical antennas.

**Index Terms**—contactless, wireless, power transfer, resonance

## I. INTRODUCTION

In the technology of wireless power transfer, there are three important factors which are: a large air gap, high efficiency and high power. These are necessary to provide power to any device or product wirelessly. Typically, it is difficult to have all three factors required in wireless power transfer technology.

The technology of wireless power transfer is categorized in four types: electromagnetic induction, microwave power transfer, laser power transfer and electromagnetic resonant coupling. In this paper, the type of electromagnetic resonant coupling is proposed. Electromagnetic induction is powerfully but usually the air gap is short, the length is around a few centimeters and the wireless power is nonradiative [1]-[9]. Nowadays the length reaches around 10cm [10]; however, electromagnetic induction is difficult to use when crossing a large air gap. Microwave power transfer and laser power transfer can cross a large air gap far beyond a few km; however, the efficiencies are lower and the wireless power is radiative [11]-[13]. Electromagnetic resonant coupling is possible to power wirelessly across a 2m air gap while the efficiency is 45-50%, power is 60W and the wireless power is nonradiative [14][15]. This kind of technology is use in filter theory at GHz

but that purposes are not for power supply but for communications [16][17]. This technology is expected to be applied to mobile phones, laptops and electric vehicles.

The helical antenna, which is for wireless power transfer, is important in this technology and the specifications should be studied because having a high efficiency and crossing a large air gap are directly related to antenna specifications. As well, other antennas, such as the helical antenna used is for near field power transfer, is also resonates because of its own inductance and capacitance. The figure of a helical antenna is like coil. The feeding point decides which type of helical antenna it is. In the case of the open end, feeding point is in the center. On the other hand, the short end's feeding point is on the edge. We proposed that, in the case of the open ended helical antenna, resonant frequencies are changed by radius, turns and pitch [18][19]. The resonant frequencies are dependant on inductance and capacitance. This is decided by the antenna structure; however, the values have limitations, which are decided by the structure of the antenna itself. This technology is wirelessly currently operated around a couple dozen MHz, however, the circuit is easy to make if the frequencies are lower. Especially, the power device is still difficult to operate at a couple dozen MHz with high efficiency and high power. Therefore, how the use at lower frequencies is possible requires further study. Before now, only the antenna in series capacitor was studied [20].

In this paper, the open and short ended helical antennas are compared. How lower frequencies are possible is studied. To this end, the capacitor in series or parallel is installed in the helical antenna. The open and short ended helical antennas are compared. Mainly, electromagnetic field analysis and experimental results are proposed.

## II. OPEN ENDED HELICAL ANTENNAS

The open and short ended helical antennas are proposed (Fig. 1). In this chapter, open ended helical antennas are studied by electromagnetic field analysis using the method of moment. Fig. 2 shows a diagram of the open ended helical antenna. The transmitting antenna and the receiving antenna are the same. The lower side is the transmitting antenna and the upper side is the receiving antenna. The feeding point is the center of antenna, which makes the antenna an open end. This antenna is for near field power transfer using couplings of magnetic field

Manuscript received November 11, 2009.

T. Imura and H. Okabe are with the Department of Electrical Engineering, The University of Tokyo, Tokyo 153-8505, Japan (e-mail: imura@horilab.iis.u-tokyo.ac.jp, okabe@horilab.iis.u-tokyo.ac.jp)

Y. Hori is with the Institute of Industrial Science, The University of Tokyo, Tokyo 153-8505, Japan (e-mail: hori@iis.u-tokyo.ac.jp).



(a) Open end and opposite of feeding point. (b) Open end and feeding point.



(c) Short end and opposite of feeding point. (d) Short end and feeding point.

Fig. 1. Helical antennas

which is different from typical antennas used for communication which use radiative power.

Fig. 3 shows the efficiency of the power transfer. The results are when the air gap is 150mm and 250mm. When the air gap is short the two resonant frequencies have a high efficiency. However, these two frequencies change related to the length of air gaps. When the air gap is longer the resonant frequency has a one with high efficiency, but if the length becomes much farther the efficiency becomes lower. The one frequency is the same as the resonant frequency of a single antenna.

Fig. 4 shows the impedance of a single antenna. The point in which reactance is 0 ohms where is resonant frequency. When the transmitting antenna and the receiving antenna are close to each other, wireless power transfer is possible using the resonance. However, when the transmitting antenna and the receiving antenna are close to each other, the mutual inductance affects the resonant frequency and one frequency splits in two.

These are explained by the equivalent circuits. The Equivalent circuit of only a single antenna is described in Fig. 5(a). Inductance  $L$  and capacitance  $C$  make resonance, and the resonance frequency is equation (1). This equation shows that when  $L$  or  $C$  is large, the frequency becomes low. The characteristic impedance is  $Z_0$  and internal resistance is  $R$ . Fig. 5(b) shows the transmitting and the receiving antennas. The left is the transmitting antenna, the right is the receiving antenna and the coupling is described as mutual inductance  $L_m$ .  $f$  is frequency and  $\omega$  is angular frequency.

Ideally, wireless power transfer is  $R = 0$ . In this case, the efficiency of wireless power transfer is described by equation (2) and (3). Equation (2) is depicted by the efficiency  $\eta_{21}$  and the transmission  $S_{21}$ . Equation (3) shows  $S_{21}$  and how it relates to  $L$  and  $C$  of a single antenna and mutual inductance  $L_m$  of two antennas.

Equation (4) is derived by resonant condition and this equation leads two resonant frequencies which are described in equation (5) and (6).

$$\omega_0 = \frac{1}{\sqrt{LC}} \quad (1)$$

$$\eta_{21} = S_{21}^2 \times 100 \text{ [%]} \quad (2)$$

$$S_{21} = \frac{2jL_m Z_0 \omega}{L_m^2 \omega^2 - \left(\omega L - \frac{1}{\omega C}\right)^2 + 2jZ_0 \left(\omega L - \frac{1}{\omega C}\right) + Z_0^2} \quad (3)$$

$$\frac{1}{\omega L_m} + \frac{2}{\omega(L - L_m) - \frac{1}{\omega C}} = 0 \quad (4)$$

$$\omega_m = \frac{\omega_0}{\sqrt{1+k}} = \frac{1}{\sqrt{(L + L_m)C}} \quad (5)$$

$$\omega_e = \frac{\omega_0}{\sqrt{1-k}} = \frac{1}{\sqrt{(L - L_m)C}} \quad (6)$$

$$(\omega_0 = 2\pi f_0, \quad \omega_m = 2\pi f_m, \quad \omega_e = 2\pi f_e)$$

Fig. 6 shows the diagram of the distributed constant circuit and the impedance. The distributed constant circuit can express resistance, reactance of impedance and express periodicity of frequency; however, this is an approximation because a distributed constant circuit is difficult in the perspective of accuracy. Despite this distributed constant circuit has the ability to express resistance at resonance and antiresonance. At resonance, the resistance becomes small and close to 0 and at the antiresonance, the resistance becomes large. When the antenna is described as a transmission line whose reactance begins at  $-\infty$  ohm at frequency is 0 Hz and when the length of transmission line equals a quarter-wave, the reactance becomes 0 ohm- resonance. Thus, to describe this resonance, the open ended helical antenna is depicted by series resonance.

Fig. 7 shows the relation between series resonance, lumped parameter circuit and impedance. The reactance is described correct, but the resistance depending frequencies are not described correctly. Therefore, in the equivalent circuit, the resistance of impedance is an approximated fixed value.

On the other hand, when  $R$  is not equal to 0 ohms equation (3) needs to include  $R$  and the efficiency decrease. The equation become complicated so the equation is skipped, however, only the results are shown in Fig. 8 when  $R = 0\Omega$  and  $R = 1\Omega$ . In this way, when the resistance of input impedance is high the efficiencies become worse directly.

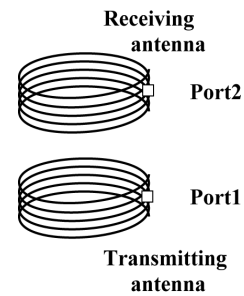
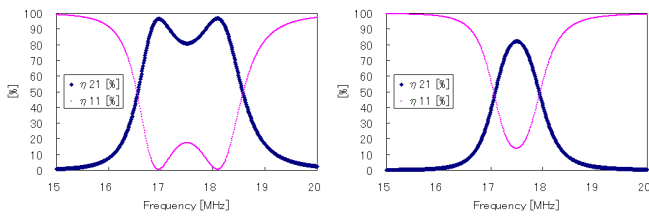


Fig. 2. Diagram of open ended helical antenna

### III. SHORT ENDED HELICAL ANTENNAS

In this chapter, the characteristics of short ended helical antennas are studied. The helical antenna is fed by the edge to operate it as the short ended helical antenna. Fig. 9 shows the diagram of the short ended helical antenna. However, this way of feeding makes antiresonance. Fig. 10 shows the efficiency around antiresonance frequencies. At antiresonance frequencies the efficiencies are very low and this short ended helical antenna is not suitable to wireless power transfer. Fig. 11 shows impedance about just an antenna only. The reactance becomes  $\pm\infty\Omega$  at antiresonant frequency. In antiresonant frequencies, the resistances increase and the efficiencies become worse. Fig. 12 shows distributed constant circuits. When the antenna is described as a transmission line whose reactance begins at 0 ohm, frequency is 0 Hz and the length of the transmission line equals to the length of a quarter-wave, the reactance becomes  $\pm\infty\Omega$ . This means antiresonance. Thus, to describe this resonance the short ended helical antenna depicted by parallel resonance is used. Fig. 13 shows the relation between lumped parameter circuit and impedance at parallel resonance.



(a) Air gap is 150mm (b) Air gap is 250mm

Fig. 3. Analysis result of frequencies and efficiency of open ended helical antennas. Radius is 150mm, turns are 5 and pitch is 5mm

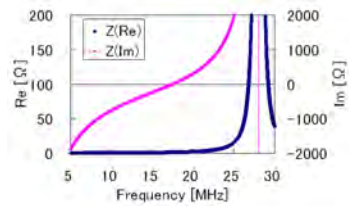
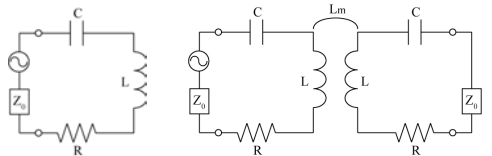
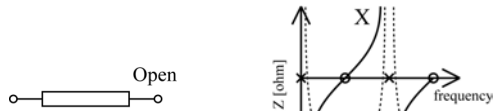


Fig. 4. Analysis result of input impedance of an open ended helical antenna

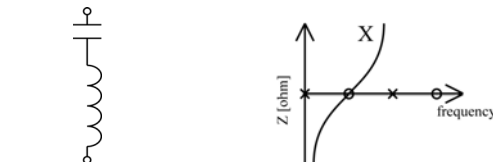


(a) One element (b) Transmitting and receiving antenna  
Fig. 5. Equivalent circuit of magnetic resonant coupling



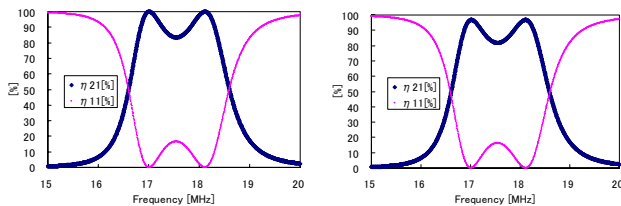
(a) Open end transmission line (b) Resistance and reactance

Fig. 6. Diagram of open end transmission line and impedance



(a) Open end lumped parameter circuit (b) Reactance

Fig. 7. Diagram of series resonance of lumped parameter circuit



(a) R=0Ω (b) R=1Ω

Fig. 8. Efficiency calculated by open end antenna's equivalent circuit.

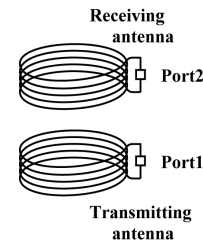


Fig. 9. Diagram of short ended helical antennas

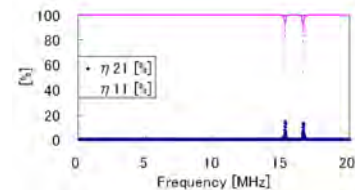


Fig. 10. Analysis result of frequencies and efficiency of short ended helical antennas. Radius is 150mm, turns are 5 and pitch is 5mm.

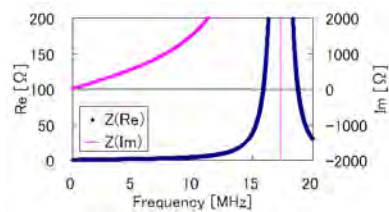
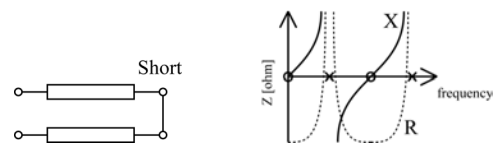


Fig. 11. Analysis result of input impedance of an open ended helical antenna.



(a) Short end transmission line (b) Resistance and reactance

Fig. 12. Diagram of short end transmission line and impedance

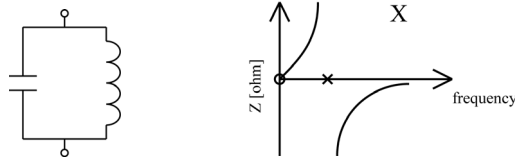


Fig. 13. Diagram of parallel resonance of lumped parameter circuit

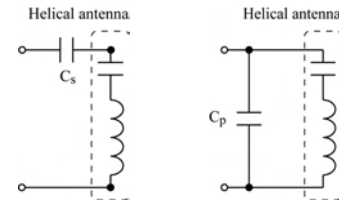
#### IV. OPEN ENDED WITH CAPACITOR

Until this chapter, the characteristics of antennas without an added capacitor were described. From here, the characteristics of antennas with an added capacitor, the addition of a capacitor in series and parallel and, in this chapter, the open ended helical antennas with a capacitor in series or parallel are studied. The open ended helical antenna creates series resonance. Thus, in equivalent circuits, antenna with an added capacitor in series is in Fig. 14 (a) and with an added capacitor in parallel is described in Fig. 14 (b). From equivalent circuits, the diagrams of reactance are shown in Fig. 15. When the capacitor is in series and the capacitance is small, the frequency becomes high. On the other hand, when the capacitor is in parallel and the capacitance changes, the frequency is not changed.

This is studied by electromagnetic field analysis. The results are shown in Fig. 16 when the capacitance  $C_s$  in series changes from 10pF to 1000pF. As well, the results are shown in Fig. 17 when the capacitance  $C_p$  in parallel changes from 10pF to 1000pF.

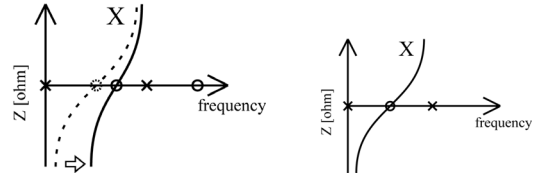
Fig. 16 shows the results of the capacitor in series. When the capacitance is small, the resonant frequencies become high. On the other hand, when the capacitor is large, the resonant frequencies become low and the frequencies are similar to the results without a capacitor. If the resonant frequency becomes much higher and closes to antiresonant frequency, the resistance at resonant frequency becomes larger. Thus, the resistance is not 0 but 4.4 ohms in Fig. 16(a). Therefore, the efficiencies get worse. As above, as far as the capacitance is not too small, the efficiency is almost the same as without the capacitor and high efficiency wireless power transfer is possible. The open ended helical antenna in series capacitor can allow resonant frequencies to be higher than if it were without capacitance. Thus, this is suitable to adjust to higher frequencies; however, it is impossible to decrease frequency on the open ended helical antennas in this way.

Fig. 17 shows the results if the capacitor is installed in parallel. When the capacitance becomes larger the antiresonant frequency becomes smaller and closes to resonant frequency. Thus, the resistance at resonant frequency becomes higher and the efficiency of wireless power transfer becomes worse. This way is not suitable for wireless power transfer.



(a) Capacitor in series (b) Capacitor in parallel

Fig. 14. Diagram of equivalent circuits of series resonance in an open ended helical antenna with installed capacitance.



(a) Capacitor in series (b) Capacitor in parallel

Fig. 15. Diagram of reactance with series resonance of the open ended helical antenna with capacitance

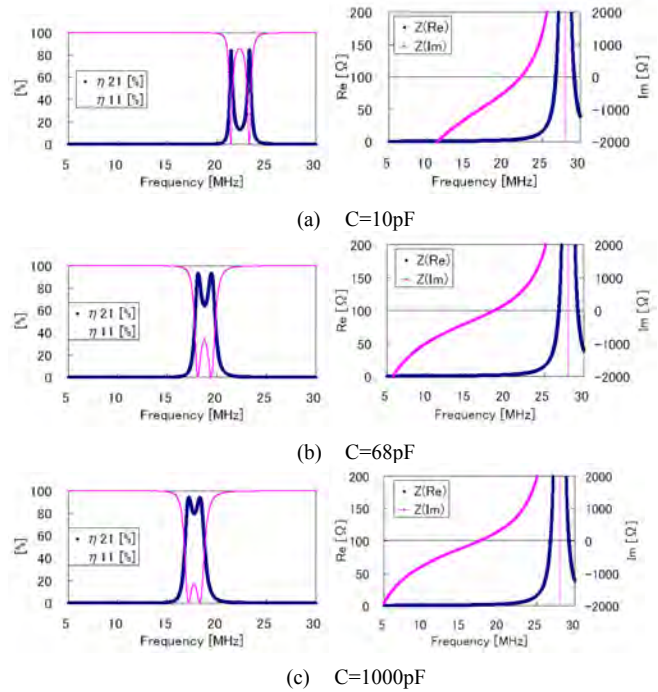
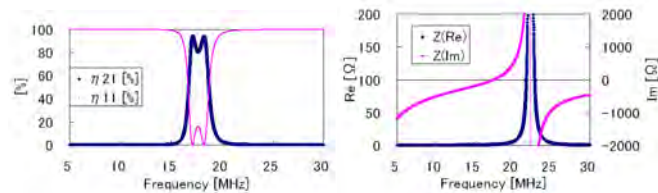


Fig. 16. Analysis results of open ended helical antennas with capacitor in series. Left are efficiencies of the transmitting antenna and the receiving antenna. Right are impedances in a single antenna.



(a) C=10pF



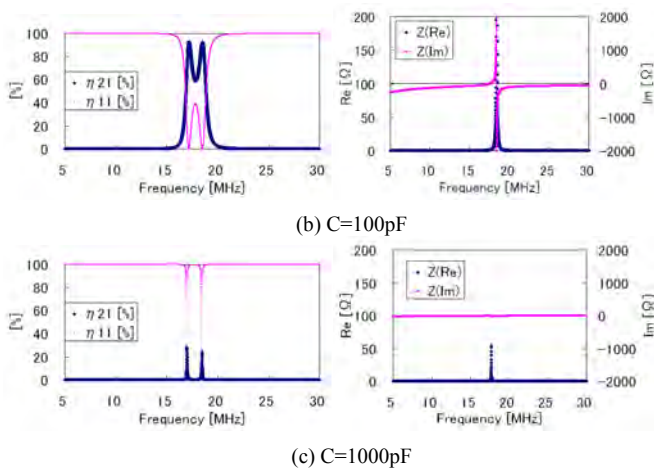


Fig. 17. Analysis results of open ended helical antenna with capacitor in parallel. Left are efficiencies of the transmitting antenna and the receiving antenna. Right are impedances at a single antenna

### V. SHORT ENDED HELICAL ANTENNAS WITH CAPACITOR

In this chapter, short ended helical antennas with a capacitor in series or parallel are studied. The short ended helical antennas create parallel resonance. Thus, in equivalent circuits, an antenna with an added capacitor in series is in Fig. 18(a) and an antenna with an added capacitor in parallel is Fig. 18(b). From equivalent circuits, diagrams of reactance are shown in Fig. 19. When the capacitor is in series, the circuits include series resonance of L and C. When the capacitance is small, the frequency becomes high. On the other hand, when the capacitor is in parallel, the capacitance is added to the capacitance of the antenna itself. Thus, the resonant frequency becomes small.

This is studied by electromagnetic field analysis. The results are shown in Fig. 20 when the capacitance  $C_s$  in series changes from 10pF to 1000pF. As well, the results are shown in Fig. 21 when the capacitance  $C_p$  in parallel changes from 10pF to 1000pF.

Fig. 20 shows the results of the capacitor in series. When the capacitance is small, the resonant frequencies become high. On the flip side, when the capacitance is large, the resonant frequencies become low and the frequencies are close to the results without the capacitor. If the capacitance is chosen correctly, the high efficiency wireless power transfer is possible. However, if the resonance frequency becomes much higher, the resonant frequency comes close to antiresonance frequency. As a result, resistance at resonant frequency becomes larger, e.g.) 4.5 ohm in Fig. 20 (a). Therefore, the efficiencies get worse. In comparing short ended helical antennas without a capacitor to short ended helical antennas with a capacitor in series, the case with a capacitor causes resonance. The antiresonance frequency does not change and only resonance frequency changes. The more resonance frequency moves away from the antiresonance frequency the more resistance moves toward the 0. With the capacitor in series in the short ended helical antenna, resonant frequency can be lower than the antiresonance frequency. However, it becomes worse if the resonant frequency is too small.

In comparing the open ended helical antenna in Fig. 4 to the short ended helical antenna in Fig. 11, the resonant frequency of the open ended helical antenna is equal to the antiresonance frequency of short ended helical antenna because the antennas operate as part of a transmission line. When the edges of the antennas switch from being forming an open end to forming a short end, the resonance frequency also switches to the antiresonance frequency. The short ended helical antenna with a capacitor in series can power at less frequency than the open ended helical antenna because the short ended helical antenna has a capacitor in series which causes resonance frequency to be less than the antiresonance frequency.

Fig. 21 shows the results when the capacitor is in parallel. The antiresonance becomes smaller as the capacitance become larger. Whatever the case, there is no resonance in these range so the efficiency of the wireless power transfer is low and this composition is not suitable for wireless power transfer.

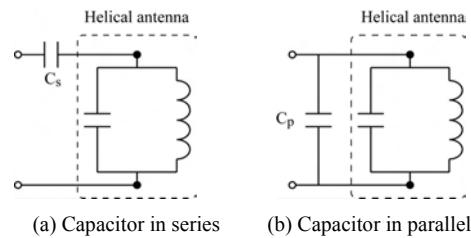


Fig. 18. Diagram of equivalent circuit of parallel resonance about short ended helical antenna with installed capacitance.

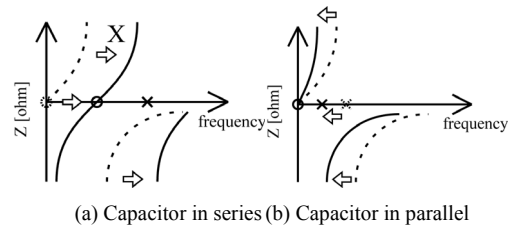
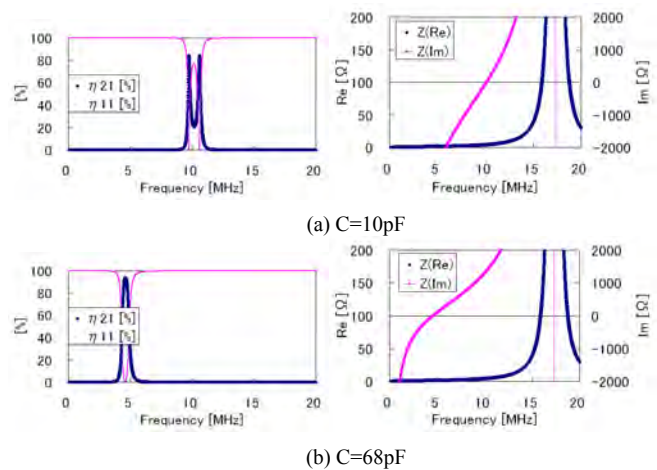
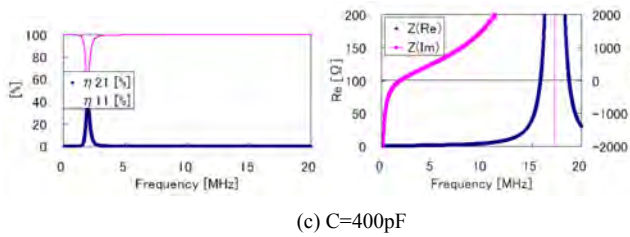


Fig. 19. Diagram of reactance with parallel resonance of the short ended helical antenna with the capacitance

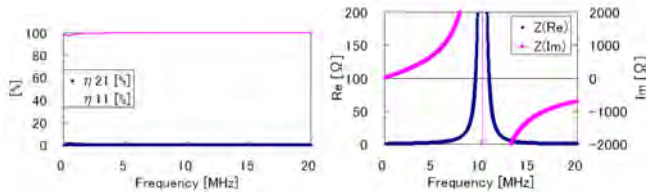


(b) C=68pF

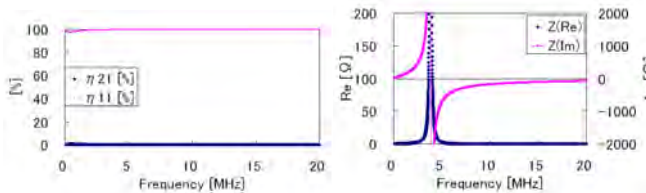


(c) C=400pF

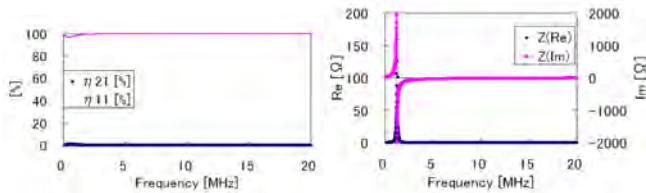
Fig. 20. Analysis results of short ended helical antennas with capacitor in series. Left are efficiencies of the transmitting antenna and the receiving antenna. Right are impedances at a single antenna.



(a) C=10pF



(b) C=100pF



(c) C=1000pF

Fig. 21. Analysis results of short ended helical antennas with capacitor in parallel. Left are efficiencies of the transmitting antenna and the receiving antenna. Right are impedances at a single antenna.

## VI. EXPERIMENTAL RESULTS OF HELICAL ANTENNAS WITH CAPACITOR IN SERIES

The open ended helical antenna which can make series resonance by itself or being installed with a capacitor in series and the short ended helical antenna which can also make series resonance by being installed with a capacitor in series are suited to the wireless power transfer that is indicated using electromagnetic field analysis in previous chapters. This is examined the experimentation in this chapter.

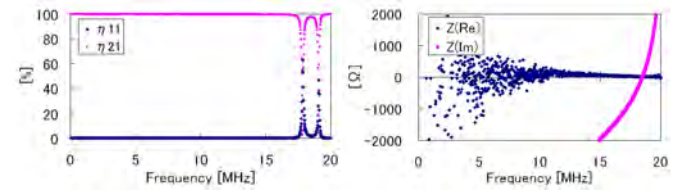
The experimentation is that the open end and short ended helical antennas with a capacitor in series. Fig. 22 shows the results when the open ended helical antenna is installed with a capacitor in series. Fig. 23 shows the results when the open ended helical antenna is installed with a capacitor in parallel.

Fig. 22 shows that when the capacitance becomes small, the resonance frequency becomes high and when the capacitance becomes large, the resonance frequency becomes low. The more the capacitance of the capacitor is large, the more the

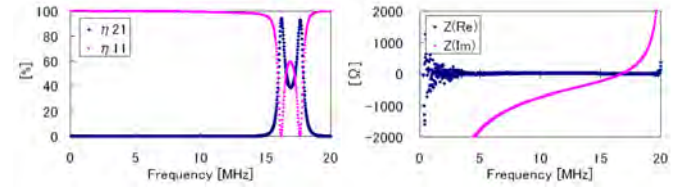
resonance frequency becomes far from the antiresonance frequency, and it becomes easier to power high efficiency. When the capacitor is in series in the open ended helical antenna the resonance frequency inevitably becomes higher than the resonance frequency of open ended helical antenna without the capacitor. These are confirmed by experimentation results.

Fig. 23 shows that the installed capacitor in series acts as it is in series with the inductance of antenna which cause series resonance. The high efficiency wireless power transfer in adjusting the capacitance is shown. These results indicate that the short ended helical antenna in series can operated at lower frequencies than the open ended helical antenna. This is confirmed by experimentation.

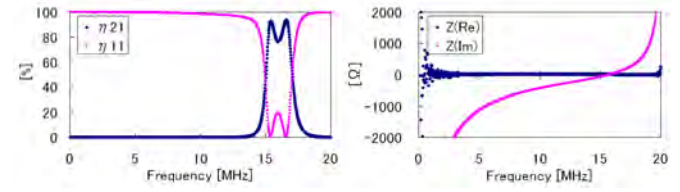
As above, the result of experimentation is almost the same as the results of the electromagnetic field analysis.



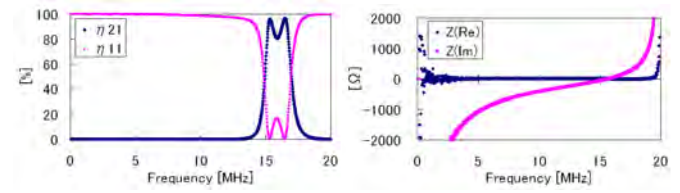
(a) C=10pF



(b) C=68pF

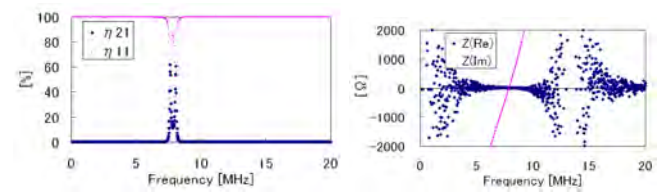


(c) C=1000pF

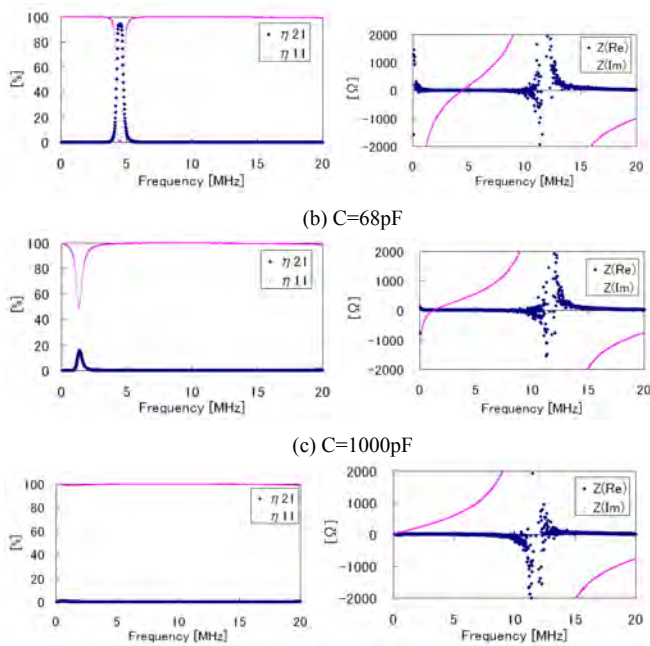


(d) Open ended helical antenna without capacitor

Fig. 22. Experimental results of open ended helical antenna with capacitor in series. Left are efficiencies of the transmitting antenna and the receiving antenna. Right are impedances at a single antenna.



(a) C=10pF



(d) Short ended helical antenna without capacitor

Fig. 23. Experimental results of short ended helical antenna with capacitor in series. Left are efficiencies of the transmitting antenna and the receiving antenna. Right are impedances at a single antenna.

## VII. CONCLUSION

The characteristics of the open and short ended helical antennas with a capacitor in series and parallel are studied. For the purpose of high efficiencies in wireless power transfer, the series resonance is useful. To this end, just the open ended helical antenna, the open ended helical antenna with capacitor in series and the short ended helical antenna with capacitor in series is very useful. When the open ended helical antenna was installed the capacitor in series, the resonant frequency becomes high. On the other hand, the short ended helical antenna with an installed capacitor in series causes the resonance and the resonant frequency to be lower than the open ended helical antenna. Therefore, the short ended helical antenna with a capacitor in series can transfer high efficiency power at lower frequencies. For high efficiency wireless power transfer, resistance of input impedance needs to be close to 0 ohms. Thus, the resonance frequency should be apart from the antiresonance frequency. Experimental results verify that open and short ended helical antennas with a capacitor in series can power wirelessly with a high efficiency.

## REFERENCES

- [1] J. Yungtaek and M. M. Jovanovic, "A contactless electrical energy transmission system for portable-telephone battery chargers," *IEEE Trans. Ind. Electron.*, vol. 50, no. 3, pp. 520-527, 2003.
- [2] K. Hatanaka, F. Sato, H. Matsuki, S. Kikuchi, J. Murakami, M. Kawase and T. Satoh, "Power transmission of a desk with a cord-free power supply", *IEEE Transactions on Magnetics* 38 (September (5)) (2002), pp. 3329-3331.
- [3] A. Alden, T. Ohno, "A POWER RECEPTION AND CONVERSION SYSTEM FOR REMOTELY-POWERED VEHICLES", *ICAP 89 Antennas and Propagation*, vol.1, pp535-538, Apr. 1989.

- [4] Chwei-Sen Wang, Stielau O.H., Covic G.A., "Design Considerations for a Contactless Electric Vehicle Battery Charger", *IEEE Transactions on Industrial Electronics*, vol.52, Issue5, pp1308-1314, 2005.
- [5] Y. Kamiya, T. Nakamura, T. Sato, J. Kusaka, Y. Daisho, S. Takahashi, K. Narusawa, "Development and performance evaluation of advanced electric micro bus equipped with non-contact inductive rapid-charging system", *Proceedings of the 23rd international electric vehicle symposium (EVS), Electric/ hybrid-electric session*, pp. 1- 14, 2007. 12
- [6] Sato F., Murakami J., Matsuki H., Kikuchi S., Harakawa K., Satoh T., "Stable Energy Transmission to Moving Loads utilizing New CLPS", *IEEE Transactions on Magnetics*, Vol.32, No.2, pp.5034-5036, 1996.
- [7] Sato, F., Murakami, J., Suzuki, T., Matsuki, H., Kikuchi, S., Harakawa, K., Osada, H., Seki, K., "CONTACTLESS ENERGY TRANSMISSION TO MOBILE LOADS BY CLPS -TEST DRIVING OF AN EV WITH STARTER BATTERIES", *IEEE Transactions on Magnetics*, Vol.33, No.2, pp.4203-4205, 1997.
- [8] Zhang Bingyi, Liu Hongbin, Zhao Yisong, Ying Yong, Feng Guihong, "Contactless Electrical Energy Transmission System Using Separable Transformer", *Proceedings of the Eighth International Conference on Electricalmachines and Systems*, Vol.3, pp.1721-1724, 2005.
- [9] HIDEKI AYANO, HIROSHI NAGASE, HIROMI INABA, "A Highly Efficient Contactless Electrical Energy Transmission System", *Electrical Engineering in Japan*, Vol.148, No.1, 2004.
- [10] KAMIYA Yushi , NAKAMURA Kouji , NAKAMURA Toru , DAISHO Yasuhiro , TAKAHASHI Shunsuke , YAMAMOTO Kitao , SATO Takeshi , MATSUKI Hidetoshi , NARUSAWA Kazuyuki, "Development and Performance Evaluation of a Non-contact Rapid Charging Type Inductive Power Supply (IPS) System for Electric Vehicles (First Report) : Design Optimization of Track & Pick up Part of IPS and Performance Evaluation of the System", *Transactions of the Society of Automotive Engineers of Japan*, 38(6), pp.175-180,2007.11.
- [11] Brown W.C., "Status of the Microwave Power Transmission Components for the Solar Power Satellite", *IEEE Transactions on Microwave Theory and Techniques*, vol.Mtt-29, NO.12, December 1981.
- [12] N. Shinohara, H. Matsumoto, "Wireless Charging System by Microwave Power Transmission for Electric Motor Vehicles", *IEICE. C*, Vol.J87-C, No.5, pp.433-443, 2004.
- [13] Brown W.C., "The History of Power Transmission by Radio Waves", *IEEE Trans. MTT*, Vol.32, No.9, 1984, pp.1230-1242
- [14] André Kurs, Aristeidis Karalis, Robert Moffatt, J. D. Joannopoulos, Peter Fisher, Marin Soljačić, "Wireless Power Transfer via Strongly Coupled Magnetic Resonances," in *Science Express* on 7 June 2007, Vol. 317. no. 5834, pp. 83 – 86.
- [15] Aristeidis Karalis, J.D. Joannopoulos and Marin Soljačić, "Efficient wireless non-radiative mid-range energy transfer," *Annals of Physics*, Volume 323, Issue 1, January 2008, Pages 34-48, January Special Issue 2008.
- [16] Hong, J.-S., "Couplings of asynchronously tuned coupled microwave resonators," *Microwaves, Antennas and Propagation, IEE Proceedings*, Volume 147, Issue 5, pages 354-358, Oct 2000.
- [17] T. Kawaguchi, Z. Ma, Y. Kobayashi, "Design of an Elliptic Function Bandpass Filter Using Microstrip Spiral Resonators", *The transactions of the Institute of Electronics, Information and Communication Engineers. C*, J88-C(12), pp.1040-1048, 2005.
- [18] Takehiro Imura, Toshiyuki Uchida, Yoichi Hori, "Experimental Analysis of High Efficiency Power Transfer using Resonance of Magnetic Antennas for the Near Field - Geometry and Fundamental Characteristics -", *IEE Japan Industry Applications Society Conference*, No.2-62, pp.539-542, Kochi, Japan, 2008.8.
- [19] Takehiro Imura, Yoichi Hori, "Wireless Power Transfer using Electromagnetic Resonant Coupling", *The Journal of The Institute of Electrical Engineers of Japan*, Vol.129, No.7, 2009.7.
- [20] Takehiro Imura, Hiroyuki Okabe, Toshiyuki Uchida, Yoichi Hori, "Study on Open and Short End Helical Antennas with Capacitor in Series of Wireless Power Transfer using Magnetic Resonant Couplings", *Proceedings of the 35th Annual Conference of the IEEE Industrial Electronics Society, IECON 2009*, pp. 3884-3889, Nov 3-5, 2009.



**Takehiro Imura** (S'09) received the B.S. degrees in electrical and electronics engineering from Sophia University, Tokyo, Japan and received the M.S degree from in Electronic Engineering from the University of Tokyo in 2007 and proceeded to Ph.D. course in Electrical Engineering of the University of Tokyo. He is now researching the wireless power transfer for EVs using electromagnetic resonant couplings.



**Okabe Hiroyuki** received the B.S. degrees in electrical and electric Systems engineering from Saitama University in 2008, Saitama, Japan and proceeded to M.S course in Electrical Engineering of the University of Tokyo. He is now researching the wireless power transfer for EVs using electromagnetic resonant couplings.



**Yoichi Hori** (S'81–M'83–SM'00–F'05) received the B.S., M.S., and Ph.D. degrees in electrical engineering from The University of Tokyo, Tokyo, Japan, in 1978, 1980, and 1983, respectively.

In 1983, he joined the Department of Electrical Engineering, The University of Tokyo, as a Research Associate, where he later became an Assistant Professor, an Associate Professor, and, in 2000, a Professor. In 2002, he moved to the Institute of Industrial Science as a

Professor in the Information and System Division and, in 2008, to the Department of Advanced Energy, Graduate School of Frontier Sciences, The University of Tokyo. During 1991–1992, he was a Visiting Researcher with the University of California, Berkeley. His research fields include control theory and its industrial applications to motion control, mechatronics, robotics, electric vehicles, etc.

Prof. Hori has been the Treasurer of the IEEE Japan Council and Tokyo Section since 2001. He was the recipient of the Best Paper Award from the IEEE TRANSACTIONS ON INDUSTRIAL ELECTRONICS in 1993 and 2001 and of the 2000 Best Paper Award from the Institute of Electrical Engineers of Japan (IEEJ). He is a member of the Society of Instrument and Control Engineers, the Robotics Society of Japan, the Japan Society of Mechanical Engineers, the Society of Automotive Engineers of Japan, etc. He is currently the President of the Industry Applications Society of the IEEJ, the President of the Capacitors Forum, and the Chairman of the Motor Technology Symposium of the Japan Management Association.

# Basic Experimental Study on Helical Antennas of Wireless Power Transfer for Electric Vehicles by using Magnetic Resonant Couplings

Takehiro Imura\*, Hiroyuki Okabe\*\* and Yoichi Hori\*\*\*

\*Department of Electrical Engineering, The University of Tokyo, Tokyo, Japan. Email: imura@horilab.iis.u-tokyo.ac.jp

\*\*Department of Electrical Engineering and Information Systems, The University of Tokyo, Tokyo, Japan.  
Email: okabe@horilab.iis.u-tokyo.ac.jp

\*\*\*Institute of Industrial and Science, The University of Tokyo, Tokyo, Japan. Email: hori@iis.u-tokyo.ac.jp

**Abstract**—Wireless power transfer is required for diffusion of Electric Vehicles (EVs), because it can make the process of the automatic charging system of EVs. The technology of wireless power transfer requires three main elements: large air gaps, high efficiency and a large amount of power. However, there is no principle to be realized. Recently, the technology of electromagnetic resonant coupling is proposed and is named WiTricity. With this technology, there are large air gaps, high efficiency and large amount of power. In this paper, feasibility of wireless power transfer for EV by electromagnetic resonance coupling is studied. We make small size antennas that can be equipped on the bottom of a vehicle and we studied the electrical characteristics of the antenna by equivalent circuits, electromagnetic analysis and experimentation. The length of air gaps between a transmitting antenna and a receiving antenna affect resonance frequencies. The resonance frequency changes from two to one depending on the length of air gaps. Until a certain distance, maximum efficiencies are not changed. Large air gaps are weak couplings. In the weak coupling at resonance, magnetic resonance couplings can transfer energy with high efficiency. The specifications results at high power are proposed. In this paper, the feasibility of wireless power transfer with large air gaps and high efficiency by small sized antennas that can be equipped for EVs is proposed.

**Keywords** - Contactless power transfer, Wireless, Resonance, Coupling, Magnetic

## I. INTRODUCTION

Wireless power transfer is required for diffusion of Electric Vehicles (EVs), because it can make convenient charging system of EVs. This system can be provided automatic charging systems for the consumer market. When one parks the car, the system charges power to your EV automatically by wireless power transfer. EV needs to be charged once a day. Typically, you would use a code and plug in your EV at home, but you don't need it if you use wireless power transfer technology.

The technology of wireless power transfers, electromagnetic induction and microwave power transfer are famous, however, electromagnetic resonance coupling have only been proposed recently [1][5]. The technology of wireless power transfer

requires three main elements: large air gaps, high efficiency and a large amount of power. The electromagnetic resonance coupling is the only technology that deals with large air gaps, high efficiency and large amounts of power. Until now, this phenomenon was explained by the mode coupling theory; however, the size of antennas is too big to be equipped on the bottom of EVs. The characteristics of antennas and relation between power and efficiency are not proposed, in this theory.

In this paper, however, we consider the antenna size for EVs. We use small antennas that can be equipped on the bottom of EVs. The characteristics of antennas, relation of air gaps, frequency and relation of power and efficiency are shown.

## II. SYSTEM OF WIRELESS POWER TRANSFER AND CONFIGURATION OF EXPERIMENT

The entire system of wireless power transfer for EVs are shown in Fig. 1. A high frequency power source distributes power through transmitting antenna. The transmitting antenna sends energy to a receiving antenna using electromagnetic resonance couplings wirelessly. The energy with high frequencies are rectified and charged by batteries or electric double layer capacitors (EDLCs) which are the energy storage mediums.

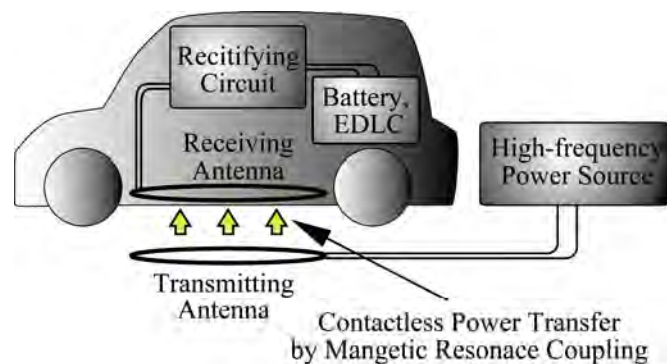


Fig. 1 Concept of contactless power transfer system for EV

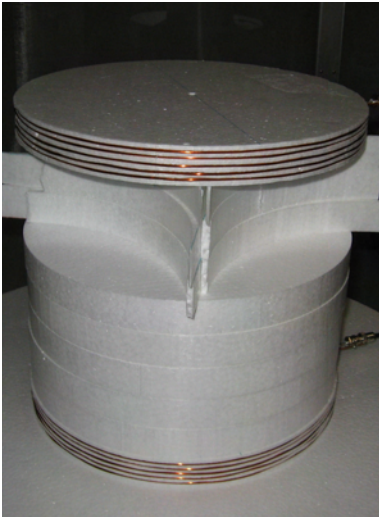


Fig. 2 Transmitting of antenna and Receiving antenna



Fig. 3 Shielded room

In this paper we will study the antenna, which is very important in wireless power transfer because it decide how large the air gaps and efficiency are. We will consider only the antenna size that can be equipped on the bottom of EVs and use 150mm radius antennas (Fig. 2). The transmitting antenna and the receiving antenna are same. Electromagnetic resonance coupling can not radiate like microwave power transfer. Electromagnetic resonance couplings transfer power by connecting the electromagnetic fields of the two antennas to form a link that does not allow power to radiate outward, and thus conserves energy. The experiment was held in a shielded room at the University of Tokyo (Fig. 3).

The Parameters of the antenna are shown in Fig. 4 and table 1. Through a coaxial cable, bottom transmitting antenna is fed power. The power is transferred to top receiving antenna with wireless magnetic resonance coupling. The experimental set up is shown in Fig. 5. Reflection  $S_{11}$  and transmission  $S_{21}$  is measured by the vector network analyzer (VNA). Ratio of power reflection is  $\eta_{11}$  and transmission is  $\eta_{21}$  defined by equations (1) and (2). Ratio of power transmission means efficiency of power transfer.

$$\eta_{11} = S_{11}^2 \times 100 \quad [\%] \quad (1)$$

$$\eta_{21} = S_{21}^2 \times 100 \quad [\%] \quad (2)$$

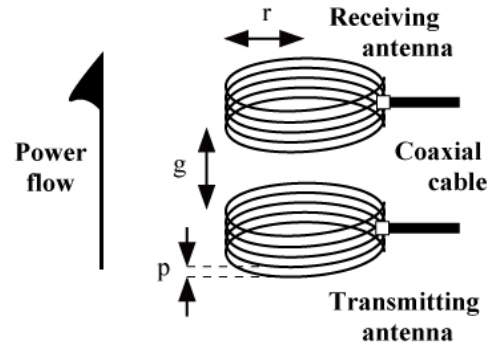


Fig. 4 Parameters of antennas

Table 1 Parameters of antennas

Parameters	Values
radius	$r = 150 \text{ mm}$
pitch	$p = 3 \text{ mm}$
wire size	$w = 2 \text{ mm}$

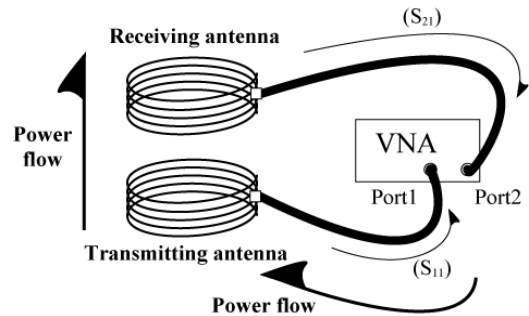


Fig. 5 Experimental set up

### III. EXPERIMENTAL RESULT AND REVIEW BY EQUIVALENT CIRCUITS

The experiment's results are shown in Fig. 6. In this case, air gaps are short  $g = 100\text{mm}$  and  $g = 150\text{mm}$ . Resonant frequencies divide into two frequencies that are shown in Fig. 6 (a) and (b). In this case, at resonant frequencies efficiency of power transfer is very high and approximately 97% power can be transfer from a transmitting antenna to a receiving antenna. When the air gaps are changed, resonant frequencies are changed but maximum efficiency is not changed. In this case,

air gaps become long-approximately  $g \approx 200\text{mm}$  and two resonant frequencies become one. Maximum efficiency is still the same as two frequencies; however, thus it is 97% that is shown in Fig. 6 (c). The longer the air gaps become, the more efficiency is lost. In this case, air gaps are 250mm and the efficiency becomes 80% (Fig. 6 (d)).

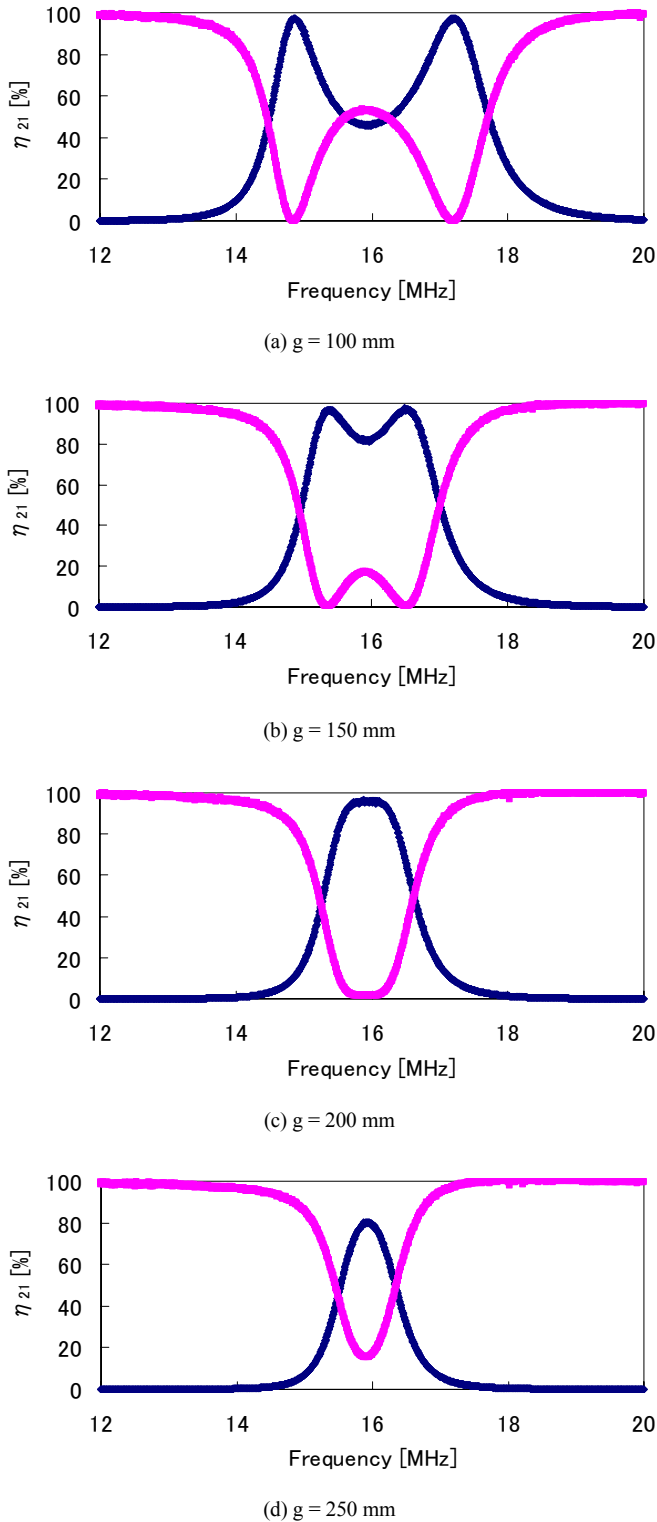


Fig. 6 Experimental result of efficiency in each gap

The relation of maximum efficiency to air gaps is shown in Fig. 7. The results of electromagnetic analysis were conducted by the Method of Moment process (Cal.) and the results (Exp.) are shown. Two resonant frequencies are  $f_m$  and  $f_e$  ( $f_m < f_e$ ). The efficiency in Fig. 7 is the efficiency at  $f_m$ . The relation of resonant frequencies to air gaps is shown in Fig. 8. The relation of coefficient couplings to air gaps is shown in Fig. 9. The coupling coefficients during experiment had small errors these were caused by characteristic impedance.

When air gaps are large, the coupling coefficients become small. Nevertheless, the efficiency of power transfer is very high. By electromagnetic analysis, when air gaps are  $g = 200\text{mm}$ , the couplings coefficient is only  $k=0.057$ . This means, in wireless power transfer using magnetic resonant couplings, if the coupling is weak, the electromagnetic resonance coupling can still transfer power enough to have large air gaps.

The coupling coefficient is set up by two resonant frequencies. The equivalent circuit of the magnetic resonance coupling is shown in Fig. 10. The only loss is copper, and in this case we ignore resistance  $R$  in order to prevent the equation from becoming complicated. As well, the loss is so small that it is insignificant. So, in this equation,  $R = 0$ .  $L$  is self induction and  $C$  is capacitance. These are decided by the distribution parameter system. The coupling coefficient is represented by mutual inductance  $L_m$ . The transmission  $S_{21}$  is equivalent (3). Then efficiency of power transfer is set up by equivalent (3) and (2). Equivalent (4) is delivered by resonant condition that leads to two equivalent frequencies in equivalent (5) and (6). By two resonant frequencies, the coupling coefficient is lead to equation (7). Angular frequency is  $\omega$ .  $Z_0$  is characteristic impedance.

$$S_{21}(\omega) = \frac{2jL_m Z_0 \omega}{L_m^2 \omega^2 - \left(\omega L - \frac{1}{\omega C}\right)^2 + 2jZ_0 \left(\omega L - \frac{1}{\omega C}\right) + Z_0^2} \quad (3)$$

$$\frac{1}{\omega L_m} + \frac{2}{\omega(L - L_m) - \frac{1}{\omega C}} = 0 \quad (4)$$

$$\omega_m = \frac{\omega_0}{\sqrt{1+k}} = \frac{1}{\sqrt{(L + L_m)C}} \quad (5)$$

$$\omega_e = \frac{\omega_0}{\sqrt{1-k}} = \frac{1}{\sqrt{(L - L_m)C}} \quad (6)$$

$$k_m = \frac{L_m}{L} = \frac{\omega_e^2 - \omega_m^2}{\omega_e^2 + \omega_m^2} \quad (7)$$

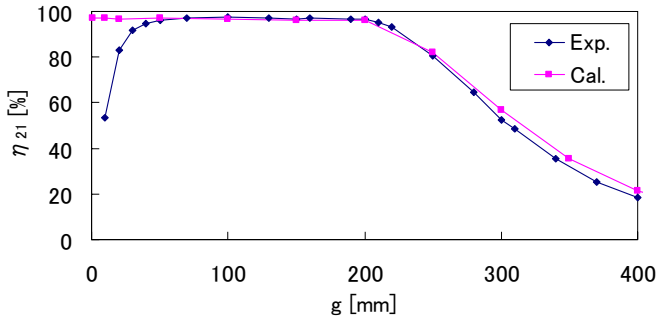


Fig. 7 Air gaps  $g$  vs. efficiency of power transfer  $\eta_{21}$

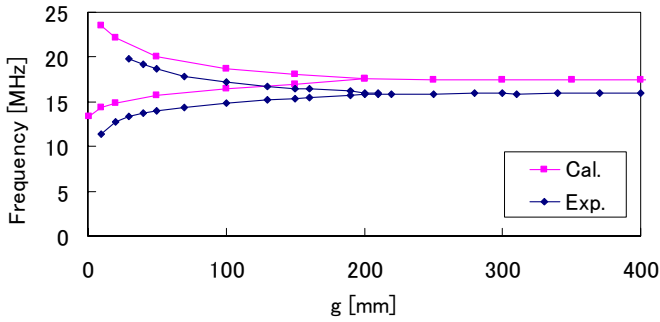


Fig. 8 Air gaps  $g$  vs. two resonant frequencies  $f_m$  and  $f_e$  ( $f_m < f_e$ )

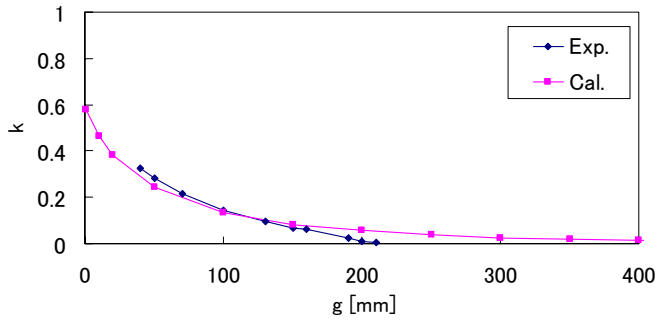


Fig. 9 Air gaps  $g$  vs. coupling coefficient  $k$

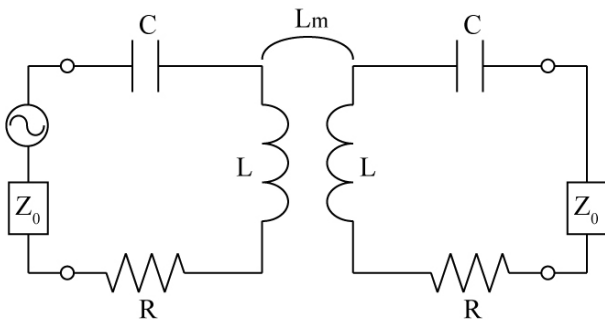


Fig. 10 Equivalent circuit of magnetic resonant coupling

#### IV. EXPERIMENTAL RESULT OF RELATION EFFICIENCY TO POWER

Theoretically, the efficiency of power transfer does not depend on amount of power. Experimental verification is needed, however, because the effect of heat, arc, etc. is not known until the fact that the power efficiency is constant is confirmed. The air gap is 200mm and the frequency is set maximum efficiency 15.9MHz. The power is changed from -15dBm to 5dBm. This result is shown in Fig. 11. The result shows the efficiencies are approximately 95-96% and is almost constant.

(We will propose the result at maximum power will be 100W in the full paper.)

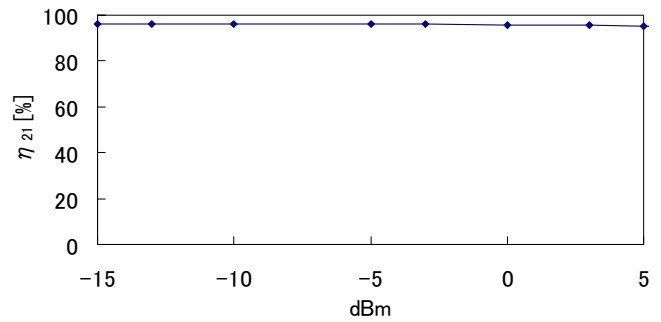


Fig. 11 Power vs. efficiency

#### V. CONCLUSIONS

Characteristics of antennas for magnetic resonance couplings are studied by equivalent circuits, electromagnetic analysis and experimentation. The antenna's size is small to be equipped to the bottom of EVs. The resonant frequencies change from two points to one point depending on the length of air gaps. Until a certain distance, the maximum efficiencies at resonant frequency are not changed. The efficiencies are approximately 95-97%. Wireless power transfer is possible when coupling coefficient  $k=0.057$ . Weak couplings can transfer power wirelessly though they have large air gaps. Characteristics of efficiency at high power are shown.

#### REFERENCES

- [1] Y. Kamiya, T. Nakamura, T. Sato, J. Kusaka, Y. Daisho, S. Takahashi, K. Narusawa, "Development and performance evaluation of advanced electric micro bus equipped with non-contact inductive rapid-charging system", Proceedings of the 23rd international electric vehicle symposium (EVS), Electric/hybrid-electric session, pp. 1- 14(CD-ROM). 2007. 12
- [2] Brown W.C., "Status of the Microwave Power Transmission Components for the Solar Power Satellite", IEEE Transactions on Microwave Theory and Techniques, vol.Mtt-29, NO.12, December 1981.
- [3] N. Shinohara, H. Matsumoto, "Wireless Charging System by Microwave Power Transmission for Electric Motor Vehicles",



IEICE. C, Vol.J87-C, No.5, pp.433-443, 2004.

- [4] André Kurs, Aristeidis Karalis, Robert Moffatt, J. D. Joannopoulos, Peter Fisher, Marin Soljačić, “Wireless Power Transfer via Strongly Coupled Magnetic Resonances,” in Science Express on 7 June 2007, Vol. 317. no. 5834, pp. 83 – 86.
- [5] Aristeidis Karalis, J.D. Joannopoulos and Marin Soljačić, “Efficient wireless non-radiative mid-range energy transfer,” Annals of Physics, Volume 323, Issue 1, January 2008, Pages 34-48, January Special Issue 2008.

# Basic Study of Improving Efficiency of Wireless Power Transfer via Magnetic Resonance Coupling Based on Impedance Matching

Teck Chuan Beh\*, Takehiro Imura\*, Masaki Kato\*\* Yoichi Hori\*\*

\*Department of Electrical Engineering

\*\*Department of Advanced Energy

The University of Tokyo, Tokyo, Japan

E-mail: beh@horilab.iis.u-toko.ac.jp, imura@horilab.iis.u-toko.ac.jp,

kato@horilab.iis.u-toko.ac.jp, hori@horilab.iis.u-toko.ac.jp

**Abstract**-Wireless power transfer is essential for the spread of Electric Vehicle(EV) usage as it provides a safe and convenient way to charge the EVs. Recently, a highly efficient mid-range wireless power transfer technology using electromagnetic resonance coupling, WiTricity, was proposed. Studies show that the resonant frequencies of the two antennas change according to the air gap in between the antennas. To achieve maximum efficiency using this system, the resonance frequencies of the antennas and the frequency of the system has to be matched. However, when this technology is applied in the MHz range (which allows small sized antennas), the usable frequency is bounded by the Industry-Science-Medical(ISM) band. Hence a method to fix the resonance frequency within the ISM band is required. In this paper, the possibility of using impedance matching (IM) networks to adjust the resonance frequency of a pair of antennas at a certain distance to 13.56MHz is studied. We studied the electrical characteristics of the antenna with equivalent circuits, electromagnetic analysis and experiments. The equivalent circuits are used as reference to calculate the parameters of the IM circuits. The simulations and experiments shows that the IM circuits can change the resonance frequency to 13.56MHz for different air gaps, thus improving the power transfer efficiency.

**Key Words**- Wireless power transfer, Resonance, Coupling, Magnetic, Impedance matching,

## I. INTRODUCTION

Nowadays, with the development of mobile appliances such as mobile phones and laptops, as well as the recent boom of EVs, the need for a technique to wirelessly charge these applications has increased. Wireless power transfer is essential in the spread of EV usage as it provides a safe and convenient way of charging EVs. An EV has to be charged a lot more frequently than a regular gasoline engine car as its energy storage medium (battery or capacitor) has a much lower energy density compared to petroleum. Therefore, a wireless power transfer system can be used in the automatic charging system which makes charging the EVs more convenient. Also, as the process of plugging the power cord into the socket will be unnecessary, the danger of being electrocuted due to the wear and tears of an old cord, or rain will be avoided, making the charging process safer. For

example, the power transmitting antenna can be placed in the car park, and the receiving antenna can be placed in the car. This enables the EV to be charged wirelessly just by being in the parking box. To achieve this, the wireless power transfer system must satisfy these three conditions: high efficiency, large air gaps, and high power.

Presently, the most popular wireless power transfer technologies are the electromagnetic induction, and the microwave power transfer. However, the electromagnetic induction has a short range, and microwave power transfer has a low efficiency as it uses radiation. Recently, a highly efficient mid-range wireless power transfer technology using electromagnetic resonance coupling, WiTricity, was proposed. It satisfies all three conditions to make wirelessly charging EVs possible as it has a high efficiency at mid range (approximately 90% at 1m and 50% at 2m [1] at 60W).

Until now, this phenomenon was explained using the Mode Coupling theory. However, this theory is often complicated, and inconvenient when it comes to designing the circuits around the system.

In this paper, we study this phenomenon using antenna design theories and circuit design theories. The characteristics of the antennas are explained using equivalent circuits, electromagnetic analysis, and experiments. The frequency characteristics of the antennas and the relation to its efficiency are studied, and a tuning circuit is inserted to increase its efficiency by changing the resonance frequency to match the frequency of the power source. The parameters of the tuning circuit are calculated based on the equivalent circuit and impedance matching theories. Its effects are studied with experiments and simulations.

## II. WIRELESS POWER TRANSFER SYSTEM USING MAGNETIC RESONANCE COUPLING

### *Wireless Power Transfer System*

As shown in Fig. 1, the wireless power transfer system involves resonating two identical antennas with a high frequency power source. The power is transmitted through magnetic resonance coupling in between the two antennas at the resonance frequencies. The power transmitted to the receiving antenna is then rectified and used to charge energy

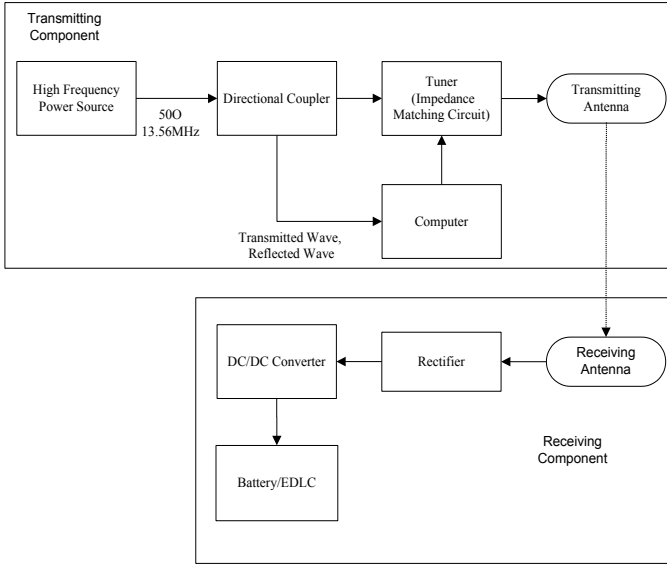


Fig. 1. Wireless Power Transfer System with Tuning Circuit

storage mediums such as batteries and electric double later capacitors (EDLC).

In the system that involves changing the resonance frequency of the antennas, a directional coupler is installed before the transmitting antenna to measure the transmitted power and reflected power in between the antennas. The measured values are input into a computer (PC) which is used to control the parameters of the IM circuit. The IM circuit functions as a tuner to change characteristics of the antennas so that the resonance frequency can be adjusted.

#### Equivalent circuits

Electromagnetic resonance coupling involves creating an LC resonance, and transferring the power with electromagnetic couplings without radiating electromagnetic waves. Hence, the magnetic coupling and electric coupling can be represented as mutual inductance and mutual capacitance respectively as shown in Fig. 2.

$Z_0$  in Fig. 2 represents the characteristic impedance, and  $R_{load}$  is the impedance of the load. The ohm loss and the radiation loss of the antennas are represented by  $R$ . In this paper, the power is transferred via magnetic coupling. Therefore the coupling can be represented by mutual induction  $L_m$ .

Next the resonance frequency is calculated based on the equivalent circuit. To satisfy the resonance condition, the reactance of Fig.2 must be 0, as in equation (1). The condition in equation (1) can be satisfied by two resonant frequencies as calculated in equation (2) and (3). The coupling coefficient  $k$  can be calculated from equation (2) and (3) to become equation (4)

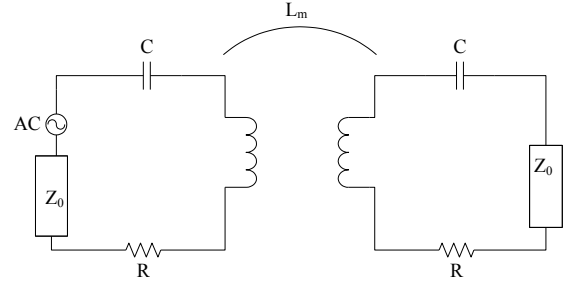


Fig. 2. Equivalent Circuit of Power Transfer System Without Tuning Circuit

$$\frac{1}{\omega L_m} + \frac{2}{\omega(L - L_m) - \frac{1}{\omega C}} = 0 \quad (1)$$

$$\omega_m = \frac{\omega_0}{\sqrt{1+k}} = \frac{1}{\sqrt{(L + L_m)C}} \quad (2)$$

$$\omega_e = \frac{\omega_0}{\sqrt{1-k}} = \frac{1}{\sqrt{(L - L_m)C}} \quad (3)$$

$$k = \frac{L_m}{L} = \frac{\omega_e^2 - \omega_m^2}{\omega_e^2 + \omega_m^2} \quad (4)$$

Next, the efficiency of the power transfer is calculated based on the equivalent circuit. The ratio of power reflection  $\eta_{11}$  and transmission  $\eta_{21}$  can be defined by equations (5) and (6), where  $S_{11}$  is the reflected wave and  $S_{21}$  is the transmitted wave. To simplify the calculations,  $R$  is considered to be  $0\Omega$ . Here,  $S_{21}$  can be calculated with equation (7)[2].

$$\eta_{11} = S_{11}^2 \times 100[\%] \quad (5)$$

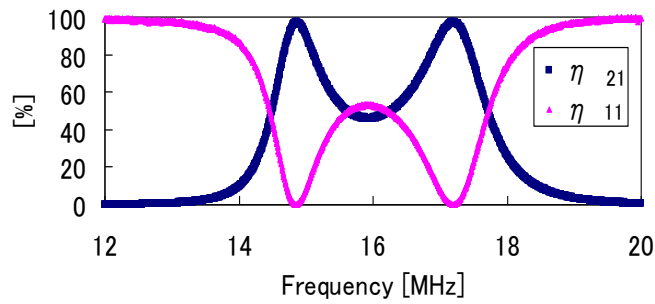
$$\eta_{21} = S_{21}^2 \times 100[\%] \quad (6)$$

$$S_{21} = \frac{2jL_m Z_0 \omega}{L_M^2 \omega^2 - (\omega L - \frac{1}{\omega C})^2 + 2jZ_0(\omega L - \frac{1}{\omega C}) + Z_0^2} \quad (7)$$

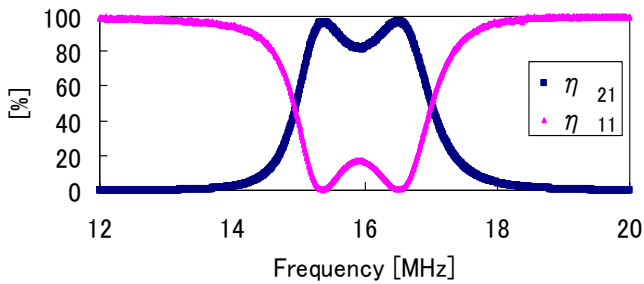
#### Frequency Characteristics

As the air gap between the antennas increases, the coupling in between the antennas weakens, and the coupling coefficient will be smaller. Therefore, the impedance of the circuit will change as the air gap changes, thus affecting the power transfer efficiency.

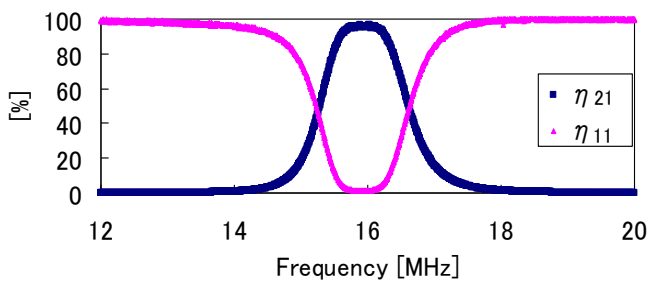
Fig. 3 shows the ratio of power reflection  $\eta_{11}$  and transmission  $\eta_{21}$ , and the frequency characteristics of the system when the air gap ( $g$ ), is changed in between 100mm-250mm. The antenna used here is a self resonating 5 turn, 150mm radius, 5mm pitch, open type helical antenna. Fig. 4 shows the relationship of the coupling factor and the air gap.



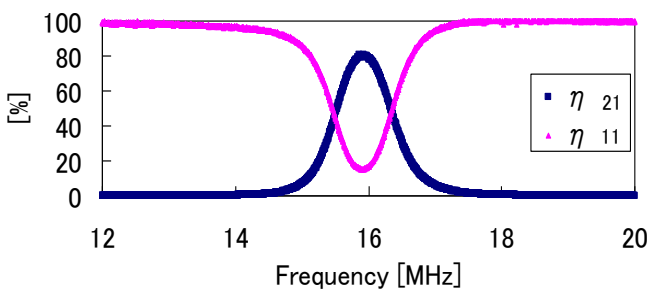
(a) gap = 100mm



(b) gap = 150mm



(c) gap = 200mm



(d) gap = 250mm

Fig. 3. The efficiency vs frequency graph for each gap [2]

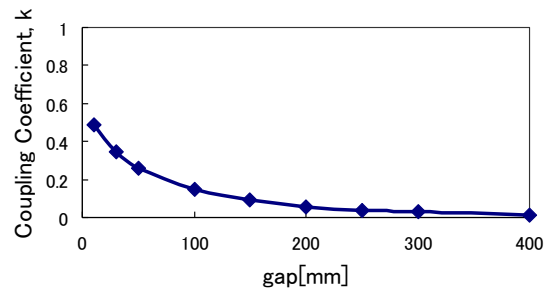


Fig. 4. Coupling factor and air gap [2]

As shows in the figures above, when the gaps are small and the coupling is strong, there exist two resonance frequencies that permit maximum efficiency power transfer. As the gap becomes larger, the two resonance frequencies moves closer to each other and eventually becomes one. If the gap gets even larger, the maximum efficiency will drop.

### ISM Band

As stated in the section above, the resonance frequency changes as the coupling factor changes, and the maximum efficiency power transfer occurs at the resonance frequency. Therefore, a system that matches the frequency of the power source and the resonance frequency is needed. There are two ways to achieve resonance. One is to match the frequency of the power source to the resonance frequency, and the other is to match the resonance frequency to the power source. The former can be easily achieved by applying a feedback control for the efficiency to the power source. However, when this power transfer system is applied in the MHz range, the usable frequency range is bounded by the Industry-Science-Medical(ISM) band. According to the ISM band, the usable frequency ranges are extremely small. For example at 13.56MHz, the range is  $13.56\text{MHz} \pm 7\text{kHz}$ .

As a result, to apply this technology in the MHz range, the frequency of the power source must be fixed at a usable range, and a tuner must be used to match the resonance frequency of the antennas to the frequency of the power source. In this

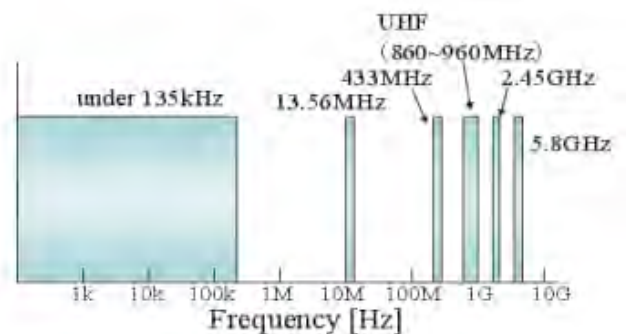


Fig. 5. ISM Band

paper, a tuner based on the impedance matching theory is used to match the resonant frequency of the antennas to the frequency of the power source that is fixed at 13.56MHz.

#### IMPEDANCE MACHING

Impedance matching is a technique commonly used in power transfer systems and communication systems to improve the efficiency of the system. In theory, the resonance frequency of the antenna can be matched to a particular frequency by using this technique. This section briefly explains the theory behind this technique, and studies its effect using simulation.

In Fig. 6, when the impedance of the power source is defined as  $Z_{source}$  and that of the load is defined as  $Z_{load}$ , the power transferred to the load is written in equation (8). The power transferred to the load reaches its maximum when  $Z_{source}=Z_{load}$ , as in equation (9). Therefore, when the impedance of the load in the source's point of view matches  $Z_{source}$ , the circuit is considered matched and the maximum efficiency is achieved.

$$P = I^2 Z = \frac{V^2}{Z_{source}} \left( \frac{1}{\frac{Z_{source}}{Z_{load}} + 2 + \frac{Z_{load}}{Z_{source}}} \right) \quad (8)$$

$$P_{max} = \frac{V^2}{4Z_{source}} \quad (9)$$

The impedance matching circuit can be considered as a two-port network that can be described with equation (10). The matching conditions are satisfied when the parameters are equal to equation (11).

$$\begin{pmatrix} V_1 \\ I_1 \end{pmatrix} = \begin{pmatrix} A & B \\ C & D \end{pmatrix} \begin{pmatrix} V_2 \\ I_2 \end{pmatrix} \quad (10)$$

$$Z_{source} = \sqrt{\frac{AB}{CD}} \quad (11)$$

$$Z_{load} = \sqrt{\frac{DB}{CA}}$$

There are three main types of impedance matching circuits which are L,  $\pi$  and T type. In this paper, the L type matching circuit was used to match the resonance frequency of the antennas to the frequency of the power source that was fixed at 13.56MHz.

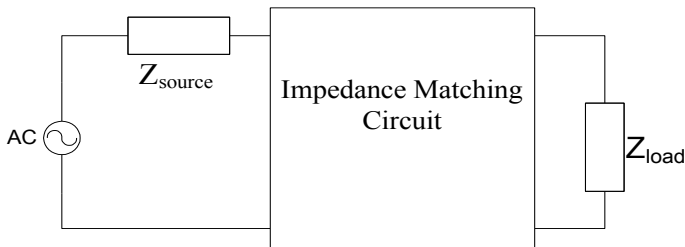


Fig. 6. Theory of impedance matching

#### A. Simulation Results

A simulation was conducted to test the effects of the impedance matching networks on the antennas. The equivalent circuit used in the simulation is shown in Fig. 7, where an impedance matching network is inserted in between the power source and the transmitting antenna. The antenna simulated here is a 5 turn, 15cm radius, 5mm pitch, open type spiral antenna that is self resonating at 13.56MHz. Here, both the input and output impedance,  $Z_{source}$  and  $Z_{load}$  is considered to be  $Z_0$ , 50  $\Omega$ . For simplification purposes, the Ohm loss and radiation loss of the antenna, R is considered 0  $\Omega$  in the simulation. Using the vector network analyzer (VNA), the L and C parameters of the antennas were calculated to be 10300nH and 13.26pF respectively. The inductor ( $L_1$ ) used in the impedance matching circuit is set at 6000nH, and combined with capacitor  $C_1$  to make a variable inductor. The parameters of the tuning circuit satisfy equation (11), the matching condition of the circuit.

The coupling coefficient k was varied from 0.03 to 0.20, and the frequency characteristics were calculated based on S parameter (Scattering Parameter) theories and confirmed using pSpice. The  $S_{21}$  to frequency graphs are as shown in Fig. 8.

Based on Fig. 8, it is observed that the matching circuit is theoretically capable of changing the resonance frequency of the antennas to 13.56MHz for different air gaps. Also, given that they are two identical antennas, when the coupling weakens, the resonance frequency of the antennas is equal to their self resonance frequency. Therefore, if the self resonance frequency of the antennas is set at 13.56MHz, there will be no need for impedance matching for that air gap. When the gap gets even larger and the coupling becomes weaker, the maximum efficiency of the system drops. This means that the system is at maximum efficiency up to a certain distance, ( 200mm for this antenna ) and becomes a less ideal power transfer system after that distance.

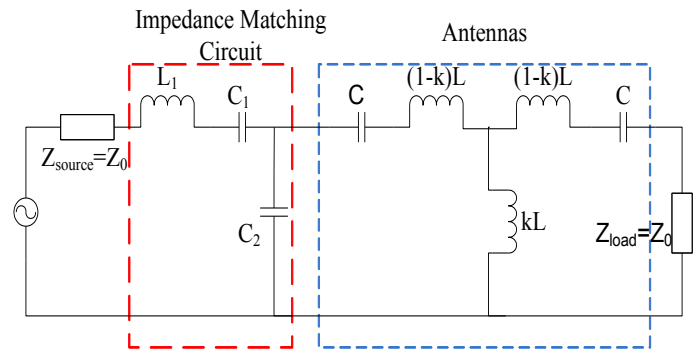


Fig. 7. Equivalent circuit of experiment setup

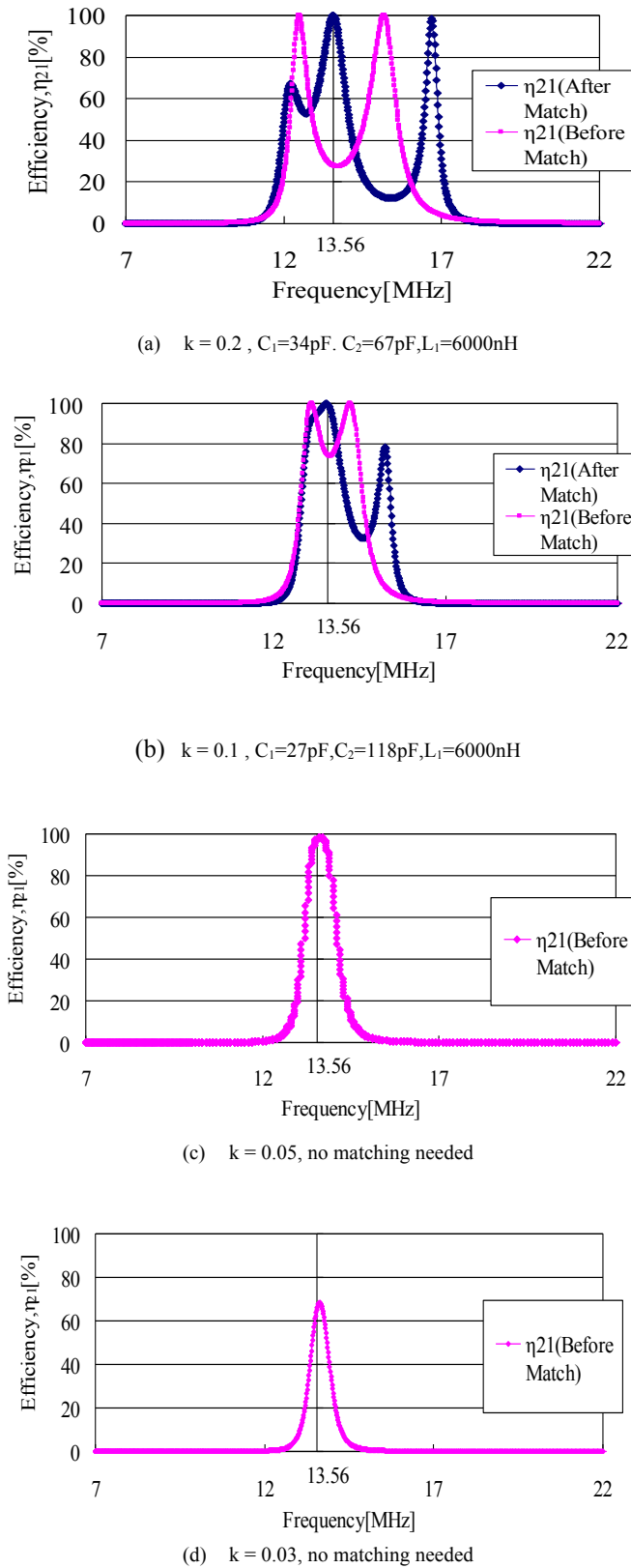


Fig.8 Simulation results. The graphs of pre and post matching antenna frequency characteristics for each coupling coefficient

### A Experiment Setup

The experiment is set up according to Fig. 7. Each antenna is connected to the VNA with coaxial cables. The VNA is used to provide the power source, and to measure the  $S_{11}$  and  $S_{21}$  parameters of the system. The experiment is conducted at low power. The system is expected to function similarly in high power situations as stated in [2].

Fig. 9 shows a picture of the antenna used in the experiment with the tuning circuit attached to it. The inductor is made using a coil and a ferrite core, and multiple ceramic condensers connected in parallel are used to form the capacitors  $C_1$  and  $C_2$ .

In this experiment, the air gap is fixed at 9cm with the antennas coaxial (no displacement along the x-y plane). The coupling coefficient  $k$  here is estimated to be 0.135 based on electromagnetic analysis and pre-match resonance frequencies of the system.

### B. Experiment Results and Comparisons with Simulations

Fig. 10. shows the comparisons of the simulation results and the experiment results. Here, the parameters used in the matching system for both the simulation and the experiments are  $C_1=32\text{pF}$ ,  $C_2=78\text{pF}$ . With inductor  $L_1$  fixed at approximately 5750nH.

The experiment results show that the resonance frequency can be tuned to match 13.56MHz with an impedance matching circuit, and the efficiency at that frequency is increased from 50% to 70%. Also, the equivalent circuit model can be used to estimate the frequency characteristics of the pre and post matched systems.

In the post matched system experiment result, the efficiency  $\eta_{21}$  at the resonance frequency is lower than that of the simulation result. However, it can be said that the loss is not due to a mismatched system as the power reflection ratio  $\eta_{11}$  is extremely low, meaning no power is reflected back to the power source. In other words, the loss is due to other factors such as radiation loss, the low Q value of the system (due to the usage of L type impedance matching networks), loss from the ferrite core used to make the inductor, and Ohmic loss of the inserted matching circuit.

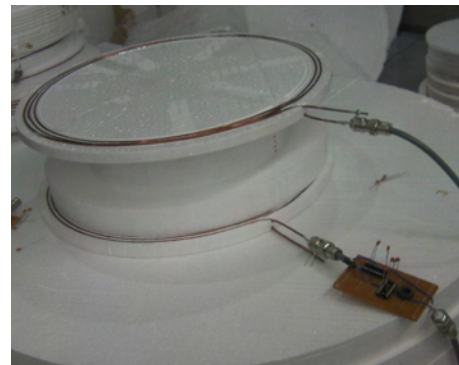
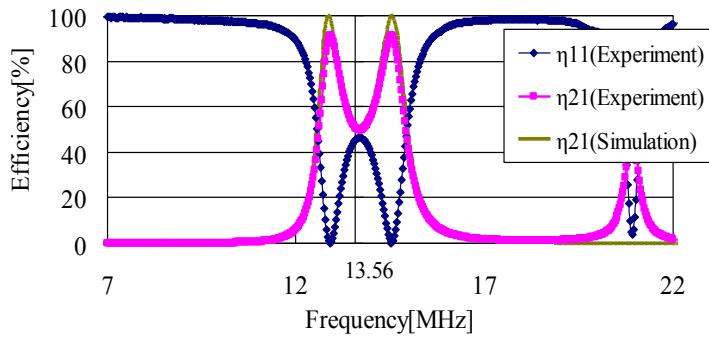
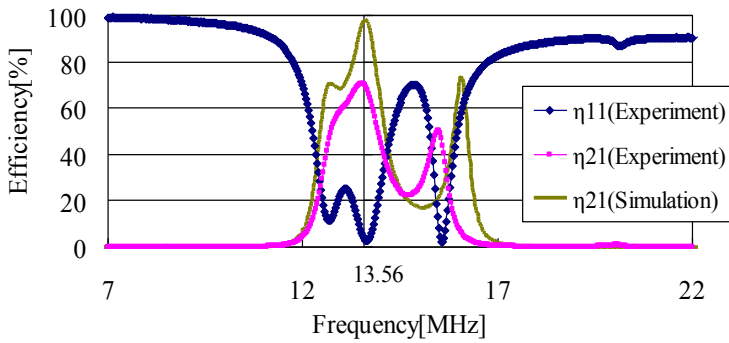


Fig. 9. Transmitting antenna with tuning circuit and receiving antenna used in the experiment



(a) Before Matching



(b) After Matching

Fig. 10. Experiment Results and Comparison with Simulation Results. Here, the parameters used in the matching system are  $C_1=32\text{pF}$ ,  $C_2=78\text{pF}$ . With inductor  $L_1$  fixed at  $5750\text{nH}$  and the gap at  $9\text{cm}$

### CONCLUSION

We studied the frequency characteristics and the power transfer efficiency of the antennas using equivalent circuits, electromagnetic analysis, simulations and experiments. The

resonance frequency of the antennas changes as the air gap changes. Since the maximum power transfer efficiency occurs at the resonance frequency, the resonance frequency must match the frequency of the power source. When this is applied in the MHz range (which allows smaller size antennas), the usable frequency range is bounded by the ISM band. Therefore, a system which uses an impedance matching network to match the resonant frequency of the antennas to a power source fixed at  $13.56\text{MHz}$  was proposed.

The tuning parameters of the impedance matching circuits were estimated using the equivalent circuits. The effects were analyzed with equivalent circuits, electromagnetic analysis, simulations and experiments. The experiment and simulation results show that the resonance frequency of the system can be changed using impedance matching circuits. They also show that the equivalent circuit model can be used to estimate the frequency characteristics.

### REFERENCES

- [1] Andre Kurs, Aristeidis Karalis, Robert Mofatt, J.D Joannopoulos, Peter Fisher, Marin Soljacic, "Wireless Power Transfer via Strongly Coupled Magnetic Resonance", Science Express, 7 June 2007, Vol. 317. no. 5834, pp. 83-86
- [2] Takehiro Imura, Hiroyuki Okabe, Yoichi Hori, "Basic Experimental Study on Helical Antennas of Wireless Power Transfer for Electric Vehicles by using Magnetic Resonant Couplings", Vehicle Power and Propulsion Conference, 2009.IEEE Pages 936-940
- [3] Aristeidis Karalis, J.D. Joannopoulos and Marin Soljacic, "Efficient wireless non-radiative mid-range energy transfer," Annals of Physics, Volume 323, Issue 1, January 2008, Pages 34-48, January Special Issue 2008
- [4] Takehiro Imura, Yoichi Hori, "Wireless Power Transfer using Electromagnetic Resonant Coupling", The Journal of The Institute of Electrical Engineers of Japan, Vol129, No.7, 2009.7
- [5] Takehiro Imura, Toshiyuki Uchida, Yoichi Hori, "Experimental Analysis of High Efficiency Power Transfer using Resonance of Magnetic Antennas for the Near Field - Geometry and Fundamental Characteristics -", IEE Japan Industry Applications Society Conference, No.2-62, pp.539-542, Kochi, Japan, 2008.8.
- [6] N.Shinohara, H. Matsumoto, "Wireless Charging System by Microwave Power Transmission for Electric Motor Vehicles", IEICE.C, VolJ87-C, No.5, pp.433-443, 2004

# Multi-receiver and Repeater Wireless Power Transfer via Magnetic Resonance Coupling – Impedance Matching and Power Division Utilizing Impedance Inverter

K. E. Koh<sup>\*</sup>, T. C. Beh<sup>\*\*</sup>, T. Imura<sup>\*\*</sup>, and Y. Hori<sup>\*\*</sup>

<sup>\*</sup>Department of Electrical Engineering, The University of Tokyo, Japan

<sup>\*\*</sup>Department of Advance Energy, The University of Tokyo, Japan

**Abstract**—Future applications of wireless power transfer will include powering various devices in a room, charging electric vehicles in a parking area, charging moving robots and so on. Therefore practical wireless power transfer must be able to support complicated configurations for example combination of multi-receiver and repeaters. Many past works have discussed on methods for improving efficiency and more recently extended the methods to multi-receiver system. However controllable power division among receivers is also an important feature as receivers nearer to the transmitter tend to absorb more power compared to further antennas. In this paper, a new impedance matching and power division method utilizing impedance inverters only at receiver sides is proposed. The mathematical equations in the proposed method are then generalized for arbitrary number of receivers and arbitrary number of repeaters.

**Index Terms**—Magnetic Resonance Coupling, Multi-Receiver and Repeaters, Power Division, Wireless Power Transfer

## I. INTRODUCTION

An ideal wireless power transfer must be able to transfer power efficiently regardless of the receiving end at least in the effective region. However magnetic resonance coupling method is efficient only in a fixed distance and orientation. When the receiver is moved away from its optimal operating point, the efficiency falls off rapidly [1]. Furthermore, in a wireless power transfer consist of multiple receivers, the receiver nearer to the transmitter tend to absorb more power [2]. Many past papers have proposed different ways to resolve the efficiency issue but not on power distribution.

Paper [3]-[5] explored the possibilities of multi-receiver system using either equivalent circuit or coupled mode theory. Efficiency analysis at different conditions are provided but methods for improving efficiency and power distribution are not proposed. Often wireless power transfer is analyzed using equivalent circuit [3] [6]-[11], however the equations for system with more antennas quickly becomes complex or rigorous to be analyzed [3][9]. Therefore, band-pass filter representations is proposed by [12][13]. The design equations are very simple even with many repeaters added in the power transfer system. However the

method is impractical due to inapplicable to multi-receiver and all the antennas' positions need to be controllable.

Other attempts include adding and adjusting a third coil to improve the transfer efficiency [14][15]. The method however is limited to specific case. Frequency tracking method where the frequency of the source is varied for different conditions has also been proposed [1][16][17]. Efficiency improvement using this method is only obtainable when the antennas are strongly coupled. In practical applications, the wireless power transfer should stay inside an allowable industrial, scientific and medical band which is narrow. Therefore, tuning frequency is not a feasible method for wireless power transfer. In [7][18], impedance matching circuit is inserted in the transmitter side based on equivalent circuit model. Transfer efficiency is optimized regardless of the receiving end. However controllable power distribution is not possible using this method.

In a multi-receiver system, not only the transfer efficiency is important but also the power distribution among the receivers. Power distribution depends on both the load impedances and the relative positions of the receivers to the transmitter. Assuming identical load connected to each receiver, the receiver nearer to the transmitter tend to absorb most of the power while the further receiver may not obtain enough to function properly. In this paper, method for impedance matching and controllable power division is proposed. The design equations are derived and then generalized for arbitrary number of receivers and arbitrary number of repeaters. Simulations using LTspice were performed to validate the new method.

## II. MULTI-RECEIVER WIRELESS POWER TRANSFER

Fig. 1 shows an equivalent circuit of a two-receiver wireless power transfer. The coupling in between the top receiver and transmitter is  $k_{12}$  while the coupling in between the bottom receiver and transmitter is  $k_{13}$ . Cross coupling in between the two receivers is assumed to be zero in this method. The couplings between antennas are expressible in terms of impedance inverter [19]:

$$k_{12} = \frac{K_{12}}{\omega_0 \sqrt{L_1 L_2}} \quad k_{13} = \frac{K_{13}}{\omega_0 \sqrt{L_1 L_3}}, \quad (1)$$



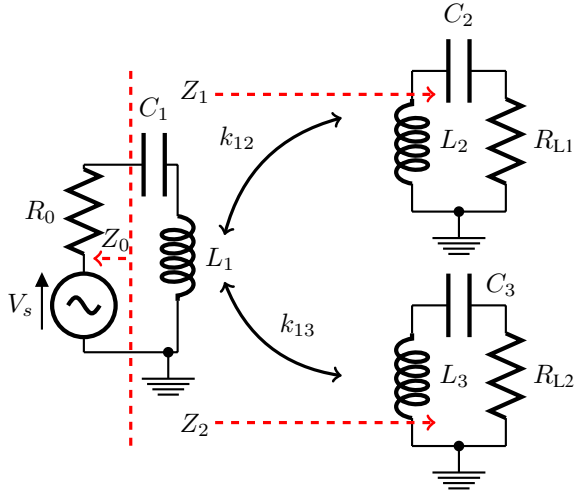


Figure 1. Equivalent circuit of a two-receiver system.

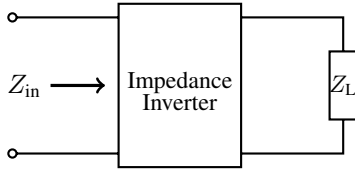


Figure 2. Operation of impedance inverter.

where  $K_{12}$  and  $K_{13}$  are inverters' characteristic impedance.

Impedance inverter as the name implies inverts the impedance connected to the inverter. Fig. 2 and (2) show the impedance  $Z_{in}$  looking into the impedance inverter that is connected to load,  $Z_L$ . There are many applications and many types of impedance inverter [20]. In this paper, impedance inverter is used to represent the couplings between antennas given by (1) and also impedance matching which will be explained in later part of this section.

$$Z_{in} = \frac{K^2}{Z_L}. \quad (2)$$

External coupling coefficient is the ratio of the resonator's termination resistance to the resonator's "reactance slope parameter" [12][19]:

$$k_{01} = \frac{R_0}{\omega_0 L_1} \quad k_{23,1} = \frac{R_{L1}}{\omega_0 L_2} \quad k_{23,2} = \frac{R_{L2}}{\omega_0 L_3}. \quad (3)$$

Assuming all the antennas possess similar resonant frequencies and that the power source is also operating at very near these resonant frequencies, the impedances of all the antennas are therefore ignorable. From Fig. 1, (1), (2) and (3):

$$Z_0 = R_0 = k_{01} \omega_0 L_1$$

$$Z_1 = \frac{K_{12}^2}{R_{L1}} = \frac{k_{12}^2}{k_{23,1}} \omega_0 L_1$$

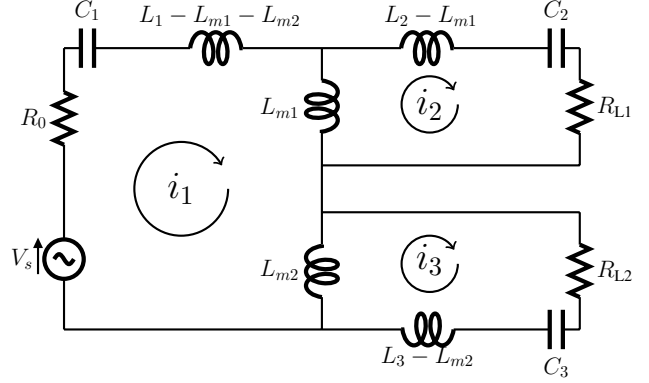


Figure 3. Alternative circuit of two-receiver wireless power transfer.

$$Z_2 = \frac{K_{13}^2}{R_{L2}} = \frac{k_{13}^2}{k_{23,2}} \omega_0 L_1. \quad (4)$$

Where  $Z_1$  is the impedance looking from the source to the top receiver in Fig. 1 and  $Z_2$  is the impedance looking from the source to the bottom receiver.

Circuit in Fig. 1 is redrawn in Fig. 3 with mutual inductance terms to derive impedance matching and power division equations. The current loop equations for Fig. 3 are given as:

$$\begin{aligned} V_s &= i_1 R_0 - i_2 j \omega_0 L_{m1} - i_3 j \omega_0 L_{m2} \\ 0 &= i_2 R_{L1} - i_1 j \omega_0 L_{m1} \\ 0 &= i_3 R_{L2} - i_1 j \omega_0 L_{m2}. \end{aligned} \quad (5)$$

Solving current  $i_2$  and  $i_3$  in terms of  $i_1$  and replace the load impedances and mutual inductances with (1) and (3):

$$\frac{V_s}{i_1} = k_{01} \omega_0 L_1 + \frac{k_{12}^2}{k_{23,1}} \omega_0 L_1 + \frac{k_{13}^2}{k_{23,2}} \omega_0 L_1. \quad (6)$$

Equation (6) implies that circuit in Fig. 1 and Fig. 3 can be simplified into circuit shown in Fig. 4. The first term in (6) is the power supply termination impedance, the second term is impedance  $Z_1$  and third term is impedance  $Z_2$  in Fig. 1. Using maximum power transfer theorem [21], impedance matching is achieved when:

$$\begin{aligned} Z_0 &= Z_1 + Z_2 \\ k_{01} &= \frac{k_{12}^2}{k_{23,1}} + \frac{k_{13}^2}{k_{23,2}}. \end{aligned} \quad (7)$$

and because of same current flowing through  $Z_1$  and  $Z_2$ , power division ratio is:

$$\begin{aligned} Z_1 &: Z_2 \\ \frac{k_{12}^2}{k_{23,1}} &: \frac{k_{13}^2}{k_{23,2}}. \end{aligned} \quad (8)$$

For controllable power division and impedance matching without having to change the antennas' positions, the external coupling coefficients of all the receivers should

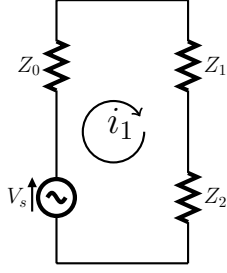


Figure 4. Simplified two-receiver circuit.

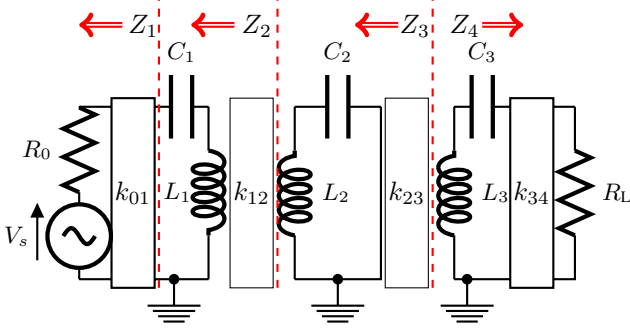


Figure 5. Equivalent circuit for wireless power transfer with repeater.

be modifiable. Impedance inverter circuits are inserted in between the receiver antennas and the load so that the new external coupling coefficients' values are [19]:

$$k_{23,1} = \frac{K_{23,1}^2 / R_{L1}}{\omega_0 L_2} \quad k_{23,2} = \frac{K_{23,2}^2 / R_{L2}}{\omega_0 L_3}. \quad (9)$$

Where  $K_{23,1}$  and  $K_{23,2}$  are the characteristic impedances of the inverters to be implemented in the top receiver and bottom receiver respectively. The impedance inverter circuit implemented throughout this paper is the same as in [2].

In addition to deriving impedance matching and power division method, (6) also provides important information regarding multi-receiver wireless power transfer. Firstly, receivers appear as series connection viewing from the source. Secondly, assuming same antennas are utilized in the system, power distribution is proportional to square of coupling coefficients and inversely proportional to the load impedances.

### III. NEW IMPEDANCE MATCHING METHOD FOR SYSTEM WITH REPEATERS

Although wireless power transfer via magnetic resonance coupling is able to transmit power more efficiently compared to induction method, the transmittable distance is still limited to a few meters. This range is extendable by using repeater antennas. However as more antennas are added into the system, existing equivalent circuit equations quickly become complicated. Paper [22] resort to search algorithms and [9] uses computer aided design (CAD). Band-pass filter design method is simple but is impractical due to stringent conditions exerted by band-pass filter equations. In this paper, not only power division

methods, but also new impedance matching method for wireless power transfer with repeaters is proposed. The new method combines the advantages of both existing equivalent circuit and band-pass filter method.

Consider a wireless power transfer with a repeater antenna in between the transmitter and receiver and cross coupling does not exist. The equivalent circuit is shown in Fig. 5. Assuming impedance matching is to be performed by modifying impedance  $Z_4$  in Fig. 5, therefore

$$Z_4 = Z_3. \quad (10)$$

In order to satisfy (10), the required  $k_{34}$  is to be calculated. Using (2) and Fig. 5:

$$\begin{aligned} Z_1 &= R_0 \\ Z_2 &= \frac{K_{12}^2}{Z_1} \\ Z_3 &= \frac{K_{23}^2}{Z_2}. \end{aligned} \quad (11)$$

Again assuming the system is in resonance and therefore impedance of the antennas are ignorable. Using the same form of equations as in (1) and (3) and equalizing  $Z_4$  to  $Z_3$ , the required  $k_{34}$  is derived:

$$k_{34} = k_{01} \times \frac{k_{23}^2}{k_{12}^2}. \quad (12)$$

An impedance inverter can be inserted in the box labelled  $k_{34}$  in Fig. 5 to realise (12).

### IV. GENERALIZATION EQUATION FOR SYSTEM WITH BOTH MULTI-RECEIVER AND REPEATERS

The equations derived in Sec. II and Sec. III are expandable for wireless power transfer with arbitrary number of repeaters and arbitrary number of receivers. Consider a wireless power transfer with  $m$  number of receivers and  $(n - 2)$  number of repeaters for each receiver in Fig. 6. Impedance inverters are inserted in between every receiver antenna and the corresponding load for impedance matching and power division. The number of repeaters in each transmission path need not be the same. Cross coupling between all the repeaters and receivers are assumed to be zero. External coupling coefficient  $k_{01}$  in (13) can be broken down into  $m$ -number of parts:

$$k_{01} = \frac{R_0}{\omega_0 L_1} = \sum_{i=1}^{i=m} k_{01,i}. \quad (13)$$

According to (8), the percentage of power received by each receiver will be:

$$i \mid_{i=1 \text{ to } m} = \frac{k_{01,i}}{k_{01}} \times 100\%. \quad (14)$$

Finally, the external coupling coefficient of each receiver has to be:

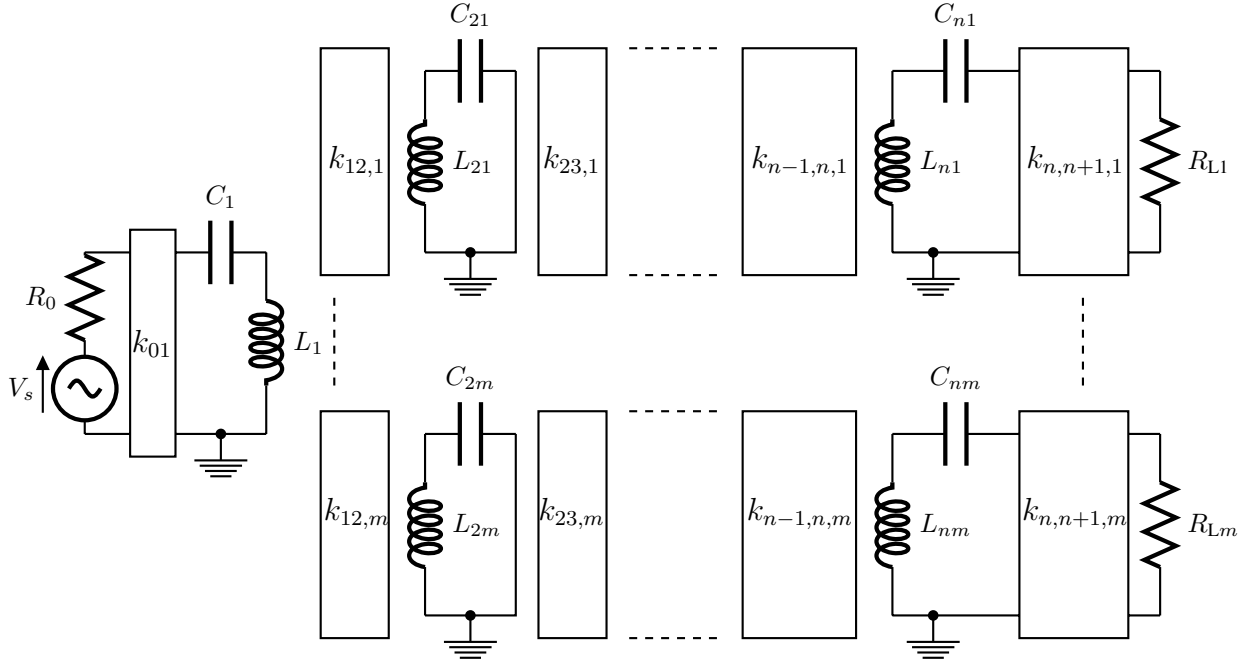


Figure 6. Wireless power transfer with arbitrary number of receivers and repeaters.

$$k_{n,n+1,i} \mid_{i=1 \text{ to } m} = k_{01,i}^{(-1)^{n+1}} \times \prod_{j=1}^{j=n-1} k_{j,j+1,i}^{2(-1)^{j+1+n}}. \quad (15)$$

Where  $k_{n,n+1,i} \mid_{i=1 \text{ to } m}$  is realisable using impedance inverters:

$$k_{n,n+1,i} \mid_{i=1 \text{ to } m} = \frac{(K_{n,n+1,i \mid_{i=1 \text{ to } m}})^2 / R_{Li}}{\omega_0 L_{ni}}. \quad (16)$$

## V. SIMULATION RESULT

Calculations and simulation results of multi-receiver and repeater cases are given in this section to demonstrate the proposed power division method. The equivalent circuit of a two-receiver system and with one repeater inserted between the first receiver and the transmitter is simulated using LTspice. Cross coupling in between the receivers and repeaters are assumed to be zero in this paper. The element values of the system are listed below:

$$\begin{aligned} \omega_0 &= 2\pi \times 13.56 \text{ MHz} \\ L_1 &= L_{21} = L_{31} = L_{22} = 10 \mu\text{H} \\ C_1 &= C_{21} = C_{31} = C_{22} = 13.8 \text{ pF} \\ R_0 &= R_{L1} = R_{L2} = 50 \Omega \\ k_{12,1} &= k_{23,1} = 0.05 \\ k_{12,2} &= 0.1. \end{aligned}$$

The internal resistances of the antennas are set to zero in this simulation. The power ratio  $P_1 : P_2$  for this first simulation is set to 1, where  $P_1$  is the power received by

load  $R_{L1}$  and  $P_2$  is the power received by load  $R_{L2}$ . Using (13) to (16):

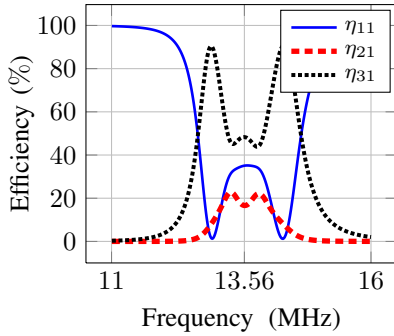
$$\begin{aligned} k_{01} &= 0.0587 \\ k_{01,1} &= k_{01,2} = 0.0293 \\ k_{34,1} &= 0.0293 \\ k_{23,2} &= 0.3413 \\ K_{34,1} &= 35 \Omega \\ K_{23,2} &= 121 \Omega. \end{aligned}$$

Fig. 7(a) shows the simulation result before applying the method. Due to impedance mismatched, the reflection ratio,  $\eta_{11}$  is around 35% at the resonance frequency 13.56 MHz. The transmission efficiency,  $\eta_{21}$  to the first receiver, which is separated with the transmitter by a repeater antenna is around 16%. The transmission efficiency,  $\eta_{31}$  to the third receiver is around 48%. The simulation result after inserting inverter circuits with characteristic impedance calculated above is shown in Fig. 7(b). Reflection ratio is suppressed to almost none, and both receivers obtain almost equalised power as desired.

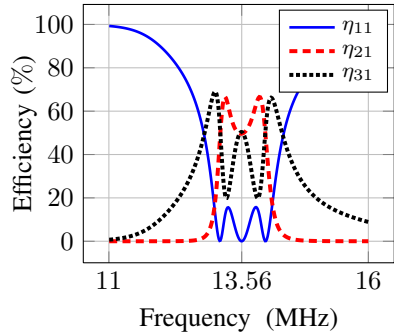
In the second simulation, power ratio  $P_1 : P_2$  is set to be  $\frac{7}{3}$ . Using the same calculation steps as the previous simulation case, the characteristic impedance of the inverters to be inserted in the first receiver and second receiver are respectively:

$$\begin{aligned} K_{23,1} &= 42 \Omega \\ K_{23,2} &= 156 \Omega. \end{aligned}$$

Fig. 8 shows the simulation result after applying the method. Similar to equal power distribution case, reflection



(a)



(b)

Figure 7. Simulation result of equal power division: a) before impedance matching. b) after impedance matching.

ratio,  $\eta_{11}$  is suppressed to almost none. Transmission efficiency,  $\eta_{21}$  to the first receiver is around 70% and transmission efficiency,  $\eta_{31}$  to the third receiver is around 30% as desired.

Above two simulation cases are performed without considering internal resistances of the antennas to validate the proposed equations. The equal power distribution case with internal resistances of all the antennas set to  $1 \Omega$  is simulated. Fig. 9 shows that the frequency response with  $1 \Omega$  internal resistance is close to the response of Fig. 7(b). Therefore it is reasonable to omit the values in the method's equations as magnetic resonance coupling antennas should have low internal resistances [23]. Reflection ratio,  $\eta_{11}$  is still close to none, however both transmission efficiencies are lower in this case with  $\eta_{21}$  equal to 46.7% and  $\eta_{31}$  equal to 48.5%. Derivation of loss equations for various configuration of wireless power transfer is reserved for future work.

## VI. CONCLUSION

In a multi-receiver wireless power transfer via magnetic resonance coupling, not only high transfer efficiency but also controllable power division is important. New impedance matching and power division method is proposed and generalized for arbitrary number receivers and arbitrary number of repeaters. Due to systematic circuit representation using impedance inverter, the design equations are simple. Impedance matching and power division conditions are in terms of coupling coefficients. In order to exert controllable power division without having to change

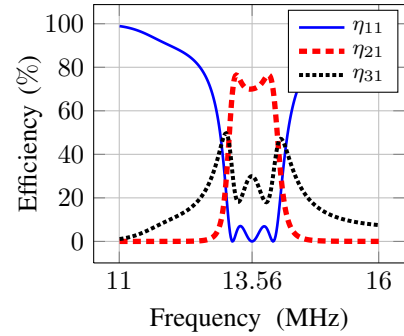


Figure 8. Simulation result of 70%-30% power division after impedance matching.

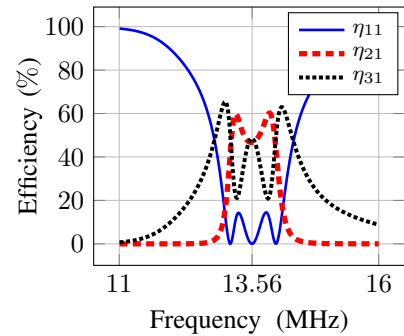


Figure 9. Simulation result of equal power distribution considering internal resistance after impedance matching.

the antennas' position, the external coupling coefficients of the receivers can be modified by inserting impedance inverter circuit in between receiver and the corresponding termination resistor.

Future work of this research includes derivation of loss equations, cross coupling consideration and construction of automatic impedance matching and power division system.

## VII. ACKNOWLEDGEMENT

The authors would like to thank the following people for their support during the course of this effort: Prof. Hiroshi Fujimoto, Dr. Alexander Viehweider, Masaki Kato, Hongzhong Zhu and Vissuta Jiwariyavej.

## REFERENCES

- [1] A. P. Sample, D. A. Meyer, and J. R. Smith, "Analysis, experimental results, and range adaptation of magnetically coupled resonators for wireless power transfer," *IEEE Trans. Ind. Electron.*, vol. 58, no. 2, pp. 544-554, Feb. 2011.
- [2] K. E. Koh, T. C. Beh, T. Imura, and Y. Hori "Novel band-pass filter model for multi-receiver wireless power transfer via magnetic resonance coupling and power division," *2012 IEEE 13th Annu. Wireless and Microwave Technology Conf. (WAMICON)*, pp. 1-6, Apr. 2012.
- [3] B. L. Cannon, J. F. Hoburg, D. D. Stancil, and S. C. Goldstein, "Magnetic resonant coupling as a potential means for wireless power transfer to multiple small receivers," *IEEE Trans. Power Electron.*, vol. 24, no. 7, pp. 1819-1825, Jul. 2009.
- [4] A. Kurs, R. Moffatt, M. Soljagic, "Simultaneous mid-range power transfer to multiple devices," *Appl. Physics Lett.*, vol.96, no.4, pp. 044102-044102-3, Jan. 2010.

- [5] J.W. Kim et al., "Analysis of wireless energy transfer to multiple devices using CMT," *2010 Asia-Pacific Microwave Conf. Proc. (APMC)*, pp.2149-2152, Dec. 2010.
- [6] T. Imura, "Study on maximum air-gap and efficiency of magnetic resonant coupling for wireless power transfer using equivalent circuit," *IEEE Int. Symp. Ind. Electron. (ISIE 10)*, Jul. 2010, pp. 3664-3669.
- [7] T. C. Beh, M. Kato, T. Imura and Y. Hori, "Basic Study of Improving Efficiency of Wireless Power Transfer via Magnetic Resonance Coupling Based on Impedance Matching," *IEEE Int. Symp. Ind. Electron. (ISIE 10)*, Jul. 2010, pp. 2011-2016.
- [8] T. Imura and Y. Hori, "Maximizing air gap and efficiency of magnetic resonant coupling for wireless power transfer using equivalent circuit and neumann formula," *IEEE Trans. Ind. Electron.*, vol. 58, no. 10, pp. 4746-4752, Oct. 2011.
- [9] M. Dionigi and M. Mongiardo, "CAD of efficient wireless power transmission systems," *IEEE MTT-S Int. Microwave Symp. Dig. (MTT)*, Jun. 2011, pp. 1-4.
- [10] S. Cheon et al., "Circuit-model-based analysis of a wireless energy-transfer system via coupled magnetic resonances," *IEEE Trans. Ind. Electron.*, vol. 58, no. 7, pp. 2906-2914, Jul. 2011.
- [11] F. Z. Shen et al., "Circuit analysis of wireless power transfer by "coupled magnetic resonance";" *IET Int. Communication Conf. Wireless Mobile and Computing (CCWMC 2009)*, Dec. 2009, pp. 602-605.
- [12] I. Awai, T. Komori, "A simple and versatile design method of resonator-coupled wireless power transfer system," *2010 Int. Conf. Communications, Circuits and Systems (ICCCAS)*, Jul. 2010, pp. 616-620.
- [13] I. Awai, T. Komori, T. Ishizaki, "Design and experiment of multi-stage resonator-coupled WPT system," *2011 IEEE MTT-S Int. Microwave Workshop Series on Innovative Wireless Power Transmission: Technologies, Systems, and Applications (IMWS)*, pp.123-126, May. 2011.
- [14] J. W. Kim, H. C. Son, K. H. Kim, Y. J. Park, "Efficiency analysis of magnetic resonance wireless power transfer with intermediate resonant coil," *IEEE Antennas Wireless Propag. Lett.*, vol. 10, pp. 389-392, 2011.
- [15] N. Oodachi et al., "Efficiency improvement of wireless power transfer via magnetic resonance using transmission coil array," *2011 IEEE Int. Symp. Antennas and Propagation (APSURSI)*, pp. 1707 - 1710, Jul. 2011.
- [16] W. Fu, B. Zhang, D. Qiu, "Study on frequency-tracking wireless power transfer system by resonant coupling," *IEEE 6th Int. Power Electronics and Motion Control Conf.*, pp. 2658-2663, May 2009.
- [17] Y. Tak et al., "Investigation of adaptive matching methods for near-field wireless power transfer," *IEEE Trans. Antennas Propag.*, Vol. 59, pp. 1769-1773, May 2011.
- [18] T. Imura, "Optimization using transmitting circuit of multiple receiving antennas for wireless power transfer via magnetic resonance coupling," *2011 IEEE 33rd Int. Telecommunications Energy Conf. (INTELEC)*, pp. 1-4, Oct. 2011.
- [19] G. L. Matthaei, L. Young, and E. M. T. Jones, *Microwave Filters, Impedance Matching Networks and Coupling Structures*. Norwood, MA: Artech House, 1980.
- [20] R. E. Collin, *Foundations for Microwave Engineering*, 2<sup>nd</sup> ed., NJ:John Wiley and Sons, Inc., 2001.
- [21] J. D. Irwin , R. M. Nelms, *Basic Engineering Circuit Analysis*. 10<sup>th</sup> ed., NJ:John Wiley & Sons, Inc., 2010.
- [22] T.C. Beh, "Automated impedance matching system for robust wireless power transfer via magnetic resonance coupling," M.S. thesis, Dept. Advance Energy, The University of Tokyo, Kashiwa, Chiba, 2011.
- [23] A. Karalis, J. D. Joannopoulos, and M. Soljaicic, "Efficient Wireless Non- Radiative Mid-Range Energy Transfer," *Ann. Phys.*, Vol. 323, No. 1, Jan. 2008, pp. 34-38, doi:10.1016/j.aop.2007.04.017.